Exploring quantum circuits with a cQED architecture: application to compressibility measurements.

Matthieu Desjardins

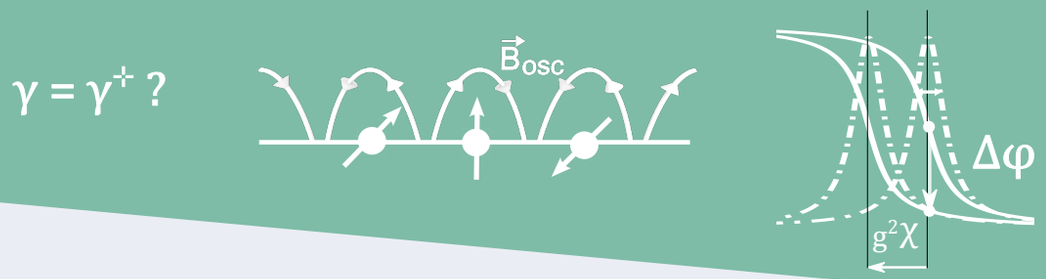

On-chip electronic circuits at cryogenic temperature are instrumental to studying the quantum behavior of electrons. In particular, quantum dots circuits represent tunable model systems for the study of strong electronic correlations, epitomized by the Kondo effect. In this thesis, carbon nanotube based-quantum dot circuits are embedded in coplanar microwave cavities, with which circuit quantum electrodynamics (cQED) has reached an outstanding degree of control of the light-matter interaction. Here, microwave cavity photons are used to probe the charge dynamics in the quantum dots circuit. More precisely, the high finesse cavity allows us to measure the compressibility of the electron gas in a dot with an unprecedented sensitivity.

Simultaneous measurements of electronic transport and compressibility show that the Kondo resonance observed in the conductance is transparent to microwave photons. This reveals the predicted frozen charge dynamics in the quantum dot for this peculiar mechanism of electron transport and illustrates that the many-body Kondo resonance in the conductance is associated to correlations arising from spin fluctuations of a frozen charge.

A second quantum phenomenon addressed in this thesis is the possible emergence of a new quasi-particle in condensed matter, called Majorana bound state, which would be its own anti-particle. For that purpose, a ferromagnetic gate has been placed below a nanotube in order to generate a synthetic spin-orbit coupling. The observation of Andreev bound states in such a device is a first promising step towards the detection with a cQED architecture of Majorana bound states in a carbon nanotube.

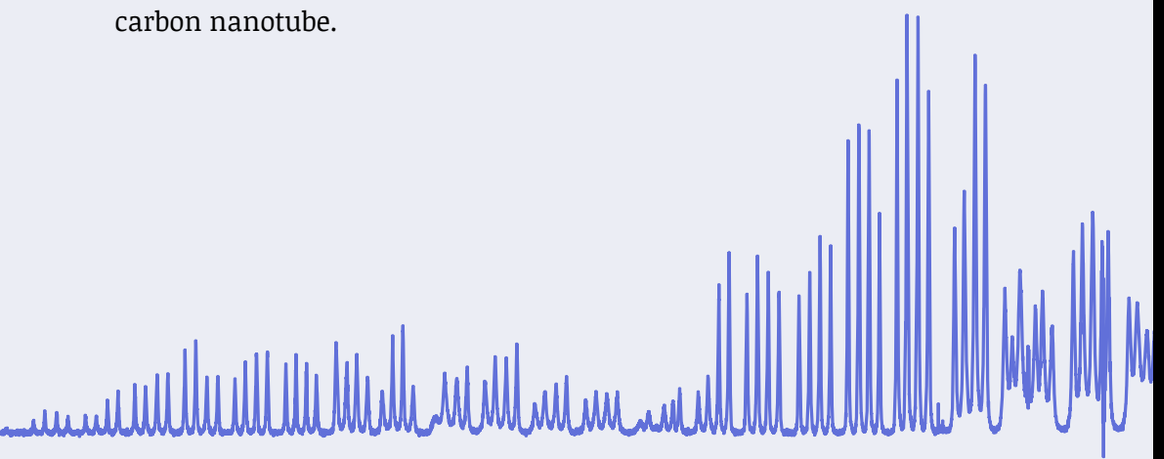

Matthieu Desjardins — Exploring quantum circuits with a cQED architecture — 2016

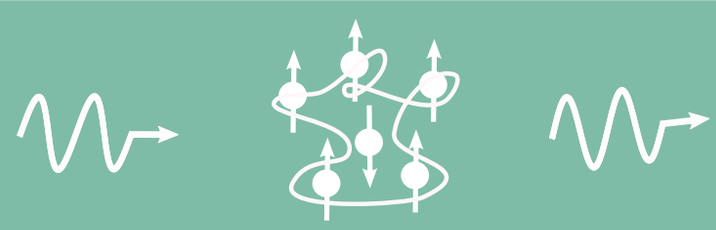

Exploring quantum circuits with a cQED architecture: application to compressibility measurements.

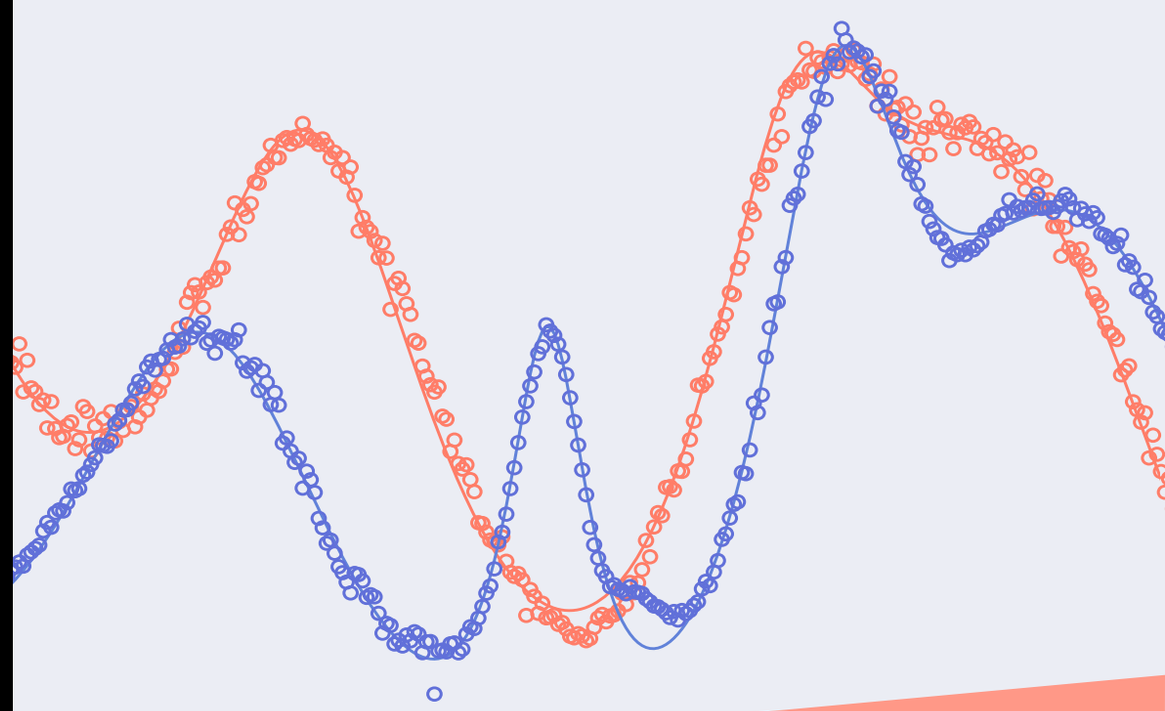

Matthieu Desjardins

lpa

ENS

THÈSE DE DOCTORAT
de l'Université de recherche
Paris Sciences Lettres –
PSL Research University

préparée à
l'École normale supérieure

Exploring quantum circuits with a cQED architecture: application to compressibility measurements

par Matthieu Desjardins

École doctorale n°564
Spécialité: Physique
Soutenue le 16.12.2016

Composition du Jury :

M. Jesper Nygård
University of Copenhagen
Rapporteur

M. Klaus Ensslin
ETH Zürich
Rapporteur

Mme. Hélene Bouchiat
Université Paris Sud
Examinatrice

M. Cristian Urbina
CEA Saclay
Examinateur

M. Christoph Bruder
University of Basel
Examinateur

M. Takis Kontos
Ecole Normale Supérieure
Directeur de thèse

ENS ÉCOLE NORMALE SUPÉRIEURE | PSL RESEARCH UNIVERSITY PARIS

Abstract

On-chip electronic circuits at cryogenic temperature are instrumental to studying the quantum behavior of electrons. In particular, quantum dot circuits represent tunable model systems for the study of strong electronic correlations, epitomized by the Kondo effect. In this thesis, carbon nanotube based-quantum dot circuits are embedded in coplanar microwave cavities, with which circuit quantum electrodynamics (cQED) has reached a high degree of control of the light-matter interaction. Here, microwave cavity photons are used to probe the charge dynamics in the quantum dot circuit. More precisely, the high finesse cavity allows us to measure the compressibility of the electron gas in the dot with an unprecedented sensitivity.

Simultaneous measurements of electronic transport and compressibility show that the Kondo resonance observed in the conductance is transparent to microwave photons. This reveals the predicted frozen charge dynamics in the quantum dot for this peculiar electron transport mechanism and illustrates that the many-body Kondo resonance in the conductance is associated to correlations arising from spin fluctuations of a frozen charge.

A second quantum phenomenon addressed in this thesis is the possible emergence of a new quasi-particle in condensed matter, called Majorana bound state, which would be its own anti-particle. For that purpose, a ferromagnetic gate has been placed below a nanotube in order to generate a synthetic spin-orbit coupling. The observation of Andreev bound states in such a device is a first promising step towards the detection with a cQED architecture of Majorana bound states in a carbon nanotube.

Key words : Mesoscopic physics, Carbon nanotube quantum dots, Cavity quantum electrodynamics, Kondo effect, Electronic compressibility, Majorana fermions.

Résumé

Les circuits électroniques mesurés à des températures cryogéniques permettent d'étudier le comportement quantique des électrons. En particulier, les circuits de boites quantiques sont des systèmes accordables modèles pour l'étude des électrons fortement corrélés, symbolisée par l'effet Kondo. Dans cette thèse, des circuits de boîtes quantiques à base de nanotube de carbone sont intégrés à des cavités micro-onde coplanaires, avec lesquelles l'électrodynamique quantique en cavité (cQED) a atteint un degré de contrôle remarquable de l'interaction lumière-matière. Les photons de la cavité micro-onde sont ici utilisés pour sonder la dynamique de charge dans le circuit de boîtes quantiques. Plus précisément, la cavité micro-onde de grande finesse nous a permis de mesurer la compressibilité du gaz d'électrons dans une boîte avec une sensibilité sans précédent.

Des mesures simultanées de transport électronique et de la compressibilité montrent que la résonance Kondo observées dans la conductance est transparente aux photons micro-ondes. Cela révèle le gel de la dynamique de charge dans la boîte quantique pour ce mécanisme particulier de transport d'électrons et illustre que la résonance Kondo à N-corps dans la conductance est associée aux corrélations issues des fluctuations de spin d'une charge gelée.

Nous étudions aussi dans cette thèse la possible émergence d'une nouvelle quasi-particule, appelée état lié de Majorana, et qui serait sa propre anti-particule. Dans ce but, une grille ferromagnétique a été placée sous le nanotube pour créer un couplage spin-orbit artificiel. L'observation d'états d'Andreev dans un tel dispositif est un premier pas prometteur vers la détection avec une architecture cQED d'états liés de Majorana dans les nanotubes de carbone.

Mots clés : Physique mésoscopique, Boîtes quantiques avec des nanotubes de carbone, Electrodynamique quantique en cavité, Effet Kondo, Compressibilité électronique, Fermions de Majorana.

Remerciements

En préambule de ce manuscrit, je voudrais remercier chaleureusement toute l'équipe avec laquelle j'ai passé quatre années passionnantes. Un grand merci à Takis qui a dirigé cette thèse avec un constant enthousiasme, j'ai beaucoup apprécié ta disponibilité et la confiance que tu nous accordes. Tes idées portées par une équipe aux talents multiples ont donné lieu à de belles réalisations expérimentales; j'en décris deux dans ce manuscrit pour lesquelles j'ai été particulièrement impliqué, la mesure de la compressibilité d'un nuage Kondo et la création d'un spin-orbit artificiel avec une grille ferromagnétique. C'est ici l'occasion pour moi de souligner que ce travail est un résultat collectif, réalisé dans une équipe à la bonne humeur constante, emmenée par un directeur de thèse cultivant avec soin sa 'funkiness'. Les coéquipiers que j'ai le plus côtoyés pendant ces quelques années étaient Laure Bruhat et mes deux homonymes, Matthieu Darthailh et Baillergeau. Il y a eu aussi le collègue Jérémie Viennot, parti ensuite pour les terrains d'aventure de Boulder après nos sorties à Fontainebleau et dans les Aravis. Enfin les derniers arrivés qui prennent la relève, Tino Cubaynes et Lauriane Contamin. Les derniers résultats sur le couplage spin-orbit artificiel et l'intriguant pic à énergie nulle, trop récents pour être mentionnés dans cette thèse, n'auraient pu voir le jour sans la contribution de Lauriane. Je tiens aussi à remercier Audrey Cottet dont la proximité avec notre équipe permet d'avoir une description théorique fine des manips, un tel soutien est une chance pour un groupe expérimental. Les travaux de simulation NRG de Mahn-Soo Choi et de Minh-Chu Lee depuis la Corée, pour expliquer la manip Kondo, nous ont aussi été très bénéfiques. J'aimerais aussi remercier André Thiaville et Stanislas Rohart à Orsay, pour m'avoir généreusement et régulièrement fait profiter de leur expertise et mis sur la voie très prometteuse des grilles ferromagnétiques en Cobalt/Platine. Je profite aussi de ce préambule pour remercier tous ceux qui ont relu mon manuscrit, en particulier Lauriane, Audrey et Takis. L'arrivée à la fin de ma thèse de François Mallet et de Zaki Leghtas au sein de l'équipe laisse entrevoir de belles perspectives pour les prochaines manips.

Nos voisins ont tout autant contribué à cette bonne ambiance avec la joyeuse équipe de Qélec, Benjamin Huard, Daniejla Markovic et le duo Emmanuel Flurin et Philipe Campagne, rejoints ensuite par Landri Bretheau, Sébastien Jezouin, Quentin Ficheux, Nathanaël Cottet et Raphaël Lescanne. Sans oublier, un étage au-dessus, la physique méso emmenée par Bernard Placais et Glenwdal Fève, et qui ont contribué à la fidèle équipe d'Antrebloc, j'ai nommé Quentin Wilmart, Arthur Marguerite, Andreas Inhofer, et son compatriote Holger Graaf. Je ne m'aventurerais pas à mentionner tous les collègues opticiens que je croisais avec plaisir aux pots et autres Friday bars, ainsi que dans les couloirs verts de l'ENS. Couleur des couloirs qui m'amène à remercier aussi Bouygues Construction d'avoir un peu pimenté ces années.

Le travail présenté dans ce manuscrit a nécessité de nombreuses heures de fabrication en salle blanche, il convient donc de remercier particulièrement José Palomo et Michaël Rosticher, toujours disponibles, et jamais à court d'idées. Je souhaite aussi saluer l'importante contribution des différents services techniques avec Olivier Andrieu et son équipe, qui ont permis à mon cryostat de ne jamais manquer d'hélium, avec les électroniciens David Darson, Anne Dennis et Philippe Pace pour les amplis et les PCBs, et avec l'atelier qui nous ont fourni toutes les pièces mécaniques. Je souhaite aussi mentionner la précieuse aide de Yann Colin et l'infatigable équipe de Didier Courtiade. Je salue aussi la direction du LPA avec à sa tête Jean-Marc Berroir, et le remarquable travail d'Anne Matignon et Fabienne Reynia, remplacée en cours de thèse par Olga Hodges.

Je souhaite aussi remercier sincèrement les membres de mon jury, Jesper Nygard, Klaus Ensslin, Hélene Bouchiat, Cristian Urbina, et Christophe Bruder, venus du Danemark, de Suisse ou de France pour ma soutenance et qui ont lu attentivement ce manuscrit.

Je terminerai en adressant mes remerciements à ma famille et mes amis qui suivaient avec un intérêt curieux le destin de mes puces refroidies à l'hélium. Je n'ai pas trouvé de nouveaux Bosons, mais peu importe, c'est aussi grâce à vous que ces années parisiennes ont été formidables.

Contents

Introduction

In 1964, Jun Kondo understood a peculiar electronic transport mechanism, involving the quantum nature of the electron, but its observation was at that time limited to bulk material [1, 2]. This physics has recently been studied with an exquisite control in tailored nanosystems [3–5]. Quantum electronic circuits are nowadays instrumental in fundamental physics to simulate and probe fundamental quantum effects.

In this thesis, on-chip electronic circuits were realized to probe quantum behavior of electrons. These microscopic circuits have patterns of typical size of a few hundreds of nanometer, only a thousand times bigger than the size of an atom. By changing the scale of an electronic circuit, the physics laws change and new phenomena, of which manifestations are hidden at our scale, occur. If properly engineered, these on-chip electronic circuits are able to behave like a quantum system. For this reason, they are part of the field of mesoscopic physics, which concerns objects subject to quantum mechanics that can be engineered with human-sized tools.

One of the first and the most famous on-chip circuit is a silicon-based transistor, which is nowadays widely used in our electronic technology. Such a device was used by physicists to demonstrate the wave nature of electrons with the obervation of the electronic resistance quantization [6]. The phase coherence of electronic waves is key to preserve quantum effects at a mesoscopic scale. That is why the quest towards quantum behaviors of electrons was closely linked to the discovery of low disorder materials with high mobility electron gas, where the phase coherence length becomes comparable to the circuit size. Long phase coherence lengths were for example reached for two-dimensional electron gas in circuits made with GaAs heterostructures or later in graphene, a single atomically thin sheet of graphite [7–9]. Such circuits should be placed at very low temperature as the energy scale of the probed quantum phenomena is very small.

In parallel of the quest for novel materials, instrumental techniques have been developed allowing physicists to design electronic circuits with reduced size. If the electron gas is confined on a region with a size of the same order than the electron wavelength, the

dimensionality of the electron gas is reduced. Electron gas can be trapped in a zero-dimensional box, called quantum dot [10]. Electronic transport in quantum dot circuits is at the heart of this thesis.

The smallest electrical wire was discovered by chance in carbon compounds of combustion [11, 12]. This tube is a rolled-up graphene sheet, and happens to host a one-dimensional electron gas with the highest mobility, combined with a low-disorder crystalline structure. The advent of lithography techniques gives the opportunity to integrate nanotubes in electronic circuits and benefit from their promising electronic properties. A carbon nanotube can be contacted with two electrodes and the current flowing in the electrodes is governed by the electron gas in the nanotube. Due to the small size of the tube, interactions between electrons control the electronic transport through it. Because of Coulomb repulsion, the carbon nanotube is a single electron transistor : when switched on by the electrostatic potential of a third electrode, electrons flow only one by one, when switched off, no electron can enter the dot.

Besides charge, electrons have an extra quantum degree of freedom, the spin, which opens a new path for electrons when the transistor is switched off by interactions. This path is only effective at low temperature because it relies on the coherent entanglement of electron spins. A carbon nanotube quantum dot acts as a single magnetic impurity that forms a many-body singlet state with the spins of electrons in the electrodes. This transport mechanism, the Kondo effect, was discovered 80 years ago in bulk material, with diluted ferromagnetic impurities [2]. This effect has become one of condensed matter core topics, as it is a paradigmatic situation of many-body correlations. The observation of this phenomenon in an on-chip circuit that isolates a single magnetic impurity, allows us to investigate the charge dynamics of the impurity. We have measured that although an electrical current is flowing between electrodes that are $500nm$ away, no charge can be added in the nanotube quantum dot. In the Kondo regime, the electron gas trapped in the nanotube is therefore incompressible, the compressibility being defined as $\frac{\partial N}{\partial \mu}$, where N is the number of electrons and μ the chemical potential of the gas.

The measurement of the compressibility of the nanotube electron gas has been realized in this thesis by coupling it to a microwave electromagnetic field [13, 14]. In optics, spectroscopy by absorption of a monochromatic electromagnetic field is a natural way to access internal degrees of freedom. Here we use a high finesse microwave cavity to probe the dynamics of electrons in a quantum dot circuit. A high finesse cavity traps a monochromatic electromagnetic field between two highly reflecting mirrors. The lowest mode of this oscillator can be used as a very sensitive probe to detect the motion of electrons in the quantum dot circuit. Microwave fields present two main advantages : commercially available components have a higher phase stability than their optical

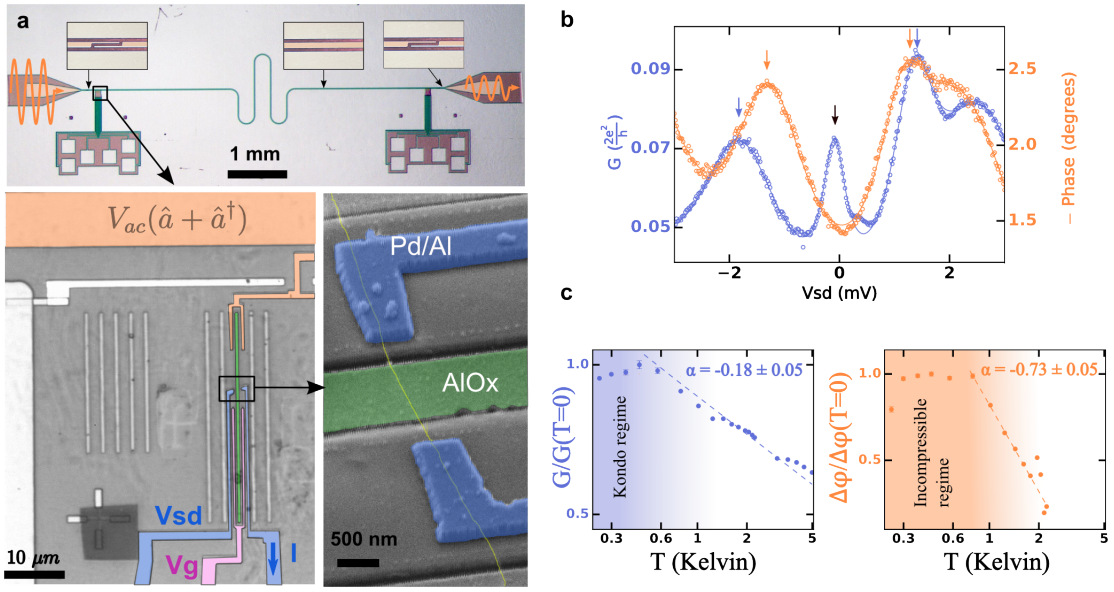

FIGURE 1: **Compressibility measurement of a Kondo quantum dot. a.** A carbon nanotube based quantum dot circuit is capacitively coupled to a coplanar waveguide microwave cavity. The chemical potential of the dot is controlled by the gate voltage V_g. A potential bias V_{sd} is applied between the two electrodes (in blue) which delimit the quantum dot. **b.** Simultaneous bias dependence of the conductance and the microwave phase of a Kondo resonance. The microwave phase is proportional to the compressibility of the quantum dot. The black arrow marks the Kondo resonance. Normal single electron transfer are marked with blue (orange) arrows for the conductance (compressibility). **c.** Temperature dependence of the conductance and the phase on a Kondo ridge. The dashed lines show linear fit in log scale that corresponds to a logarithmic law $-\alpha \log(T)$.

counterparts, as they are less sensitive to mechanical disturbance [15]. The second one is that microwaves couple well to electronic circuits, as cavities can be made from superconducting LC resonator [16]. In the case of a compressibility measurement, one also benefits from a third advantage, which is the fact that the microwave frequency is much smaller than the typical frequencies in a quantum dot circuit. Microwave cavity is therefore a non-invasive probe, which brings additional information to electronic transport on the low-frequency charge dynamics of the circuit.

The idea of coupling quantum dot circuits to microwave cavity is borrowed from the field of circuit Quantum Electrodynamics (cQED). As seminal cavity QED experiments which succeeded to couple a single atom to a single photon in a cavity, cQED has reached an exquisite control of the quantum light-matter interaction [17]. Circuit QED is based on superconducting circuits with a Josephson junction, which can encode a quantum bit (qubit) [18], a bit of information that contrarily to classical 0 or 1 bits, can be in a superposition of the two states $|0\rangle$ or $|1\rangle$. Such a qubit can be manipulated with microwave cavities and is a promising building block for quantum information technologie.

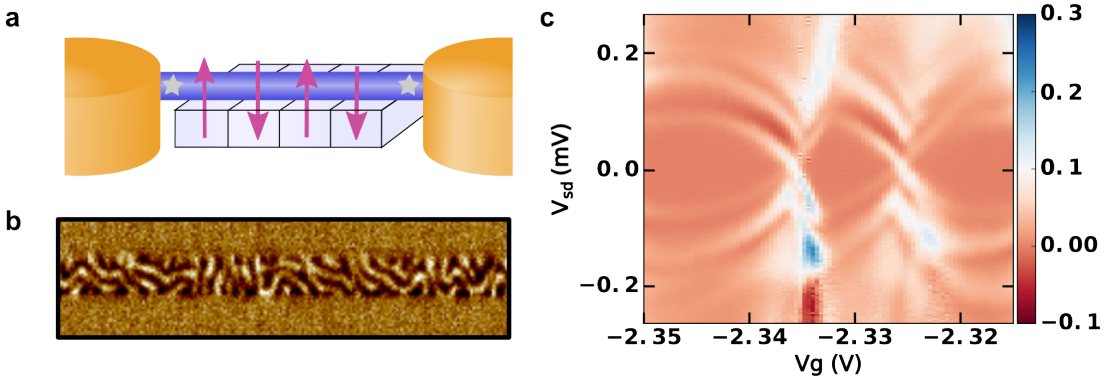

FIGURE 2: **Set-up for engineering Majorana bound states in carbon nanotube. a.** Scheme of a carbon nanotube above a ferromagnetic bottom gate, producing a rotating magnetic field (purple arrows). The carbon nanotube is contacted with two superconducting electrodes (yellow). In the topological regime, two Majorana bound states (represented here by a star) emerge at both boundaries of the nanotube. **b.** Magnetic force microscope image of a buried Nickel ferromagnetic electrode. **c.** Conductance color-plot with respect to gate voltage V_g and bias voltage V_{sd} between two superconducting electrodes. The resonances correspond to Andreev bound states induced by superconducting proximity effect.

A processor made out of several qubits could use entanglement to go beyond sequential processing, and to speed up its calculus performance to solve complex problems, as predicted by quantum information theory [19]. Such a processor could also simulate quantum problems, that cannot be computed with classical processors. By modeling the quantum behavior of electrons, these digital simulators could be used in chemistry, medicine or material science. The growing toolbox developed in the last years in the cQED field may be applied also to mesoscopic circuits when integrating them into microwave cavities. Following this perspective, a cQED architecture is used in this thesis to probe mesoscopic circuits, acting as analog simulators to study complex quantum problems, like the many-body Kondo effect.

The set-up of a carbon nanotube-based electronic circuit embedded in a cQED architecture could also be used to study an other intriguing quantum phenomena, which is the possible emergence of new quasi-particles, called Majorana bound states. This condensed matter version of a Majorana fermion is an equal superposition of an electron and a hole [20]. Such an electronic quasi-particle is its own anti-particle, and has therefore zero energy. Furthermore they are very robust to local perturbation, as their emergence and disappearance is governed by the topology of the whole subspace of states defined by the Hamiltonian. Even more intriguing, these elusive quasi-particles obey to non-abelian statistics. They can be engineered in a one-dimensional system, such as a carbon nanotube, by using superconductivity that pairs electrons and hole. Their emergence also requires the combination of strong-spin orbit coupling and a magnetic field [21, 22]. First signatures of Majorana bound states have been observed in semi-conductors that

have a strong spin-orbit coupling [23–26], which is not the case for carbon nanotubes. Nevertheless both the recquired magnetic field and the spin-orbit coupling could be mimicked by placing the nanotube above a ferromagnetic gate [27, 28]. Such a strategy has been initiated during this thesis. The integration of this device in a microwave cavity could furthermore reveal their peculiar particle/anti-particle duality [29].

The thesis is organized as follows : the first chapter starts with the description of quantum dot circuits. After explaining how confinement and interactions lead to single electron transfer, I will present the Kondo effect, where constructive interferences give rise at low temperature to an extra charge transfer mechanism, which involves the spin degree of freedom of electrons. I will then describe the superconducting proximity effect that leads to pairing of electrons in a normal conductor contacted with a superconducting electrode. This pairing modifies the spectrum of the normal conductor, yielding Andreev bound states inside a induced superconducting gap. In presence of strong spin-orbit coupling and a magnetic field this pairing creates Majorana bound states, which are finally briefly discussed.

The second chapter addresses the implementation of a quantum dot circuit in a cQED architecture. One first describes the coupling of microwave cavities to single atoms and their electronic counterpart, the superconducting circuits. I will then focus on the specificity of mesoscopic circuits which combine single orbitals and electrodes with many fermionic degrees of freedom. The compressibility measurement of a quantum dot with a microwave cavity is described and compared to previous experimental set-ups.

The third chapter outlines the experimental methods used for the nano-fabrication and for the DC and RF measurements of the on-chip electronic circuit. Details are given in this chapter on the implementation of carbon-based circuits in superconducting cavities, as well as the fabrication of buried ferromagnetic bottom gates.

The fourth chapter presents the main result of this thesis : a dual measurement of the conductance and the compressibility of a quantum dot in a Kondo regime. In our set-up, the microwave phase signal is directly proportional to the compressibility and the large electron-photon coupling as well as the large quality factor allow us to detect non-invasively the tiny compressibility of the quantum dot with an unprecedented sensitivity. We observe that the Kondo resonance visible in conductance is absent in the microwave phase signal, indicating that the charge dynamics in the dot is frozen in the Kondo regime (figure 1). The temperature dependence of the phase and the conductance further confirms that the conductance and the residual compressibility rely on different physical principles, as the compressibility depends on the width of the dot level, whereas the conductance depends on the width of the Kondo many-body resonance. This result

illustrates that at low frequency, an electrical current is flowing in the Kondo regime through the dot, whereas the charge on the dot is frozen.

In the last chapter, one first reviews the Majorana bound states signatures that have been observed, and those which could be obtained by coupling these peculiar excitations to a microwave cavity. After addressing the specificities of Majorana bound states in carbon nanotubes, I will conclude this thesis with experimental results on Andreev bound states in a carbon nanotube above a ferromagnetic gate, coupled to a microwave cavity (figure 2).

Chapter 1

Quantum electronic circuits

Mesoscopic physics benefits from a wealth of materials with reduced spatial dimension, from semi-conducting hetero-structures hosting two-dimensional electron gases (2DEG), to semi-conducting nanowires or carbon nanotubes, which are used in this thesis. Nanofabrication allows for an even greater confinement of the electron gas, in metallic islands with size on the order of the electron wavelength. These electron boxes, called quantum dots, display a discrete spectrum for electrons similar to the orbitals of atoms. By integrating these quantum dots in electronic circuits at low temperature (sub-Kelvin temperature), they behave as single electron transistors (section 1.1). The interest of such electronic circuits with artificial atoms is their tunability, allowing different regimes of electronic transport to be accessed. The interplay between interactions and the spin degree of freedom of the electrons can for example lead to a many-body effect, the Kondo effect, which opens a new path for electron transfer (section 1.2). The variety of the electronic excitations can be further increased by playing with the nature of the electrodes. Superconducting electrodes induce for example electron pairing inside the quantum dot (section 1.3). This pairing combined with spin-orbit coupling could for example lead to peculiar excitations, called Majorana fermions. These quasi-particles are their own antiparticle and are predicted to follow a non-abelian statistic (section 1.4).

1.1 Carbon nanotube quantum dots

1.1.1 Carbon nanotubes : a one-dimensional semiconducting material with ballistic properties

Carbon nanotubes are ideal candidates for quantum dot transport experiments as they inherit from graphene its ballistic electronic transport property. In addition, they are, unlike graphene, a semi-conducting material, allowing for confinement of electrons in a quantum dot.

They are either metallic or semi-conducting, depending on the way the graphene sheet is rolled up[1]. But even metallic nanotubes have often a narrow gap induced by curvature or strain in the lattice. These narrow-gap nanotubes happen to be more suitable for

[1]Rolling up a graphene strip impose a quantization of the momentum that is perpendicular to the longitudinal axis of the nanotube, as electrons have a periodic circular movement in this direction. Hence the band structure of the nanotube is determined by vertical plane cuts in the Dirac cone graphene dispersion 3-D map $E(\overrightarrow{k})$, each plane corresponding to one subband. The planes near the graphene K and K' points determine the lowest energy band. If they intercept the Dirac point then the nanotube is metallic, if not it is semi-conducting. The gap has the same order of magnitude as the distance between two bands with a different perpendicular momentum, which is inversely proportional to the nanotube diameter.

electronic transport experiments, as disorder tends to localize massive electrons, found in nanotubes with bigger gap[2] [30].

The band structure for the quasi-momentum along the nanotube longitudinal axis, $k_{\parallel}$, is bent for energies near the gap Δ_{gap} :

$$E(k_{\parallel}) = \pm\sqrt{\left(\hbar v_f k_{\parallel}\right)^2 + \Delta_{gap}^2/4} \tag{1.1}$$

Nevertheless narrow gap nanotubes with many electrons ($E_F \gg \Delta_{gap}$) have with good approximation a linear dispersion with a constant mean momentum $\langle p \rangle = \pm\hbar v_f$, stemming from the Dirac cones[3]. The Fermi velocity, $v_f \sim 8 \times 10^5 m.s^{-1}$ [30], is one order magnitude bigger than other semiconductors. This high Fermi velocity increases the mean free path and the phase relaxation length of the electrons in the nanotube, as both quantities are proportional to v_f. It also increases the energy separation $\Delta_{band} \sim hv_f/R$ between two bands with different quantized circumferential momenta, R being the nanotube radius. Consequently, at low energy, nanotubes can be considered as one-dimensional semi-conductors with a single ballistic conduction channel.

Carbon nanotubes also inherit from graphene its K-K' degeneracy[4]. This degeneracy roughly correspond to clockwise/counter-clockwise rotation around the longitudinal axis of the nanotube and add two differents angular momenta linked to the valley K or K'. The valley is a priori a good quantum number, as K-K' intervalley scattering would either require breaking time reversal symmetry, or rely on high energy scattering events. Nevertheless, a mixing term $\Delta_{K-K'}$ is empirically relevant for understanding usual experiments. The lifting of the degeneracy can for example come from short range disorder affecting the honeycomb lattice [30].

Reducing the dimensions of the electronic gas allows electrons to be confined into quantum dots. These artificial zero-dimensional objects can be patterned out of single-wall carbon nanotubes, but also graphene, molecules, semiconducting nanowires, or two-dimensional electron gases. In a semi-conducting carbon nanotubes quantum dot, the electrostatic confinement of the electron is realized by two potential barriers, that appear at the interfaces between a semi-conducting and a metallic material. These barriers, named Schottky barriers, appear when adjusting the two work functions of the materials, and can be tuned with the help of the electrostatic potential of a lateral gate.

[2]The mass is inversely proportional to the curvature of the dispersion relation E(k). The latter is more bent as the gap increases.

[3]The quasi-momentum $k_{\parallel}$ is measured here from the quasi-momentum of one Dirac point, which is the minimum energy of the conduction band.

[4]A state near the K point has a time-conjugate state near the K' point.

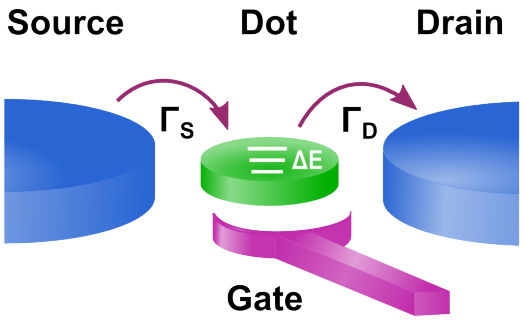

FIGURE 1.1: **Quantum dot in an electronic circuit.** Electrons from the source hop to the quantum dot and then to the drain. A gate electrode tunes the position of the quantized levels, spaced by ΔE, with respect to the source and drain electrodes. The source-drain current hence depends on the properties of the quantum dot. Γ_s and Γ_d are the tunneling rates from the corresponding electrodes.

The confinement of the electronic wavefunction in a potential well leads to the quantization of the energy levels, like for the electronic shells in atoms. The high Fermi velocity increases the confinement energy in a carbon nanotube quantum dot of length L, as $\Delta E = hv_f/(2L)$. For $1\mu m$-long carbon nanotubes, $\Delta E \sim 1.7meV \sim 20K$ [30]. Hence, the discrete spectrum of a quantum dot is well resolved in sub-Kelvin experiments.

1.1.2 Electronic transport with quantum dot

Quantum dots with an energy spectrum in the meV can be probed naturally by electronic transport when integrating it in an electronic circuit. The most elementary circuit is made of a source and a drain electrodes, together with a third nearby electrode, the gate (see figure 1.1). By applying a small bias voltage V_{sd} to the source, electrons can be transferred from the source to the dot, and then escape into the drain. The electrical current gives information on the electronic transmission of the quantum dot.

Because the quantum dot is a conducting island that is only tunnel coupled to the source and drain electrodes, its potential is fixed by the electrostatic environment. Hence the gate electrode potential V_g tunes the position of the energy level with respect to the source and drain by electrostatic influence. As for a transistor, the electronic transmission of the dot can be tuned by the gate voltage, via the position of the energy level.

Sweeping the gate voltage on a large scale fills the quantum dot with electrons. A large bias $V_{sd} \sim 1meV$ allows also nearby excited states to be probed. Hence the conductance map with respect to the two knobs, the bias voltage V_{sd} and the gate voltage V_g provides information on the whole spectrum of the artificial atom.

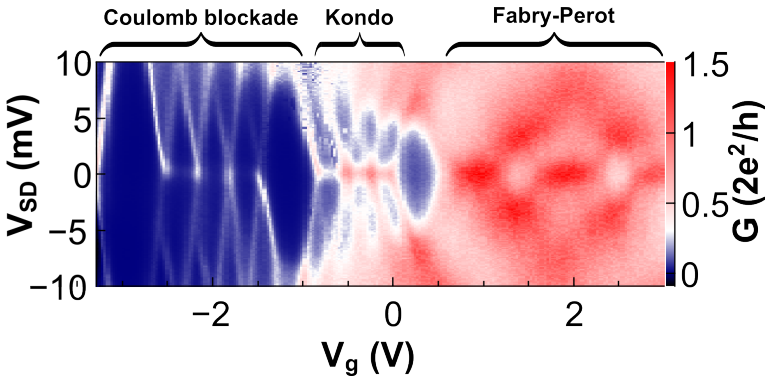

FIGURE 1.2: **Differential conductance in the V_g, V_{sd} plane for different regime.** The Coulomb blockade regime shows diamonds with sharp resonances, whereas the Fabry Perot regime shows a checker board pattern. The Kondo regime happens in between with an increase of the conductance at zero bias.

The electronic circuit introduces two additional energy scales besides the confinement energy ΔE, the tunneling rate Γ and the charging energy E_c :

- Γ describes the transparency of the contacts between the nanotube and the electrodes. It is the rate at which electrons in the quantum dot tunnel to the continuum of the source or the drain electrode and is given by the Fermi's golden rule.
- E_c is the energy taking into account Coulomb repulsions. It scales like the inverse of the capacitance of the quantum dot, and increases consequently when the metallic island becomes smaller.

In nanotube based quantum dots, both these quantities are of the same order of magnitude as the level spacing. The interplay between all energies scales k_bT, ΔE, Γ and E_c defines two main electronic transport regimes :

- **The Fabry-Perot regime :** For negligible charging energy $E_c \ll kT \ll \Gamma \sim \Delta E$, electrons behave as non interacting electronic plane waves. The two potential barriers delimiting the quantum dot act as scatterers for electrons, with a probability for the wavefunction to be either transmitted or reflected. As the coherence is preserved in the nanotube, the quantum dot behaves as a Fabry Perot cavity for the electronic wavefunctions. The gate moves the energy level of the quantum dot, which smoothly and periodically tunes the electronic transmission of the dot. It gives a checkerboard pattern for the conductance in the V_g, V_{sd} map, with a period set by ΔE, as shown in figure 1.2.
- **The Coulomb blockade regime :** In the regime of low transparency $\Gamma, k_bT \ll E_c$, the electronic wavefunction is more localized on the dot. Hence, charge fluctuations are turned off by interactions, as the ratio E_c/Γ increases. The charge in

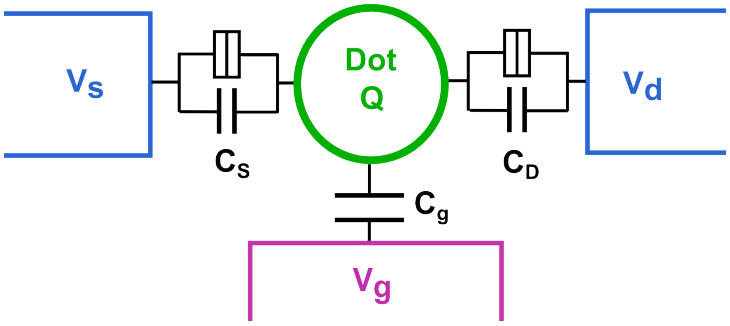

FIGURE 1.3: **Circuit representation of closed quantum dot.** V_s (resp. V_d) is the source (resp. drain) potential, V_g the gate one. In a closed quantum, the charge Q on the dot is only an integer number of electrons. The potential of the dot, and the corresponding number of charges, is fixed by the surrounding electrostatic potential and their corresponding capacitances.

the dot becomes then an integer number of electrons and a capacitance appears in parallel of the tunnel junction, see figure 1.3. Electronic transport occurs then only, when the electrostatic environment, tuned by the gate voltage, compensates the Coulomb repulsion of the dot electrons. This gives rise to sharp resonances for periodic gate voltages, in between which the integer number of electrons in the dot is locked. These resonances form diamonds in the V_g, V_{sd} map, called Coulomb diamonds. This Coulomb blockade regime is described in more details in the next section.

The Fabry Perot regime and the Coulomb blockade regime can both be reached for a same nanotube at different gate voltage regions, as shown in the V_g, V_{sd} map of the figure 1.2. A third regime, the Kondo regime, happens for the intermediate situation $k_bT \ll \Gamma \lesssim E_c$, showing an enhancement of the conductance at zero bias. This regime will be describe in greater details in section 1.2.

1.1.3 Number of charges in the dot

For a closed quantum dot with small tunnel barriers, the quantum dot is an isolated metallic island with N electrons [10]. The value of N is governed by the electrostatic energy of the system. The quantum dot faces several electrodes, that are at constant potentials V_i and have capacitances C_i with the metallic island, see 1.3.

The electrostatic energy E_{el} is then the sum of the energies stored in each capacitor and the work done by the sources to keep V_i constant :

$$E_{el} = \sum_i \frac{1}{2} C_i (V_{dot} - V_i)^2 - V_i C_i (V_i - V_{dot}) = \sum_i \frac{1}{2} C_i V_{dot}^2 - \frac{1}{2} C_i V_i^2 \qquad (1.2)$$

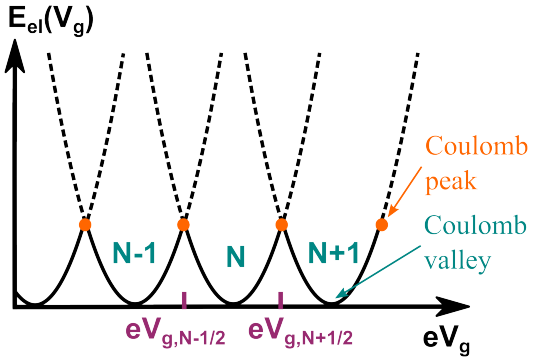

FIGURE 1.4: **Electrostatic energy with respect to the gate voltage $\mathbf{V_g}$ at $\mathbf{V_{sd} = 0}$.** The number of electrons in the dot is the one which minimizes the electrostatic energy at a given gate voltage. Single electron transfer from the source to the drain happens when it costs the same energy to have N or $N+1$ electrons in the dot (orange dots). It corresponds to gate voltages $V_{g,N+1/2}$. As N is only an integer, the electrostatic energy can not go to zero. In other words, the charge in the dot can not completely screen the electric field induced by the surrounding electrodes.

V_{dot} is the electrostatic potential of the dot and is linked to N by :

$$Q = -eN = \sum_i C_i(V_{dot} - V_i) \tag{1.3}$$

Note that e is the elementary charge, so that $e > 0$. For N electrons in the dot

$$E_{el}(N) = \frac{e^2}{2C_\Sigma}\left(N - \frac{\sum_i C_i V_i}{e}\right)^2 \tag{1.4}$$

where $C_\Sigma = \sum_i C_i$ is the sum of all capacitances. One defines the charging energy as $E_c = \frac{e^2}{2C_\Sigma}$. At each gate voltage V_g, N is the integer which corresponds to the lowest $E_{el}(N)$, see figure 1.4. An electron can be added in the dot if $E_{el}(N+1) = E_{el}(N)$. At $V_{sd} = 0$, this happens for a gate voltage $V_{g,N+1/2}$, when the image charge on the gate is a half-integer number of electrons :

$$C_g V_{g,N+1/2} = e(N + \frac{1}{2}) \tag{1.5}$$

At these gate voltages and $V_{sd} = 0$, electrons can be transferred from the source to the drain. These resonant conditions are referred to as a Coulomb peaks.

In the out-of equilibrium situation $V_{sd} \neq 0$, the conditions for which electrons are transferred from the source to the drain can be determined by the fact that electrons always move towards smaller chemical potentials. The chemical potential in the dot $\mu(N)$ is equal to the energy cost of adding one electron to the dot :

$$\mu(N) = E_{el}(N+1) - E_{el}(N) = 2E_c\left(N + \frac{1}{2} - \frac{C_g V_g + C_s V_s + C_d V_d}{e}\right) \tag{1.6}$$

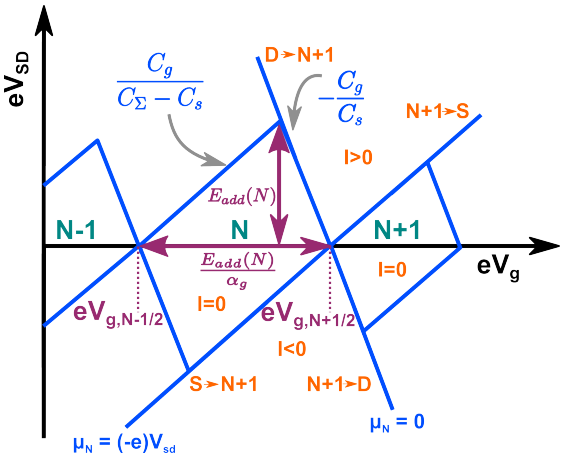

FIGURE 1.5: **Charge stability diagram of a single dot for an asymmetric bias voltage $V_s = V_{sd}$ and $V_d = 0$.** The blue lines correspond to the set of conditions $(\mu(N) = -eV_{sd}, \mu(N) = 0)$ (see equation (1.7)). Within a diamond delimited by these lines, the charge in the dot is fixed, and takes an integer value labeled in green. The direction of single-electron transfer is written in orange, S being the source, and D the drain, and it defines the sign of the resulting electronic current. The positive and negative slopes are respectively $C_g/(C_\Sigma - C_s)$ and $-C_g/C_s$. The slopes take into account the fact that $V_s = V_{sd}$ has also an electrostatic influence.

The single-electron transfers are then conditioned by the following rules $(e > 0)$:

$$\begin{aligned} &\text{From source to a dot with } N \text{ electrons:} && \mu(N) < -eV_s \\ &\text{From a dot with } N \text{ electrons to the drain :} && \mu(N) > -eV_d \end{aligned} \tag{1.7}$$

These inequalities define lines in the $V_{sd} - V_g$ plane. These lines delimit areas corresponding to a given direction of the electron transfer, for example from the source to the dot, or from the dot to the source (see figure 1.5). The lines form periodical diamonds, inside which transport cannot happen and the charge in the dot is fixed to an integer.

The charging energy can be directly read off each diamond, as it corresponds to its half-height. The N^{th}-diamond width $e(V_{g,N+1/2} - V_{g,N-1/2})$ equals E_c/α_g where $\alpha_g = C_g/C_\Sigma$ is the gate capacitive lever arm. This lever arm links the effect of the gate voltage V_g to the chemical potential of the dot.

In electronic transport experiments, it is more convenient to measure the differential conductance through the device $\frac{\partial I}{\partial V_{sd}}$, as it presents sharper features. The conductance exhibits a Coulomb peak at each charging degeneracy point $V_g = V_{g,N+1/2}$. Outside of this peak, when electrons cannot be transferred, this is called the Coulomb valley (see figure 1.4).

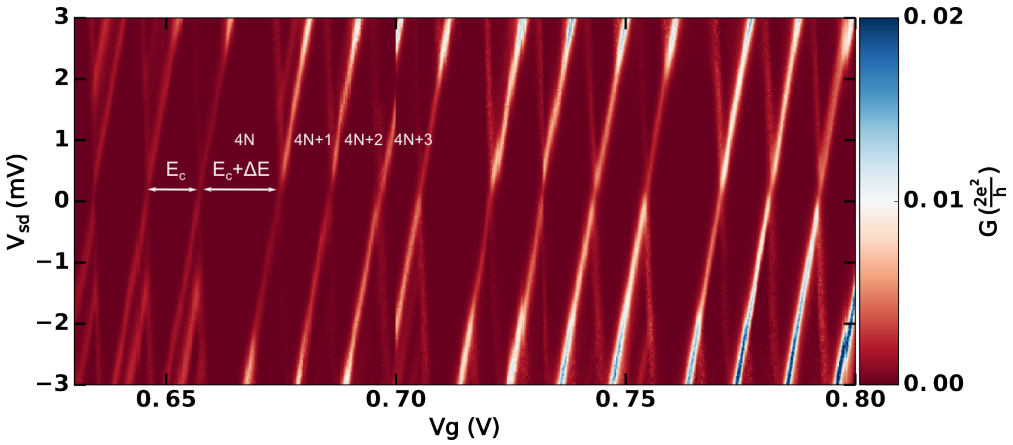

FIGURE 1.6: **Conductance map V_g-V_{sd} measured in a carbon nanotube quantum dot** The four-fold periodicity of the Coulomb diamonds is a signature of the spin and valley degeneracy of the dot energy levels. Both the charging energy E_c and the level spacing ΔE are around $3meV$. With the Fermi velocity of graphene, the confinement energy would correspond to a dot with a length around $500nm$.

As we often focus on a single Coulomb peak, it is convenient to express the dot chemical potential relatively to the resonant condition $\mu(N, V_{g,N+1/2}) = 0$:

$$\epsilon_d = \mu(V_g) - \mu(V_{g,N+1/2}) = -e\alpha_g \left(V_g - V_{g,N+1/2}\right) \tag{1.8}$$

$\epsilon_d = 0$ corresponds to a Coulomb peak, $\epsilon_d = \pm E_c$ to the Coulomb valley.

Up to now, we have only considered the effect of the interactions to determine the energy required to add an extra electron in the dot. Nevertheless, one has also to take into account the discrete spectrum of the quantum dot. In carbon nanotubes, each orbital is four-fold degenerate (spin and valley). The diamonds have thus a four-fold periodicity, each fourth diamonds having in the simplest case an addition energy $E_c + \Delta E$ [31], as shown in figure 1.6.

1.1.4 Stationary regime

Around a Coulomb peak the number of electrons in the dot is not frozen by electrostatics. It fluctuates in time $N(t)$, with electrons tunneling between the dot and the electrodes. Nevertheless the electronic fluctuations are in most cases much faster than the time evolution of the probe excitation of the system at frequency ω : $\hbar\omega \ll max(\Gamma, k_bT)$. We are then mostly interested by quantities in the stationary regime, like the mean charge $n = \langle N \rangle$, or the average current $I = e\langle \frac{dN}{dt} \rangle$.

Electron fluctuations come either from thermal (sequential regime) or quantum fluctuations (coherent regime) induced by tunnel barriers. These fluctuations compete with

the charging energy that dominates in the Coulomb valley. The energy scale of the fluctuations k_bT/E_c or Γ/E_c determines the width of the Coulomb peak, as derived below. Following the picture set in the previous sections, the quantum dot is described as a single orbital coupled to a source and drain continuum. It is only occupied by either N or N+1 electrons and is detuned by ϵ_d from the chemical potential of the lead.

1.1.4.1 Sequential regime

Let us first treat the tunneling process as a small perturbation, and neglect coherent effects. In that case, tunneling events are sequential and random. Hence we can use a semi-classical approach based on electronic occupation probabilities and tunneling rate into $\Gamma^+(\epsilon_d)$ and out of the dot $\Gamma^-(\epsilon_d)$.

In the framework of a single orbital with no spin and valley degeneracies, the electron dynamics reduces to a master equation with two probabilities : p_N (resp. p_{N+1}) being the probability to have N, resp. $N+1$, electrons in the dot :

$$\begin{aligned} \hbar\frac{\mathrm{d}p_N}{\mathrm{d}t} &= -\Gamma^+ p_N + \Gamma^- p_{N+1} \\ \hbar\frac{\mathrm{d}p_{N+1}}{\mathrm{d}t} &= -\Gamma^- p_{N+1} + \Gamma^+ p_N \end{aligned} \tag{1.9}$$

The stationary conditions $\frac{\mathrm{d}p_N}{\mathrm{d}t} = \frac{\mathrm{d}p_{N+1}}{\mathrm{d}t} = 0$ yields the following probabilities :

$$\begin{aligned} p_N &= \frac{\Gamma^-}{\Gamma^- + \Gamma^+} \\ p_{N+1} &= \frac{\Gamma^+}{\Gamma^- + \Gamma^+} \end{aligned} \tag{1.10}$$

The mean charge in the dot is then :

$$n = \langle N \rangle = N + \frac{\Gamma^+}{\Gamma^- + \Gamma^+} \tag{1.11}$$

The current can also be deduced from the master equation approach. Because of current conservation, it is equivalent to count current through the source or the drain.

$$I = \frac{e}{\hbar}\left(\Gamma_S^+ p_0 - \Gamma_S^- p_1\right) = \frac{e}{\hbar}\left(\frac{\Gamma_S^+\Gamma_D^- - \Gamma_S^-\Gamma_D^+}{\Gamma^- + \Gamma^+}\right) \tag{1.12}$$

$\Gamma_i^\pm$ with $i = S, D$ are the tunneling rates for the source and drain, ($\Gamma^\pm = \Gamma_S^\pm + \Gamma_D^\pm$). They differ when a voltage V_i is applied and are obtained using Fermi's Golden rule $2\pi|t_i|^2\delta\left(E_{final} - E_{initial}\right)$:

$$\begin{aligned}&\Gamma_i^{\pm} = 2\pi|t_i|^2 \int \nu_i \, \mathrm{d}\epsilon_\mathrm{k} \, f\left(\pm\left(\epsilon_k - (-e)V_i\right)\right) \delta\left(\epsilon_k - \epsilon_d\right) = \Gamma_i f\left(\pm\left(\epsilon_d + eV_i\right)\right) \\ &\text{with } \Gamma_i = 2\pi|t_i|^2\nu_i\end{aligned} \tag{1.13}$$

Where f is the Fermi Dirac function for the temperature k_bT[5].

The temperature broadening k_bT sets the slope of the dot occupancy at equilibrium (zero bias) :

$$n = N + f(\epsilon_d) = N + \frac{1}{2} - \frac{1}{2}\tanh\left(\frac{\epsilon_d}{2k_bT}\right) \tag{1.14}$$

and also the width of the conductance peak :

$$G = \frac{e^2}{h}\frac{\Gamma_L\Gamma_R}{\Gamma_L+\Gamma_R}\frac{1}{4k_BT\cosh^2\left(\frac{\epsilon_d}{2k_BT}\right)} \tag{1.15}$$

1.1.4.2 Coherent regime

The sequential tunneling approach is only valid for $\Gamma = \Gamma_s + \Gamma_d \ll k_bT$. When k_bT decreases, quantum coherence starts to play a role and the master equation treatment does not hold anymore.

Atomic physics teach us that the energy distribution of electrons escaping an atomic level towards a continuum of states is a Lorentzian. In our case it means that $\frac{\partial n}{\partial \epsilon_d}$ is the opposite of a Lorentzian :

$$\frac{\partial n}{\partial \epsilon_d} = -\frac{2S}{\pi\Gamma}\frac{\Gamma^2}{\Gamma^2 + 4\epsilon_d^2} \tag{1.16}$$

where S is the degeneracy of the atomic level. The mean number of electrons in the dot for S=1 is hence

$$n = N + \frac{1}{2} - \frac{2}{\pi}\arctan\left(\frac{2\epsilon_d}{\Gamma}\right) \tag{1.17}$$

The mean charge in the dot can be more formally derived with Green's function techniques. We can also recover it from a scattering type argument. We use the following Hamiltonian :

$$H = \epsilon_d d^\dagger d + \sum_k t_k d^\dagger c_k + t_k^* c_k^\dagger d + \sum_k \epsilon_k c_k^\dagger c_k \tag{1.18}$$

where $d^\dagger$, resp. $c_k^\dagger$, creates an electron in the dot, resp. in the continuum with momentum k. The Heisenberg equation of motion for an operator x is $-i\hbar\frac{\mathrm{d}x}{\mathrm{d}t} = [H, x]$ and gives the following time dependent equation for the electron operator in the bath :

$$i\hbar\frac{\mathrm{d}c_k(t)}{\mathrm{d}t} = \epsilon_k c_k + t_k d \tag{1.19}$$

[5]We used here that $1 - f(\epsilon) = f(-\epsilon)$.

A solution of $c_k(t)$ with initial condition at $t = t_0$ matching a free propagating electron in the reservoir is :

$$c_k(t) = e^{-i\epsilon_k(t-t_0)/\hbar}c_k(t_0) - it_k\int_{t_0}^{t} \mathrm{d}\tau e^{-i\epsilon_k(t-\tau)/\hbar}d(\tau) \tag{1.20}$$

The first part describes an 'incoming' electron with a free evolution and the second part refers to the electronic wave packet that has interacted with the dot. The evolution of the dot operator is :

$$\begin{aligned}\frac{\mathrm{d}d(t)}{\mathrm{d}t} &= -i\frac{\epsilon_d}{\hbar}d(t) + i\sum_k t_k^* c_k(t) \\ &= -i\frac{\epsilon_d}{\hbar}d(t) + i\sum_k t_k^* e^{-i\epsilon_k(t-t_0)/\hbar}c_k(t_0) - \sum_k |t_k|^2\int_{t_0}^{t}\mathrm{d}\tau e^{-i\epsilon_k(t-\tau)/\hbar}d(\tau)\end{aligned} \tag{1.21}$$

The above equation is a closed equation with $d(t)$ that depends on its own history $\int_{t_0}^{t}\mathrm{d}\tau g(\tau)d(\tau)$. The last integral can be simplified by saying that under the integral $d(\tau)$, one has to a good approximation (rotating wave approximation) : $d(\tau) \simeq e^{-i\epsilon_d(\tau-t)\hbar}d(t)$. For $\tau \ll t$, the 'incoming' electrons in the reservoir are not affected by the presence of the dot, therefore a factor $e^{-0^+(t-\tau)}$ can be put inside the integral[6] :

$$\begin{aligned}\sum_k |t_k|^2\int_{t_0}^{t}\mathrm{d}\tau e^{-i\epsilon_k(t-\tau)/\hbar}d(\tau) &= \sum_k |t_k|^2\int_{\infty}^{t}\mathrm{d}\tau e^{-i(\epsilon_k-\epsilon_d+i0^+)(\tau-t)/\hbar}d(t) \\ &= \sum_k |t_k|^2\frac{i\hbar}{\epsilon_k-\epsilon_d+i0^+}d(t)\end{aligned} \tag{1.22}$$

The imaginary part of the latter is $\Gamma/2$ where $\Gamma = 2\pi\nu(E_f)|t_{E_f}|^2$ is given by the Fermi's golden rule, with the assumption that both $|t_k|^2$ and the density of states $\nu(\epsilon_k)$ in the reservoir are constant. The real part is zero if the reservoir has a symmetric band structure[7]. The time evolution of $d(t)$ is then :

$$\begin{aligned}\frac{\mathrm{d}d(t)}{\mathrm{d}t} &= -i\frac{\epsilon_d}{\hbar}d(t) - \frac{\Gamma}{2\hbar}d(t) + i\sum_k t_k^* e^{-i\epsilon_k(t-t_0)/\hbar}c_k(t_0) \\ &= -i\frac{\epsilon_d}{\hbar}d(t) - \frac{\Gamma}{2\hbar}d(t) + i\nu t^*\int \mathrm{d}\epsilon e^{-i\epsilon(t-t_0)/\hbar}c_\epsilon(t_0)\end{aligned} \tag{1.23}$$

The integral solution for $d(t)$

$$d(t) = -i\int_{-\infty}^{t}\mathrm{d}\tau e^{-i(\epsilon_d+i0^+-i\Gamma/2)/\hbar\tau}\nu t^*\int \mathrm{d}\epsilon\, e^{-i\epsilon(t-t_0)/\hbar}c_\epsilon(t_0) \tag{1.24}$$

[6] With this factor one can then take as the lower boundary of the integral : $t_0 \to -\infty$

[7] If not, the real part of the integral depends a priori on ϵ_d but can be taken as constant as it is a slowly varying function of ϵ_d, and therefore only leads to a renormalization of ϵ_d.

allows one to find the mean number of charges :

$$n = \left\langle d^\dagger(t)d(t)\right\rangle = \int \frac{\mathrm{d}\epsilon}{\pi} \frac{\Gamma/2}{(\epsilon-\epsilon_d)^2+(\Gamma/2)^2} \left\langle c_\epsilon^\dagger(t_0)c_\epsilon(t_0)\right\rangle . \tag{1.25}$$

The time t_0 corresponds to a time when the incoming electrons have not interacted with the dot, so the mean value of number of electrons in the bath is given by the Fermi-distribution[8] $\left\langle c_\epsilon^\dagger(t_0)c_\epsilon(t_0)\right\rangle = f(\epsilon)$.

The differential conductance $\frac{\partial I}{\partial V_{sd}}$ corresponds, at zero bias, to the transmission through this orbital state, and can be considered as a Breit-Wigner resonance across the quantum dot with a finite lifetime Γ and transition rates in and out Γ_S, Γ_D:

$$G = \frac{e^2}{h}\frac{4\Gamma_s\Gamma_d}{\Gamma^2+4\epsilon_d^2} \tag{1.26}$$

The conductance is maximum in the symmetric case $\Gamma_s = \Gamma_d$. At resonance $\epsilon_d = 0$, the conductance can reach the non-degenerate conductance quantum $\frac{e^2}{h}$.

The finite density of states $\frac{\partial n}{\partial \epsilon_d}$ leads to the conductance of the quantum dot. It also changes the response of the mean number of charges to a modification of the electrostatic potential. Indeed, if the potential δV_i of an electrode is slowly oscillating, it induces oscillations in the dot chemical potential $\delta\epsilon_d = eC_i\delta V_i$. Because of equation (1.17), the mean number of electrons in the dot oscillates like $\frac{\partial n}{\partial \epsilon_d}\delta\epsilon_d$, for $\epsilon_d \sim 0$. As the mean chemical potential of the dot depends on the mean charge number (1.6), the oscillations of $\delta\langle\epsilon_d\rangle$ reads :

$$\delta\langle\epsilon_d\rangle = \frac{-eC_i}{C_{dot} - e^2\frac{\partial n}{\partial\epsilon_d}}\delta V_i \tag{1.27}$$

Therefore the quantum dot finite density of states acts as an additional capacitance in the circuit, increasing the sum of the surrounding capacitances that is in the denominator of the level arm $\delta\langle\epsilon_d\rangle/\delta V_i$.

This additional capacitance is called the quantum capacitance C_q and appears in series to the classical capacitance C_{geo} [32]. It stems from the inclusion of the Fermi energy in the chemical potential $\mu = V(r)+E_F$, where $V(r)$ is the classical electrostatic potential :

$$C^{-1} = \frac{\partial\mu}{\partial Q} = \frac{\partial V}{\partial Q} + \frac{\partial E_f}{\partial Q} = C_{geo}^{-1} + C_q^{-1} \tag{1.28}$$

In this section, interactions between electrons have only been taken into account as a contribution to the electrostatic environment through the charging energy. The dynamics of an electron is then described without taking into account correlation effects. In a many-body situation, the conductance or the quantum capacitance can not be calculated

[8] n does not depend on t as we derive here the stationary value

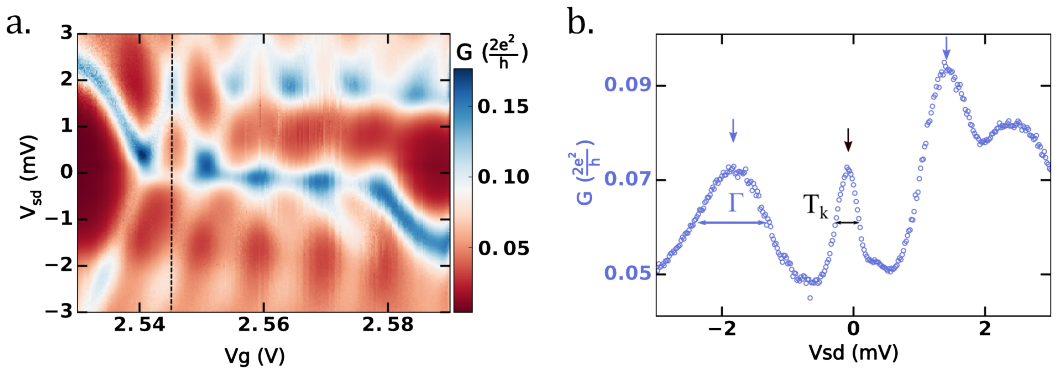

FIGURE 1.7: **Carbon nanotube in the Kondo regime a.** Conductance map V_g-V_{sd}. Four conductance ridges appear inside four Coulomb diamonds, where interactions forbid to transfer electrons in the dot. The diamonds have broad edges as $\Gamma/E_c \sim 2meV$. The ridges are absent for the left and rightmost diamonds, suggesting that the ridges are linked to the charge occupation. **b.** Cut at constant gate voltage for the first ridge (black dashed line in a., showing the Kondo resonance (black arrow) at zero bias voltage. Conductance peak marked with blue arrows correspond to dot energy level accessible at higher energy.

easily with the above method. In practice, the Lorentzian approximation still holds in the presence of interactions, which renormalize the height and width of the resonances. The next section describes a situation where interactions induce nevertheless quantum correlations between the electrons in the dot and in the continuum, leading to the Kondo effect.

1.2 Kondo physics

1.2.1 Kondo effect in quantum dots

The Kondo effect manifests itself as an enhancement of scattering events between electronic states within a continuum, when the temperature decreases [33]. In a metallic alloys, these scattering events lead to an increase of the resistance. On the contrary, in quantum dot transport experiments, scattering increases the transmission between the source and the drain [34–36]. More precisely, when the temperature decreases, conductance peaks emerge inside the diamonds, although electrostatic energy forbids electrons to enter in the dot, as shown in figure 1.7.

Inside the diamonds, adding an electron requires an extra charging energy E_c. Such violation of the energy conservation principle is nevertheless not a surprise in quantum mechanics. Virtual states lying at higher energy E_c have a lifetime given by the Heisenberg principle $\Delta t \sim \hbar/E_c$. If this time is comparable to the tunneling time $\Delta t \sim \hbar/\Gamma$,

then electrons can be transferred from the source to the drain, with the help of virtual states. This transport process, named co-tunneling, arise when $\Gamma \lesssim E_c$, but remains yet small, as it is a second order process.

This therefore can not explain Kondo ridges, whose conductance is of the same order of magnitude as for Coulomb peaks (see figure 1.7). For that, we need to consider the spin degree of freedom of a spin-degenerate level in the QD. Kondo physics happens when there is an odd number of electrons in the dot, and when they can not leave the dot because of electrostatic interactions (Coulomb valley). The last dot level is then singly occupied by an electron with a net spin.

If Γ is of the order of E_c, an electron from the electrode (later on referred to as conduction electron) can tunnel into the dot, on a virtual state, like in the co-tunneling case. But due to Pauli principle, only conduction electrons with opposite spin can occupy the virtual state. This favors opposite spin correlations and gives rise to an anti-ferromagnetic coupling between the electron in the dot and conduction electrons at the Fermi level. At temperatures lower than the Kondo temperature T_k, this anti-ferromagnetic coupling leads to a coherent screening of the spin in the QD by the nearby conduction electrons. A many-body bound state emerges, called the Kondo cloud, and the spins of the conduction electrons are then entangled with the spin of the electron in the quantum dot.

The Kondo temperature happens to be the universal scale for all the physical quantity related to the Kondo cloud, and therefore can be considered as the binding energy of this bound state. If the source and drain are voltage biased with a potential $eV_{sd} \simeq T_k$, it breaks the bound state. Therefore the Kondo resonances are close to zero bias, with a width given by T_k (see figure 1.7).

The increase of the conductance by the spin fluctuations can be grasped by looking at figure 1.8. Initially, a singly occupied level is detuned from the Coulomb peak resonances, and electrons cannot be added in the dot. Nevertheless, the charge can be transferred via virtual states. As we focus on processes where the spin degree of freedom is involved, let us consider processes for which the spin is flipped when the electron is transferred form the source to the drain. To see the effect of the temperature, we need to consider processes where electrons enter twice in the dot. Between the first and the second interaction of the electron with the dot, the electron is in a virtual state in the electrodes at energy ϵ. In figure 1.8, we present two processes (in yellow and pink) that interfere constructively :

- An electron in the source with the spin down enters into the dot, and therefore has to form a singlet state (yellow arrows). The electron with spin up leaves the dot and occupy a virtual states at energy ϵ, with a probability $1 - f(\epsilon)$, where f

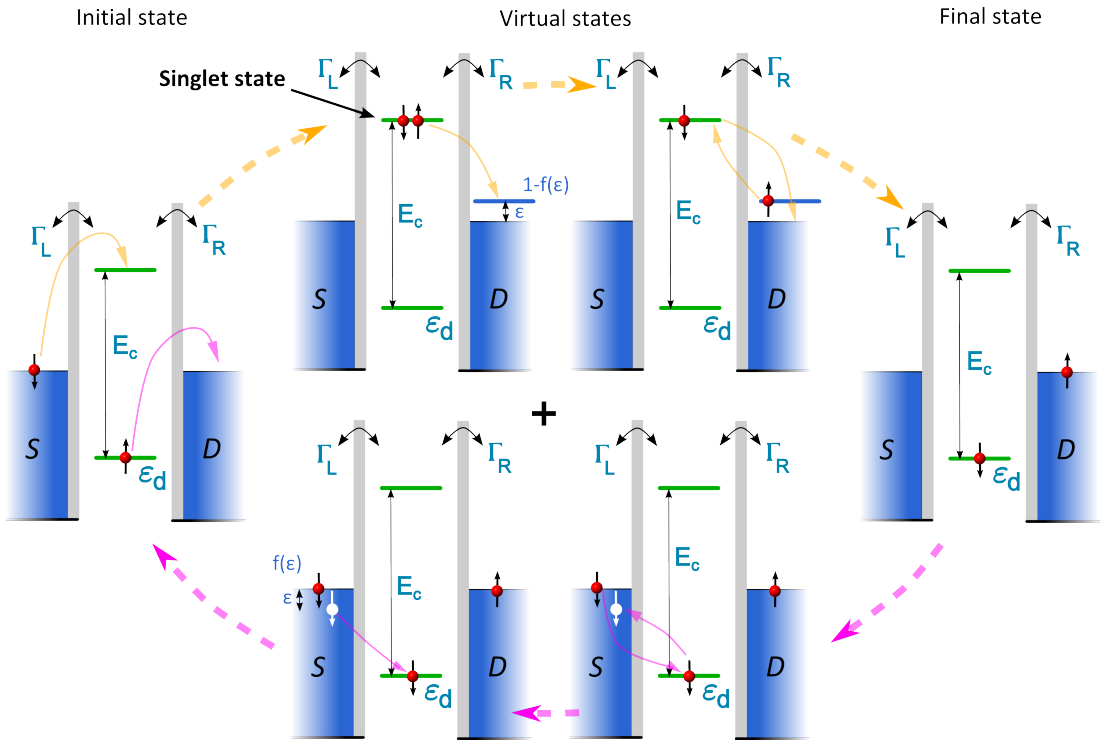

FIGURE 1.8: **Spin-flip charge transfers leading to the Kondo resonance.** Between the initial and the final state an electron is transferred from the source to the drain and the spin of the electron in the dot is flipped. This can be done by either forming a singlet virtual state (top panel) or leaving the dot empty (down panel). The first process (yellow arrows) uses an unoccupied virtual states with the Fermi-Dirac statistics $(1 - f(\epsilon))$ and the second one (pink arrows) an occupied virtual state with the Fermi-Dirac statistics $f(\epsilon)$. In the first process, the electrons in the singlet state has to be swapped, so the probability amplitude acquires a minus sign. The sum of the amplitude probabilities is then proportional to $\left(f(\epsilon) - \frac{1}{2}\right)$, and therefore depends on the temperature. The dashed arrow let us envision an electron trajectory leading to the emergence of a bound state.

is the Fermi-Dirac function at temperature k_bT. As the electrons of the singlet are swapped, the wavefunction acquires a minus sign. The electron on the virtual states relaxes at the Fermi energy by entering once again in the dot.

- The electron in the dot tunnels into the drain, leaving the dot unoccupied (pink arrows). In this process, two electrons never occupy the dot at the time, so the wavefunction does not acquire a minus sign. In this process, the virtual state is a hole and therefore obey to the statistics $f(\epsilon)$.

The two processes interfere, thus we have to add the amplitude probabilities :

$$-1 \times (1 - f(\epsilon)) + f(\epsilon) = 2\left(f(\epsilon) - \frac{1}{2}\right) = 2\tanh\left(\frac{\epsilon}{2k_bT}\right) \tag{1.29}$$

To obtain the whole transmission probability one have to sum over all the intermediate virtual states and take into account that these virtual states have a finite lifetime $\sim \hbar/\epsilon$

given by the Heisenberg uncertainty principle :

$$\int \frac{\mathrm{d}\epsilon}{\epsilon} \tanh\left(\frac{\epsilon}{2k_bT}\right) \sim \ln k_bT \tag{1.30}$$

Hence, the transmission diverges logarithmically at low temperature.

This schematic picture highlights the role of spin fluctuations at the Fermi level, which give rise to constructive interferences. One can also envision the emergence of a bound state, the electron being trapped by a circular trajectory that combines both spin-flip processes.

Nevertheless, this picture does not say anything about the temperature scale of the divergence, which is neither Γ nor E_c. Both last quantities are related to single electron tunneling, whereas the Kondo effect is a many-body resonance. In fact, in the picture sketched above, we use an electron with a well defined spin in the electrode localized near the electrode. Nevertheless, the eigenstate in a continuum are delocalized, so the single quasi-particle with well a defined spin near the electrode is the superposition of propagating electrons. A more complete description of the Kondo resonance can be done within the Anderson model as in the following [33].

1.2.2 Anti-ferromagnetic coupling

The Kondo physics can be modeled by the Anderson Hamiltonian. This Hamiltonian contains the three key ingredients for the Kondo physics : the same degeneracy of the states between a quantum dot and a continuum, a charging energy E_c and a tunnel coupling between the quantum dot and the continuum, called here the lead.

$$H = H_d + H_{lead} + H_t \tag{1.31}$$

The quantum dot Hamiltonian is :

$$H_d = \epsilon_d n_d + E_c n_d \left(n_d - 1\right) \tag{1.32}$$

where ϵ_d is the chemical potential of the last occupied level and $n_d = \sum_{\sigma\in(\Uparrow,\Downarrow)} d_\sigma^\dagger d_\sigma$ the occupation operator (d_σ destroys an electron with spin σ).

In the following, only one electrode will be considered, as the goal is to grasp why the temperature increases the scattering of electrons within a continuum. The continuum Hamiltonian writes :

$$H_{lead} = \sum_{k,\sigma} \left(\epsilon_{k\sigma} - \epsilon_f\right) c_{k\sigma}^\dagger c_{k\sigma} \tag{1.33}$$

where k labels the electron momentum. Finally, the tunneling Hamiltonian writes :

$$H_t = \sum_{k,\sigma} t_k d_\sigma^\dagger c_{k\sigma} + h.c \tag{1.34}$$

If the potential t_k of the tunnel barrier is high enough so that $t_k = const(k) \equiv t$, one can express the tunneling Hamiltonian with the $c_{x=0,\sigma}$ the Fourier transform of $c_{k\sigma}$ at the position of the dot ($x = 0$) :

$$H_t = 2Nt \sum_\sigma d_\sigma^\dagger c_{x=0,\sigma} \quad \text{as } c_{x=0,\sigma} = \frac{1}{2N} \sum_k c_{k\sigma} \tag{1.35}$$

The tunneling Hamiltonian corresponds then to a local interaction.

Let us consider a quantum dot occupied by a single electron, and a conduction electron with the opposite spin in the continuum. The nearest excited state is at energy $+E_c$ when the conduction electron with the opposite spin tunnels into the dot. Considering the second order in the perturbation theory, the ground state energy of the unperturbed Hamiltonian is lowered by the virtual excited state by -J, where

$$J = (2N)^2 \frac{|t|^2}{E_c} \tag{1.36}$$

Due to the Pauli principle, the ground state, where the spin in the continuum is the same as in the dot, has a virtual excitation with a higher energy $E_c + \Delta E > E_c$.

Hence the tunneling Hamiltonian leads to a lower energy for the ground state with anti-aligned spins. From the perspective of the conduction electrons, it can be replaced by an anti-ferromagnetic scattering term[9] V that favors spin anti-alignment ($J > 0$).

$$V = J \overrightarrow{s} . \overrightarrow{S} \tag{1.37}$$

$\overrightarrow{S}$ is the spin of the last electron in the dot and $\overrightarrow{s}$ is the spin of the conduction electron close to the dot (x=0).

1.2.3 Kondo resonance

To understand how the scattering term V enhances the conductance it is useful to look at the transmission matrix T, with a Taylor expansion that looks like [33] :

$$T(\epsilon) = V + V \frac{1}{\epsilon - H_{lead} + i0^+} V + ... \tag{1.38}$$

[9] V can not be directly mapped onto H_t, as scattering terms that do not involve the spin of the electron in the dot have been disregarded, in order to focus only on the Kondo physics.

$|\langle k'|\,T\,|k\rangle|^2$ is the transition rate from a state k to a state k' in the lead, both with energy ϵ. The perturbation V can be rewritten as a sum of terms that flip the spin or leave it unchanged.

$$V = \frac{J}{2N}\sum_{k,k'}\left[\left(c^\dagger_{k\uparrow}c_{k'\uparrow} - c^\dagger_{k\downarrow}c_{k'\downarrow}\right)S_z + c^\dagger_{k\uparrow}c_{k'\downarrow}S_- + c^\dagger_{k\downarrow}c_{k'\uparrow}S_+\right] \tag{1.39}$$

The first order term of the T-matrix, $T^{(1)}$, gives the Fermi's Golden rule, that does not depend on the temperature. To understand the logarithmic enhancement of the transmission with the temperature, let us focus on the second order scattering terms that flip the spin of the conduction electrons, for example $\langle k'\downarrow|\,T^{(2)}\,|k\uparrow\rangle$.

As detailed in figure 1.9, the intermediate electronic states $|q\sigma = \uparrow or \downarrow\rangle$ with energy ϵ_q can be either an electron or a hole. Figure 1.9 shows that scattering events that involve an electron, resp. a hole, as intermediate state, pick up a -1, resp. a $+1$, as phase factor. Hence the spin degree of freedom of the magnetic impurity breaks the symmetry between electrons and hole at the second order of perturbation.

The probability that an electron, resp. an hole, occupies the intermediate state at energy ϵ_q depends on the probability $(1 - f(\epsilon_q - \epsilon_f))$, resp. $f(\epsilon_q - \epsilon_f)$, here f is the Fermi-Dirac function at temperature k_bT. Using equation (1.38), the amplitude of $T(\epsilon)^{(2)}$ is $-\frac{(1-f(\epsilon_q-\epsilon_f))}{\epsilon-\epsilon_q}$ for scattering events involving an electron with energy ϵ_q as intermediate state, and $\frac{f(\epsilon_q-\epsilon_f)}{\epsilon-\epsilon_q}$ for a hole with energy ϵ_q.

By summing over all the possible intermediate states with energy ϵ_q, the matrix element $\langle k'\downarrow|\,T^{(2)}\,|k\uparrow\rangle$ is proportional to :

$$J^2\int\frac{\mathrm{d}\epsilon_\mathrm{q}}{\epsilon-\epsilon_q}\nu(\epsilon_q)\left(f(\epsilon_q-\epsilon_f)-\frac{1}{2}\right) = -J^2\int\frac{\mathrm{d}\epsilon_\mathrm{q}}{\epsilon-\epsilon_q}\nu(\epsilon_q)\tanh\left(\frac{\epsilon_q-\epsilon_f}{2k_bT}\right) \tag{1.40}$$

This integral diverges at high energy, so we need to introduce a cut-off D to take into account the finite bandwidth. Considering that the density of states in the lead is constant $\nu(\epsilon_q) \sim \nu(\epsilon_f)$, the integral for transmission between states at the Fermi level $\epsilon = \epsilon_f$ is proportional to :

$$J^2\nu(\epsilon_f)\int_{-D}^{D}\frac{\mathrm{d}\epsilon_\mathrm{q}}{\epsilon_f-\epsilon_q}\tanh\left(\frac{\epsilon_q-\epsilon_f}{2k_bT}\right) \sim -J^2\nu(\epsilon_f)\ln\left(\frac{D}{k_bT}\right) \tag{1.41}$$

Up to the second order, the matrix elements for scattering events with a spin flip at the Fermi level are :

$$\langle k'\downarrow|\,T(\epsilon=\epsilon_f)\,|k\uparrow\rangle = \tau\left(1-2J\nu(\epsilon_f)\ln\left(\frac{k_bT}{D}\right)\right) = \tau\left(1-\ln\left(\frac{T}{T_k}\right)\right) \tag{1.42}$$

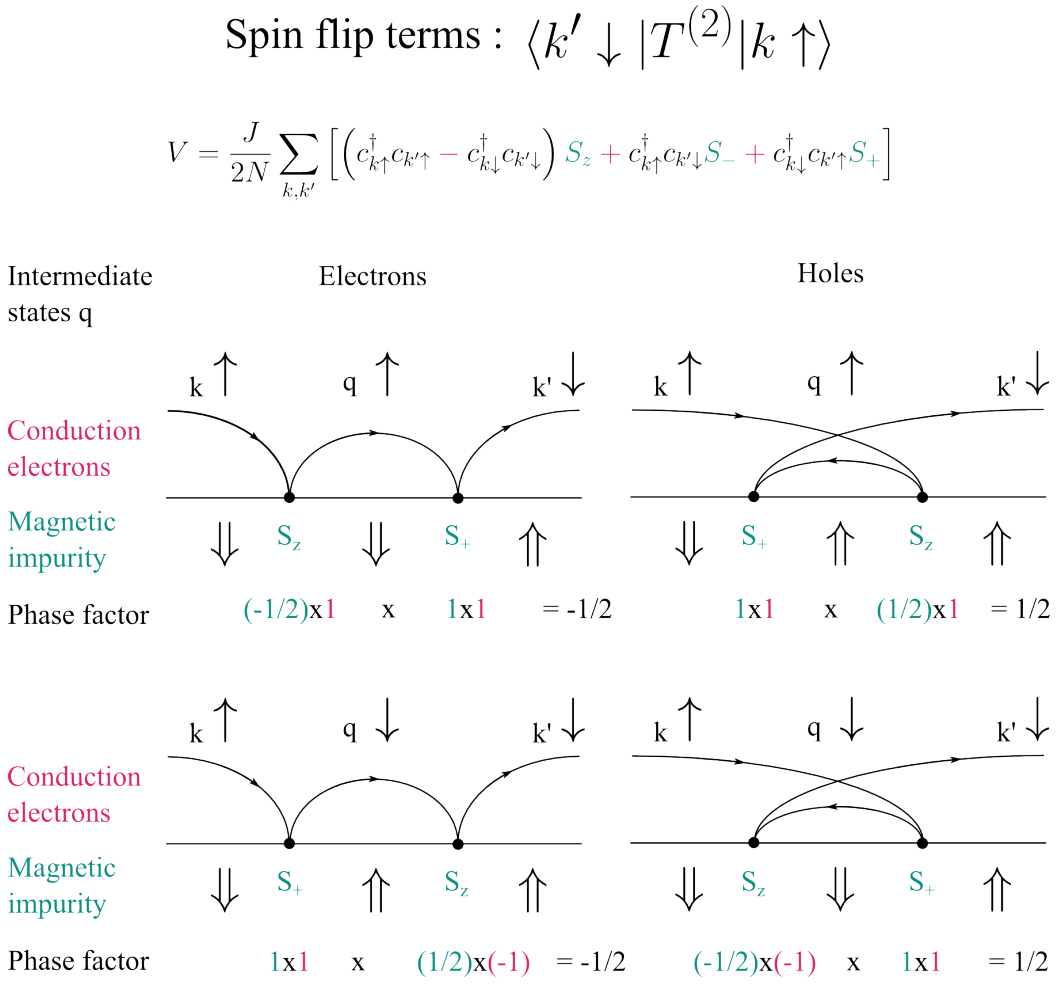

FIGURE 1.9: **Diagrams for the second order T matrix elements** These are the four processes that flip the spin of the incoming electron $|k \uparrow\rangle$ to the outgoing $\langle k' \downarrow|$. They involve an intermediate state with momentum q. The scattering is due to the potential V. The signs coming from spin of the conduction electrons are written n pink and those coming from the spin impurity in blue. The prefactor for each process is the product of two scattering processes.

where $\tau = \langle k' \downarrow | T^{(1)} | k \uparrow \rangle$ is the first order of the transmission given by the Fermi golden rule. $T_k = D/k_b e^{-1/(2J\nu(\epsilon_f))}$ is the Kondo temperature. This shows that the number of scattering events that flip the spin[10] diverges when T is smaller than T_k.

Abrikosov calculated all orders of the expansion and it turns out that they all present the same logaritmic divergence [37].

For $T < T_k$, perturbation theory cannot be used anymore. At zero temperature, the conductance can be calculated by considering that the ground state of the Kondo model is a singlet [38]. Under this assumption, the scattering formalism lead to a conductance

[10] The other scattering terms are proportional to $\int \frac{d\epsilon_q}{\epsilon - \epsilon_q + i0^+} (1 - f(\epsilon - \epsilon_q) + f(\epsilon - \epsilon_q)) = \int_{-D}^{D} \frac{d\epsilon_q}{\epsilon - \epsilon_q + i0^+}$ which tends to zero at $\epsilon = \epsilon_f$.

that reaches the maximal value for one channel : $G = \frac{2e^2}{h}$, accompanied by a $\frac{\pi}{2}$ phase shift for the scattering wave function [34, 39].

The perturbation calculation shows the fact that the conductance in the Kondo regime is carried by spin fluctuations. This is furthermore confirmed by calculating the magnetic susceptibility of the magnetic impurity, which has the same logarithmic divergence with respect to T_k. Another important point raised by the calculation is that this divergence only arises from the states in the close vicinity of the Fermi energy. In fact, the $T(\epsilon)$ matrix spin-flip elements are proportional to $ln(D/|\epsilon - \epsilon_f|)$ for $|\epsilon| >> \epsilon_f$. This observation gave the idea to Anderson to integrate out the electronic degrees of freedom far away from the Fermi level, which leads to a renormalization of the coupling parameter J. By projecting the T matrix on the reduced band $D - \delta D$, he found that J is shifted by

$$\delta J = 2\nu(\epsilon_f)\frac{\delta D}{D}J^2 \tag{1.43}$$

The integral of this last equation shows that $k_bT_k = De^{-1/\left(2J\nu(\epsilon_f)\right)}$ is invariant upon scaling D or J. This confirms that J is not the binding energy of the Kondo cloud as we could have guessed looking at the Anderson Hamiltonian, but that k_bT_k is the only energy scale of the Kondo problem. Consequently all theoretical and experimental observations scale with the Kondo temperature. Conductance, current noise spectral density, magnetic suspectiblity, etc., depend only on the ratio $\frac{T}{T_k}$, $\frac{eV}{k_bT_k}$, $\frac{g\nu_B B}{k_bT_k}$, $\frac{\hbar\omega}{k_bT_k}$,...[40, 41]. The temperature T_k defines the width of the Kondo resonance. in principle, also the length of the Kondo cloud $\frac{k_bT_k}{\hbar v_f}$ or the time scale of the electronic correlations with the magnetic impurity $\frac{\hbar}{k_bT_k}$ can be defined using T_k.

The calculation done by Anderson inspired Wilson to develop a method, based on a logarithmic discretization of the energy around the Fermi energy [42]. He was then able to calculate with numerical renormalization group technique (NRG) all physical quantities like the conductance, the specific heat, etc.

1.3 Superconducting proximity effect

1.3.1 Superconducting electrodes

Superconducting electrodes are described by the Bardeen Cooper Schriffer (BCS) Hamiltonian [43] :

$$H = \sum_{k,\sigma}\xi_k c^\dagger_{k,\sigma}c_{k,\sigma} + \sum_{k,\sigma}\Delta c^\dagger_{-k,-\sigma}c^\dagger_{k,\sigma} + h.c. \tag{1.44}$$

where $\hat{c}^{\dagger}_{k,\sigma}$ refers to the plane wave electron with momentum k, spin σ and kinetic energy ξ_k. The pairing potential Δ is a complex parameter and pairs two electrons with opposite spin and opposite momentum[11]. The states created by $\hat{c}^{\dagger}_{k,\sigma}$ are no longer eigenstates of the BCS Hamiltonian.

The ground state of this Hamiltonian is very different from a simple Fermi sea filled with electrons. It is formed by a 'condensate' of an infinite number of electron pairs, named Cooper pairs :

$$|GS\rangle = \Pi_k \left(u_k + v_k \hat{c}^{\dagger}_{-k,-\sigma} \hat{c}^{\dagger}_{k,\sigma}\right) |0\rangle \tag{1.45}$$

A Cooper pair is a superposition of $|0\rangle$ and two electrons with opposite spins and opposite momenta[12]. A Cooper pair has zero total spin, and zero total momentum. u_k and v_k are phase factors, named coherence factors. As a Cooper pair is a bound state of two electrons close to the Fermi energy, it has a negative energy and so there is no limitation on the number of pairs in the condensate[13].

Cooper pairs can be seen as a bound state of two electrons, but in fact pairs always exchange electrons with each other, so that the superconductivity is truly an ensemble with macroscopic quantum coherence. We can define a length over which two electrons stay together in a Cooper pair. After a time Δt, the Heisenberg principle states that the energy is spread over $\Delta E \sim \hbar/\Delta t$. Hence, the distance traveled by the Cooper pair at the speed v_f before splitting ($\Delta E = \Delta$) is [43] :

$$\xi = \frac{\hbar v_f}{\pi \Delta}. \tag{1.46}$$

The excited states are found from the diagonalization of the BCS Hamiltonian :

$$H_{sc} = \sum_{k,\sigma} E_{k\sigma} \gamma^{\dagger}_{k\sigma} \gamma_{k\sigma} \tag{1.47}$$

The BCS quasiparticles created by the operator $\gamma^{\dagger}_{k\sigma}$ are called Bogoliubov quasiparticles, with energy $E_k = \sqrt{\xi_k^2 + \Delta^2}$. The minimum excitation energy is thus Δ, so the BCS ground state is protected by an energy gap. Above this gap, the quasiparticles form a continuum with a density of states : $\nu_S(E) = \frac{E}{\sqrt{E^2-\Delta^2}} \nu_N$, where $\nu_N = \nu_N(\xi_k = E_f)$

[11] The magnitude and the phase of the pairing potential Δ are uniform in the k-space. This case, called s-wave superconductivity, happens when the interaction that pairs electron is local isotropic in the position space. The orbital wavefunction of the pair is therefore symmetric, meaning that the pair has to be a spin-singlet state.

[12] $|0\rangle$ corresponds to the state with no electron and no hole.

[13] The Cooper pairs can not be considered as bosons because they have a different commutation rule : as $\left[\hat{C}^{\dagger}_k, \hat{C}^{\dagger}_k\right] = \delta_{k,k'} (1 - n_{k,\uparrow} - n_{-k,\downarrow})$, where $n_x = \hat{c}^{\dagger}_x \hat{c}_x$. Therefore the BCS ground state can not be strictly identified to a Bose-Einstein condensate

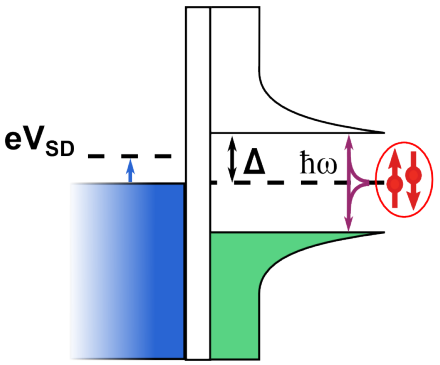

FIGURE 1.10: **Quasiparticle excitations in a superconducting material :** A continuum of quasiparticles that are superpositions of electrons and holes can only be reached for an energy bigger than Δ. If a normal electrode has a positive bias eV with respect to a superconducting electrode, electrons can be injected in the continuum. Similarly, if the bias is negative, holes can be injected in the superconductor, i.e., electrons are flowing to the normal electrode. The superconducting material presents hence a symmetric density of states for electrons. Exciting a Cooper pair from the condensate involves two conjugate quasiparticles and requires therefore a photon with an energy $\hbar\omega$ bigger that 2Δ. Consequently, this symmetric density of states is then also adapted to deal with photon-absorption spectroscopy.

is the density of states in the normal state. These quasiparticles are superpositions of electrons and holes :

$$\begin{aligned} \gamma_{k,\uparrow} &= u_k c_{k\uparrow} - v_k c^{\dagger}_{-k\downarrow} \quad \text{with} \quad u_k = e^{-i\frac{\phi}{2}} \sqrt{\frac{1}{2}\left(1 + \frac{\xi_k}{\sqrt{\Delta^2 + \xi_k^2}}\right)} \\ \gamma^{\dagger}_{-k\downarrow} &= u_k^* c^{\dagger}_{-k\downarrow} + v_k^* c_{k\uparrow} \qquad\qquad v_k = -e^{i\frac{\phi}{2}} \sqrt{\frac{1}{2}\left(1 - \frac{\xi_k}{\sqrt{\Delta^2 + \xi_k^2}}\right)} \end{aligned}$$

For $\xi_k \gg \Delta$, $\gamma\dagger_{k,\sigma}$ (resp $\gamma_{k,\sigma}$) is like an electron (resp a hole).

Excitations of these quasiparticles are commonly realized by injection of an electron (or a hole), or by absorption of a photon. As both $\gamma_{k,\uparrow}$ and $\gamma^{\dagger}_{-k\downarrow}$ are a superposition of an electron and a hole, there is a finite probability to inject an electron or a hole in the superconducting continuum. Hence, the spectroscopy of a superconducting electrode by a normal electrode gives a symmetric density of states with respect to the Fermi energy with a gap for $|eV| < \Delta$[14] (see figure 1.10).

This representation of the density of quasiparticles is also adapted to deal with photon-absorption spectroscopy. Photon absorption conserves the momentum and the spin, so it can only transfer a Cooper pair in the BCS ground state to an excited state with two

[14] At equilibrium, the Fermi energy of a normal electrode match the ground state energy of the Cooper pair condensate.

conjugate quasiparticles $\gamma^{\dagger}_{k_0,\sigma}\gamma^{\dagger}_{-k_0,-\sigma}$ of energy 2Δ. In that case, the symmetric density of states is not related to the injection of an electron and a hole, but related to the two conjugate excited quasiparticles (see figure 1.10).

1.3.2 Andreev reflections and Andreev bound states

In a superconducting electrode, evanescent quasiparticles exist also for energy lower than the gap $|E| < \Delta$, but they decay over the length $\kappa^{-1}(E) = \frac{\sqrt{\Delta^2 - E^2}}{h v_f}$ [15]. When an electron from a normal metal impinges on a superconductor with an energy below the gap, it cannot be injected into the superconducting electrode. It is nevertheless reflected as a hole, so that two electrons are transferred in the superconducting electrode as evanescent quasiparticles, that will decay in the condensate as a Cooper pair (see the figure 1.11 a). These reflections at the interface between a normal and a superconducting electrode are called Andreev reflections. The incident electron is reflected as its particle conjugate (a hole) at the same energy and with a phase : $\chi(E,\phi) = -\phi - \arccos\left(\frac{E}{\Delta}\right)$[16], where ϕ is the macroscopic phase of the superconducting electrode. An incident hole is also reflected as its conjugate electron, with a phase $\chi(E,-\phi)$.

If a coherent conductor is connected to two superconducting electrodes, the electrons and holes bounce back and forth on the superconducting interfaces (see figure 1.11 b). As soon as coherence is preserved, only discrete bound states emerge from constructive interference, called Andreev Bound States (ABSs). They come by pair of states for each conduction channel, one at negative energy $-E_A$, and one excited state at positive energy E_A. Like Cooper pairs, they are not eigenstates of the electron number operator but they have an even parity and zero total spin.

Each Andreev reflections transfers a Cooper pair from one superconducting electrode to the other one. The transfer of Cooper pair across a non superconducting material is the microscopic description of the Josephson effect. The associated supercurrent I is the derivative of the Andreev bound states energy $I = \frac{\partial E_A}{\partial \phi}$.

A pair of ABS is associated with a pair of interference conditions with right-moving/left-moving electrons. If there is scattering inside the channel, which means than an electron (or hole) can be reflected from right moving to left moving, the pair of ABS couple together, and they repel each other when they become close in energy. Therefore there is an avoided-crossing between ABS that are close to zero energy. This is not the case

[15] These are eigenstates of (1.44) with imaginary energy

[16] The Andreev reflections can be well modeled by matching the wavefunction of electrons and holes in the normal electrode to the wavefunction of evanescent states in the superconducting electrode. This model implies that the superconducting order parameter Δ is a step function at the interface, which is a good approximation if the superconducting electrode is much bigger than the normal one[44].

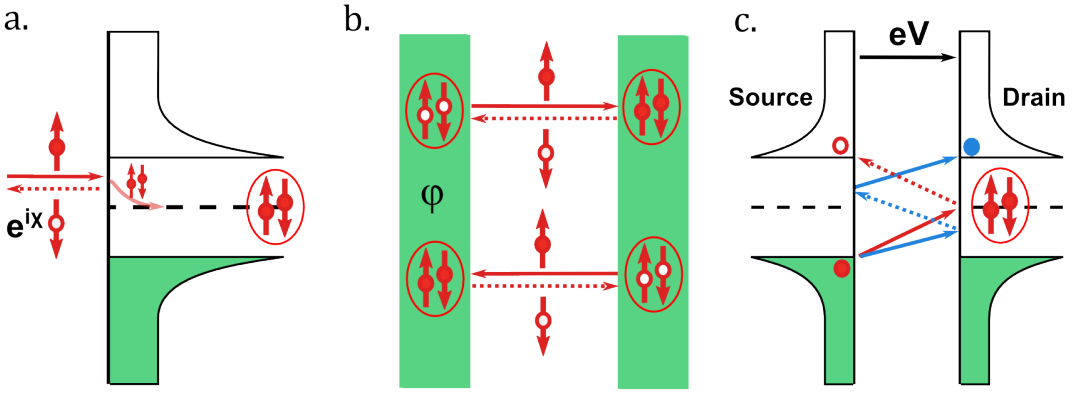

FIGURE 1.11: **Andreev reflections. a.** An electron from a normal electrode with energy smaller than the superconducting gap is reflected as a hole at the interface with a superconducting electrode. Two electrons are transferred in the superconductor and decay as a Cooper pair in the superconducting condensate. **b.** A pair of Andreev bound states appears in a normal region which has two superconducting interfaces. A phase bias ϕ drives $2e$ current, as the energies of ABS depend on ϕ. **c.** If there is a potential drop in the normal region, electrons and holes acquire kinetic energy. If $eV = \Delta$, a Andreev reflection (in red) can bring a electron from the lower continuum to the upper continuum in the source and leaves a Cooper pair in the drain. Two Andreev reflections (in blue) allow one to bring an electron from the lower source continuum to upper drain continuum, requiring $eV = \Delta/3$.

for Majorana bound states that will be presented in section 1.4, whose crossings are topologically protected.

The precise spectrum of the Andreev bound states depends on the characteristics of the Josephon junction. If the length of the conduction channel L is shorter than the superconducting length ξ defined in (1.46), the junction is called a weak link and is only characterized by the channel transmission[17] [45] τ. In that case, two ABS appear within the gap for each conduction channel with energy $\pm E_A$(see figure 1.12) :

$$E_A = \Delta\sqrt{1 - \tau \sin^2 \frac{\phi}{2}} \tag{1.48}$$

For small transmissions $\tau \ll 1$, we recover as expected the usual Josephson effect, which carries a supercurrent : $I(\phi) = I_c \sin(\phi)$, where I_c is the critical current.

When $L > \xi$, the interference conditions for the ABS are modified. The phase accumulated by the electron inside the conductor is bigger than the phase acquired at each Andreev reflection, and several ABSs appear with energy scale given by the length, $\hbar v_f / L$. The length of the junction should be here understood as an effective length of the trajectories of the electron inside the normal conductor. If the interface between

[17] A scattering potential with a delta function, allowing a phase difference between two superconductors is actually sufficient to trap Andreev bound states.

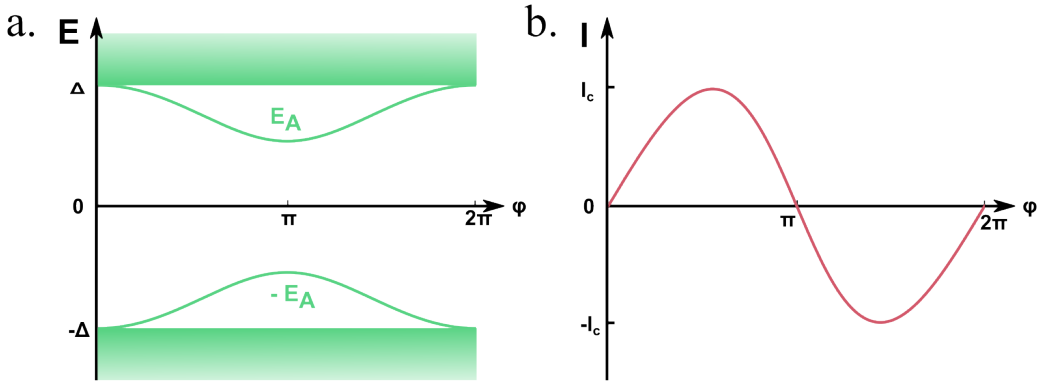

FIGURE 1.12: **Andreev bound states and the related superconducting current for two superconductor connected by a weak link. a.** ABS energy depends on ϕ, the superconducting phase difference. At zero phase bias as the Andreev bound states are stuck to the continuum, whereas at $\phi = \pi$, they repel each other. Like for the bulk density of states, this representation is well adapted for electronic transport spectroscopy : one can transfer electrons from a normal probe through ABS reflections at voltage bias $+E_A$ and holes at bias $-E_A$. Photon absorption at energy $2E_A$ can transfer an ABS from its ground state to its excited states. **b.** Supercurrent carried by the lowest energy ABS with respect to the phase.

the normal and the superconducting material is not perfect, the electrons can be reflected as a normal electron instead than as a hole, increasing this effective length. This trapping of electrons fills the subgap density of states with states at increasingly lower energy when the effective length increases. In the diffusive case, the subgap spectrum will even depend on the ergodicity of the electron trajectories in the normal conductor. The gap is consequently filled up to a minimum energy, called the mini-gap : $E_{mini\,gap} \sim t \times min(\Delta, E_{Thouless})$, with t being the transmission of normal/superconductor interface and $E_{Thouless}$ the Thouless energy[18].

When two superconducting electrodes are biased with a voltage drop eV, one can not deal with ABS anymore, but Andreev reflections can still explain electronic transport features, as shown 1.11 c. An electron from the lower continuum of the superconducting source acquires a kinetic energy eV before being reflected on the drain as a hole. The hole going towards the source also acquires the energy $(-e) \times (-V)$. If $2eV$ is larger than 2Δ, the hole ends up in the upper superconducting continuum of the source, leaving a Cooper pair in the drain. Similar processes involving Multiple Andreev Reflections (MAR) happen above specific voltages $eV = \frac{2\Delta}{n}$, $n \in N$. Consequently, $n/2$ Cooper pairs will be transferred if n is even while if n is odd an extra electron is also transferred[19].

[18] The Thouless energy is $E_{Thouless} = \hbar/\tau_D$ where τ_D is the diffusion time in the normal conductor.

[19] A voltage bias leads to periodic oscillations of the phase as $\dot{\phi} = \frac{eV}{\hbar}$, and therefore to Cooper pair oscillations between the source and the drain. With that picture, the MAR resonances can also be viewed as inelastic tunneling of Cooper pairs into the drain. The radiated energy is absorbed to excite n quasiparticle in the source continuum, so that eV should be an integer fraction of Δ. Note that if the

Therefore MAR give resonances in the subgap conductance when eV is a integer fraction of Δ. These resonances decrease with the number of reflections as t^n, $(1-t)$ being the probability for electron or hole in the normal region of being back-scattered . They are therefore absent at low voltage[20] and suppressed for interfaces with low transparency.

1.3.3 Andreev bound states in quantum dot

Quantum dots are interesting candidate for hosting Andreev bound states, because their discrete spectrum leads to well separated conduction channels and therefore allow one in principle to isolate single pairs of ABS. Carbon nanotubes are well suited because their ballistic properties preserve the coherence on the scale of the quantum dot. Nevertheless quantum dots have other energy scales that may compete with the superconducting pairing Δ, namely the charging energy E_c or the Kondo temperature T_k.

Let us first focus on the case where E_c and T_k are much lower than Δ. If $\Gamma \gg \Delta$, the time spent in the dot $\hbar/\Gamma$ is much shorter than the correlation time of Cooper pairs $\hbar/\Delta$ so that the quantum dot behaves like a weak link and the Cooper pair can tunnel via Andreev bound states in the dot. These Andreev bound states still remain when $\Gamma \ll \Delta$ and can be even expressed as a superposition of zero and two electrons in the dot.

A Schrieffer-Wolf transformation can be indeed performed on the Hamiltonian $H = \sum_\sigma d_\sigma^\dagger d_\sigma + t\sum_{k,\sigma} d_\sigma^\dagger c_{k\sigma} + h.c + H_{sc}$, where H_{sc} is described by equation (1.47). This yields, at the second order in the tunneling amplitude t the effective dot Hamiltonia[21] [46] :

$$H_{d,\text{eff}} = \tilde{\epsilon_d} n_d + \left(\Gamma_C d_\uparrow^\dagger d_\downarrow^\dagger + h.c.\right) \tag{1.49}$$

The dot energy level $\tilde{\epsilon_d}$ is renormalized and the pairing potential Γ_C is :

$$\tilde{\epsilon_d} = \epsilon_d \left(1 - \pi|t|^2\nu_N \frac{1}{\sqrt{\Delta^2 - \epsilon_d^2}}\right) \text{ and } \Gamma_C = \pi t^2 e^{i\phi}\nu_N \frac{1}{\sqrt{1-\left(\frac{\epsilon_d}{\Delta}\right)^2}} \tag{1.50}$$

environment can absorb the energy radiated by the Cooper pairs at the frequency $\nu = \frac{V}{2\pi\phi_0}$, Cooper pairs can also be transferred from the source to the drain, at this voltage bias that is a priori not a fraction of 2Δ.

[20] As $\dot{\phi} = \frac{eV}{\hbar}$, one can still deal at low bias voltage with ABS, whose energy is varying adiabatically in times. ϕ varying from 0 to π it brings the ground state ABS close in energy to the excited one. If a Landau-Zehner transition happens at $\phi = \pi$, the excited state can then be brought into the continuum at $\phi = 2\pi$. Hence ABS can act as an 'elevator' [45].

[21] This transformation allows one to derive an effective Hamiltonian for the dot, for weak tunneling $\Gamma \ll \Delta$. The subspace of the dot is then reduced to the four states of lowest energy: $|0\rangle$, $|\uparrow\rangle$, $|\downarrow\rangle$ and $|\uparrow\downarrow\rangle$.

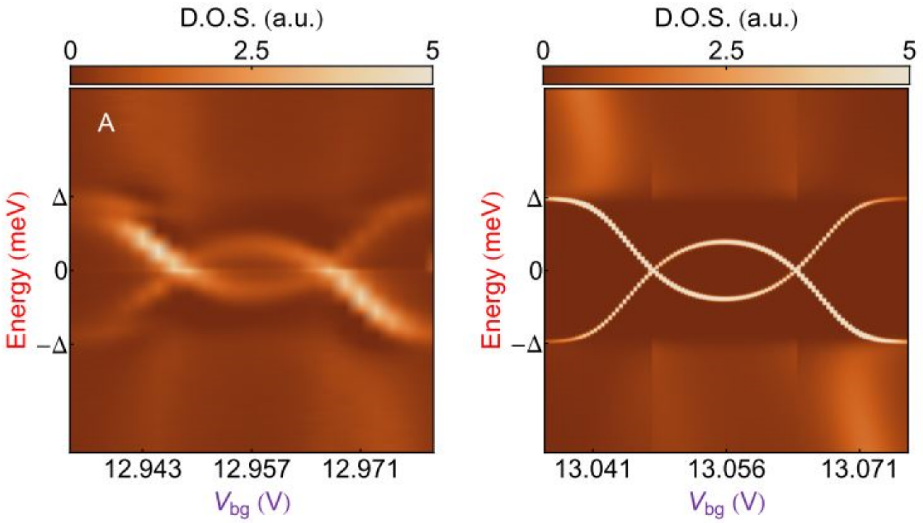

FIGURE 1.13: **Andreev bound states in a carbon nanotube** Figure taken from [44]. Left pannel : The device in [44] allowed them to measure the density of states of a carbon nanotube contacted by two superconducting aluminium electrodes. V_{bg} is a back gate potential. The pair of ABS crosses at gate voltages corresponding to an edge of a Coulomb diamond. In the middle there is an odd number of electrons, deduced by the presence of a Kondo ridge when superconductivity is removed. At the Coulomb peak, there is a ground state transition between an ABS and the magnetic doublet. Right panel : NRG calculation reproducing the experimental data. In that case, $\Gamma \sim \Delta \sim E_c/10$.

In the subspace with an even number of electrons, there are two eigenstates with energy $E_\pm = \tilde{\epsilon_d} \pm \sqrt{\tilde{\epsilon_d}^2 + |\Gamma_C|^2}$ which look very much like Cooper pairs :

$$|\Psi_\pm\rangle = \left(\frac{\Gamma_C^*}{\sqrt{|\Gamma_C|^2 + E_\pm}} + \frac{E_\pm}{\sqrt{|\Gamma_C|^2 + E_\pm}} d_\uparrow^\dagger d_\downarrow^\dagger \right) |0\rangle \tag{1.51}$$

The subspace with an odd number of electrons in the dot is spin degenerate at the energy $\tilde{\epsilon_d}$ with two states $|\uparrow\rangle$, $|\downarrow\rangle$, sometimes called the magnetic doublet.

Coulomb repulsion, $(\Gamma, \Delta) \ll E_c$, forbids the exchange of two electrons with a superconducting electrode so that the Andreev states are not the ground state. Experimental realisation of tunneling spectroscopy of a quantum dot connected to superconducting electrodes have yet observed bound states inside the superconducting gap for $\Gamma \sim \Delta < E_c$ in nanowires [47] or in carbon nanotubes[44], as shown in figure 1.13. The tunneling spectroscopy probes excitations between subspaces with different electrons parity. If there is an even number of electrons in the dot, the QD ground state is the state $|\Psi_-\rangle$ and the lowest excited state with one more electron is the magnetic doublet. If there is an odd number of electrons in the dot, the ground state is the magnetic doublet and

the lowest excited state is $|\Psi_+\rangle$. A quantum dot is alternatively occupied by an even and odd number of electrons by sweeping the gate voltage, so there is a transition in the ground state between ABS and magnetic doublet with the gate voltage, shown in figure 1.13.

This ground state transition induced by parity switching leads to a reserved sign of the supercurrent [48]. If the quantum dot level is singly occupied, a transfer of a Cooper pair implies that the spin of the electron in the dot is flipped twice, and that the transmitted Cooper pair acquires a phase -1 [49]. This minus sign corresponds to π shift in the Cooper pair phase, and electrodes with a phase-bias ϕ behave like a Jopheson junction whose current-phase relation has been shifted by π, $I = I_c \sin(\phi + \pi)$. This peculiar behaviour called 0 to π-junction transition [50] has been recently observed in carbon nanotubes. This situation with a degenerate magnetic doublet is the ingredient for the emergence of the Kondo effect. Hence if $T_k \gg \Delta$, the superconducting proximity effect is blurred and Kondo physics dominates. This competition between the Kondo effect and the superconducting proximity effect has been observed in this thesis in carbon nanotube, as presented in chapter 5.

1.4 Majorana bound states

1.4.1 Properties of Majorana quasi-particle

A Majorana fermion is a particle that is also its own anti-particle. It means, in a second quantization language, that the creation and annihilation operators are the same : $\gamma^\dagger = \gamma$. Such particles, historically studied in high energy physics, have been recently envisioned as quasi-particles in condensed matter [21, 22]. These quasi-particles are predicted to emerge at the interfaces of a p-wave superconductor, a superconductor that pairs electrons with the same spin, as opposed to a s-wave superconductor. In a 2D p-wave superconductor, these Majorana fermions are expected to be located at defects, such as vortices. In 1D, they appear at the boundaries of such p-wave superconductor.

Kitaev modeled [20] the case of a 1D p-wave superconductor as a chain of N sites occupied by spinless fermions c_i, with a chemical potential μ, a tunnel amplitude t between adjacent sites, and a pairing potential Δ :

$$H_{Kitaev} = \sum_{i=1}^{N} \left(-\mu \left(c_i^\dagger c_i - \frac{1}{2} \right) - t \left(c_i^\dagger c_{i+1} \right) + \Delta c_i c_{i+1} \right) + h.c. \tag{1.52}$$

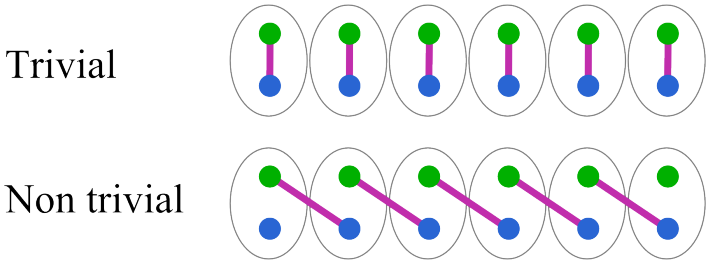

FIGURE 1.14: **Kitaev chain in the trivial and non trivial phase.** Each fermionic site is indicated by a grey circle. The two Majoranas stem from the partition (green/blue) between the real and imaginary parts of the electronic wavefunction. In the trivial phase (top), two Majoranas on each site are paired, whereas in the non-trivial phase (bottom), two Majoranas from neighboring sites are paired together. It leaves two unpaired Majorana at each extremity.

From each fermionic operator on the site i, one can define two Majorana operators $\gamma_{i,1}$, $\gamma_{i,2}$, being the real part and the imaginary part of c_i :

$$\begin{aligned} \gamma_{i,1} &= c_i^\dagger + c_i \\ \gamma_{i,2} &= i\left(c_i^\dagger - c_i\right) \end{aligned} \tag{1.53}$$

The Majorana quasi-particle is then an equal superposition of an electron and a hole.

If $|\Delta| = t = 0$ and $\mu < 0$, the Hamiltonian rewritten with γ operators reads :

$$H_{trivial} = -\mu \sum_{i=1}^{N} \gamma_{i,1}\gamma_{i,2} \tag{1.54}$$

In that 'trivial' case, two Majorana operators on the same site are paired together. But if $|\Delta| = t > 0$ and $\mu = 0$, the Hamiltonian takes the form :

$$H_{Kitaev} = it \sum_{i=1}^{N-1} \gamma_{i+1,1}\gamma_{i,2} \tag{1.55}$$

where Majoranas are paired from two neighbouring sites, as shown in figure 1.15. One can define new fermionic operators associated to these pairs of Majorana :

$$\tilde{c_i} = \frac{1}{2}\left(\gamma_{i+1,1} + i\gamma_{i,2}\right) \tag{1.56}$$

The Hamiltonian can be rewritten has :

$$H_{non\,trivial} = 2t \sum_{i=1}^{N-1} \left(\tilde{c_i}^\dagger \tilde{c_i} - \frac{1}{2}\right) \tag{1.57}$$

In this non-trivial case, two Majoranas, located at each end of the chain $\gamma_{1,1}$ and $\gamma_{N,2}$, do not appear in the Hamiltonian any more. One can nevertheless form a fermionic operator as a combination of the two non local Majoranas :

$$\tilde{c}_N = \frac{1}{2}\left(\gamma_{1,1} + i\gamma_{N,2}\right) \tag{1.58}$$

Importantly, as this operator is absent from the Hamiltonian, it costs zero energy to occupy the two non-local Majoranas with one fermion. This means that there is a degeneracy between the state with 0 or 1 fermion occupying the two Majoranas. This differs from conventional superconductors where the ground state is always occupied by an even number of electrons.

As a first consequence of the ground state degeneracy, it is allowed to add or extract an electron in the chain without energy cost. The wavefunction of this fermionic state happens to be localized at both boundaries of the chain. If the chain is connected to two electrodes, electrons can be consequently transmitted through this effective superconductor at zero bias [22].

A second striking feature is that these Majoranas are protected from environmental perturbations. In fact, as the two Majoranas are well separated on each extremity of the chain, the fermionic operator is insensitive to local perturbations. This is expected to yield a long coherence time for the fermionic state, because decoherence sources are most of the time local. Furthermore, this zero energy state is protected by a gap from the high-energy fermionic excitations of the p-wave superconductor. The robustness of the Majorana is also enhanced by the fact that their emergence and disappearance is controlled by geometrical considerations on the subspace regrouping all the eigenstates of the Hamiltonian. The topology of the subspace defined by the trivial Hamiltonian (equation (1.54)) cannot be connected to the one given by the non trivial Hamiltonian (equation (1.57)), as it will be briefly explained later. Physically, it means one has to close and reopen the gap to move from the trivial to the non-trivial phase.

In the non-trivial Hamiltonian, the counting of the quasi-particle changes dramatically. One cannot count particles that are their own antiparticle, as the usual number operator[23] is : $\gamma_i^\dagger \gamma_i = \gamma_i^2 = 1$. The information on the state occupancy can nevertheless be traced back by the parity of the fermionic operator associated to a pair of Majorana. As a pair of Majorana is only either empty or occupied by one fermion, it is useful to define the parity operator $P_i \equiv 1 - 2c_i^\dagger c_i$, with eigenvalue $+1$ (even parity) or -1 (odd parity).

[22] One can therefore talk of 'teleportation' of an electron, but this should not be confused with teleportation of information : any manipulation performed on one Majorana can not be detected on the other, as only non-local measurements can lift the fermionic occupancy degeneracy

[23] From the commutation relation of c_i, one finds that $\{\gamma_i, \gamma_j\} = 2\delta_{ij}$

Considering several pairs of Majorana, two different parity operators P_i, P_j commute together so parity operators define a basis of Majorana pairs for the Hilbert space.

The parity of two Majoranas can be measured by recombining it into a fermion. In fact, if a pair of Majoranas are brought close together, they hybridize and the 0 or 1 fermionic occupancy is not degenerate anymore. These two states are split by an energy ϵ :

$$H_{merge} = \frac{i}{2}\epsilon\gamma_{i,1}\gamma_{i,2} = \epsilon\left(c_i^\dagger c_i - \frac{1}{2}\right) \tag{1.59}$$

The energy splitting increases with the overlap of the localized Majoranas wavefunction. As a Majorana is a superposition of an electron and a hole, the fusion of a pair of Majoranas gives either an electron or a hole, depending of the parity P_i of the pair.

For a set of N Majorana pairs, the ground state degeneracy is 2^{N-1}, depending on the parity of each pair, the total parity being conserved. The most striking behavior of the Majorana fermions is that the ground state changes by exchanging non-interacting Majorana quasi-particles. Therefore exchange rules of indistinguishable Majoranas are governed by non abelian statistics[24]. Exchange of Majoranas inside a given manifold, called braiding, becomes a non-commutative operation : the order of a braiding sequence matters.

To give an example, let us consider two pairs of Majoranas with fermionic occupation $|n_1 n_2\rangle$, $n_i = 0$ or 1. The braiding of the two Majoranas that do not belong to the same pair transforms the state $|00\rangle$ in the state $\frac{1}{\sqrt{2}}(|00\rangle + i\,|11\rangle)$. This new state can not be written as $e^{i\phi}\,|00\rangle$, and corresponds to a rotation on the Bloch sphere, $|00\rangle$ being the south pole and $|11\rangle$, the north pole.

Nevertheless as no braiding operations can be achieved in 1D, without merging the Majoranas, one has to consider at least a network of 1D chain, or to move to 2D systems. Importantly, the exchange should be adiabatic[25] in order to stay in the ground state manifold.

The following subsection aims at giving a 'flavor' on the topological difference between the trivial and the non trivial Hamiltonian. The Hamiltonian of the Kitaev chain in the momentum space can be written as a 2x2 matrix in the Bogoliubov-de Gennes basis $\left(c_k, c_{-k}^\dagger\right)$ [51] :

$$H_{kitaev} = \begin{pmatrix} \mu - 2t\cos(k) & -2i\Delta\sin(k) \\ 2i\Delta\sin(k) & -\mu + 2t\cos(k) \end{pmatrix} = E(k)n(\vec{k})\cdot\vec{\tau} \tag{1.60}$$

[24] A statistic is abelian when exchanging to identical particle yields only a phase factor for the many body states. For bosons the phase factor is +1 and fermions −1

[25] The adiabatic time scale is given by the energy gap, that protects the manifold.

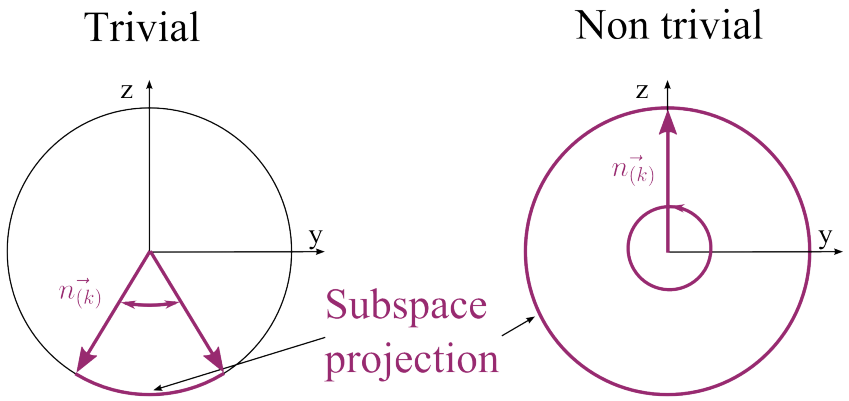

FIGURE 1.15: **Topology of the trivial and non trivial subspace.** The Hilbert space is projected onto a Bloch sphere and each state corresponds to a unitary vector $\vec{n(k)}$, parametrized by k. For both the trivial and non trivial, $\vec{n(k)}$ lies in the $y-z$ plane. In the trivial phase, the subspace stays close to the south pole, whereas in the non trivial it is wrapped all along the Bloch sphere.

The vector $\vec{\tau}$ is connected to the set of Pauli matrices, τ_x, τ_y, τ_z associated to the $\left(c_k, c^\dagger_{-k}\right)$ basis. Equation (1.60) shows that the Hilbert space can be projected onto the Bloch sphere defined by the Pauli matrices $\vec{\tau}$. Each state k is associated to a unitary vector $\vec{n}(k)$ on this sphere.

Let us look at how this vector behaves when k is moving within the Brillouin zone. If $\mu < 0$ and $t \sim \Delta \ll |\mu|$, the vector $\vec{n(k)}$ is blocked around the south pole of the Bloch sphere. On the contrary, if $\mu \sim 0 \ll t \sim \Delta$, $\vec{n(k)}$ turns around the Bloch sphere when k is moving in the k-space. From these two different behaviors, one can say that the two subspaces defined by the eigenstates of the two Hamiltonian are topologically non-equivalent[26]. More formally, one can define a topological integer number, called the Chern number, in order to quantify the difference between the 'trivial' and the 'non-trivial' case. It corresponds to the Berry phase integrated around a closed loop $\frac{i}{2\pi} \oint dk \, \langle n(k)|\nabla n(k)\rangle$. In our case, it simplifies to the number of times the normalized vector wraps the center of the Block sphere, 0 in the trivial and 1 in the non trivial phase. Kane describes this integer number as a 'quantum polarization', identifying $e \, \langle n(k)|i\nabla n(k)\rangle \sim \langle n| \, e\vec{r} \, |n(k)\rangle$ and making the analogy of a dipole whose integer number of charges at each edge would depend on the topology[27].

[26] In a more mathematical terms, the subspace defined by the states of the Hamiltonian is called a bundle, parametrized by k.

[27] The Berry phase takes into account a phase accumulated by a eigenstate $|n\rangle$ moving adiabatically with a parameter $\lambda(t)$: $|\Psi(t)\rangle = e^{-i\int E_n(t)dt} \, |n(\lambda(t))\rangle$ The eigenenergy $E_n(t)$ correspond to a dynamical phase related to the time evolution of the eigenstate. Nevertheless the parametric evolution of the state in the Hilbert space gives also a geometrical phase, the Berry phase. If the parametric evolution returns to the starting point (closed loop), this phase can not be eliminated by a gauge transformation, so the geometrical phase accumulated on the path has to be taken into account.

1.4.2 Engineered Majorana fermions in 1D

In 2010, two proposals were made to induce a non trivial p-wave superconducting pairing in 1D quantum wire [21, 22]. Three ingredients were identified :

- a single channel with spin-orbit coupling
- a magnetic field applied perpendicularly to the spin-orbit coupling axis
- an induced s-wave superconducting pairing

The combination of these three ingredients can be understood in this way : the magnetic field polarizes the spins in the channel, in order to get an effective spinless chain, as in the Kitaev model. The spin orbit coupling rotates the spin with respect to its position, and allows the s-wave pairing induced by the superconducting proximity effect to be converted to an effective p-wave pairing.

It is summed up in the following Hamiltonian :

$$H = \left(\frac{\hbar^2 k_x^2}{2m} - \mu - \alpha_{SO} k_x \sigma_y \right) \tau_z + E_z \sigma_z + \Delta \tau_x \tag{1.61}$$

Electrons move in the 1D channel along the x direction. The magnetic field induces a Zeeman splitting E_z in the z direction, perpendicularly to the axis of the spin orbit splitting, with a spin-orbit constant α_{SO}. $\sigma_{y,z}$ are the Pauli matrices for the spin. $\tau_{x,z}$ are those related to the electron/hole subspace. Δ pairs electrons and holes of opposite spin.

If $E_z > \sqrt{\Delta^2 + \mu^2}$, the Hamiltonian is in a non-trivial superconducting phase with a gap at zero momentum :

$$\Delta_{topological} = E_z - \sqrt{\Delta^2 + \mu^2} \tag{1.62}$$

When the condition is not fulfilled, the Hamiltonian is in the trivial phase. At the boundary between the trivial and non trivial phase, the gap closes at zero momentum, yielding localized Majorana fermions, like in the Kitaev model.

The Majorana is localized over the length given by the topological gap $\xi_{top} \sim \hbar v_f / \Delta_{topological}$. The wave function can be approximated by :

$$\Psi(x) = e^{-x/\xi_{top}} e^{\pm k_f x} \tag{1.63}$$

If there is an overlap between the two Majoranas, an interference pattern gives rise to oscillations of the wavefunction inside the exponential envelope.

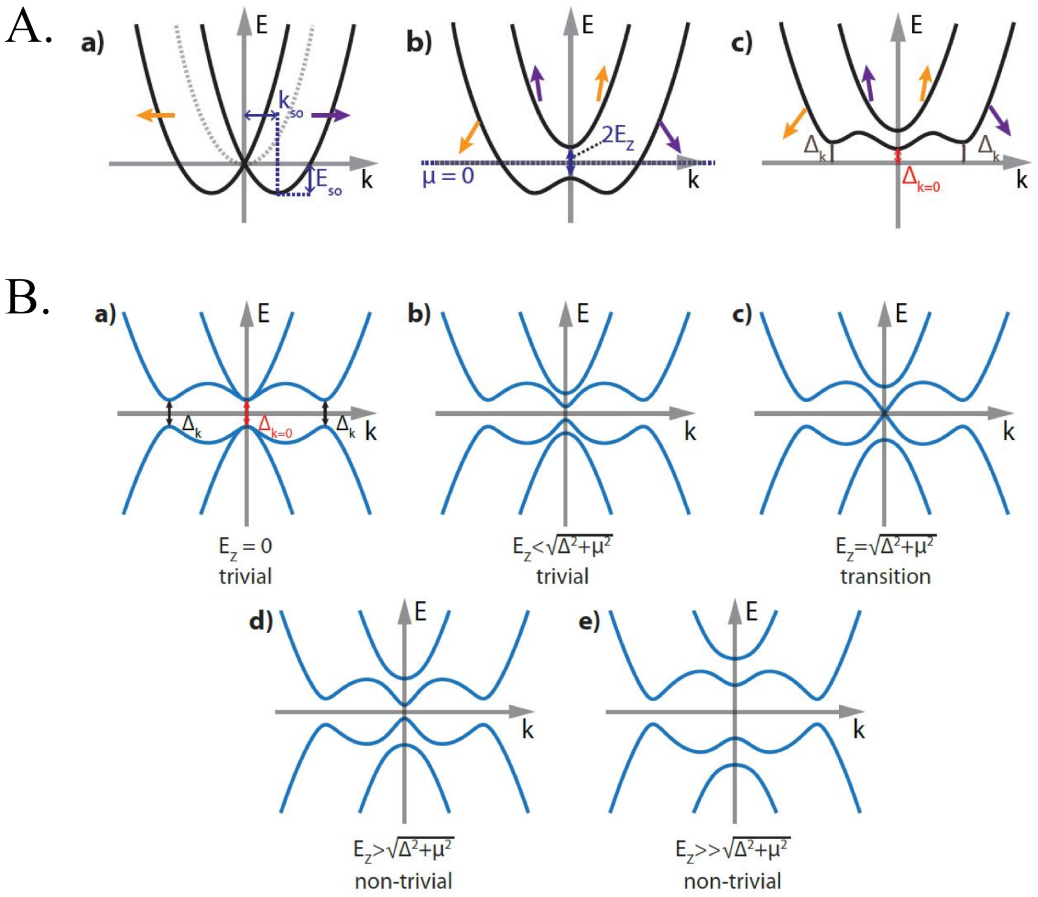

FIGURE 1.16: **Spectrum of a 1D channel with a spin orbit coupling, Zeeman splitting and s-wave superconductivity pairing A. a)** The spin orbit coupling splits the electronic dispersion in two parabolas. **b)** A perpendicular magnetic field opens up a 'helical' gap. **c)** The superconductivity couples the electron dispersion and the hole one (the mirrored of the electron one) and opens up a gap at high momentum $k = 2k_{SO}$. **B.** Evolution of the spectrum with the applied magnetic field, starting in the trivial phase, closing the gap and reopening the gap in the non-trivial phase. Figure taken from [51].

To understand the interplay between the spin-orbit coupling and the magnetic field, let us look at the electron dispersion without the superconductivity. As shown in figure 1.16, the spin-orbit coupling shifts by $k_{SO} = (m\alpha_{SO})/\hbar^2$ (resp $-k_{SO}$) the parabola corresponding to spin $|+\rangle$ (resp $|-\rangle$) in the y direction. It also shifts the minimum of the parabolas by the spin-orbit energy $E_{SO} = (m\alpha_{SO}^2)/(2\hbar^2)$. When a Zeeman field is applied perpendicularly to the spin-orbit coupling axis, it tilts the spin eigenvalues towards this second quantification axis and the mixing of the spin opens a gap at zero momentum. Inside the gap, there are two non-degenerate states with different spins. More precisely, the spin degree of freedom is locked to the momentum. The regime is referred to as 'helical', although strictly speaking, a helical state is a state with opposite momentum states having opposite spin.

The presence of the 'helical' gap is a crucial feature to enter into the non-trivial phase. At zero momentum, this gap competes with the one opened by superconductivity. Figure 1.16 shows the closing and the reopening of the gap with the magnetic field. The trivial/non-trivial characteristic cannot be deduced directly from the spectrum as it only shows the eigenvalue of the Hamiltonian and not the topology of the subspace defined by the eigenvectors.

The gap at high momentum is crucial to ensure that the closing and reopening of the gap at small momentum is not affected by the states at high momentum. At zero magnetic field it is equal to the induced superconducting gap. At finite Zeeman splitting, it is reduced by a factor depending on the ratio E_z/E_{SO}. If this ratio is small, the high momentum gap evolves as $\Delta_k \sim \Delta\left(1 - \frac{1}{24}\frac{E_Z}{E_{SO}}\right)$ [51].

Therefore, even though the spin-orbit coupling does not enter in the condition for the opening of the topological gap, it is crucial that it is strong enough to preserve the gap at high momentum.

The combination of spin-orbit interaction and a perpendicular magnetic field can be replaced by a periodic rotating magnetic field along the wire, as sketched in the figure 1.17. The Hamiltonian :

$$H = \frac{1}{2} g\mu_B B_o \overrightarrow{f\left(\frac{x}{2\lambda}\right)} \cdot \vec{\sigma} \tag{1.64}$$

described a rotating field, which has a constant norm B_0 and oscillates with a period 2λ. $|\overrightarrow{f\left(\frac{x}{2\lambda}\right)}| = 1$ and $\vec{\sigma}$ are the Pauli matrices. Performing an unitary operation aligning the local spin quantization axis with the local magnetic field direction, the transformed Hamiltonian gives an effective spin-orbit term and a Zeeman term perpendicular to the spin-orbit [28]. The Zeeman term is given by B_0, and in the case of carbon nanotubes with a linear dispersion the spin-orbit energy is inversely proportional to λ, the spin-orbit length [27] :

$$E_{SO} = \frac{\hbar v_f}{2\lambda} \tag{1.65}$$

The spin-orbit coupling is then a multiple of the confinement energy and can therefore reached in confined nanostructure energies in the meV range.

This artificial spin-orbit coupling is relevant to induce Majorana bound states in semiconductors that have a weak spin-orbit coupling, such as carbon nanotubes. A helical order can also emerge in carbon nanotubes grown from ^{13}C, thanks to the ordering of nuclear spins via RKKY interactions [52, 53].

In this thesis, we follow the strategy that uses an external rotating field. Such a rotating field can come from a ferromagnetic gate electrode. We describe in the third chapter the nanofabrication methods developed to stamp a carbon nanotube above a ferromagnetic

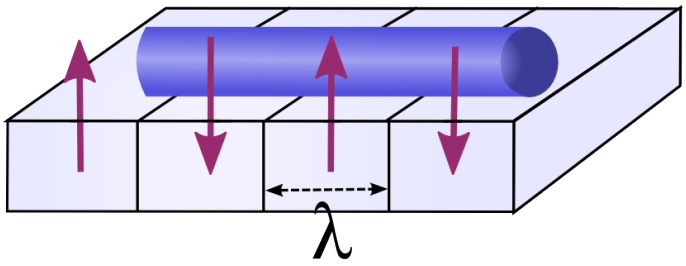

FIGURE 1.17: **Schematic picture of spin-orbit coupling induced by a rotating field.** The purple arrow represent a rotating magnetic field along the wire axis. λ is the period of the rotation

gate and in the fifth chapter, preliminary experimental results from such a device are presented.

Chapter 2

Circuit QED architecture

Electronic transport measurements are the most direct way to probe the quantum dot circuits presented in the first chapter. In the experiments presented in chapter 4 and 5 of this manuscript, the response of the circuit to microwave excitations is also measured, by coupling the circuit to a high finesse microwave cavity. A high finesse cavity confines a monochromatic electromagnetic field, with highly reflecting mirrors, so that the field is weakly coupled to the environment. A first advantage to move at higher frequency is that the $1/f$ noise of the background charge is reduced compared to dc transport measurement. The use of a cavity, a high quality factor resonator, furthermore increases the sensitivity of a measurement. A second advantage of microwave cavities is that they can be done with on-chip superconducting circuits, that are in a lumped elements regime. This gives control on the coupling mechanism, which determines the dynamics of the quantum dot circuit to be probed. A microwave cavity gives therefore access to internal dynamics of quantum dot circuit, that cannot be probed by transport measurement. If the cavity is for example coupled to the gate electrode of a quantum dot, one can measure the dot compressibility, which is the linear charge response of the dot to a modulation of its chemical potential.

Microwave light can reach quantum regime at temperature routinely achievable with commercial dilution refrigerator, since $7GHz \sim 30\mu eV \sim 300mK$. Quantum light-matter interaction has been achieved with microwave cavities coupled either to atoms or to superconducting qubits, which are described in the first section of this chapter. The discussion is then extended to the mesoscopic circuits, made of quantum dots and reservoirs, which have many fermionic degrees of freedom. We will focus on the case where a microwave cavity measures the compressibility of a quantum dot and compare this measurement technique with previous set-up. The last section describes the experimentally relevant parameters in the measurement of the dot compressibility with a microwave cavity.

2.1 From atomic QED to circuit QED

This chapter presents the description of the interaction between cavity photons and atoms, or their condensed matter counterparts, of which dynamics can be reduced to few numbers of degrees of freedom.

2.1.1 Light matter coupling in atomic QED

A high finesse photonic cavity confines light with highly reflective mirrors. Cavity photons are stored in a discrete set of modes, each being a harmonic oscillator. In this

chapter, only one photonic mode is considered to be relevant for the interaction with the system. This mode at the frequency ω_c is described by the Hamiltonian : $\hat{H}_{cav} = \hbar\omega_c \hat{a}^\dagger \hat{a}$, with $\hat{a}$ being the operator that annihilates a photon in the cavity.

Seminal atomic cavity quantum electrodynamics (QED) experiments were realized with 3-dimensional superconducting cavities, with resonances in the microwave range. In those experiments, a beam of circular Rydberg atoms,[1] which are quasi-resonant with the cavity photons, moves through the cavity (see figure 2.1).

Valence electrons of an atom have a discrete energy spectrum and the dipole interaction couples the electron motion with the light. In most experiments, because of the small size of the atoms compared to the photon wavelength, the electric field can be considered as constant over the size of the atom. The electrical dipole Hamiltonian then writes :

$$H_{dip} = -\hat{\vec{D}} \cdot \vec{E} \tag{2.1}$$

with $\vec{D}$ the atomic dipole operator $q\hat{\vec{r}}$.

This dipole interaction couples two discrete electron states Ψ_g, Ψ_e, if they have a non zero matrix element $\frac{\hbar\Omega}{2} = \int \mathrm{d}r^3 \Psi_e^*(\vec{r}) \left(-e\vec{r} \cdot \vec{E}\right) \Psi_g(\vec{r})$. The discrete electronic levels are not regularly spaced because the atomic confinement potential is non harmonic. Consequently the electric field oscillating at frequency ω_c couples preferably to a transition between two states for which the Bohr frequency $E_e - E_g = \hbar\omega_{at}$ is the closest from ω_c. Here g, resp. e, refers to the ground, resp. excited state. The interaction between the light and the atom can be mapped onto a two-level Hamiltonian, the Jaynes-Cummings Hamiltonian :

$$H_{Jaynes-Cummings} = \hbar\omega_c \hat{a}^\dagger \hat{a} + \hbar\omega_{at} |e\rangle\langle e| + \frac{\hbar\Omega}{2} \left(|g\rangle\langle e| + |e\rangle\langle g|\right) \left(\hat{a}^\dagger + \hat{a}\right) \tag{2.2}$$

The vacuum Rabi frequency Ω is typically of the order of $100kHz$ for Rydberg atoms [54]. This off-diagonal term induces a transverse coupling between the ground and excited states.

The coupling of the oscillating magnetic field to the electron spin can be disregarded because it is much smaller than the electronic dipole coupling. More precisely, the ratio between the electric dipole and magnetic dipole is equal to $d/(\alpha a_0)$ where d is the dipole length, a_0 the Bohr radius and $\alpha \simeq 1/137$ the fine constant structure [55][2].

[1] Circular Rydberg atoms have principal quantum number around $N = 50$ and a maximum angular momentum.

[2] The size of the dipole in a Rydberg atom is $N^2 a_0$, where N is the principal quantum number and a_0 the Bohr radius [54]

Depending on the relation between ω_c and ω_{at}, two regimes are described by the Jaynes-Cumming Hamiltonian [54] :

- **A dispersive regime**, where the frequencies are detuned by $\Delta = \omega_{at} - \omega_c \gg \sqrt{n+1}\Omega$. In that case, the atom and the photons exchange energy only virtually. At the second order of perturbation, the interaction lowers the cavity frequency by $\hbar\Omega^2/4\Delta$, if the electron is in $|g\rangle$ and increases the cavity frequency by the same amount if it is in $|e\rangle$. Hence the state of the electron is encoded in the cavity frequency. Symmetrically, the cavity field also shifts the electronic energy, $E_g \rightarrow E_g - n\hbar\Omega^2/4\Delta$ and $E_e \rightarrow E_e + (n+1)\hbar\Omega^2/4\Delta$. These light-shifts are a manifestation of the AC Stark effect.

- **A resonant regime** with $\omega_c = \omega_{at}$. The two degenerate non-interacting eigenstates $|g, n+1\rangle$ and $|e, n\rangle$ are hybridized by the dipole interaction, yielding two states $|\pm, n\rangle$. They are an equal superposition of the previous degenerate states $|\pm, n\rangle = \frac{1}{\sqrt{2}}(|g, n+1\rangle \pm |e, n\rangle)$, separated by the energy $2\hbar\Omega\sqrt{n+1}$. Electric field and atoms exchange energy at the rate Ω, which leads to Rabi oscillations between the two states. The Jaynes Cummings Hamiltonian does not take into account dissipation but this light matter entanglement is only effective if the the dissipation in the cavity κ and the atomic decoherence rate Γ are smaller than Ω (strong coupling regime). In the weak coupling regime $\Omega \ll \Gamma, \kappa$, the fast exponential decoherence blurs the Rabi oscillations, equivalently saying that the two states $|\pm, n\rangle$ are not resolved anymore in energy.

Strong coupling has been achieved with Rydberg atoms, yielding to the observation of Rabi oscillations in the resonant regime [56]. In the dispersive regime, the coupling of the microwave cavity to Rydberg atoms resolved single photon quantum jumps with a quantum non demolition (QND) readout [57], or controlled the number of photons with a quantum feedback procedure [58]. The sensitivity of the electric field measurement even approached the Heisenberg limit using non-classical Schrödinger-cat-like states carried by Ryberg atoms [59].

2.1.2 Light matter coupling using a circuit QED architecture

The idea of coupling a microwave cavity to a two-level system was subsequently transposed to solid states physics. In condensed matter, electric field couples naturally to the electron motion but there are many dissipation sources. The electronic circuits presented in this section behave as a two-level system and are coupled to an on-chip microwave coplanar cavity.

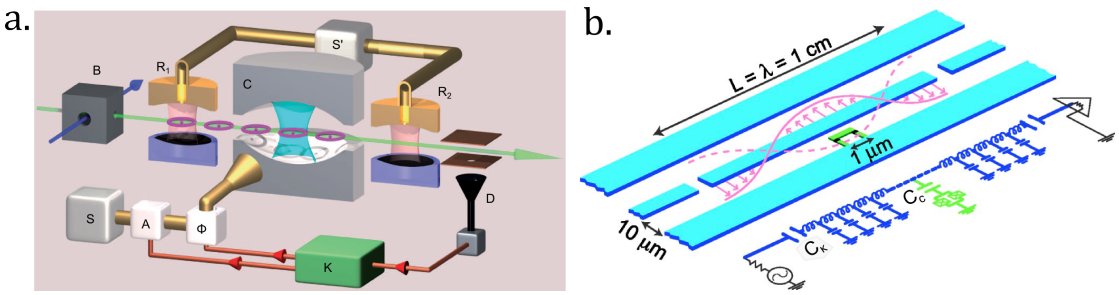

FIGURE 2.1: **Cavity and circuit QED. a.** Scheme of an atomic QED quantum feedback experiment. Rydberg atoms are prepared are by a laser beam (B) and send trough a high finess 3D cavity (C). (R1) and (R2) produce electronic superposition of the ground and excited states by applying $\pi/2$ pulses with (S'). They act as a Ramsey interferometer, an interformeter for which the two paths are the ground and excited states. The states of the electron is then mesured by ionization in a detector (D). A controller (K) allows a feedback on the tone send by the source (S). Source: [58] **b.** Schematic layout and equivalent lumped circuit representation of circuit QED. A high finess cavity is made from a coplanar waveguide, that is only coupled to input and output lines by a load capacitance C_κ. The electric field (pink arrows) is in the plane whereas the magnetic field is out-of plane. The wavelength of the mode represented here is the length of the central stripe line $\lambda = L$. This mode has one anti-node in the center of the cavity and two anti-nodes at its boundaries. A Cooper pair box is placed in the anti-node of the electric field and is coupled to the central stripe line with a capacitance C_c. The Cooper box is made with two Josephson junctions allowing the Josephon coupling to be controlled by magnetic flux. In this thesis, similar coplanar cavities are used but with a lower energy mode, $\lambda = L/2$, which has only two anti-nodes at each boundary. In that case the electronic circuit to be coupled to the cavity should be consequently placed near a boundary. Source : [16]

An on-chip microwave cavity is a LC-resonator made from a coplanar waveguide, with a central stripe line of finite length. The lowest mode of these resonators has a wavelength that is twice of the resonator length. The electric field has then two anti-nodes at each end of the waveguide, allowing the cavity to be coupled efficiently to input and output microwave lines. Figure 2.1 shows the lowest excited mode, with a frequency twice bigger.

One possibility to realize a two-level system is to use superconducting circuits. These circuits are made of a superconducting island, which is coupled via a Josephson junction (JJ) to another superconducting electrode, acting as a reservoir of Cooper pair. These circuits are 'cousins' of a quantum dot coupled to a fermionic reservoir, whose coupling to a microwave cavity will be presented in details in the next section. However, their dynamics is dramatically different, because in superconducting circuits there is little dissipation, once the superconducting gap is the biggest energy scale of the system. In the following, I briefly present two regimes of these superconducting circuits, the Cooper pair box and the transmon.

The superconducting circuits have two energy scales, E_J the Josephon energy and E_c the charging energy of the island. The first regime which was studied, called the Cooper

pair box [60, 61], is when E_c is bigger than E_J. In that case, the charging energy imposes that there is only an integer number N of Cooper pair in the island. Since the Cooper pairs share a common phase, the dynamics of the electronic circuit is a collective phenomenon. Thus, the charge degree of freedom of the island is sufficient to describe the state of the circuit by a state $|N\rangle$. Transitions between the two states $|N\rangle\langle N+1|$ or $|N+1\rangle\langle N|$ occur via the coherent exchange of a Cooper pair between the island and the reservoir, with the Josephson coupling E_J. The number of Cooper pair in the box depends on its chemical potential ϵ_{CPB}, which, like for quantum dots, can be tuned by a DC gate.

In this electrical circuit realization, the coupling to the cavity is a capacitive coupling : the cavity potential oscillations modulate the chemical potential of the Cooper pair box with a gate lever arm $\alpha = \frac{C_c}{C_\Sigma}$. Here, C_c is the capacitance between the Cooper pair box and the central stripe line of the cavity, and C_Σ the sum all the capacitances of the island, including those to the ground plane that screen the induced oscillations. The circuit QED device can finally be mapped onto a Jaynes Cummings Hamiltonian [16] :

$$\begin{aligned} H =& \hbar\hat{a}^\dagger\hat{a} + \underbrace{\frac{\epsilon_{CPB}}{2}\left(|N+1\rangle\langle N+1| - |N\rangle\langle N|\right)}_{\text{chemical potential}} - \underbrace{E_J\left(|N+1\rangle\langle N| + |N\rangle\langle N+1|\right)}_{\text{Josephson energy}} \\ & \underbrace{+\frac{e\alpha V_{rms}}{2}\left(\hat{a}^\dagger + \hat{a}\right)\left(|N+1\rangle\langle N+1| - |N\rangle\langle N|\right)}_{\text{capacitive coupling}} \\ \underset{\epsilon_{CPB}=0}{=}& \hbar\omega_c\hat{a}^\dagger\hat{a} + \hbar\omega_{qbit}\sigma_z + \hbar\Omega\sigma_x\left(\hat{a}^\dagger + \hat{a}\right) \end{aligned} \tag{2.3}$$

Above, σ_z and σ_x are the Pauli matrices in the eigenbasis of the qubit, with eigenstates that are a superposition of $|N\rangle$ and $|N+1\rangle$. For simplicity, the Hamiltonian in the qubit basis has been written at the charge degeneracy point $\epsilon_{CPB} = 0$. The cavity field couples to the charge polarization N on the island and induces consequently a transverse coupling σ_x in the qubit basis. The vacuum Rabi frequency is $\hbar\Omega = eV_{rms}\alpha$, where V_{rms} is the root mean square potential of a single cavity photon. There is a direct analogy to the dipole interaction $\hbar\Omega = dE_0$ where E_0 is the electric field in the cavity and d is the distance between the antenna made of the Cooper pair box and its reservoir, renormalized by α.

In circuit QED (cQED), the dipole has a macroscopic size, which gives a coupling constant bigger than the dissipation. To get a strong coupling with coherent light-matter exchange of energy, the coherence of the qubit matters. The strong coupling was first obtained in the Cooper pair box regime [17]. However, in the limit $E_J \ll E_c$, the

qubit is very sensitive to charge noise, as its eigenbasis is close to the charge states N and N+1. Therefore the regime $E_J \gg E_c$ is particularly interesting to get a better coherence time [62]. In the case $E_J \gg E_c$, the dynamics of the circuit reduces to the dynamics of the superconducting phase difference between the Cooper pair box and the reservoir [63]. For small variations of the phase, the quantum fluctuations in the phase across the Josephson junction are small and we can ignore that the phase is a periodic variable [64]. The phase can be taken as a classical variable and the Josephson junction behaves as an inductance, as the phase dependence of the Josephson energy is $E_J \cos(\phi) \simeq E_J(1 - \phi^2/2)$. Because of both the macroscopic coherence of the phase and the long range of the Coulomb interactions, the dynamic of the superconducting circuit is a collective oscillation of electrons, similarly to an electromagnetic mode. The electronic circuit mode with frequency ω_{plasma} and the cavity mode with ω_c can be computed using classical lumped elements representation. Both modes are described by two conjugate variables, the phase ϕ and the charge Q, which can be quantized like a harmonic oscillator giving the creation operator $\hat{b}^\dagger = \frac{\hat{\phi}}{\phi_{ZPF}} - i\frac{\hat{Q}}{Q_{ZPF}}$. The two modes are coupled with the same dipole coupling constant[3] as in the Cooper pair box :

$$H = \hbar\omega_c \hat{a}^\dagger \hat{a} + \hbar\omega_{plasma} \hat{b}^\dagger \hat{b} + g\left(\hat{a}^\dagger \hat{b} + \hat{b}^\dagger \hat{a}\right) - \frac{\alpha}{2}\hat{b}^\dagger \hat{b}^\dagger \hat{b}\hat{b} \tag{2.4}$$

The last term in the Hamiltonian describes the non linearity of the plasma mode, stemming form the fourth-order of the Taylor expansion of the Josephson energy : $E_J cos(\phi) = E_J\left(1 - \phi^2/2 + \phi^4/24 + O(\phi^6)\right)$. The plasma mode is weakly anharmonic so that only two levels couple preferably to the cavity. This electronic circuit version of artificial atoms, called a transmon, currently reaches the strong coupling regime with typical vacuum Rabi frequency of $\Omega/2\pi \sim 200Mhz$ and typical non-linear term $\alpha/2\pi \sim 200Mhz$ [65–67].

This circuit version of cavity QED has been extended to other condensed matter systems in cavities. Double quantum dots (DQD) are promising closed systems that can be coupled to a microwave cavity. A single electron can occupy either the left or the right dot, with orbitals that are tunnel coupled. The two states of the DQD are then the bonding and anti-bonding states. If the electric field is more strongly coupled to the chemical potential of one of the two dots, the electric field induces a transverse coupling in the eigenbasis of the bounding and anti-bonding states. Such DQDs in microwave cavities have succeeded in reaching the lasing threshold, acting as a micromaser [68]. Nevertheless these charge qubits are very sensitive to the background charge noise. A solution is to define an eigenbasis from the spin of the electron, that has a much weaker coupling to the environment and therefore longer coherence times. Spin qubits can be

[3] The coupling is a capacitive coupling between the two modes 1 and 2 with Hamiltonian $\frac{C_c}{C_{\sigma_1} C_{\sigma_2}} Q_1 Q_2$

made out of DQD with an artificial spin-orbit coupling, with the use of non colinear ferromagnetic electrodes. Such a device has recently been realized and achieved a spin coherence time of 60ns such that the strong coupling was almost reached [69].

Strong coupling has been recently reached using a Cooper pair splitter circuit, a microscopic equivalent circuit of the Cooper pair box, where a Cooper pair oscillates between a DQD and a superconducting reservoir [46].

In summary, this section discussed the coupling of a microwave cavity to different types of micro and nano-circuits. The dynamics of these devices could be mapped onto the Jaynes Cummings Hamiltonian, as for atomic QED. This relies on the fact that the capacitive coupling induces non-zero matrix elements between eigenstates of the qubit. In a more general way, this means that the coupling Hamiltonian between the qubit and the cavity does not commute with the non-interacting Hamiltonian. This coupling form is referred to as a transverse coupling, versus a longitudinal coupling, which would be proportional to the σ_z matrix of the qubit. The longitudinal or transverse nature of the coupling will be discussed again in chapter 5, when coupling Majorana fermions to photons.

In the solid state systems presented above, the analogy to atomic physics is possible because one can reduce their dynamics to a small number of degrees of freedom. However, this may not always be true for quantum dot circuits, in the open limit where electrons can tunnel to fermionic reservoirs which contain a continuum of states. We discuss below the specific approaches that can be used for electronic circuits with many degrees of freedom.

2.2 Mesoscopic cQED

In this section, we derive the microwave response of a quantum dot circuit. We start in section 2.2.1 by modeling the quantum dot as an admittance in parallel of a LC resonator. We then turn on to a more complete description, by introducing an Hamiltonian which is useful when dealing with electron-photon coupling in mesoscopic circuits (section 2.2.2). We then derive the equation of motion of the cavity field, using the input-output formalism (section 2.2.3). The dynamics of the cavity field is modified by the response of the electronic circuit to the cavity field. In section 2.2.4, the dynamics of the cavity is solved in the case of a linear response of the circuit, meaning that the photonic modulation is small compared to the energy scale of the electronic circuit. We apply this result to the simplest case of a quantum dot capacitively coupled to the cavity (section

2.2.5). Finally, we consider a more general case, where the source and drain electrodes are also coupled to the cavity (section 2.2.6).

2.2.1 An open electronic circuit : a quantum dot and its fermionic reservoir

This section presents the specificity of the coupling between photons and an open circuit. This is done by considering the simplest open circuit : a single quantum dot and its reservoir, which is studied in this thesis.

In this circuit, exchange of electrons between the dot and the reservoir can be switched on or off, by adjusting the chemical potential of the dot ϵ_d with respect to the Fermi energy ϵ_f of the reservoir (Coulomb resonance). The electric field in the cavity modulates the quantum dot chemical potential. At resonance $\epsilon_d = \epsilon_f$, oscillations of the dot chemical potential mediated by the cavity induce charge oscillations between the dot and the reservoir. This switchable dipole modifies the polarizability, classically described by the refractive index n. Like in classical optics, this polarizability shifts the resonance frequency of the cavity.

In a lumped element picture, the cavity is affected by the dot effective quantum capacitance $C_q = e^2 \frac{\partial \langle n \rangle}{\partial \epsilon_d}$, which was introduced in the previous chapter in section 1.1.4.2. More precisely, for frequencies much lower than the electron dynamics $\omega \ll \Gamma$ the AC response of the dot is described by the admittance $g(\omega) = i\tilde{C}\omega + R\tilde{C}\omega^2$ (figure 2.2). Here, $\tilde{C}$ accounts for the geometrical capacitance C_{geo} and quantum capacitance C_q that are in series [70]. For $\omega \ll \Gamma$, the resistance R is expected to be universal for a non-interacting system, and does not depend on the tunnel coupling t_{tunnel} of the quantum dot $R(\epsilon_d, t_{tunnel}) = \frac{h}{4e^2}$ [32, 70].

The quantum dot is usually coupled to the central stripe line at an anti-node for the electric field. The lumped element description of the central stripe line is a LC resonator, which is then shunted to the ground by this admittance. Hence $\tilde{C}$ is in parallel to the LC resonator (see figure 2.2), and shifts its eigenfrequency $\omega_{res} = \frac{1}{\sqrt{L_{res} C_{res}}}$ by :

$$\Delta\omega_{res} \sim \frac{-\omega_{res}}{2C_{res}} \tilde{C} \propto \frac{-\omega_{res}}{2C_{res}} C_q \tag{2.5}$$

Nevertheless this simple description of the dot by an effective admittance $g(\omega) = i\tilde{C}\omega + R\tilde{C}\omega^2$ does not give the exact coupling factor that links the quantum capacitance to the frequency shift. To derive the exact $\tilde{C}$ seen by the cavity, we need to look at the charge redistribution in the circuit generated by the oscillating potential of the cavity

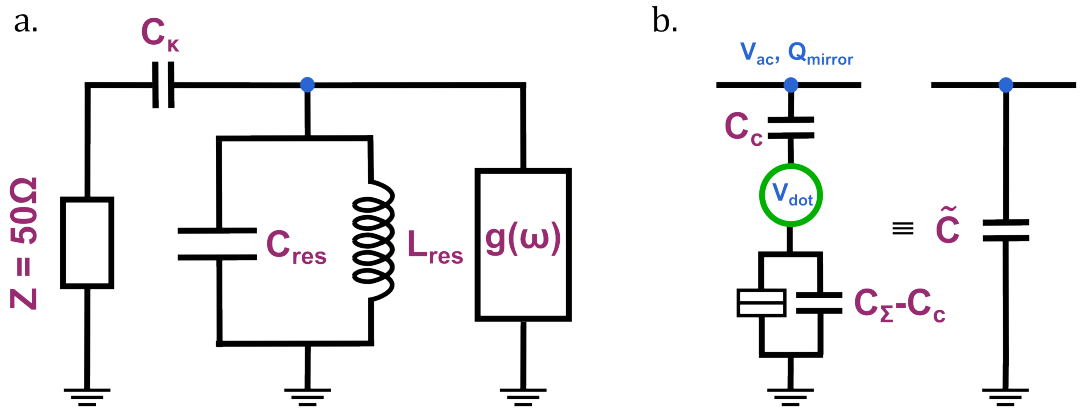

FIGURE 2.2: **Circuit representation of a quantum dot coupled to a microwave cavity. a.** The cavity is modeled by LC circuit with corresponding capacitance C_{res} and inductance L_{res}. A quantum dot circuit corresponding to an effective admittance $g(\omega)$ is connected at one electrical anti-node of the cavity. At this anti-node, the cavity is also coupled to a 50Ω-impedance line. **b.** Representation of the quantum dot circuit connected to the cavity. C_c is the coupling capacitance to the dot. C_Σ is the sum of all the capacitances seen by the dot. Except C_c they are all grounded at frequency of the cavity. To get the exact capacitance seen by the cavity $\tilde{C}$, one has to derive the mirror charge Q_{mirror} induced by charge repartition on the circuit.

$V_{ac}(t)$. For $\omega \ll \Gamma$, the voltage oscillations induced by the cavity are much slower than the electrons dynamics in the quantum dot circuit. This separation of time scales means that the charge number in the dot is always at its equilibrium mean value $\langle n \rangle$ and adjusts itself instantaneously to the voltage oscillations. This approximation is called the adiabatic approximation.

The potential of the dot $\langle V_{dot} \rangle$ is capacitively coupled to the central stripe line of the cavity via C_c. Following the same reasoning as in [71], the mirror charge image on the cavity, induced by the quantum dot is :

$$\delta \langle Q_{mirror} \rangle = C_c(\delta V_{ac} - \delta \langle V_{dot} \rangle) \tag{2.6}$$

The dot potential is then only determined by the mean number of charge and the capacitive effect of δV_{ac} (see chapter 1)[4] :

$$\delta \langle V_{dot} \rangle = \frac{\delta \langle \mu_{dot} \rangle}{-e} = \frac{-e}{C_\Sigma} \delta \langle n \rangle + \frac{C_c}{C_\Sigma} \delta V_{ac} \tag{2.7}$$

[4]We consider the simplest case where the potential of the electrodes (drain, source, gate) at the frequency ω_{res} are set to ground.

This mirror charge corresponds to an effective capacitance between the central stripe line and the ground :

$$\tilde{C} = \frac{\delta \langle Q_{mirror} \rangle}{\delta V_{ac}} = \underbrace{e\alpha \frac{\partial \langle n \rangle}{\partial \epsilon_d} \frac{\partial \epsilon_d}{\partial V_{ac}}}_{\text{quantum capacitance}} + \underbrace{(1-\alpha) C_c}_{\text{classical capacitance}} \tag{2.8}$$

where $\alpha = \frac{C_c}{C_\Sigma}$ is a coupling lever arm related to the AC coupling.

As $\tilde{C}$ is in parallel to the LC resonator, the quantum capacitance $C_q = e\alpha \frac{\partial \langle n \rangle}{\partial \epsilon_d} \frac{\partial \epsilon_d}{\partial V_{ac}} \ll C_{res}$ shifts the resonance frequency by[5]

$$\Delta\omega_{res} \sim \frac{-\omega_{res}}{2C_{res}} \tilde{C} = g^2 \hbar \frac{\partial \langle n \rangle}{\partial \epsilon_d} \tag{2.9}$$

with

$$\hbar g = \sqrt{-e\alpha \frac{\partial \epsilon_d}{\partial V_{ac}}} V_{RMS} \tag{2.10}$$

We use root mean square voltage of a single photon $V_{RMS} = \sqrt{\frac{\hbar\omega_{res}}{2C_{res}}}$ [71]. $\frac{\partial \epsilon_d}{\partial V_{ac}} = -e\alpha$ is the lever arm related to C_c, so the coupling constant simply reads :

$$\hbar g = e\alpha V_{RMS} \tag{2.11}$$

The frequency shift is then proportional to the square of the lever arm α. If we had considered that the quantum capacitance acts as a classical capacitance in parallel to the LC resonator as in equation (2.5), we would have found that the frequency shift is proportional to the lever arm, and not its square. Contrary to a classical description, the charge on the metallic island is not zero, which gives the extra factor $\frac{\partial \epsilon_d}{\partial V_{ac}}$ in the coupling constant. One can therefore state that a quantum dot cannot be modeled as a lumped element with the impedance that obeys the classical addition rule.

Furthermore we have seen in chapter 1 that the quantum capacitance could renormalize the lever arm $\frac{\partial \epsilon_d}{\partial V_{ac}}$. This effect becomes significant if the quantum capacitance $C_q \sim 1/\Gamma$ becomes comparable to the sum of the geometric capacitances $C_\Sigma \sim 1/E_c$ and renormalizes consequently the coupling constant :

$$\hbar g = e\alpha V_{RMS} \times r(\Gamma/E_c) \tag{2.12}$$

where $r(.)$ is a function of the ratio Γ/E_c.

The reactive part of the quantum dot admittance shifts the eigenfrequency with a coupling factor that is defined by the lever arm. The resistive part of the admittance induces

[5] We have omitted the shift which results from the classical capacitance because it is a constant.

dissipation in the cavity. The resistive behavior constitutes the first correction in ω/Γ to the adiabatic approximation. In fact, the electrons tunnel with a delay, characterized by the RC time of the admittance. This delay induces a slight out-of-equilibrium situation between the dot and the reservoir, leading to inelastic tunneling. This delay effect implies consequently dissipation and therefore a broadening of the cavity linewidth. For a non-inderacting quantum dot, an universal relation, the Korringa-Shiba relation [72, 73], exists between the frequency shift $\Delta\omega_{res}$ of the cavity and its broadening $\Delta\kappa$:

$$\frac{\Delta\kappa}{(\Delta\omega_{res})^2} = \frac{\pi}{2}\frac{\omega_{res}}{g^2} \tag{2.13}$$

When the ratio ω/Γ increases, the reactive part moves from a capacitive behavior to an inductive one [14, 74]. The sign of the frequency shift consequently changes[6] and this transition occurs for $\omega \sim \Gamma$, for which the reactive part becomes negligible. The universality of the Korringa-Shiba relation starts to break down when ω/Γ increases, showing a departure from the universality of charge relaxation [74]. In the capacitive regime, an approximate scaling between $\Delta\kappa$ and $(\Delta\omega_{res})^2$ remains beyond the adiabatic approximation, with a renormalized charge relaxation resistance [74].

As a conclusion, the quantum dot and its reservoir behave effectively as an admittance in parallel to the LC cavity resonator, which shifts the eigenfrequency of the resonator. Nevertheless, contrary to superconducting circuit, the lumped element approach is limited, when looking at the exact coupling mechanism. This formalism is also restricted to the adiabatic limit. This limits calls for a microscopic description of the electron-photon coupling, which is the main point of the next section.

2.2.2 Microscopic description of the electron-photon coupling

The dynamics of a nanocircuit is governed by tunneling electrons, which tunnel between the different circuit elements, in response to electrical potential oscillations induced by the cavity. It is therefore appealing to write the electron-photon coupling as the product of an electron density $\widehat{\Psi}(\overrightarrow{r})$ refering to all tunneling charge in the nanocircuit and a scalar photonic pseudo-potential $V_\perp(\overrightarrow{r})$ [75] :

$$H_{e-ph} = -e\int d^3r\widehat{\Psi}^\dagger(\overrightarrow{r})V_\perp(\overrightarrow{r})\widehat{\Psi}(\overrightarrow{r})(\widehat{a}+\widehat{a}^\dagger) \tag{2.14}$$

The operator $\widehat{a}$ is the single cavity mode annihilation operator. The term $V_\perp(\overrightarrow{r})$ encodes the spatial dependence of the electric field in the nanocircuit. This can be fully justified by a microscopic description using gauge invariance as minimal ingredient [75].

[6] $iC\omega$ becomes $-i/L\omega$

Above, $\widehat{\Psi}(\overrightarrow{r})$ describes the spatial density of electrons which can tunnel between different elements of the nanocircuit. The term $\widehat{\Psi}(\overrightarrow{r})$ can be decomposed onto the local states in the different circuit elements, each being described by its wavefunction density $\phi^*_{o,i}(\overrightarrow{r})$ and an operator $\hat{c}^\dagger_{o,i}$:

$$\hat{\Psi}^\dagger(\overrightarrow{r}) = \sum_{o,i} \phi^*_{o,i}(\overrightarrow{r})\hat{c}^\dagger_{o,i} \tag{2.15}$$

The label o refers to an orbital of a circuit element i. Here the orbitals should be understood in a broad meaning, referring to a localized state of a confined nanoconductor portions as well as states in fermionic reservoirs. The generality of this electron-photon coupling allows to cover the diversity of excitations $\hat{c}^\dagger_{o,i}$ in mesoscopic circuits.

The coupling Hamiltonian (2.14) is valid under two assumptions. The first one is that the plasmon dynamics in the electrodes and their biasing circuit is much faster than the tunneling dynamics in the mesoscopic circuit and the dynamics of the cavity. This means that the plasmons rebalance immediately the charge locally after tunneling events, and that the currents which screen the excess charge induced by tunneling do not need to be treated explicitly. The second assumption is that there is no closed loop in the electronic circuit, disregarding Aharonov-Bohm-like effect, and consequently disregarding coupling mechanisms relying on the magnetic flux.

The inclusion of a general spatial dependence of the potential $V_\perp(\overrightarrow{r})$ goes beyond both the dipolar approximation of atomic QED where the electric field is constant and the coarse-grained spatial variation of lumped element circuits used in circuit QED. The use of a tunneling electron density and a photonic pseudo potential is well adapted to describe the electric coupling between many microscopic orbitals in a mesoscopic circuit to cavity field dressed by the plasmonic modes from the fermionic reservoirs.

Using the decomposition of the tunneling density on the orbitals of the nanocircuit, the coupling Hamiltonian reads :

$$H_{e-ph} = h_{int}(\widehat{a} + \widehat{a}^\dagger) \tag{2.16}$$

with :

$$h_{int} = \sum_{o,i} g_{o,i}\hat{c}^\dagger_{o,i}\hat{c}_{o,i} + \sum_{oj\neq o'i'} \left(\gamma_{oi,o'i'}\hat{c}^\dagger_{o,i}\hat{c}_{o',i'} + h.c.\right) \tag{2.17}$$

and :

$$\hbar g_{o,i} = -e\int d^3r |\phi_{o,i}(\overrightarrow{r})|^2 V_\perp(\overrightarrow{r}) \tag{2.18}$$

$$\gamma_{o,i,o',i'} = -e\int d^3r \phi^*_{o,i}(\overrightarrow{r})\phi_{o',i'}(\overrightarrow{r})V_\perp(\overrightarrow{r}) \tag{2.19}$$

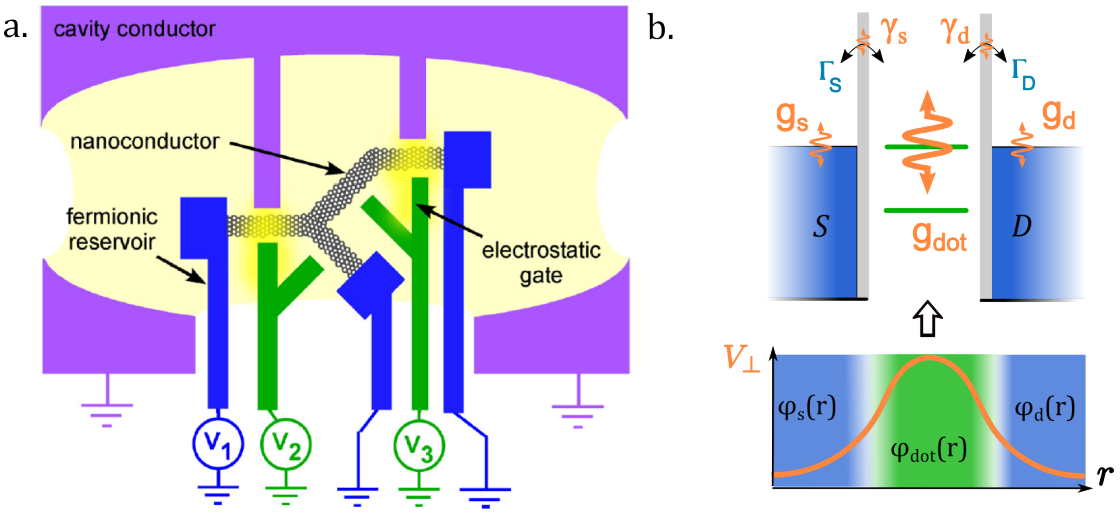

FIGURE 2.3: **General description of the coupling between the cavity pseudo-potential and a nanocircuit. a.** Scheme of a nanocircuit with gates (in green) and electrodes (in blue) embedded in a microwave cavity (in purple). Gates connected to the cavity (in purple) bring the AC potential closer to the nanocircuit, shaping the photonic peusdo potential seen by the circuit. The clouds represent field inhomogeneities. Source : [75] **b.** Quantum dot (top panel) with quantized orbitals (in green) and source and drain electrode (in blue). $\Gamma_{s,d}$ are the tunneling rates to the source and drain. The cavity shakes the different chemical potential with different strengths g_i, $i = dot, s, d$. The constant g_i is the spatial average of the pseudo-potential $V_\perp$ (in orange) and the wavefunction ϕ_i. In principle, the photonic potential modulates also the tunneling rates Γ_i, with the coupling constant γ_i. This term is disregarded in this thesis.

Two different coupling mechanisms appear :

- The term $g_{o,i}$ couples the photons to $\hat{n}_{o,i} = \hat{c}^\dagger_{o,i}\hat{c}_{o,i}$ and therefore modulates the energy level $\epsilon_{i,o}\hat{n}_{i,o}$. Here $\hat{n}_{i,o} = \hat{c}^\dagger_{o,i}\hat{c}_{o,i}$ is the number of electron in the orbital o of the circuit element i.
- The term $\gamma_{o,i,o',i'}$ describes a modulation of the tunnel coupling term between two orbitals $t_{o,i,o',i'}\hat{c}^\dagger_{o,i}\hat{c}_{o',i'}$. It is much smaller than the modulation of the energy levels because it is proportional to the wavefunction overlap of two different orbitals.

2.2.3 Equation of motion for the cavity field

Given the above coupling Hamiltonian, one can derive the equation of motion of the cavity field with an input/output formalism. This formalism allows to treat the full dynamics of the cavity mode $\hat{H}_{int} = \hbar\omega_c\hat{a}^\dagger\hat{a} + H_{e-ph}$ and its coupling to the external electromagnetic environment, inevitable because of leaks but also necessary to read out the cavity.

Such coupling to the external electromagnetic environment is modeled by a bath of independent harmonic oscillators $H_{bath} = \sum_q \hbar\omega_q\hat{b}^\dagger_q\hat{b}_q$, later called modes [76]. A cavity

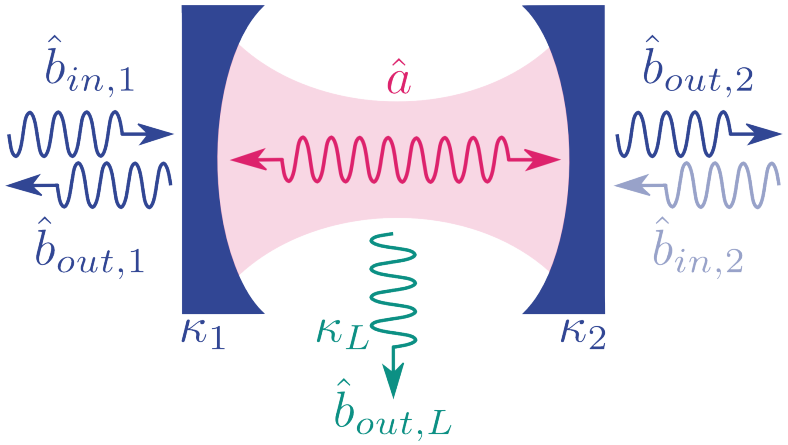

FIGURE 2.4: **Input-output formalism.** A cavity with mode $\hat{a}$ is coupled to the input and output lines by two port 1 and 2. For each port, one can define ingoing $\hat{b}_{in}$ and outgoing $\hat{b}_{out}$ modes. A third port L describes the dissipation. Each port i is characterized by a coupling constant κ_i. Source : [46]

photon can be converted into a bath photon, or vice versa, so that the coupling Hamiltonian is : $H_{cav-bath} = -i\hbar \sum \left[f_q \hat{a}^\dagger \hat{b}_q - f_q^* \hat{b}_q^\dagger \hat{a} \right]$. Within the rotating wave approximation, non-resonant processes can be neglected. We can also consider that the transition amplitude $f_q = f$ is constant over the range of frequencies relevant for the cavity. With a constant density of states $\rho(\omega_q) = \rho$ for the bath, the decay rate of a cavity photon into the bath is : $\kappa = 2\pi f^2 \rho$ (Fermi golden rule).

The equation of motion given by the commutator of $\hat{a}(t)$ and $\hat{H}_{int} + H_{bath}$ is then [76]:

$$\frac{d}{dt}\hat{a}(t) = \frac{i}{\hbar}\left[\hat{H}_{int}, \hat{a}\right] - \frac{\kappa}{2}\hat{a}(t) - \sqrt{\kappa}\hat{b}_{in}(t) \tag{2.20}$$

The bath adds a damping term[7] κ and a source term $\hat{b}_{in}(t)$. This term describes the input modes, which are modes of the bath that have not yet interacted with the cavity at the time t [76].

Note that the input mode $\hat{b}_{in}(t)$ has not the same dimension as the harmonic oscillator excitation $\hat{b}_q$. In fact, $\hat{b}_{in}^\dagger(t)\hat{b}_{in}(t)$ corresponds to a photon flux. The power carried by a monochromatic input mode is consequently : $P_{in}(t) = \hbar\omega \left\langle \hat{b}_{in}^\dagger(t)\hat{b}_{in}(t) \right\rangle$.

Similarly, we can consider outgoing modes in the bath [76]. These are defined from solutions of the equation of motion for $\hat{b}_q$, with final condition ($t \to \infty$) requiring that $\hat{b}_q(t)$ matches the free evolution of a mode in the bath (instead of an initial condition for input modes). The evolution of this outgoing mode is better understandable by reversing the arrow of time : it evolves freely from the future back to the present

[7] The factor one half for the damping rate comes from the fact that κ is the energy decay rate and not the amplitude decay rate.

where it interacts with the cavity[8]. The equation of motion given by the commutator $\left[H_{int} + H_{cav-bath} + \hat{H}_{bath}, \hat{b}_q\right]$ sets a relation between the input and the output modes :

$$\hat{b}_{out}(t) = \hat{b}_{in}(t) + \sqrt{\kappa}\hat{a}(t) \tag{2.21}$$

The outgoing field is a sum of the reflected incoming field and the field radiated by the cavity.

For simplicity, equation (2.20) has been derived for one port of coupling constant κ. The cavity has nevertheless two ports labeled $i = 1, 2$ with κ_1, κ_2. Internal losses κ_l can be taken into account in a third one. As we neglect correlation effects (Markovian approximation), the total decay rate is then $\kappa = \kappa_1 + \kappa_2 + \kappa_l$.

The cavity is usually excited through a single port $b_{in,1}$. For the other ports, the ingoing fields $\left\langle \hat{b}_{in,2}(t) \right\rangle$ and $\left\langle \hat{b}_{in,l}(t) \right\rangle$ can be neglected in the semi-classical regime where $b_{in,1}$ is large enough so that $\langle \hat{a} \rangle \gg 0$.

The equation of motion for $\hat{a}(t)$ is then :

$$\frac{d}{dt}\hat{a}(t) = -i\omega_c\hat{a}(t) - \frac{\kappa}{2}\hat{a}(t) - i\sum_i g_i\hat{n}_i(t) - \sqrt{\kappa_1}b_{in,1}(t) \tag{2.22}$$

Here only the dominant coupling to the orbital level has been considered :

$$H_{e-ph} = \sum_i \hbar g_i\hat{n}_i(\hat{a} + \hat{a}^\dagger) \tag{2.23}$$

and we have replaced the double subscript i, o by i, by considering only one orbital for each circuit element.

To solve the photon dynamics one needs the dynamics of the electronic circuit $\hat{n}_i(t)$. The next section derives it in the framework of linear response of the circuit to the photonic excitation. We will stay in a semi-classical picture, where the cavity field modulates the chemical potential by capacitive coupling.

[8]The reader with a background in scattering theory could see the parallel with retarded, resp. advanced states, which are solutions of the full Hamiltonian, with initial condition, resp. final conditions, matching incoming waves, resp. outgoing waves.

2.2.4 Semi-classical linear response

The dynamics of the electron in the circuit is given by the Hamiltonian of the circuit and the electron-photon coupling Hamiltonian :

$$H_{circuit} + H_{e-ph} = H_{circuit} + \sum_i \hbar g_i \hat{n}_i (\hat{a} + \hat{a}^\dagger) \tag{2.24}$$

Let us consider the case in which the drive is a classical monochromatic wave $\left\langle \hat{b}_{in,1}(t) \right\rangle \simeq b_{in} e^{-i\omega_d t}$. We can consequently neglect quantum fluctuation in the cavity $\langle \hat{a}(t) \rangle \simeq \bar{a} e^{-i\omega_d t}$, and only focus on the frequency ω_d because we are generally interested in the transmission at the drive frequency. The coupling to photons corresponds to the modulation of the chemical potential $\delta\epsilon_j = g_j \left(\bar{a} e^{-i\omega_d t} + \bar{a}^* e^{i\omega_d t} \right)$.

If the modulation is small compared to the energy scales of the electronic circuit $\delta\epsilon_j \ll E_c, \Gamma$, the charge occupation responds linearly to the excitation. We can define a charge susceptibility $\chi_{i,j}$ that characterizes the linear response of the charge number $\langle \hat{n}_i(t) \rangle$ through an excitation of the chemical potential $\delta\epsilon_j$ of element j:

$$\langle \hat{n}_i(t) \rangle = \frac{1}{\hbar} \sum_j \int \mathrm{d}t' \chi_{i,j}(t - t') \delta\epsilon_j(t') \tag{2.25}$$

The linear susceptibility $\chi_{i,j}$ is then local in the frequency space : $\langle \hat{n}_i(\omega) \rangle = \frac{1}{\hbar} \sum_j \chi_{i,j}(\omega) \delta\epsilon_j(\omega)$. $\chi_{i,j}(t)$ is real so $\chi_{i,j}(\omega)$ is complex, its real part describing the reactive part of the response and its imaginary part the dissipation[9]. The susceptibility only depends on $H_{circuit}$, and if $\hat{n}_j$ is the occupation number related to the chemical potential ϵ_j, it can be calculated using the Kubo formula : $\chi_{i,j}(t) = -i\theta(t) \langle [\hat{n}_i(t), \hat{n}_j(0)] \rangle$.

The linear response of the circuit at the cavity field at frequency ω_d is then :

$$\langle \hat{n}_i(t) \rangle = \sum_j g_j \chi_{i,j}(\omega_d) \bar{a} e^{-i\omega_d t} + g_j \chi^*_{i,j}(\omega_d) \bar{a}^* e^{-i\omega_d t} \tag{2.26}$$

Combining this linear response with the Fourier transform of equation (2.22), the average amplitude $\bar{a}$ at frequency ω_d is:

$$\bar{a} = \frac{-\sqrt{\kappa_1} b_{in}}{i(\omega_c - \omega_d) + \dfrac{\kappa}{2} + i \sum\limits_{i,j} g_i g_j \chi_{i,j}(\omega_d)} \tag{2.27}$$

In this thesis, we measure the transmission of the cavity, sending a drive term at the first port and measuring the complex amplitude of the outgoing mode at the second

[9] Causality imposes that $\chi_{i,j}(t < 0) = 0$ and leads to the Kramers-König relation, which couples the real and imaginary parts of the spectral response.

port. This outgoing mode is directly proportional to the amplitude of the cavity field $\hat{b}_{out,2}(t) = \sqrt{\kappa_2}\hat{a}(t)$ so that the transmission reads finally :

$$T = \frac{\left\langle \hat{b}_{out,2} \right\rangle}{\left\langle \hat{b}_{in,1} \right\rangle} = \frac{-\sqrt{\kappa_1\kappa_2}}{i(\omega_c - \omega_d) + \frac{\kappa}{2} + i\sum\limits_{i,j} g_i g_j \chi_{i,j}(\omega_d)} \tag{2.28}$$

The real part of the charge susceptibilities consequently shifts the cavity resonance frequency, whereas the imaginary part affects the resonance linewidth. Hence the cavity signal gives access to the electron dynamics in circuit in the linear regime. The coupling factors g_i are non zero if the pseudo-potential $V_\perp(\overrightarrow{r})$ is non zero on the state i. So the shape of the pseudo-potential determines the susceptibilities measured by the cavity. The cavity is sensitive to the hopping transitions between orbitals induced by the cavity potential modulation. Consequently, if all orbitals are equivalently modulated, there will not be any response in the cavity. A transverse coupling relies on the spatial variation of the pseudo-potential. This highlights the importance of shaping strong spatial inhomogeneities in the pseudo-potential, depending on the linear response we want to probe.

Until now, we did not specify the orbitals i or their dynamics. We will first derive the linear susceptibility in the simple case where the cavity photons modulate the dot chemical potential and then consider a more general case where they also modulate the source and the drain potential.

2.2.5 Charge susceptibility of a quantum dot

If the electron-photon coupling is only a coupling to the chemical potential of the dot, meaning in the above formalism that the pseudo potential is only non-zero on the dot, the coupling Hamiltonian reads $H_{e-ph} = \hbar g\hat{n}(\hat{a} + \hat{a}^\dagger)$ where $g = \alpha e V_{rms}$.

The charge susceptibility probed by the cavity is then :

$$\chi(t) = -i\theta(t)\left\langle [\hat{n}(t), \hat{n}(0)] \right\rangle \tag{2.29}$$

In the adiabatic limit, where the charge dynamics of the electrons in the dot is much faster than the AC modulation, the mean number of electrons follows instantaneously the chemical potential modulation: $\delta\left\langle \hat{n} \right\rangle(t) = \frac{\partial n}{\partial \epsilon_d}\hbar g\left(\bar{a}e^{-i\omega_d t} + \bar{a}^* e^{i\omega_d t}\right)$. Therefore $\chi(\omega_d) \sim \hbar\frac{\partial n}{\partial \epsilon_d}$ and we find again that the quantum capacitance shifts the resonance frequency by $\Delta\omega_c = g^2\hbar\frac{\partial n}{\partial \epsilon_d}$, as derived in the lumped element circuit description. As explained in more details later, the charge susceptibility $\frac{\partial n}{\partial \epsilon_d}$ is equivalent to the compressibility of the quantum dot, a term coming from thermodynamics.

To get the dissipative part of the response, we must go beyond the adiabatic approximation and look for the frequency dependence of the charge susceptibility. Let us derive this in the sequential regime where the number of electron is derived by the master equation (see section 1.1.4.1 in chapter 1) :

$$\begin{aligned}\hbar\frac{\mathrm{d}p_{N+1}}{\mathrm{d}t} &= -\Gamma^{-}(t)\,p_{N+1}(t) + \Gamma^{+}(t)\,p_N(t) \\ &= -\Gamma^{-}(t)\,p_{N+1}(t) + \Gamma^{+}(t)\,(1-p_{N+1}(t))\end{aligned} \tag{2.30}$$

In the first step beyond the adiabatic approximation, the rates $\Gamma^{\pm}$ are modulated parametrically by the AC oscillations $\Gamma^{\pm}(t) = \Gamma^{\pm}\left(\hbar g\bar{a}e^{-i\omega_d t}\right)$[10]. In the linear response framework, $\Gamma^{\pm}(t) \simeq \Gamma_0^{\pm} + \frac{\partial\Gamma^{\pm}}{\partial\epsilon_d}\hbar g\bar{a}e^{-i\omega_d t}$. $\Gamma_0^{\pm}$ refers to the equilibrium value.

The oscillations of $p_{N+1}(t)$ at the drive frequency around its equilibrium value is $p_{N+1,\omega_d}(t) = p_{N+1,0} + \delta p_{N+1,\omega_d}e^{-i\omega_d t}$, with $p_{N+1,0} = \frac{\Gamma_0^+}{\Gamma_0^+ + \Gamma_0^-}$.

$\delta p_{N+1,\omega_d}$ is determined by the Fourier transform of the master equation :

$$-i\hbar\omega_d\delta p_{N+1,\omega_d} = -\left(\Gamma_0^- + \Gamma_0^+\right)\delta p_{N+1,\omega_d} - p_{N+1,0}\left(\frac{\partial\Gamma^+}{\partial\epsilon_d} + \frac{\partial\Gamma^-}{\partial\epsilon_d}\right)\hbar g\bar{a} + \frac{\partial\Gamma^+}{\partial\epsilon_d}\hbar g\bar{a} \tag{2.31}$$

where $\delta p_{N+1,\omega_d}$ refers to the Fourier amplitude at the drive frequency of the fluctuations of $p_{N+1}(t)$ around the equilibrium value $p_{N+1,0}$. From the equation (2.31), we can check that the evolution of $\langle\hat{n}_i(t)\rangle = p_{N+1}(t)$ in the frequency space for $\hbar\omega_d \ll \Gamma = \Gamma^+ + \Gamma^-$ is :

$$\langle n\rangle|_{\hbar\omega_d\ll\Gamma} = n_0 + \frac{\partial\langle n\rangle}{\partial\epsilon_d}\frac{\hbar g\bar{a}}{1 - i\frac{\omega_d}{\Gamma}} \simeq n_0 + \frac{\partial\langle n\rangle}{\partial\epsilon_d}\hbar g\bar{a}\left(1 + i\frac{\omega_d}{\Gamma}\right) \tag{2.32}$$

The imaginary part of the susceptibility gives the change in linewidth, using equation (2.35). As $\frac{\partial\langle n\rangle}{\partial\epsilon_d} < 0$, the quantum dot broadens the cavity linewidth by $\Delta\kappa = -2g^2\hbar\frac{\partial n}{\partial\epsilon_d}\frac{\omega_d}{\Gamma}$.

This was derived in the sequential regime where $k_bT > \Gamma$. In the coherent regime, the broadening is given by the Korringa-Shiba relation[11] : $\Delta\kappa = \frac{\pi}{2}\left(\Delta\omega_c\right)^2\frac{\omega_c}{g^2}$.

Note however that the imaginary part of the charge susceptibility does not always lead to dissipation. Tiny photonemission has been resolved in an out-of equilibrium quantum dot weakly coupled to a superconducting electrode [74]. The sharp BCS density of states that appears above the gap at $eV_{sd} = \Delta$ enhances photo-emission due to inelastic tunneling.

[10] If we consider the full dynamics, $\Gamma^{\pm}(t)$ depends on $p_{N+1}(t)$

[11] This is linked to the universality of the dot charge relaxation.

2.2.6 General coupling scheme for a quantum dot

A more general case is to additionally consider a coupling to the source g_s and the drain g_d. The electron photon coupling Hamiltonian then looks like :

$$H_{e-ph} = \hbar \left(g\hat{n}_{qd} + g_s\hat{n}_s + g_d\hat{n}_d \right) \left(\widehat{a} + \widehat{a}^\dagger \right) \tag{2.33}$$

Let us introduce the symmetric and antisymmetric part of $\hat{n}_s$, $\hat{n}_d$: $\hat{n}_\pm = \hat{n}_s \pm \hat{n}_d$. Charge conservation imposes that $\hat{n}_+ + \hat{n}_{qd}$ is constant. Omitting this constant term in the coupling Hamiltonian (as its corresponding charge susceptibilities are zero, i.e. $\chi_{\hat{n}_+ + \hat{n}_{qd},j} = 0$), the coupling Hamiltonian can be rewritten as :

$$H_{e-ph} = \hbar \left(g_{qd}\hat{n}_{qd} + g_-\hat{n}_- \right) \left(\widehat{a} + \widehat{a}^\dagger \right) \tag{2.34}$$

where $g_{qd} = g - \frac{g_s+g_d}{2}$ and $g_- = \frac{g_s-g_d}{2}$.

As derived in the main case, the transmission of the cavity is then :

$$T = \frac{\left\langle \hat{b}_{out,2} \right\rangle}{\left\langle \hat{b}_{in,1} \right\rangle} = \frac{-\sqrt{\kappa_1\kappa_2}}{i(\omega_c - \omega_d) + \dfrac{\kappa}{2} + i \displaystyle\sum_{i,j=qd,-} g_i g_j \chi_{i,j}(\omega_d)} \tag{2.35}$$

The charge susceptibilities $\chi_{i,j}(\omega_d)$ are the linear response of $\langle \hat{n}_i \rangle (\omega_d)$ to an excitation of the chemical potential ϵ_j at the frequency ω_d. Once again, we will consider that the electrons tunnel much faster than the chemical potential oscillations induced by the cavity : at the frequency ω_d the number of electron is its equilibrium mean value. The susceptibility associated to g_{qd}^2 is the compressibility :

$$\chi_{qd,qd}(\omega_d) = \hbar \frac{\partial \langle \hat{n}_{qd} \rangle}{\partial \epsilon_d} \tag{2.36}$$

The cross term $g_{qd}g_-\chi_{qd,-}(\omega_d)$ corresponds to the response of the stationary $\langle \hat{n}_{qd} \rangle (\omega_d)$ to a chemical potential modulation $\epsilon_a n_-$:

$$\chi_{qd,-}(\omega_d) = \hbar \frac{\partial \langle \hat{n}_{qd} \rangle}{\partial \epsilon_a} \tag{2.37}$$

Because $\epsilon_a n_- = \epsilon_a(n_s - n_d)$, $\chi_{qd,-}$ is the response to a slow anti-symmetric modulation : $V_s(t) = V_{ac}/2\cos(\omega_d t)$ and $V_d = -V_{ac}/2\cos(\omega_d t)$, defining $V_{ac} = 2\epsilon_a/(-e)$, $(e > 0)$[12].

Let us derive the two susceptibilities associated to $\hat{n}_-$. The time derivative of the number of charges in the source and drain are related to the average current I : $I = -e\frac{\partial \langle n_s \rangle (t)}{\partial t}$. The Fourier transform of $\langle \hat{n}_- \rangle (\omega_d)$ is then related to the Fourier transform of the current

[12] Here we use this definition of V_{ac} in order to match the DC source drain bias V_{sd} definition.

$\langle \hat{n}_- \rangle (\omega_d) = -\frac{2I_{\omega_d}}{ei\omega_d}$. Hence the susceptibility for the asymmetric modulation of the leads can be written as :

$$\chi_{-,-} = \hbar \frac{\partial \langle \hat{n}_- \rangle}{\partial \epsilon_a} = \frac{4\hbar}{e^2 i\omega_d} \frac{\partial I}{\partial V_{ac}} \tag{2.38}$$

In the adiabatic approximation $\omega_d \ll \Gamma$, the Fourier component $\frac{\partial I}{\partial V_{ac}}$ is associated to a resistive behavior so it is real and of the same order of the DC response G_{diff}[13]. $\chi_{-,-}$ corresponds then to an out-of-phase response. Following the same derivation, the susceptibility $\chi_{-,qd}$ is purely imaginary and is proportional to $\frac{\partial I}{\partial \epsilon_d}$. Both quantities consequently only impact the cavity linewidth.

Hence the coupling to the dot and the source and drain electrodes gives two terms that shift the frequency and two terms that enhance the dissipation :

$$\begin{aligned} \sum_{i,j=qd,-} g_i g_j \chi_{i,j}(\omega_d) =& g_{qd}^2 \hbar \frac{\partial \langle \hat{n}_{qd} \rangle}{\partial \epsilon_d} + g_{qd} g_- \hbar \frac{\partial \langle \hat{n}_{qd} \rangle}{\partial \epsilon_a} \\ & - i \left(g_-^2 \frac{4\hbar}{e^2 \omega_d} \frac{\partial I}{\partial V_{ac}} + g_- g_{qd} \frac{2\hbar}{e\omega_d} \frac{\partial I}{\partial \epsilon_d} \right) \end{aligned} \tag{2.39}$$

At zero bias, $V_{sd} = 0$, I is independent of ϵ_d, so the last term is zero.

Let us derive these four terms in the Keldysh formalism that treats the out-of-equilibrium situation. Disregarding Coulomb interactions in the dot, the mean charge in the dot can be written as a function of the chemical potential ϵ_d, μ_s and μ_d :

$$\begin{aligned} \langle n_{qd} \rangle (\epsilon_d, \mu_s, \mu_d) = \int \frac{\mathrm{d}\epsilon}{2\pi} G^r(\epsilon - \epsilon_d) [\Gamma_s f(\epsilon - \mu_s) G^{r*}(\epsilon - \epsilon_d) \\ + \Gamma_d f(\epsilon - \mu_d) G^{r*}(\epsilon - \epsilon_d)] \end{aligned} \tag{2.40}$$

Where G^r is a retarded Green function and f the Fermi-Dirac distribution. Derivating $\langle n_{qd} \rangle (\epsilon_d, \epsilon_a, -\epsilon_a)$ with respect to ϵ_d or ϵ_a, the four susceptibilities can be expressed as a function of a single quantity $\xi_0(\epsilon_d)$[14] and the tunnel rates to the source and drain electrodes Γ_s, Γ_d[15] :

[13] Note that the adiabatic approximation $\omega_d \ll \Gamma$ does not mean that $\chi_{-,-}$ diverges because $\omega \to 0$. A coupling to the lead $g_i \hat{n}_i (\hat{a} + \hat{a}^\dagger)$ means that the frequency ω_d is bigger than a cut-off frequency of the load lines, so that the electric field is not screened by the electrodes. Hence this frequency remains finite.

[14] $\xi_0(\epsilon_d) = -\int \frac{\mathrm{d}\epsilon}{2\pi} A(\epsilon - \epsilon_d) \frac{1}{4k_b T \cosh^2\left(\frac{\epsilon}{2k_b T}\right)}$ where $A(\epsilon - \epsilon_d) = G^r(\epsilon - \epsilon_d) G^{r*}(\epsilon - \epsilon_d)$.

[15] The derivation relies only the substitution : $\epsilon' = \epsilon - \epsilon_d$.

$$\begin{aligned}
\frac{\partial \langle n_{qd} \rangle}{\partial \epsilon_d} &= \Gamma_s \xi_0(\epsilon_d + eV_s) + \Gamma_d \xi_0(\epsilon_d + eV_d) \\
\frac{\partial \langle n_{qd} \rangle}{\partial \epsilon_a} &= -\Gamma_s \xi_0(\epsilon_d + eV_s) + \Gamma_d \xi_0(\epsilon_d + eV_d) \\
\frac{\partial I}{\partial \epsilon_d} &= \Gamma_s \Gamma_d \left[\xi_0(\epsilon_d + eV_s) - \xi_0(\epsilon_d + eV_d)\right] \\
\frac{\partial I}{\partial \epsilon_a} &= \Gamma_s \Gamma_d \left[-\xi_0(\epsilon_d + eV_s) - \xi_0(\epsilon_d + eV_d)\right]
\end{aligned} \tag{2.41}$$

V_s and V_d are the source and drain DC potentials.

At zero bias $V_s = V_d$, even in the presence of an asymmetric modulation of the electrode chemical potential by the cavity, the frequency shift is still proportional to the dot compressibility :

$$\Delta\omega_c = g_{qd} \left[g_{qd} - g_- \left(\frac{\Gamma_s - \Gamma_d}{\Gamma_s + \Gamma_d} \right) \right] \frac{\partial \langle n_{qd} \rangle}{\partial \epsilon_d} \tag{2.42}$$

Therefore, at zero bias, the contrast of a compressibility measurement $\frac{\partial \langle n_{qd} \rangle}{\partial \epsilon_d}$ depends on the tunneling rates and on the different coupling parameters g_{qd}, g_s and g_d.

- If the tunneling rates are symmetric $\Gamma_s = \Gamma_d$, or the coupling is symmetric $g_- = 0$, the frequency shift is proportional to g_{qd}^2. The contrast is reduced in the presence of coupling to the electrode as : $g_{qd} = g - \frac{g_s + g_d}{2}$.
- If the tunneling rates are asymmetric, for example $\Gamma_s \ll \Gamma_d$, the frequency shift is proportional to $(g - \frac{g_s+g_d}{2})(g - g_s)$. The sign of the frequency shift changes if the value of the coupling to the gate g is between g_s and $\frac{g_s+g_d}{2}$

Equation (2.39) allows us to quantify the contributions coming from a coupling of the photons either to the dot or an anti-asymmetrical coupling to the electrodes. This will be experimentally relevant in order to distinguish between the coupling scheme.

2.3 Compressibility measurements

As explained in the previous section, a microwave cavity can measure the quantum capacitance of the dot $e^2 \frac{\partial \langle n_{qd} \rangle}{\partial \epsilon_d}$, which also corresponds to the charge susceptibility linked to a gate potential modulation. At equilibrium (zero bias), this quantity is equivalent to the compressibility, a thermodynamic quantity.

The compressibility is the derivative of the number of charges of an electron gas with respect to its chemical potential $\frac{\partial n}{\partial \mu}$. As the chemical potential is the first derivative of

the total energy of the electron gas $\frac{\partial E_{tot}}{\partial n}$, the compressibility is the inverse of the second derivative of the total energy. It is a thermodynamic quantity in the same way as the specific heat, the magnetization, etc.

The total energy has contributions from the kinetic energy of the electrons but also from interactions via the correlation and exchange energies. In electron gas, depending on the ratio of the energy due to interactions and the kinetic energy, one can go from strongly correlated liquid to free electron gas. The measurement of this compressibility is therefore appealing for interacting systems. It was for example performed on 2DEG in the fractional quantum Hall(FQH) regime, where interacting quasiparticles play a central role in the theory [77].

Initially, capacitance measurement were done using a RC-circuit. This technique suffers from a big offset contribution, because of the large contribution of the geometrical capacitance in the 2DEG. A more precise technique, that determined the ability of the 2DEG to screen an electric field, was developed and anomalies in the compressibility in the normal and the FQH states were measured in GaAs-2DEG, giving thermodynamics evidence for a dilute interacting gas of quasiparticles in this regime [77].

The first measurement of a quantum dot capacitance was done in 1992 [78]. A quantum dot defined in a GaAS 2DEG was tunnel coupled to another AC modulated 2DEG. A High Electron Mobility Transistor was used to measure the potential shift induced by the variations of the mean number of electrons in the dot[16]. The smallest charge variations in the dot that could be detected, defined here as the sensitivity, was $\sim 10^{-1} e/\sqrt{Hz}$. This first experiment was able to get the electronic spectrum of the bound states structure and its evolution with magnetic field.

A more sensitive experiment was done a few years later, which was able to resolve the shape of the capacitance peak and distinguish its dependence on the tunnel barrier coupling (strong or weak coupling regime between the dot and the reservoir) [79]. In this experiment, they used as a detector a Single Electron Transistor made of two $Al/Al_2O_3/Al$ tunnel junctions, which increased the sensitivity of the charge in the dot by a factor 100. This SET was voltage biased near the onset of a Coulomb peak, so that the tunneling of an electron in the dot induced a small chemical potential shift in the SET leading to a measurable current. The small lever arm between the detector (the SET) and the dot ensure that the SET is in the linear regime and that there is a negligible back-action on the dot.

[16] In the dot, the residual AC modulations coming from the back gate is compensated by an extra AC oscillations from a top gate. This measurement scheme is called a capacitive bridge.

This SET was latter put on a tip allowing to measure the local compressibility a graphene sheet [80]. The local compressibility measurement was used to map out spatial fluctuations in the local density of states, revealing the structure of the disorder. The mean free path deduced from this thermodynamic measurement was in good agreement with the dual electronic transport measurement of the conductivity[17].

The sensitivity of the SET was later on enhanced by measuring it in the GHz frequency range to avoid the $1/f$ noise of background charges [81]. The measurement of the voltage or current fluctuations on the SET could not be done at microwave frequencies with the previous setup, because of the high impedance of the voltage (or current) amplifier. The SET was therefore connected to a LC resonator, whose damping is monitored by measuring the reflected power. When the chemical potential of the SET is moved towards a Coulomb peak, it enhances the dissipation of the resonator. This device, called a RF SET, was also used to resolve a capacitance of the order of $10aF$, revealing the effect of quantum fluctuation renormalization[18] [81].

The LC resonator was a lumped element version of a microwave cavity. Nevertheless because of the absence of surrounding ground planes that acts in a cavity as a Faraday cage, a lumped LC resonator is much less isolated from the electromagnetic environment. A high finesse cavity requires consequently a smaller voltage excitation to obtain a good resolution. As the sensitivity corresponds to the product of the smallest capacitance detected times the voltage excitation, microwave cavities have in principle a higher sensitivity, as shown in the experimental results of chapter 4.

2.4 Measurement with a microwave cavity

This section describes the experimentally relevant parameters that control the sensitivity of a compressibility measurement with a cavity, namely the transmission at resonance, the quality factor and the coupling constant.

2.4.1 Transmitted signal

Experimentally, one has access to the complex transmitted microwave amplitude at the cavity drive frequency. The phase shifts $\Delta\phi$ and the amplitude shifts ΔA due to finite

[17] This work also established the negligible contribution of the exchange and correlations energy to the chemical potential in graphene.

[18] The sensitivity of the charge noise of a RF-SET is $\sim 10^{-5}e\sqrt{Hz}$ [82]. In that experiment, the sensitivity of the dot charge was $\sim 10^{-3}e$, because the lever arm was 0.04.

susceptibilities are determined by the complex transmission :

$$T = \frac{-\sqrt{\kappa_1 \kappa_2}}{\frac{\kappa}{2} - i \sum_{i,j} g_i g_j \chi_{i,j}(\omega_c)} = \frac{(A_0 + \Delta A)}{A_0} e^{i\Delta\phi} \tag{2.43}$$

The above transmission is taken at $\omega_d = \omega_c$ to have a maximum signal. In the formula of the transmission 2.43, i has been changed to $-i$ compared to the transmission given in 2.35 to account for opposite Fourier transform sign conventions between quantum mechanics and electrical engineering.

For frequency and linewidth shifts small compared to κ, $\Delta\phi \ll \pi$ and $\Delta A \ll A_0$, we can expand (2.43) and get :

$$\begin{aligned} \Delta\phi &= \frac{2}{\kappa} Re\left(\sum_{i,j} g_i g_j \chi_{i,j}(\omega_c)\right) = \frac{2Q}{\omega_c} Re\left(\sum_{i,j} g_i g_j \chi_{i,j}(\omega_c)\right) \\ \frac{\Delta A}{A_0} &= \frac{2}{\kappa} Im\left(\sum_{i,j} g_i g_j \chi_{i,j}(\omega_c)\right) = \frac{2Q}{\omega_c} Im\left(\sum_{i,j} g_i g_j \chi_{i,j}(\omega_c)\right) \end{aligned} \tag{2.44}$$

Above, $Q = \frac{\omega_c}{\kappa}$ is the quality factor, which counts the number of times a photon 'bounces' on the mirrors of the cavity before escaping. The quality factor Q hence enhances the light-matter coupling, as photons interact longer with the quantum dot. The linewidth κ is the sum of $\kappa_{ext} = \kappa_1 + \kappa_2$ the controlled coupling to the outside bath and κ_{int} the undesired losses. κ_1 and κ_2 determine the transmission of the input and output ports of the cavity. Therefore one should be in the situation where $\kappa_{ext} = \kappa_{int}$, which enables to have a high qualitiy factor without lowering too much the transmission, that would lower the signal to noise ratio. In a coplanar geometry, one can show that κ_i scales like $C^2_{\kappa_i}$, where C_{κ_i} is the load capacitance [83].

For a symmetric cavity $\kappa_1 = \kappa_2$, the number of photon $n_0 \equiv \left\langle \hat{a}^\dagger \hat{a} \right\rangle_{\omega_c}$ at the resonance can be expressed with the following experimentally relevant parameters :

$$n_0 = \frac{2\sqrt{P_{in} P_{out}}}{\hbar \omega_c \kappa} \tag{2.45}$$

P_{in} and P_{out} are the power at the input port and the output port of the cavity at $\omega_d = \omega_c$, depending on $\hat{b}_{in}$, $\hat{b}_{out}$ defined in the section 2.2.6.

When measuring the transmitted microwave one loses half of the signal, because photons can also escape from the cavity in the input port. One solution is to use only one port and to measure the reflected signal. Another solution is to use asymmetric cavities with an input port that is much more closed than the output port.

2.4.2 Coupling engineering

The measurement of the compressibility by the cavity relies on a coupling to the dot chemical potential. The coupling constant reads $\hbar g = eV_{rms}\alpha$, where α is the lever arm.

The root mean square voltage of the photons can be computed by simple energetic considerations. A photon stays on average a time $1/\kappa$ in the cavity and the electrical power associated to the bare impedance of the line $Z_0 = 50\Omega$ is V_{RMS}^2/Z_0, so that :

$$\hbar\omega_c = \frac{V_{RMS}^2}{Z_0}\frac{1}{\kappa} \tag{2.46}$$

which gives :

$$V_{RMS} = \sqrt{Z_0\kappa\hbar\omega_c} \tag{2.47}$$

The lever arm α is the ratio of the induced potential on the dot δV_{dot} over the potential in the central stripe line δV_{ac}. This is consequently also the ratio of the capacitance C_c between the dot and the central conductor over the sum of the dot capacitance $C_{\Sigma_{dot}}$ The bigger is this ratio, the bigger the coupling is. Nevertheless, the DC lever arm is the ratio of the capacitance between the gate and the dot C_{DC} over $C_{\Sigma_{dot}}$. If the coupling to the cavity is too strong $C_{\Sigma_{dot}} \sim C_c$, the DC lever arm decreases and we could lose the DC gate tunability.

One strategy introduced in this thesis is to couple strongly the dot to a bottom gate, which is then equally capacitively coupled to a DC gate and to an AC gate connected to the central stripe line (see figure 2.6 **c**). The AC lever arm is then the product of the lever arm $\alpha_{dot} = \delta V_{dot}/\delta V_{bg}$ and the lever arm $\alpha_{ac} = \delta V_{bg}/\delta V_{ac}$, as shown in figure 2.5. An advantage of such a coupling scheme is that the cavity couples to the chemical potential in the same way as the DC gate. It also enables us to avoid adding an extra gate on the dot for the coupling to the cavity (usually a top gate), that could induce disorder in the dot.

The main disadvantage is that the coupling capacitance C_{ac} between the bottom gate and the AC gate could be of the same magnitude as the capacitance loading of the cavity C_κ. This would induce some leakage in the cavity, adding an effective broadening $\kappa_{coupling}$[19]. As for the loading capacitance the best compromise for this geometry is

[19] During this thesis, it was tested if the 50Ω-adaptation of the electrode bringing the AC potential from the central stripe line close to the dot matters. We have not seen any sizable effects on the global quality factor. It might be due to the fact that the length of the electrode is much smaller than the wavelength.

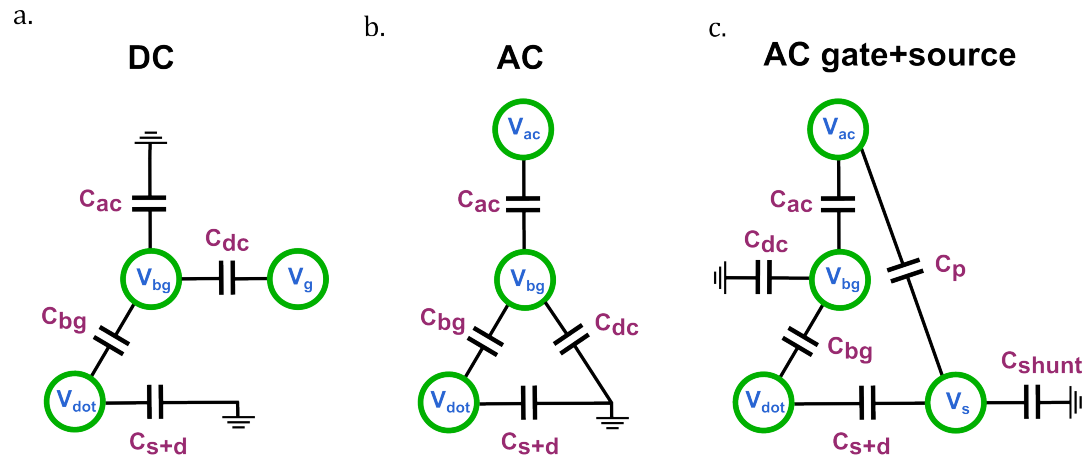

FIGURE 2.5: **Lever arms for a circuit with a bottom gate. a.** Classical circuit picture at zero frequency (DC). C_{bg} is the capacitance between the quantum dot and the bottom gate. C_{dc} is the capacitance between the bottom gate and the DC gate, at voltage V_g. C_{ac} is the capacitance between the bottom gate and the central stripe line of the cavity. C_{s+d} is the sum of the capacitances to the source and the drain that are in parallel. The potential induced in the dot by the gate voltage is given by the product of two the lever arms $\alpha_{bg} \times \alpha_{dc} \times V_g$. **b.** Classical circuit picture at the cavity frequency (AC). The potential induced in the dot by the cavity is given by $\alpha_{bg} \times \alpha_{ac} \times V_{ac}$. **c.** The source and drain electrodes may have also a coupling to the cavity central stripe line through a parasitic capacitance C_p. C_{shunt} is the capacitance of the source and the drain to the ground. The effective coupling seen by the dot is then the difference of the two lever arm $\alpha_{bg} \times \alpha_{ac} - \alpha_{parasitic}$. We have neglected $C_{bg} \ll C_{shunt}$ in the derivation of $\alpha_{parasitic}$.

to have approximately $\kappa_{coupling} = \kappa_{ext} = \kappa_{int}$, constraining the maximum coupling capacitance[20] C_{ac}.

As mentioned during the whole chapter, it is crucial to induce a gradient of potential on the scale of the nanocircuit to have an effective transverse coupling. Hence if the dot potential is modulated by the cavity, the potential of the source and the drain should be kept grounded. The effective coupling is the difference between the lever arm of the dot and the lever arm of the electrodes as shown in the figure 2.5. It is consequently favorable for the electrodes to have a big capacitance to the ground[21]. Therefore one should close the opening of the ground plane where the quantum dot circuit is placed, by

[20] In our case, C_{ac} is a fork, formed by two $300nm$-wide electrodes (see figure 2.6). Both branches are $300nm$ away from the bottom gate. Their maximum length is $7\mu m$. If there are longer, it lowers the quality factor.

[21] One should also keep in mind, that even if a metallic electrode has a very low impedance to the ground that would consequently efficiently screen the oscillating potential of the cavity, the electric field has a penetration depth, which is the skin depth $\delta = \sqrt{\frac{\rho}{\pi f \mu}}$. ρ is the resistivity of the electrode, f the frequency and μ is the permittivity. For a typical resistivity of a thin film $\rho \sim 10^{-7}\Omega \cdot m$ and using the vacuum permittivity, the skin depth is approximately 1μ in the microwaves. In a superconducting electrodes, the skin depth is approximately given by the London penetration depth.

extending the ground plane between the circuit, and the cavity central conductor. This corresponds to the thin grey electrodes shown in figure 2.6c that extends the ground plane. One can even bring additional electrodes connected to the ground plane close the source and the drain electrodes in order to increase their capacitances to the ground plane of the cavity.

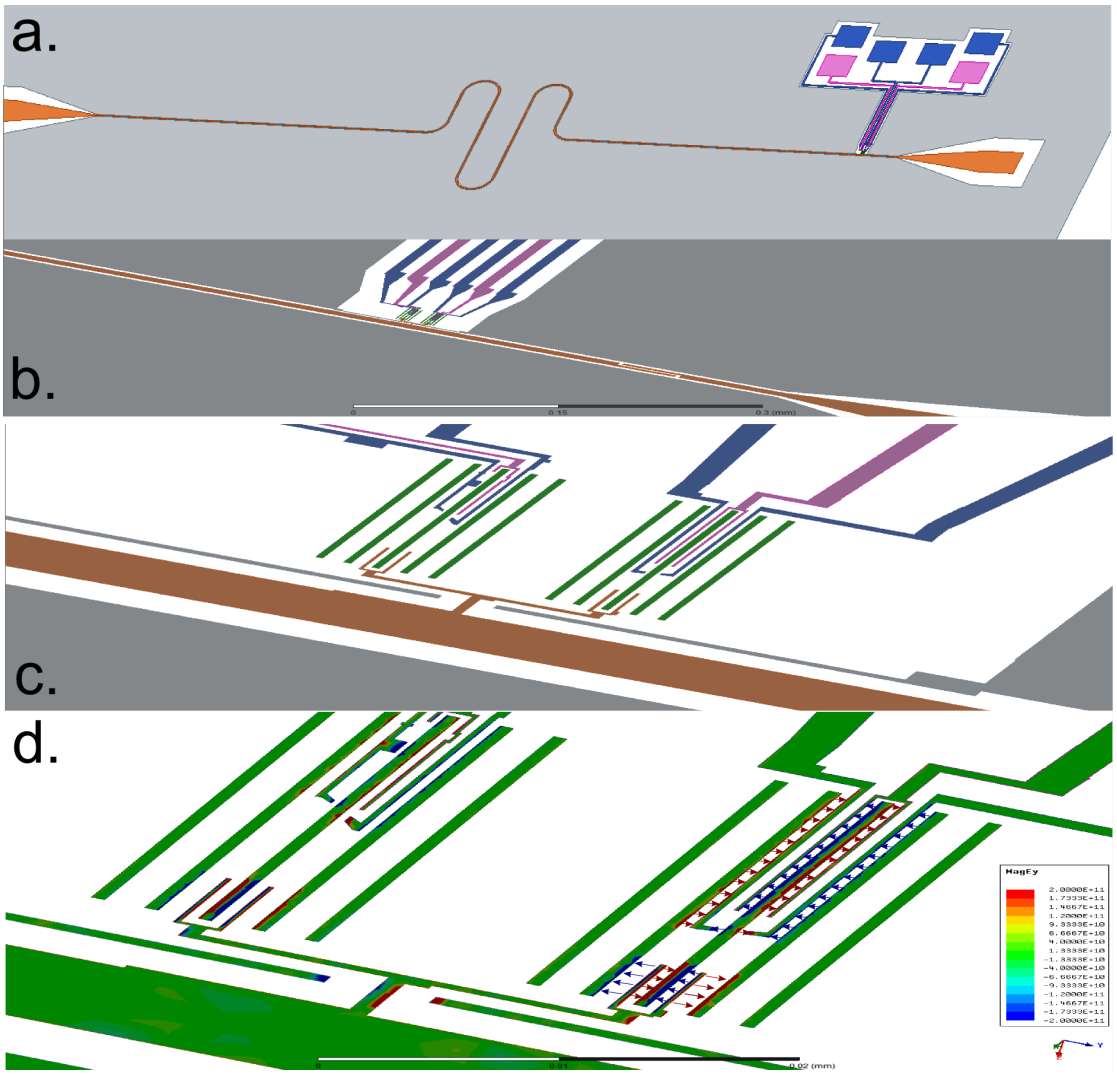

FIGURE 2.6: **Quantum dot circuit embedded in a coplanar microwave cavity. a.** A central stripe line (in brown) is inside a ground plane (in grey). Bonding pads are used to connect the nanocircuit placed in an opening of the ground plane **b.**, near one end of the central stripe line, which is connected to a load capacitance. **c.** The nanocircuit is made with two electrodes (in blue) and one DC gate (in pink). This later is capacitively coupled to a bottom gate, which is also capacitively coupled to a AC gate coming from the central stripe line (in brown). The opening of the ground plane has been closed (thin grey electrodes) to screen the cavity field which enhances the field inhomogeneities created by the AC and the bottom gates. **d.** HFSS software simulations of the electrical field. For clarity, only the in-plane field along the direction perpendicular to the bottom gates has been plotted. Blue and red color correspond to opposite directions of the field, underlined by added arrows. For sake of clarity, the field is only plotted in the metallic parts. Green color corresponds to zero field. One can see that the bottom gate has an intermediate potential between on one side the central stripe line and on the other side the gate, source or drain electrodes. One also see that the field is not completely screened at the tip of the source and drain electrodes[22].

[22]Note that the chosen color plot code does not account for fine discrepancies. A finer scale (not shown) shows that the field depends on the distance between the metallic parts, and that therefore the AC potential is a constant inside each metallic electrode. This confirms that on the scale of the circuit there is no impedance-mismatch effect. The component in the direction perpendicular to the stripe line (not shown) shows that the $1\mu m$-wide (grey) electrodes that extends the ground plane, effectively screen the cavity field.

Chapter 3

Experimental methods

The devices studied in this thesis have been fabricated with the nanofabrication facilities of the ENS clean room. The design and fabrication processes are described in section 3.1. The devices have been measured at cryogenics temperature with both low-frequency and microwave frequency measurement set-ups, as described in section 3.2.

3.1 Nanofabrication

3.1.1 Sample description and outlook of the fabrication process

Our experiments aim at coupling a microwave superconducting resonator that is centimeter long with a carbon nanotube-based nanoscale electronic circuit. The microwave resonator is a coplanar waveguide made out of a $150nm$-thick niobium film and formed by a central stripe line separated from the ground plane by a gap (figure 3.1 a). The stripe line is used as a $\lambda/2$ resonator and is connected to the input and the output of the microwave circuit by two capacitances. This Fabry Perot cavity has two anti-nodes of the electric field at both ends of the strip line, where nanoscale circuits are placed.

The sample fabrication is divided in three main steps :

- the fabrication of the superconducting resonator (see 3.1.2)
- the stamping of the nanotube on the sample (see 3.1.3)
- the fabrication of the nanocircuit around the nanotube (see 3.1.4)

In this work, a fourth step has been added because, instead of using usual side gates [13], we have developed a circuit architecture based on bottom gates 3.1.5. This allows us to couple more directly and strongly cavity photons to the carbon nanotube, but also to use a specific type of electrodes, such as ferromagnetic electrodes.

The resonator and the nanoscale circuits are fabricated using a well-known lithography technique, described in details in figure 3.2. The sample is first protected by a resist and the desired pattern is etched in the resist. The sample is then covered by a metallic film, and by removing the resist, only metals inside the patterned areas remain.

A powerful tool to design nanocircuit is to expose an electrosensitive resist with an electron beam in a Scanning Electron Microscope (SEM). The resolution is determined by the resist and the acceleration voltage of the electrons. It is about $100nm$ with a $500nm$-thick PMMA and an acceleration voltage of $20kV$. The nanocircuit is drawn

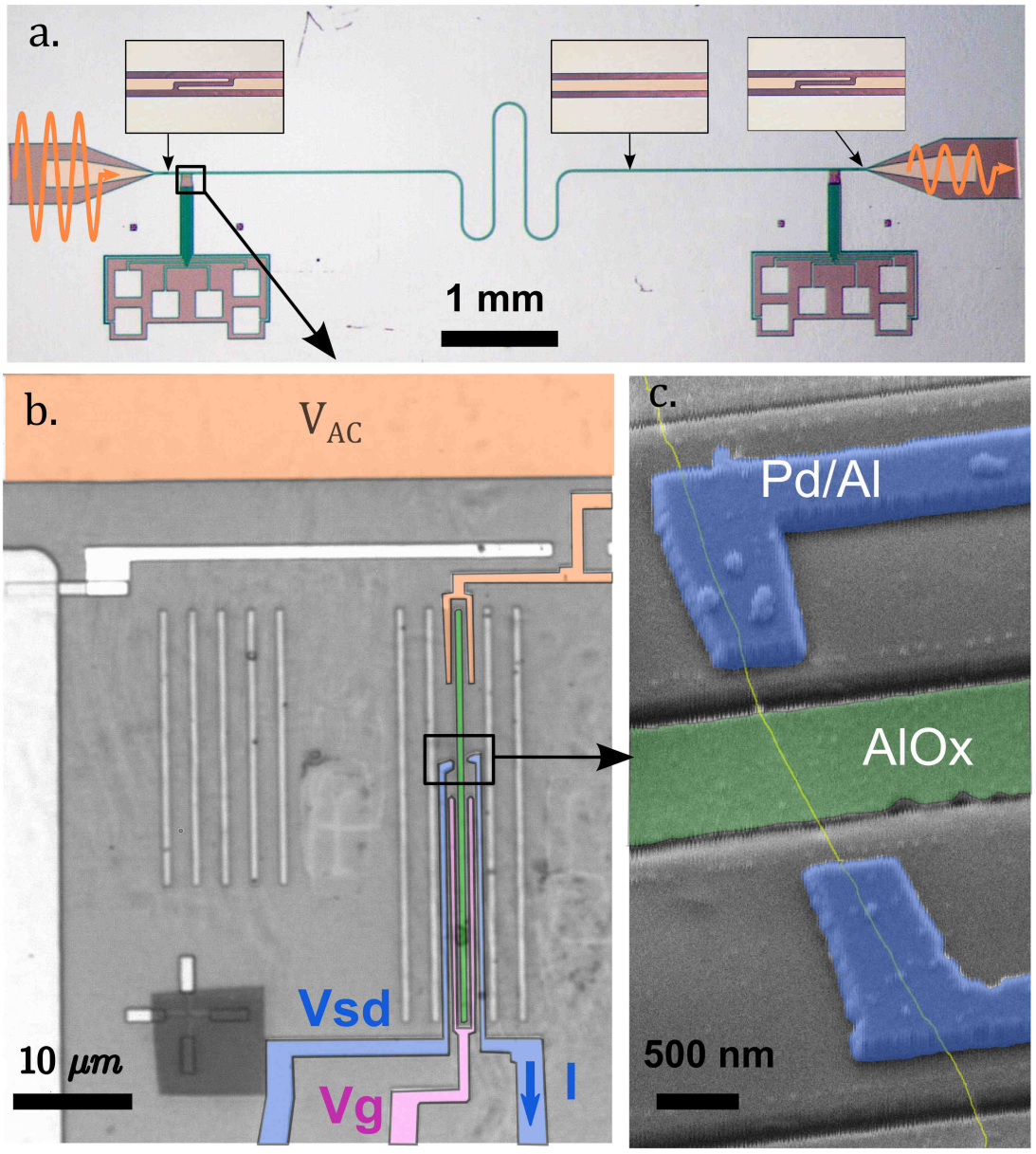

FIGURE 3.1: **Sample configuration. a.** Optical image of the final $5mm$ x $10mm$ chip. The central stripe line is colored in orange and the $3\mu m$ wide-gap between the central line and the ground plane is in pink. The central stripe line is connected on both ends to RF bonding pads by a capacitance formed by two facing $50\mu m$-long fingers. Two areas (black squares) have been opened in the ground plane where nanoscale circuits are placed. **b.** Optical image of a nanoscale circuit area. The central strip line, oscillating at the potential V_{AC}, is again colored in orange. A bottom gate in green is surrounded on one side by an electrode (in orange) that is connected to the central stripe line, and on the other side by a DC gate electrode (in pink). The nanotube is connected by a source and a drain electrodes (in blue). Source, drain and gate electrodes end up to bonding pads visible in **a. c.** A Scanning Electron Microscope (SEM) picture of a connected nanotube (in yellow) laying on a bottom gate (green). In this picture, the sample was rotated in the SEM in order to see the topography.

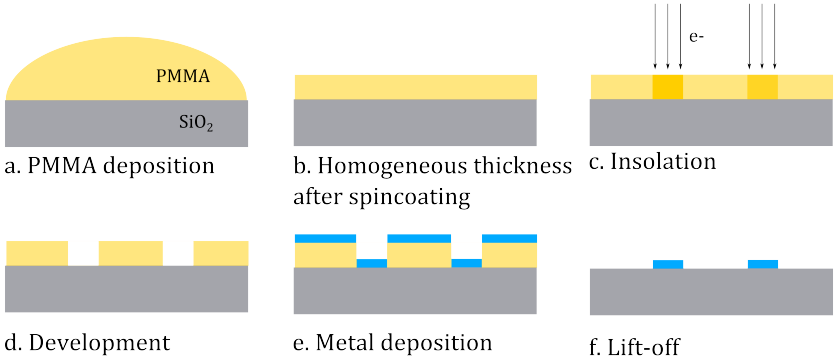

FIGURE 3.2: **Principle of lift-off positive electronic lithography. a-c.** A film with homogeneous thickness of $500nm$ is obtained by spin-coating a few drops of an electrosensitive resist, Polymethyl Methacrylate (PMMA). The sample is then backed to de-gassed solvents in the resist and the desired pattern is drawn by exposing the resist. **d.** During the development, the exposed resist is removed by placing the sample for 2 minutes in methyl isobutyl ketone (MIBK), diluted (1:3) in IPA, and then for 2 minutes in pure IPA. **e-f.** A metallic thin film is then deposited over the whole sample and only the metal inside the patterned areas remains after dissolving the resist in an acetone bath. The lift-off of the resist can be assisted by ultrasonic agitation, or by warming the acetone or even throwing acetone jets with a syringe. To reduce the final concentration of resist residues, it is useful to use several successive acetone baths. Note also that the thickness of the metal should not be bigger than roughly one third of the resist one. As a final step, IPA is used to wash acetone residues.

by deflecting the electron beam, which has a diameter of a few nanometers, inside a $100 \times 100\mu m^2$ area. The SEM can also be used to design larger patterns, like the resonator one, by moving the $100 \times 100\mu m^2$ drawing area with a precision based on an interferometric laser measurement. Using the SEM for both the resonator and the nanocircuit allows us to have the same scale reference for both of them. Furthermore, the different structures are kept aligned at each fabrication step, with the help of some gold crosses used as alignment marks.

To have a high finesse microwave cavity, carbon nanotubes are only transferred in the opening of the ground plane where the nanoscale circuit will be patterned [84]. This is because, on one hand, carbon nanotube growth requires a high temperature ($900°C$) process, that alters the superconducting Nb thin film, and produces dissipative amorphous carbon. On the other hand, the number of lithographic steps after the nanotube deposition should be limited, to avoid induced disorder in the nanotube, which would alter its tunability and its electronic spectrum. Even if carbon nanotubes are mechanically very resistant, they are also a good chemical adsorbent for all organic components used at each lithography step. And these adsorbates alter the electronic spectrum, as it relies on the Π-band formed by p-orbitals that stick out perpendicular to the surface. For both these reasons, the resonator fabrication and the nanotube growth are done on separate substrates.

3.1.2 Coplanar waveguide resonator

The coplanar waveguide is made of a ground plane and a central strip line $\sim 9.5mm$-long. It is built from a 150-thick niobium (Nb) layer, with a superconducting critical temperature around $9K$. To avoid RF dielectric losses, the Nb resonator lays on an undopped high resistivity ($10k\Omega \cdot cm$) Si substrate, covered by $500nm$ oxide. Compared to aluminium (Al), niobium has a much higher critical magnetic field, but the quality on the Nb thin film is much more sensitive to the deposition process.

Nb film can be deposited on a substrate by heating a Nb target in front of the substrate. As Nb has a high sublimation temperature, evaporation cannot be realized by heating Joule effect, but in an electron gun evaporator, where heat is provided by an electron beam focused on the Nb target. The evaporation is realized in a vacuum chamber, which is crucial for preserving the quality of the film from residual pollutions or oxidations. Using a cryogenic pump, the chamber base pressure can be lower than $10^{-9}mbar$. Nevertheless, because of thermal radiations of the heated Nb target, the walls of the evaporator chamber are de-gassing during the evaporation and therefore have to be cooled down with liquid nitrogen. In addition, the Nb is evaporated at high rate $\simeq 10\mathring{A}s^{-1}$, which is measured in situ by a quartz deposition controller. At this rate, evaporation pressures of the order of $10^{-9}mbar$ can be reached. Nb film can also be deposited in a sputtering chamber, where atoms of the Nb target are pulled off by electrons of an Ar plasma, but in our clean room facilities this technique decreases by a factor two the internal quality factor of the resonator.

It turns out that the quality of the film is much better when the resonator is designed by etching a full plane of Nb, instead of evaporating Nb on a patterned resist as described in figure 3.2. In fact, after the lift off of the resist, the edges of the film were not straight on their trench and flags on their top could not be removed. The Nb can be etched with a SF_6 plasma using a Reactive Ion Etching process ($25sccm$ at $7mTorr$ and $70W$), and the etching process gives much more regular edges, and a internal quality factor of about 150 000. Note that with an etching process, the resist left on the substrate after the lithography should be the reverse pattern of the one used for metal deposition.

The resonator is patterned using a photosensitive resist (AZ5214E) and UV exposure. A mask made of a glass plate covered by chromium filters the UV and the resist is only exposed in areas of the mask where the Cr has been previously removed. This has been done using a chemical etching with an $HClO_4 + Ce(NH_4)_2(NO_3)_6$ solution. During the exposure, the Cr surface is placed in close contact to the sample to avoid diffraction effects. The resolution of UV lithography is limited by the optical wavelength to $1\mu m$. This optical lithography technique is suitable to design large patterns like the

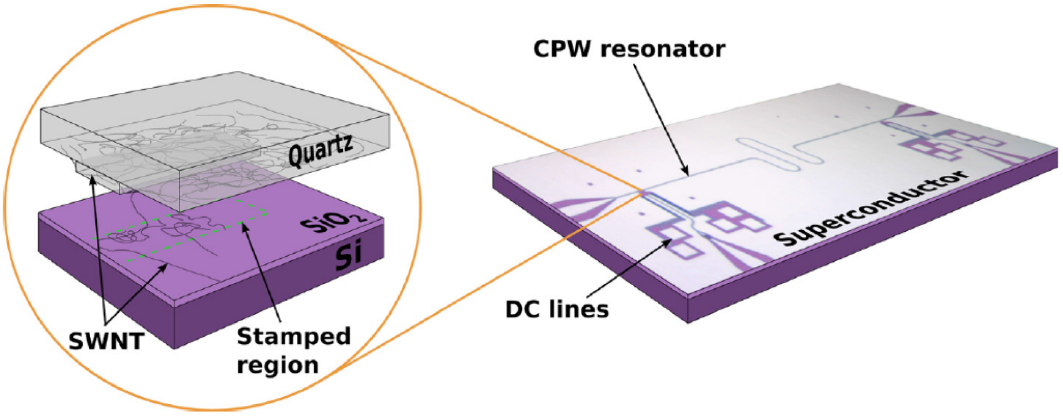

FIGURE 3.3: **Principle of carbon nanotube stamping** for combining high finesse microwave cavity with CVD-grown carbon nanotubes. Source:[84]

resonator, as it is much faster than electron-beam lithography. Once the mask is done with electronic lithography, which sets up the reference length in our process, it only requires a few seconds of UV exposure to expose several cm^2. Therefore, all the large DC lines and their bonding pads (figure 3.1), are also made during this UV lithography step, which then limits the ebeam exposure step only to four areas of $100 \times 100\mu m^2$. After the etching, the resist is removed by putting the sample in an acetone bath and the sample is cleaned from resist residues with 5 minutes of O_2 plasma ($100sccm$ at $100mTorr$ and $30W$).

3.1.3 Stamping carbon nanotubes

To avoid the presence of highly dissipative carbon residues on superconducting Nb film, nanotubes are stamped on the $100 \times 100\mu m^2$ opening of the groud plane dedicated to the nanoscale circuit, using a technique developed in the thesis of J.J. Viennot [85] and descirbed in detailed in Ref. [84]. The nanotubes are first grown by Chemical Vapor Deposition (CVD) on a $1cm^2$ quartz substrate (polycrystalline SiO_2), where pillars were previously made. The CVD growth process consists in placing the quartz, covered by a catalyst[1], in a desktop-size furnace heated up to $900°C$ in which methane and hydrogen gas flows are injected. Nanotubes are then transferred on the sample by flipping the quartz over and stamping the pillars on the desired location on the sample.

The CVD growth is actived by a catalyst made of $39\,mg\ Fe(NO_3)_3{-}9\,H_2O$, $7.9\,mg\ MoO_2$ and $32\,mg$ of Al_2O_3 nanoparticles, diluted in $30\,ml$ of IPA. Nanoparticles are selected by pipetting droplets from the top of the solution, which has beforehand decanted during 45 min after, 1 hour of sonication. Between two or four droplets are then put onto

[1] The catalyst composition is $39mg\ Fe(NO_3)_3{-}9\,H_2O$, $7.9mg\ MoO_2$ and $32mg$ of Al_2O_3 nanoparticles diluted in $30mL$ of IPA.

the quartz, and immediately blown with nitrogen flow. The concentration of catalyst is rather critical : a too low concentration does not produce any growth, whereas a high concentration leads to the formation of bundles of nanotubes. One may have a nicer repeatability and control on the density of catalysts by using iron nanoparticles that can be deposed by evaporation, but this requires an iron film thickness of a few $\mathring{A}$ that could not be reached with the available evaporators in the clean room. Attempts were also made to get a more directional growth, by lowering the CH_4 flux from $1140sccm$ to $100sccm$ and the H_2 flux from $200sscm$ to $50sscm$. Here again, the nanoparticle concentration and their surrounding topography may play a crucial role, and only directional (double wall) nanotubes were obtained when deposing catalyst on the trench of the quartz, which, up to now, does not go well with our nanofabrication process.

Compared to the process exposed in [84], some modifications were done to improve the repeatabilty of the stamping step. Pillars were previously made by deposing $5 \times 10\mu m^2$ square of aluminium on the quartz, and etching the uncovered SiO_2 with a CHF_3 process in the RIE. By replacing aluminium with nickel, which is more resistant to the CHF_3 plasma, the height of the pillars were doubled, reaching $4\,\mu m$. To improve the cleanliness of the surface on the pillars, $30s$ of an O_2 plasma ($100sccm$ at $100mTorr$ and $30W$) was used after the development and before the Ni deposition, to remove some residual PMMA.

Furthemore, during the stamping, the quartz is fixed on a glass plate, placed on an optical masker, which is normally used for optical lithography. Contrarily to [84], the quartz was not glued on this glass with a rather uncontrolled drop of PMMA but with a double sided tape, to improve the flatness and the absorption of the constraints. Double sided tape tends indeed to be more reliable than other tested methods, like PDMS, which was not sticky enough or spin-coated PMMA thin films, which presented some wetting problems.

3.1.4 Contacting the nanotube

After the stamping, transferred nanotubes are localized with the SEM, at an acceleration voltage of 2kV. The source, drain, and gate electrodes are then patterned to connect a chosen nanotube, using e-beam lithography at $20kV$. To form a quantum dot, the source and drain electrodes are typically patterned $500nm$ apart. Among the noble metals, palladium (Pd) has a good electronic contact with carbon nanotubes [86], because the wavefunctions of conduction electrons in the palladium and the nanotube have a good overlap, lowering the work function for electrons to tunnel from the metal to the nanotube. To preserve this good electronic matching, the interface between the

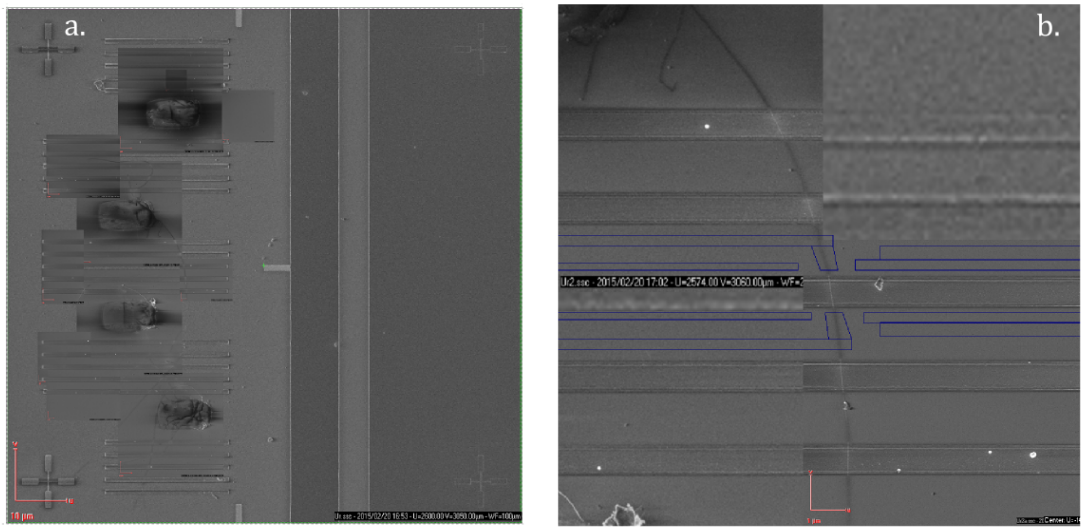

FIGURE 3.4: **CNT localization after stamping. a.** SEM image of the $100 \times 100 \mu m^2$ area after having stamped a quartz on it. The four imprints corresponding to the pillars, separated each by $15 \mu m$, are visible in between an array of bottom gates. Four alignment gold crosses are also visible on the edges. **b.** Zoom on a transferred nanotube in the area located in between the inner pillars. In blue, the sketch of the future gates and electrodes. In this sample the bottom gates were laying $135nm$ under the surface.

metal and the nanotube should be as clean as possible. Therefore, the development step should leave as little PMMA residues as possible on the tube. This is mostly controlled by the density of electrons incoming on the resist during the lithography, defined by a dose factor, which is, regarding our lithography parameters ($500nm$-thick PMMA and $20kV$ of acceleration voltage), around $470\,\mu C/cm^2$.

It is also necessary to have a clean atmosphere around the nanotube during the evaporation, and therefore to let the sample de-gassing in the evaporator at least one night at a pressure around $10^{-6}mbar$, before the evaporation. Some samples were contacted only with $Pd(80nm)$ and others with $Pd(4nm)/Al(80nm)$, to induce superconducting correlations in the nanotube.

3.1.5 Bottom gates

During this thesis, it was decided to stamp nanotubes over pre-defined bottom gates. Bottom gates aim at enhancing the coupling between the nanotube and the cavity photons. Nanotubes have diameters D around a few nanometers, so their capacitance to a metallic gate decreases rapidly such as $1/\ln(z/D)$, if z is the separating distance. Therefore, top gates are usually designed on the nanotube to be as closest as possible. But, as it requires an extra lithography step on the nanotube, top gates are usually designed not to be wider than $100nm$, to avoid exposing too much the nanotube. By shifting the

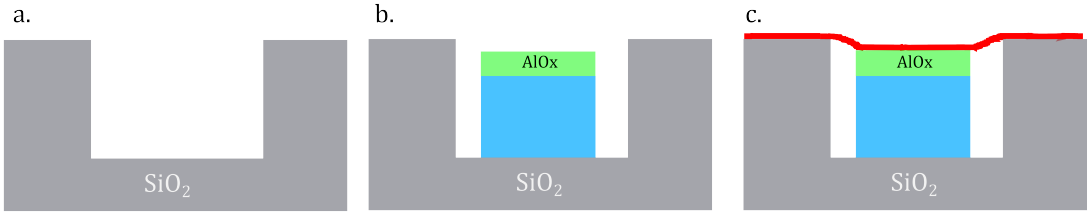

FIGURE 3.5: **Two-step fabrication of the buried bottom gates. a.** Trenches are etched in the SiO_2 oxide layer using a RIE CHF_3 plasma ($50sscm$ at $20mT$ and $70W$) and **b.** a $150nm$-narrower metallic layer is deposited inside the trenches. The metallic layer is capped by an oxide, obtained by 3 steps of static oxidation of $2nm$-thick Al layers using an O_2 pressure of $1mbar$ for $10min$. **c.** A nanotube is then stamped on the bottom gate.

lithography step of the gate before the stamping, bottom gates can have a wider lateral size and a priori a cleaner interface with the nanotube than top gates. As for top gates, an oxide layer is placed between the nanotube and the gate to avoid electric contact. The bottom gates are also buried, (see figure 3.5), so that the nanotube does not touch its lateral metallic edges. This also allows us to avoid strain in the nanotube that would be induced during the stamping, if the gate was above the sample surface. In all the samples fabricated during the thesis (except the one shown in figure 3.4), the surface of the oxide was laying between 30 and $50nm$ under the surface of the sample, so that the nanotube is laying on the $AlOx$ oxide (see figure 3.1).

3.1.5.1 Fabrication issues

The fabrication of the bottom gates should be done in two lithography steps, a first one for etching the trenches and a second one for the metal deposition. Furthermore, these steps should be done after the Nb deposition for the resonator. Otherwise, in both cases, some metallic residues stick on the edges (see figure 3.6), which would induce disorder in the nanotube. To protect the sides of the trenches, the pattern on the resist for the metallic deposition is $150nm$ narrower than the width of the trenches (see figure 3.7).

An array of bottom gates was used in order to maximize the probability during the stamping that a nanotube crosses perpendicularly one of them. It requires a fine alignment of the quartz upon the substrate, to avoid that the pillars damage the bottom gates (figure 3.4). Consequently, each $100 \times 100\mu m^2$ opening of the ground plane is stamped separately.

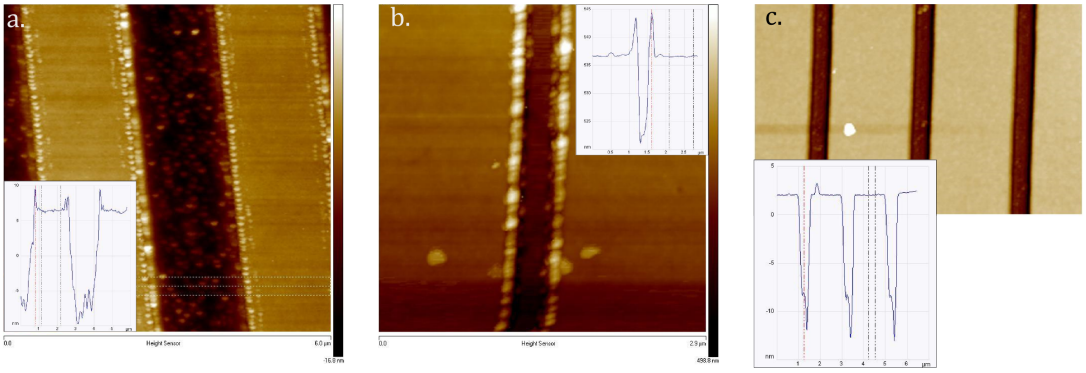

FIGURE 3.6: **Influence of the process on the topography. a.** Atomic Force Microscope (AFM) image of a buried gate that has been fabricated in one lithography step. It lets residues on the edge, with height of the order of a few nanometers. **b.** AFM image of a buried gate fabricated with two lithography steps, but where a Nb film has been deposited on it and removed by etching. In that case, it lets bigger peaks on the edge, with height of the order of $70nm$. **c.** Buried gates that were fabricated with two lithography steps and after the resonator fabrication. They are made of $50nm$-thick aluminium layer in a $80nm$-deep trench. The three images have been taken with an AFM in tapping mode. In that case, an atomic-size tip is scanned a few nanometers upon the surface. The tip is modulated at a given mechanical frequency and the frequency shift due to a force gradient is measured. In the tapping mode, the topography is deduced by adjusting the position of the tip so that the force gradient of the Van der Walls interaction is constant.

3.1.5.2 Ferromagnetic bottom gates

Bottom gates could also be used to induced a rotating magnetic field along the direction of the nanotube by using ferromagnetic gates. Nickel (Ni) thin films for example spontaneously form magnetic domains, that are called weak stripes [87]. Ni films, with typical thicknesses of $100nm$, have a perpendicular anisotropy, which means that the easy axis of their magnetization is perpendicular to the layer. As shown in figure 3.8, the perpendicular magnetization in the bulk rotates along the lateral axis [88], which induces the weak stripes domains.

This leads to spontaneous oscillations of the in-plane magnetization at the surface of the Ni film. To submit the nanotube to this periodic rotating B_{field}, a $100nm$-thick and $600nm$-wide Ni films were deposited in $130nm$-deep and $750nm$-wide trenches. The Ni bottom gates are capped by Al oxide. Domains with a width of $215 \pm 10nm$ have been measured with a Magnetic Force Microscope (MFM) (figure 3.9).

The Ni weak stripes are well suited for narrow gates, because the ferromagnetic pattern is more influenced by the edges, as the stripes prefer to be perpendicular to the edges (or exactly parallel for small roughness). Furthemore the stripes can also be oriented by applying an in-plane magnetic field. The stripes keep then the orientation at zero magnetic field [87].

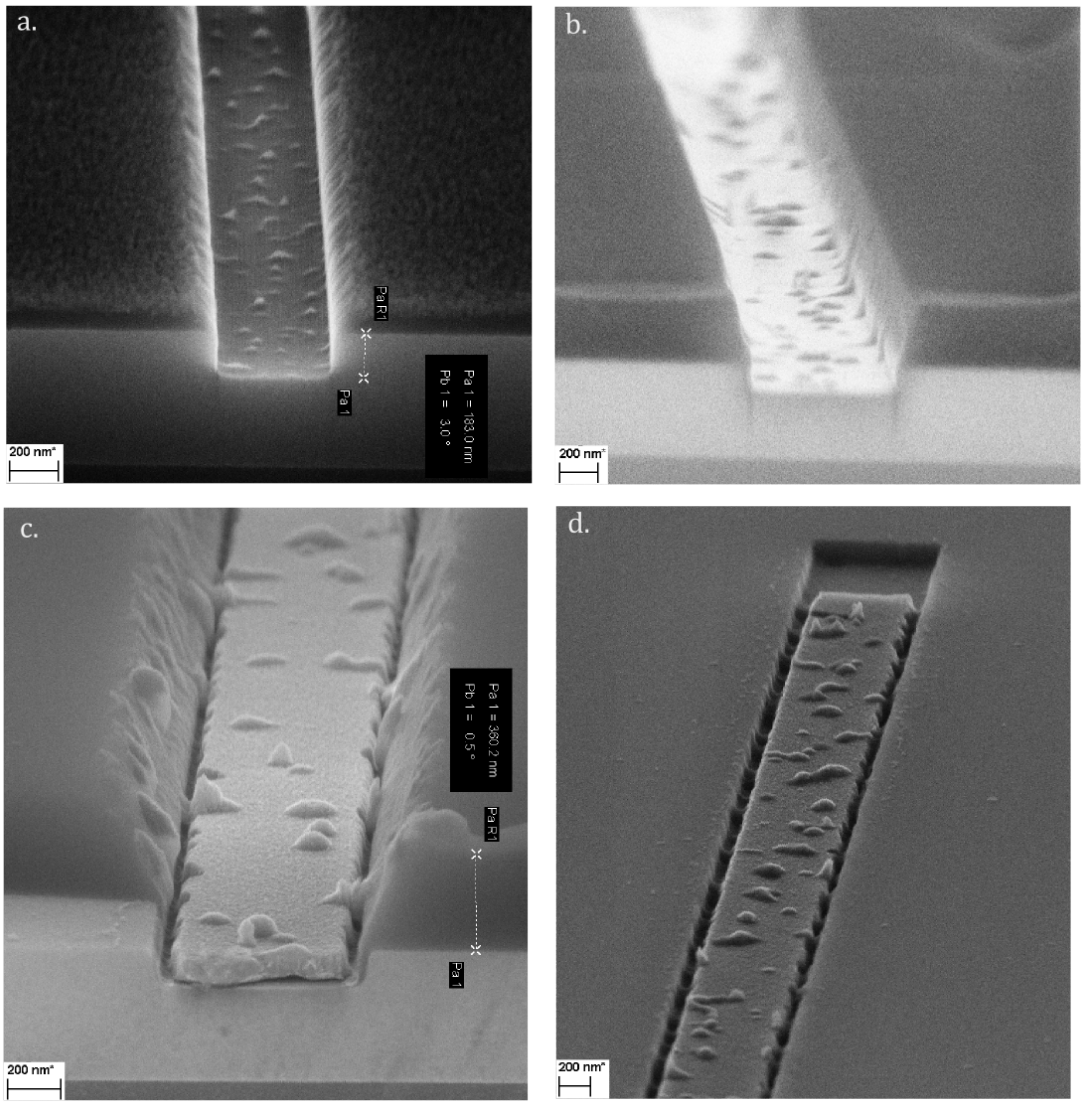

FIGURE 3.7: **SEM images for each step of the buried gate fabrication.** The sample has been cleaved and images have been taken with a specific angle to see the trenches. **a.** Image after the etching of the trench and before the lift off of the resist. The resist is also etched by the plasma. **b.** SEM image after the development of the resist and before depositing the metallic layer. For this second lithography step, the resist goes down in the trench on its edges. **c.** This can also be viewed in this picture taken after the metallic deposition. **d.** SEM image after the lift off of the metallic deposition. Courtesy of J. Palomo.

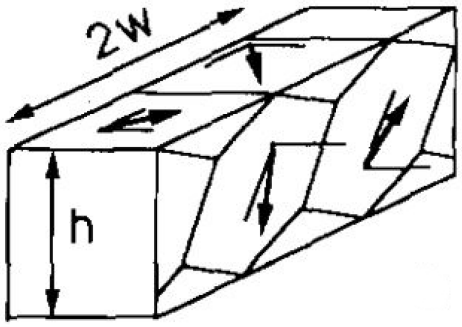

FIGURE 3.8: **Domains structure for weak stripes.** The arrows represent the magnetization that rotates along one of the horizontal axis. w is the domain width and h the thickness of the ferromagnetic layer. Figure taken from : [88].

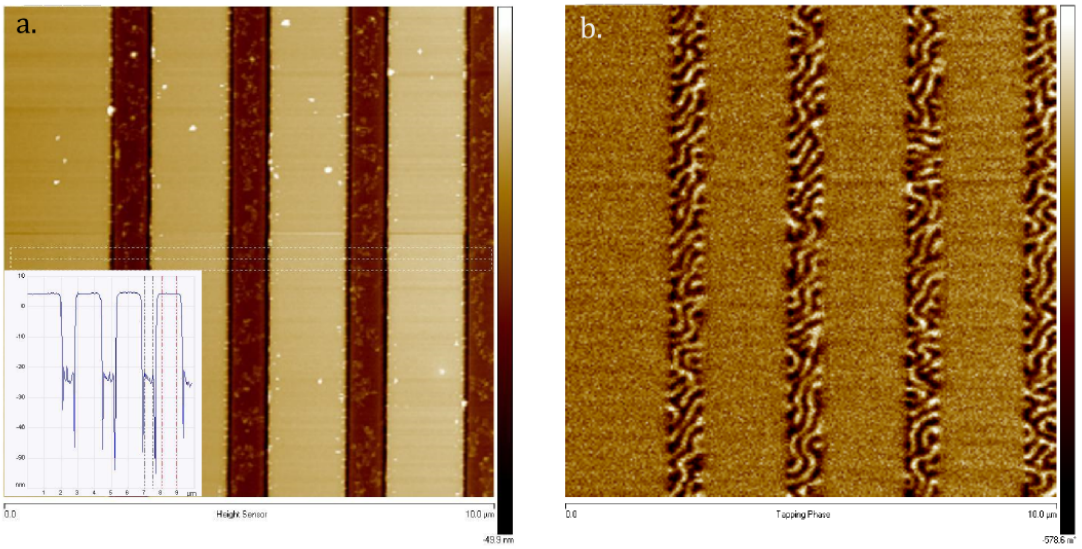

FIGURE 3.9: **a. AFM image and b. MFM phase image of buried Ni stripe lines.** A MFM is an AFM with a magnetic tip, used in the tapping mode. The tip is lifted up, in our case $50nm$ above the surface, to avoid the influence of short range Van der Waals interactions, due to the topography. The phase shift of the oscillating tip is then proportional to the variations of the magnetic field.

As MFM only measures a gradient of forces, it can not determine the absolute value of the magnetic field. Nevertheless, the tabulated saturation magnetization of the bulk Ni corresponds to a magnetic field around $600mT$ [89]. Due to the formation of the domains, the magnetization on the surface of the Ni layer is about a few dozens of percents of the saturation value. The Majorana bound states described in the fist chapter only emerge if there is a Zeeman splitting bigger than a superconducting pairing potential. The Zeeman splitting induced by the Ni magnetic stray field (a few dozens of percents of $60\mu eV$) may be too weak to compete with induced superconductivity effects in the nanotube, which are of the order of $10 - 150\,\mu eV$.

Cobalt could be used as an alternative to Ni to increase the magnetic field, as it has a

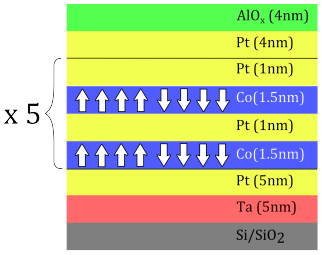

FIGURE 3.10: **Formation of vertical up and down domains in Cobalt/Platinum multilayers.** The thinness of the Co layer is the key ingredient to get a perpendicular anisotropy. Indeed, spin-orbit coupling locks the magnetization direction of Co on its crystalline axis, and for thin films, the increasing surface contribution overcomes the bulk crystalline symmetries, that normally favors in-plane magnetization. The thinness of the Pt layer is also an important parameter, as conduction electrons couple vertically the magnetizations of the stacked Co layers via RKKY interactions, which are only on the scale of λ_f, the Fermi wavelength. Vertical up-down domains appear then to minimize the stray field energy.

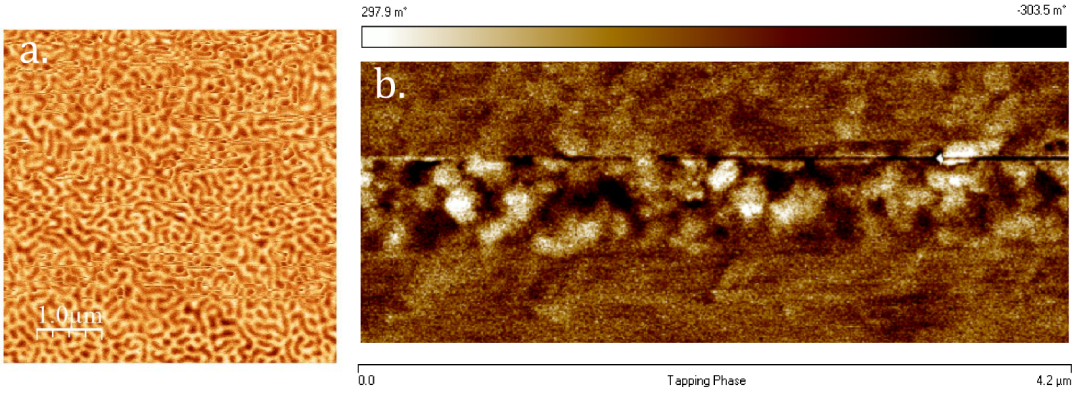

FIGURE 3.11: **MFM image of Co/Pt multilayers. a.** MFM phase image of a plain plate of a Co/Pt multilayer (arbitrary scale for the color plot). A Fourier transform analysis gives a domain width of $160nm$. **b.** MFM image of a buried Co/Pt multilayer. The etching of an h-deep trench induces some vertical roughness of the order of $\sqrt{h}$, which nevertheless does not seem to affect the magnetic pattern. In **b.**, the tantalum buffer layer was not used, which lead to a lower contrast on the MFM image (not visible here).

bulk saturation magnetization three time bigger. Indeed, multilayers alternating thin films of Co and thin films of a non-magnetic material have already been investigated in the magnetism community, because it forms up and down domains with a perpendicular anisotropy [90–93]. In our case it was decided to deposit $Pt(50A)/[Co(15A)/Pt(10A)]_{X10}/Pt(4)$ mutilayers in the Laboratoire de Physique des Solides (Orsay) and to integrate it as buried bottom gates in our set up, inside $80nm$-deep trenches (see figure 3.10).

The up and down magnetic domains of this Co/Pt multilayers form a rotating magnetic field on the surface that could be at least in the order of a few hundreds of mT. Furthermore the domains are thinner than in Ni, around $160\,nm$ (figure 3.11).

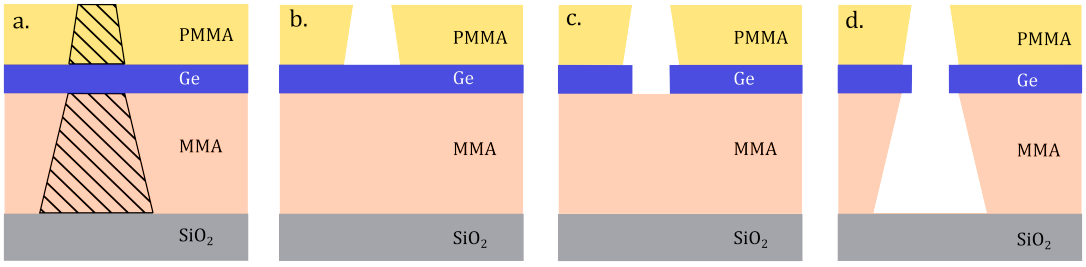

FIGURE 3.12: **Principle of a tri-layer development. a.** The shading sketches the exposed resist. (Because of multiple electron reflections, it is a simplified representation of the profile). **b.**The first layer of PMMA is developed with the usual recipe (2 minutes MIBK + 2 minutes IPA), **c.** the Ge is then etched in the RIE with a 30 seconds of a SF_6 plasma ($25sccm$ at $7mTorr$ and $70W$) and **d.** the MMA is developed with 2 minutes MIBK, with 3 seconds of ultrasonic bath at the beginning and then 2 minutes IPA. The sample is then cleaned with 30 second of O_2 plasma ($100sccm$ at $100mTorr$ and $30W$) to remove potential MMA residues in the trenches where the Co/Pt multilayer will be deposed.

These multilayers have nevertheless the experimental drawback that the $500nm$-thick PMMA layer gets burned during the evaporation, especially over the Nb resonator. To solve this problem, it was decided to use for the lithography and deposition $1\mu m$ of MMA covered by $4\,nm$ of Ge. This metallic layer is used to reflect thermal photons during the evaporation. An extra layer of $500nm$ of PMMA on the Ge is necessary to pattern the gates with the SEM (figure 3.12).

The second drawback of the Co/Pt multilayers is that the formation of the domains does not rely on geometrical constraints as for the Ni weak stripes. Domains happen to form 'bubbles' and cannot be clearly oriented by an in-plane magnetic field as for Ni thin film.

Even if the Co/Pt multilayer strengthens the magnetic field, it is crucial that the nanotube lays on the ferromagnetic gates, as the magnetic field decreases exponentially when moving away vertically from the surface [2]. To illustrate this rapid decay, the remaining magnetic field created by a single $Pt/Co(6A)/AlOx$ layer has been measured with a NV center and found to be around only $2mT$, $120nm$ away from the oxide [94].

Nevertheless, to prevent any effect of the stray magnetic field of the ferromagnetic gates on the nearby superconducting contact, it has been decided to move from $Pd(4nm)/Al(80nm)$ to $Pd(4nm)/Nb(80nm)$, as Nb has a much larger critical field.

[2] Following Maxwell laws, the periodic oscillations of the magnetic field lead to an exponential decay on the vertical axis.

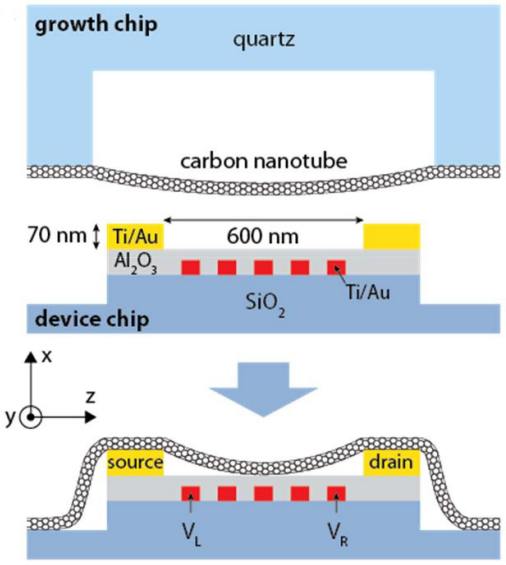

FIGURE 3.13: **Principe of pristine CNT stamping technique.** Source : [95]

3.1.6 Towards single pristine CNT's stamping

Bottom gates are useful to minimize the lithography steps experienced by the nanotube. Nevertheless in the stamping process described in 3.1.3, there is still a remaining lithography step to contact the localized nanotubes. Furthermore, this process suffers from a lack of control in the coupling of the nanotube with the source and drain electrodes and induces disorder that alters the nanotube electronic spectrum. Thus, the quality of the nanotube spectrum and its contact with the source and drain rely on statistical trials. In this thesis, 75 nanotubes were contacted in 31 resonators, but only 17 were actually connected, with a resistance at $300K$ between $10k\Omega$ and $70k\Omega$. Among the connected nanotubes, only two showed a regular spectrum that was characteristic of a clean nanotube.

Therefore, it would be very appealing to stamp a nanotube at the final step, on a chip where source and drain would have been already fabricated, as depicted in 3.13. A pristine nanotube would be suspended in between two close pillars and brought in contact with the electrodes. This would also allow us to select directly the nanotube that we want to connect, by measuring its characteristic when it comes in contact with the electrodes. If its spectrum meets the expectations, it would then be separated from the quartz and the quartz would be lifted up. Otherwise, the quartz would be moved and an other suspended nanotube would be tested. This requires that the quartz has several pillars to increase the number of choices. The reliability of such stamping process would also depend on the yield of suspended single wall carbon nanotube in between two close pillars, that could be improved by a well tuned directional growth, as described in

section 3.1.3. Having a good contact will also be challenging, as it requires very clean electrode surfaces. But we could imagine for example doing the stamping in a vacuum chamber after having stripped the electrode surfaces with an Ar plasma.

Despite these challenging experimental requirements, this stamping technique would allow us to select and measure a pristine nanotube, but also to have a better tunability on the electronic circuit. In fact, the confinement potential would in that case only be controlled by the electrostatic gate potentials, which could be then fine tuned by some extra lateral gates, like V_L and V_R in 3.13.

3.2 Measurement technique

3.2.1 Isolating the device from the electromagnetic environment

Carbon nanotube based quantum dot circuits require to isolate the device from noise fluctuations, in order to keep electrons confined in the quantum dot and to preserve interesting effects based on quantum coherence. To reduce thermal fluctuations, the electronic circuit coupled to the Nb superconducting cavity should therefore be thermalized at cryogenic temperature, typically less than $1K$.

3.2.1.1 Reaching cryogenic temperatures

In this thesis, the first part of the measurements have been carried out in a ^3He cryostat, with a base temperature of $250\,mK$. The second part has been carried out in a dilution refrigerator with a base temperature of $18mK$. These cryostats are cooled down by evaporation of cryogenic liquids.

This section focuses on the operation of a ^3He cryostat and its wiring, which has been realized during the begining of this thesis. In a ^3He cryostat, two intermediate stages, one at $4K$ and one at $1K$, help to go down to $250\,mK$:

- The $4K$ stage is cooled down by placing the cryostat inside a liquid Helium 4 dewar.
- $1K$ is reached by pumping on the ^4He bath with a needle valve. The impedance of the needle valve lowers the saturation vapor $P_s(T)$ and hence the ^4He evaporation temperature to $1K$.
- The lowest temperature, $250\,mK$, is reached by pumping on ^3He liquid. ^3He is kept in a closed circuit inside the cryostat, and pumped with an activated carbon

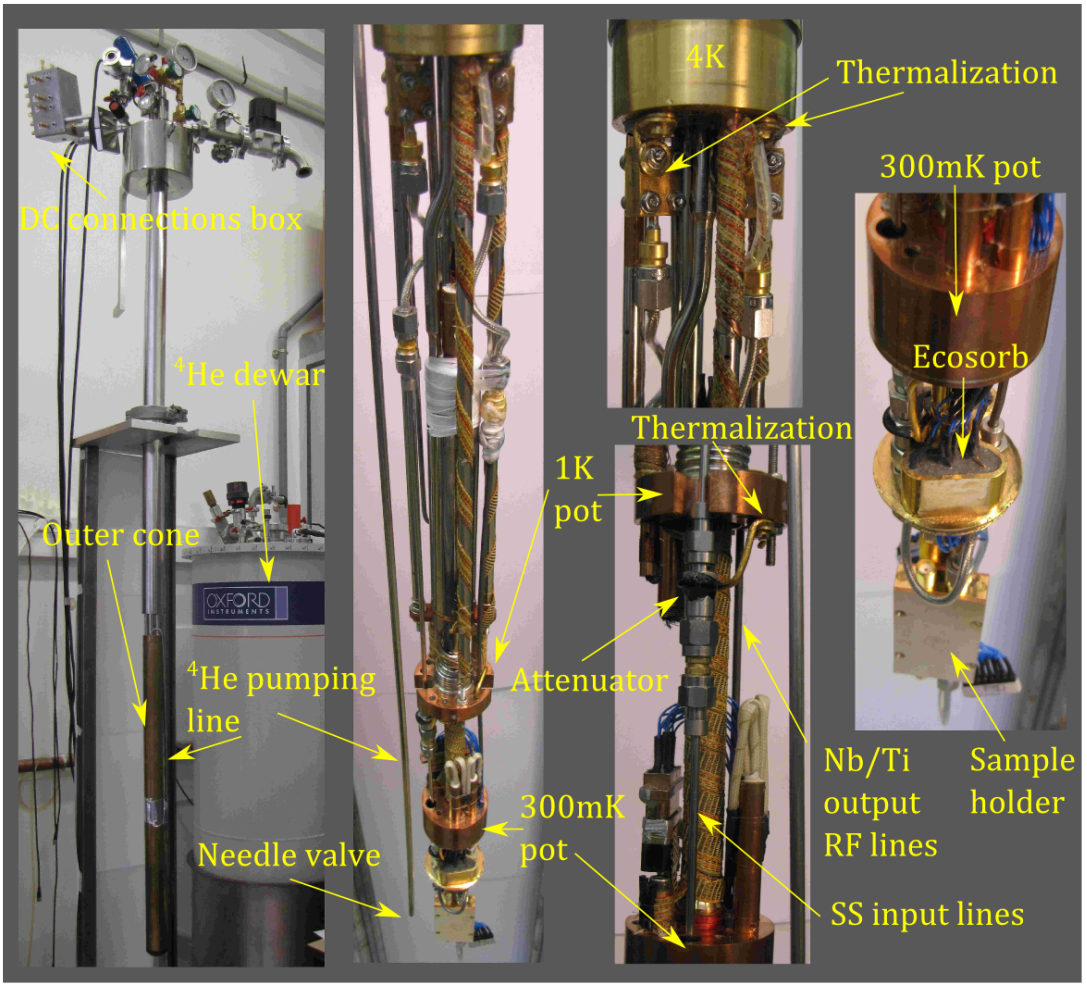

FIGURE 3.14: ^3He **cryostat and its thermalization levels.** A ^3He cryostat is placed in a ^4He dewar. Three temperature stages are visible here : the outer one is placed in the $4K$ ^4He bath, the $1K$ pot is connected to the needle valve, and $250mK$ pot is below the $1K$ pot. At $4K$, gold plates are used to thermalize the outer part of RF cable. At $250mK$, just above the sample holder, resistive manganin wires help heat to flow into a dissipative dielectric *Ecosorb MF* 117.

pump. The lowest temperature is maintained during approximately 55 hours, and the evaporated ^3He has then to be recondensed on the $1K$ pot.

This 3-stages architecture is essential to reach the lowest temperature as the $1K$ and $250mK$ stages have limited cooling powers. The cooling power $L \times \dot{n}$, with L being the latent heat, is limited by $\dot{n}$ the flow of pumped helium[3]. Consequently, the lowest temperature stage is very sensitive to the heat load, as its equilibrium temperature is governed by :

$$|\dot{Q}_{heat\,load}| = |\dot{Q}_{cooling}| = L \times \dot{n} = L \times \frac{\dot{V} \times P_s(T)}{RT} \tag{3.1}$$

[3]For the needle valve, the cooling power should be actually roughly divided by 2 to account for losses

Hence, heat loads increase the saturation pressure $P_s(T) \propto e^{-L/RT}$ and therefore the equilibrium temperature. For an HelioxVL cryostat used in this thesis, the base temperature is $235\,mK$, and increases up to $281\,mK$ when the lowest temperature stage receives additional $40\mu W$ heat load.

Heat load come from either gas convection, thermal radiations, or thermal conduction. Vacuum is made between each stage to prevent gas convection. Following the black body radiation law $Q_{radiation} = \sigma(T_{hot}^4 - T_{cold}^4)$, the $4K$-stage adsorbs $460\,W \cdot m^{-2}$ from the $300K$ radiations, the $1K$-stage $14\,\mu W \cdot m^{-2}$ from the $1K$-stage, so that the lowest temperature receives only $50\,nW \cdot m^{-2}$.

Heat loads come also from DC and RF cables that connect the sample at $250mK$ to the measurement set-up at $300K$. The Fourier law tells us that the amount of transported heat depends only on the integrated linear thermal conductivity[4] of the metal and its cross section A and length l as

$$Q_{conduction} = -\frac{A}{l} \times \int_0^T \kappa(T)\mathrm{d}T \tag{3.2}$$

By wiring the fridge, we can hence play with the choice of metal to decrease heat load, but keeping in mind that the thermal conductivity is also proportional to the electrical conductivity, according to the Wiedmann Franz law. Beryllium Copper (BeCu) or stainless steal (SS) semi-rigid coaxial cables happens to be a good compromise between the amount of conducted heat and their RF attenuation.

Nevertheless one meter-long BeCu coaxial cable carries about $2\,mW$ from $300K$ down to $4K$, so it is crucial to dissipate this heat load at the $4K$ stage. Hence the outer shield of the coaxial cable is strongly crimped with gold plated adapted copper parts to the $4K$ stage (see picture in 3.14). The copper parts are long enough, $5mm$, to also thermalize the inner part of the coaxial cable through the dielectric[5].

Two attenuators are also placed and thermalized at $1K$ and $250mK$ on the in-going RF line (see figure 3.15). This thermalizes both the inner and the outer metallic parts of the coaxial cables, as attenuators connect the core to the shield with a 50Ω resistance. Nevertheless such resistive RF cables combined with attenuation levels are not suitable for the outgoing RF line, as this carries the measured signal. Up to the $4K$-stage, a niobium-titanium coaxial cable is used for the outgoing line, which is superconducting and therefore carries microwaves without attenuation and without heat transport.

[4] $Q_{conduction} = -\frac{A}{l} \times \int_0^l \kappa(T)\frac{\partial T}{\partial x}\mathrm{d}x$

[5] The thermalization length through the dielectric is $\sqrt{\delta_d \delta_m \frac{\kappa_m(4K)}{\kappa_d(4K)}}$, where δ_d is the thickness of the dielectric, δ_m the diameter of the inner metallic part and κ_m (resp. κ_d), the metallic (resp. dielectric) thermal conductivity.

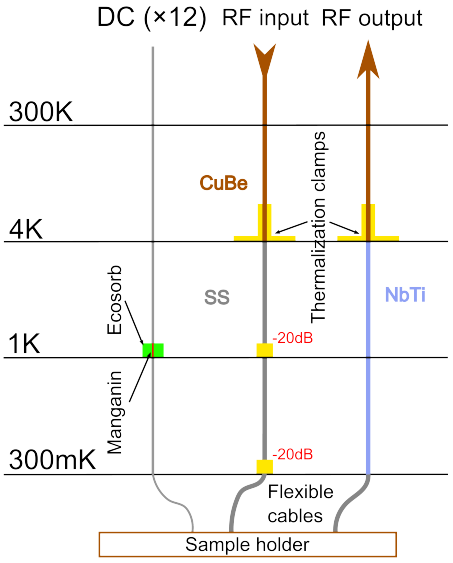

FIGURE 3.15: **Wiring the cryostat with DC and RF cables.** Attenuators are used to thermalized both the outer and inner part of a coaxial cable, with its 50 Ω resistance between the central core and the ground. They also absorb hot photons going down on the RF line.

The DC lines have much thinner cross section and carry less heat than RF cable. They are only thermalized at $250mK$, with resistive manganin wires confined in *Ecosorb MF* 117, a dissipative dielectric[6] (see figure 3.14). Both attenuators and the *Eccosorb* are also used to dissipate $300K$-radiations going down through the metallic wires.

Once wired, the base temperature of the ^3He was $250mK$ during approximately 55 hours.

3.2.1.2 Reducing the electrical noise

The electronic nanocircuit thermalized at $250mK$ should also be protected from the noise coming from the outside, to keep electromagnetic fluctuations under the $250mK$-thermal fluctuations. The ecosorb and the $-20dB$-attenuator thermalized at $250\,mK$ (see figure 3.15) ensure that the noise spectral density added by the cables is mainly set by a $250\,mK$-thermal noise power distribution. Furthermore, DC lines that carry gate voltages (and therefore no current) have a 100-Hz low-pass RC filter at $300K$ ($R = 10^5\Omega$ and $C = 100nF$). Finally, the cryostat has metallic shielding which prevents ground loops in the cryostat from picking up AC magnetic fluxes.

[6]The manganin wires have to be resistive enough so that the carried heat is preferably dissipated in the ecosorb.

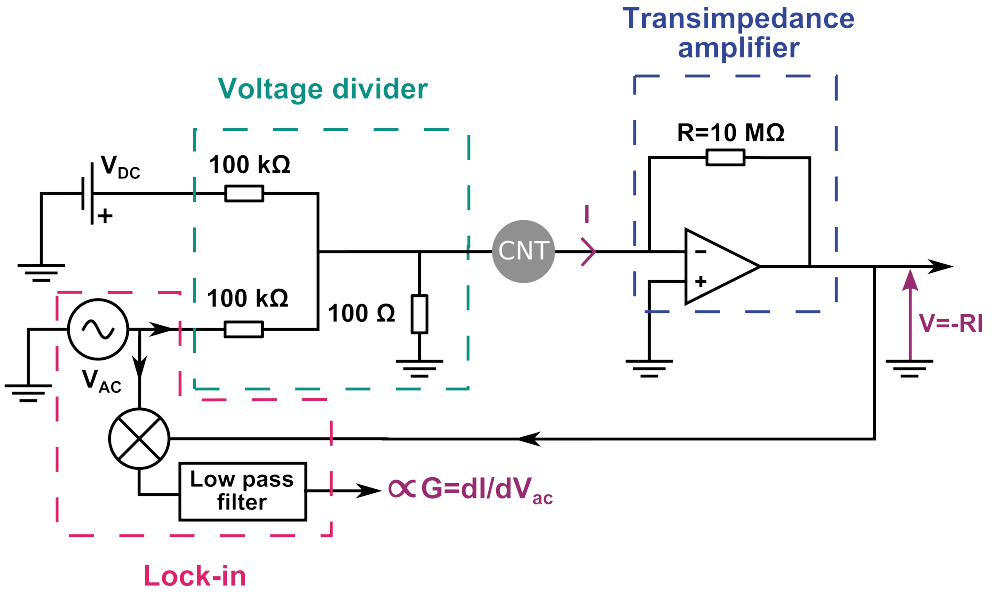

FIGURE 3.16: **Transport measurement set up.** A voltage divider divides by a factor 1000 the voltage from a DC and AC sources, which is imposed on the source electrode. The output current is amplified by a low noise I-V converter. A lock-in is used to measure the differential conductance.

3.2.2 DC measurements

The nanotube is contacted with a source (S) and a drain (D) electrodes, and can be tuned with a third gate electrode. The direct current I through it and the differential conductance $G_{diff} = \frac{\partial I}{\partial V_{sd}}$ is measured with respect to the source-drain potential difference V_{sd} or the gate voltage V_g. Nanotube have resistance of the order of $10 - 100k\Omega$, on which we typically apply a mV bias voltage V_{SD}. Hence the output current is of the order of $10nA$ and needs therefore to be amplified by a home-made low noise I-V converter with a gain $G = 10^7$. Those amplifiers transform a current I in voltage $V_{out} = -G \times I$, read by a Keithley 2000. See figure 3.16 for a sketch of the DC measurement set-up.

The differential conductance is measured by modulation technique, via a lock-in (SR7265LI). The nanotube is biased with an oscillating potential $V_{AC} = 30\,\mu V$ at the frequency $f = 2.777kHz$. This induces an oscillating current $\delta I_{AC} = \frac{\partial I}{\partial V_{sd}} \times V_{AC}$, which is also amplified by the transimpedance amplifier and then demodulated at the same frequency f.

The lock-in integrates the demodulated signal on a time constant set to $T_c = 20ms$ to average the stochastic noise :

$$\langle\, \delta I \rangle = \frac{1}{T_c} \int_0^{T_c} \delta I_{AC}(\omega t) \delta V_{AC}(\omega t) \mathrm{dt}$$

Consequently the noise spectrum of the differential conductance is filtered out of a $1/T_c = 50Hz$ window centered on the measurement frequency f. The advantage of measuring at finite frequency is to get rid of the $1/f$ noise (Flicker noise) and of the $50Hz$-noise of the power supplies[7]. The modulation frequency of the lock-in measurement is nevertheless limited to the kHz range, because the impedance of the DC lines are not adapted to carry high frequency signal and furthermore reactive elements in the circuit could distort the demodulated value of the resistance.

3.2.3 RF measurements

Physical properties of the nanoelectronic circuit can also be deduced by looking at the response in the transmission of a GHz-radiofrequency signal. The coupling of the circuit to this microwave field can be enhanced by integrating the latter in a high finesse cavity. As RF fields are carried on a 50Ω adapted circuit, the measurement of both in-phase (I) and out-of-phase (Q) quadratures gives information on the electronic circuit. Furthermore, the cavity allows to couple the circuit to a well defined mode of the electromagnetic field and consequently to design the coupling scheme, which will determine the actual measured physical quantities.

3.2.3.1 Set-up for measuring the I/Q quadratures of the field

In our case, the quadratures at the output of the cavity are measured on two lock-ins, by modulating the input RF field in the kHz range. This home-made homodyne-like detection is shown in figure 3.17 and follows the next steps :

- A RF signal from a highly phase-stable source is split into two parts. Its frequency is called the local oscillator frequency (LO).
- One part is kept as a reference and the second part is mixed with a kHz-signal coming from a lock-in, called the intermediate frequency (IF).
- The mixed signal at the frequency $\omega_{LO} \pm \omega_{IF}$ is transmitted through the cavity and then amplified at room temperature.
- It is then demodulated with the LO reference with the help of an I/Q mixer. The out-of-phase quadrature Q is simultaneously obtained by $-\pi/2$-rotating the reference. The amplitudes of the two demodulated signals, at the IF frequency, are read by the lock-ins, and give both I and Q quadrature values of the field.

[7] The measurement frequency f is also fixed to be a prime number to avoid picking up harmonics from lower frequencies, as the $50Hz$ frequency of the power supplies.

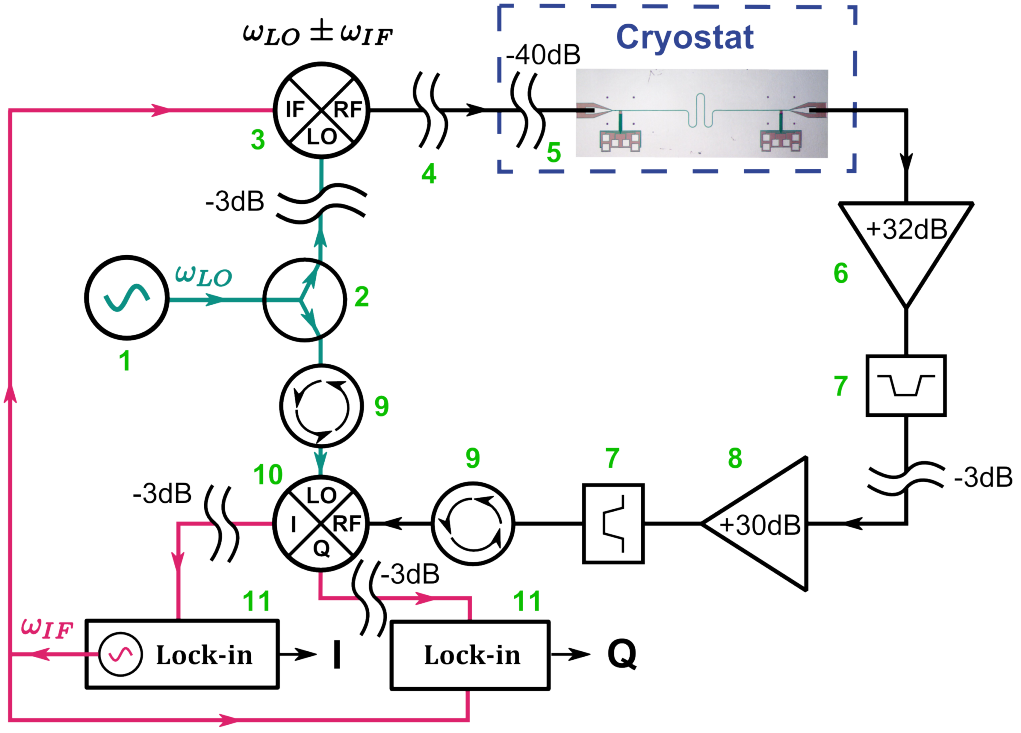

1	Agilent Source E8257D	5	XMA attenuators	9	Isolator Fairview Microwave SFI3512
2	6dB power splitter 5336 Picosecond Pulse Labs	6	Amplifier MITEQ (T_N=120K) AMF-4F-04001200-15-10P	10	IQ mixer Marki 0318L
3	Mixer MITEQ DB0218W2	7	High pass filter VHF-4600+ minicircuit 5-11GHz	11	Lock-in SR7265
4	Discrete attenuators	8	Amplifier MITEQ (T_N=530K) AFS3-00100800-45-10P-4		

FIGURE 3.17: **Microwave measurement set-up.** The two quadratures I and Q of the resonator transmitted signal are measured with a modulation/demodulation scheme. The reference signal at frequency ω_{LO} is in blue. The low-frequency signal at frequency ω_{IF} is in pink. The dashed blue line encloses the part of the set-up inside the cryostat. Attenuators (4,5), circulators[8](9) and amplifiers (6) are placed in the measurement chain.

3.2.3.2 Spectral transmission of a microwave cavity

I and Q give the modulus A_{out} and the phase φ_{out} of the transmitted signal[9] :

[8]Circulators that favor the propagation of the electromagnetic waves only in one direction are placed in the circuit. Indeed all microwave elements induce some reflections in the circuit that interfere with the signal. This is characterized by the return loss coefficient : $RL = -20\log(T)$, with T the reflection coefficient. As circulators acts as 50Ω resistors to the ground for the unfavored direction propagation, it is useful to have a circulator that is thermalized at cryogenic temperature. Nevertheless such circulators can not support high magnetic fields (typically of the order of $1T$) as they are made with ferrite dielectric acting on the microwave polarization. For these reasons, only isolators at $300K$ (that are 2-ports circulators) were used in this thesis.

[9]The minus sign is linked to the $-\pi/2$ rotation done by the I/Q mixer

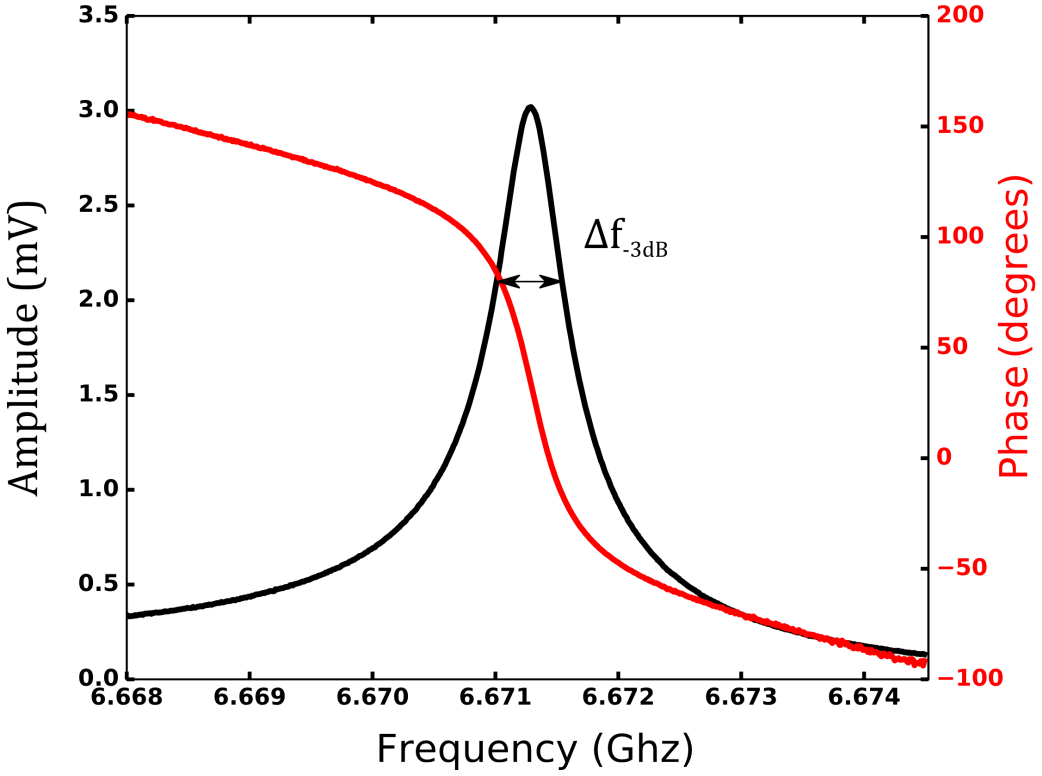

FIGURE 3.18: **Measured phase and amplitude of a microwave cavity.** A_{out} and φ_{out} has been measured with input power that corresponds to 800 000 photons inside the cavity and an arbitrary phase reference. The FWHM Δf_{-3dB} is $\sim 500kHz$, which gives a quality factor around 13 000.

$$A_{out} = \sqrt{I^2 + Q^2} \qquad \varphi_{out} = -\arctan\left(\frac{Q}{I}\right)$$

Hence, the measurement of I and Q gives the full cavity spectral transmission :

$$T(f) = \frac{A_{out}e^{i\varphi_{out}}}{A_{in}e^{i\varphi_{in}}} = |t|\frac{-i\Delta f_{-3dB}/2}{(f - f_c) + i\Delta f_{-3dB}/2}$$

The transmitted amplitude has a lorentzian shape centered at the resonance frequency $f_c = \omega_c/2\pi$, with a full width at half maximum FWHM Δf_{-3dB}, as shown in figure 3.18. $|t|$ is the transmission of the cavity at resonance. The phase experiences a π rotation around the resonance frequency and is linear with a slope $1/\Delta f_{-3dB}$ close to the resonance. Consequently, if we measure at a fixed frequency f and if the electronic circuit shifts the resonance by δf_c, the transmitted phase is then linearly shifted by $\delta\varphi \sim 2|t|Q\frac{\delta f_c}{f_c}$, with Q being the quality factor $Q = f_c/\Delta f_{-3dB}$. The transmitted phase is therefore a powerful tool to measure small frequency shifts of a high-Q cavity.

Nevertheless the RF signal at the output of a high finesse cavity is very weak and has to

be amplified by two consecutive $+30\,dB$ microwave amplifiers. These two amplifiers set the signal to noise ratio, S/N, as they are the only active elements in the circuit (aside from the sources). The noise added by the amplifier is characterized by a 'noise temperature' T_n[10]. This temperature corresponds to an effective temperature of a resistor placed at the amplifier input, which generates microwave noise. The amplitude standard deviation of this noise is $\sigma = \sqrt{4 \times Z \times k_b T_n \times \Delta f}$, where $Z = 50\Omega$ is the impedance of the line and Δf the measurement bandwidth. Therefore the amplifier with the lowest T_n should be placed first to have the lowest S/N deterioration of the RF measurement.

3.2.3.3 Number of photons in the cavity

The mean number of photons in the cavity $\bar{n}$ depends on the power at the input port of the cavity P_{input}^{dBm} and its transmission S_{cavity}.

$$\bar{n} = \frac{\sqrt{P_{input} P_{output}}}{h f_c \, \pi \Delta f_{-3dB}} = \frac{10^{\frac{P_{input}^{dBm}}{10} + \frac{S_{cavity}}{20} - 3}}{h f_c \, \pi \Delta f_{-3dB}} \tag{3.3}$$

The transmission of the cavity $S_{cavity} = 20\log(|t|)$ can be deduced by calibrating the transmission without a cavity of the microwave set up $S_{set\,up}$. This can be done by replacing the superconducting cavity by a superconducting stripe line. The $S_{set-up}(f)$ transmission is shown in figure 3.19 a.

$$S_{cavity} = P_{out}^{dBm} - P_{IF}^{dBm} - Att - S_{set\,up}$$

P_{IF} is the power in dBm fixed by the amplitude of the lock-in modulation and $P_{out} = 10\log\left(\frac{I^2+Q^2}{50\Omega \times 1mW}\right)$. Att corresponds to discrete attenuators that can be placed before the cavity input (see figure 3.17).

The input power of the cavity could not be measured directly at $250mK$ but has been deduced by measuring the transmission of all elements in the microwave circuit at room temperature, which are summed-up in the following table.

[10] It is defined as $\frac{S/N_{input}}{S/N_{output}} = 1 + \frac{T_n}{T_0}$, where T_0 is the temperature of the amplifier.

	Mixing procedure[11]	In-going RF line[12]	Out-going RF line (without the Nb/Ti line)[12]	Amplification line [13]
Transmission at 7 GHz	-11.5 dB	-49 dB	-5 dB	+60 dB

The sum of all these transmissions is $-5.5dB$, which is very close to the transmission of the whole circuit when the cryostat is cold, that can be estimated to be $-6dB$ at $7GHz$ in figure 3.19 **a**. Nevertheless the transmission measured at low temperature takes in addition into account the Nb/Ti cable on the outgoing line, the transmission of the printed circuit board (PCB) card where the sample is placed, and the transmission of Al bonding wires that connect the sample to the PCB. The transmission of the Nb/Ti is negligible as it is superconducting at $4K$. At this temperature, the transmission at $7GHz$ has been calibrated to be $-0.4dB$ for the PCB card and $-0.7dB$ for the Al-bonding wires that connect the sample to the PCB. Hence both elements contribute at most to $2dB$ to the total transmission measured at $250mK$ in figure 3.19 c.

By comparing the calibration done $250mK$ and the one done at room temperature, we can say that the calibration done at room temperature for the in-going line cable can be used at low temperature (with the PCB and the bonding wires) up to $\pm 1dB$. Hence the input power is :

$$P_{input} = P_{IF} - Att - 60 \pm 1dBm$$

The input power can be changed by adding some discrete attenuators Att, typically $-20dB$, or by changing the amplitude of the IF signal. It is indeed more suitable for the input mixer to work at fixed LO power and to vary the IF input power. The maximum input power is $P_{IF} = 10dBm$ as the mixer becomes then non linear and these non-linearities induce some unwanted higher harmonic conversion.

The power sent in the coplanar microwave cavity is nevertheless affected by parasitic 3D electromagnetic modes. The transmission of the setup without a cavity is indeed not decreasing linearly on a logarithmic scale with the frequency (see 3.19 a), as expected for a standard transmission line. This non monotonic behavior is due to some interferences with 3D modes of the sample holder box , that encloses the PCB card. This transmission drop, which can go up to $-4dB$, should be taken into account in the computation of the cavity transmission and the input power. Figure 3.19 b shows also that the transmission of the set-up with a cavity also presents some frequency ranges where the transmission

[11] Calibrated with a power meter
[12] Calibrated with a vector network analyser
[13] Calibrated with the modulation/demodulation set-up

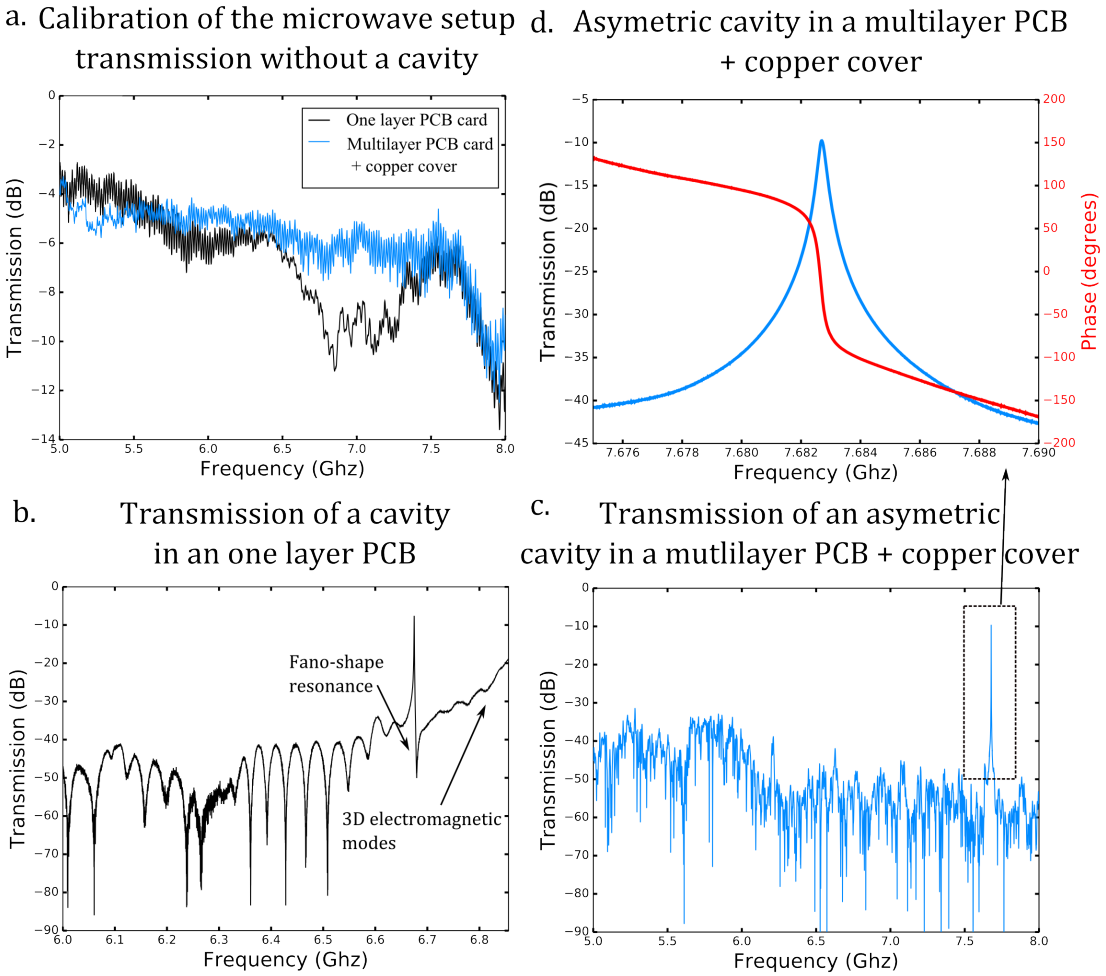

FIGURE 3.19: **Microwave transmission a.** Transmission of the microwave setup with a Nb stripe line instead of a cavity. The new PCB refers to the multilayer one with RF lines confined between two ground planes and a cooper cover about the cavity to shift 3D modes to higher frequencies. **b.** Transmission of a cavity measured in an old PCB. This is the same sample as in 3.18 measured at $P_{IF} = -1dBm$ and $-20dB$ of discrete attenuation. The transmission of the cavity has been deduced from the transmission of the setup calibrated in a. The quality factor for this scan was $Q \sim 29000$, higher than 3.18, probably due to the fact that it had not experienced any magnetic field yet, contrary to 3.18, for which some magnetic field vortexes had been trapped in the cavity. A transmission of $-10dB$ corresponds to $t \sim 0.3$ so to $Q_{ext} \sim 90000$ (see Chapter 2). **c.** Transmission of an asymmetric cavity measured in a new PCB card, with a cooper cover. The input (resp. output) capacitance of the cavity is two times smaller (resp. bigger) than in the symmetric case. As the quality factor $Q \sim 26000$ remains the same, the transmission is not changed in the asymmetric case. The new PCB card and the cooper cover lead to a lower ($\sim -15dB$) and flatter floor compared to b. **d.** Zoom of c. around the resonance for the transmission of an asymmetric cavity in a multilayer PCB card.

is enhanced by these 3D modes. These 3D modes even couple to the 2D-cavity modes and form a Fano-shaped resonance.

The coupling to some parasitic 3D modes was reduced by using a multilayer PCB card with RF lines confined between two ground planes, and by shifting the sample holder box modes to higher frequencies by reducing the space above the sample with a copper cover. Figure 3.19 shows that the transmission of the RF set-up is then much flatter, which gives at the same time a more precise estimation of the transmission of the RF line at $250mK$, which is used to determined the transmission of the cavity and the input power. The absence of 3D interfering modes is also visible in the cavity spectral transmission, which has a flatter and lower floor $\sim -40dB$ far from the resonance.

Chapter 4

Compressibility measurements of a Kondo quantum dot

This chapter presents compressibility measurements of a quantum dot using a microwave cavity. Depending on the gate voltage, the quantum dot is either in the Coulomb blockade or in the Kondo regime. This allows us to compare the compressibility between the two regimes : while the compressibility and the conductance are perfectly correlated in the Coulomb blockade regime, the electron gas in the dot is incompressible for the Kondo resonance. As presented in chapter 3, the quantum dot is a carbon nanotube stamped over a bottom gate, which is capacitively coupled to the central conductor of a coplanar microwave cavity.

The experimental results are described in the first section, which reproduces an article 'Observation of the frozen charge of a Kondo resonance' referenced with the doi : 10.1038/nature21704. The second section presents additional material that support the results shown in the first section, and discuss them in greater details.

4.1 Electrical conduction from a frozen charge

The ability to control electronic states at the nanoscale has contributed to our modern understanding of condensed matter. In particular, quantum dot circuits represent model systems for the study of strong electronic correlations, epitomized by the Kondo effect. Here, we show that circuit Quantum Electrodynamics architectures can be used to study the internal degrees of freedom of such a many-body phenomenon. We couple a quantum dot to a high finesse microwave cavity to measure with an unprecedented sensitivity the dot electronic compressibility i.e. the ability of the dot to accommodate charges. Because it corresponds solely to the charge response of the electronic system, this quantity is not equivalent to the conductance which involves in general other degrees of freedom such as spin. By performing dual conductance/compressibility measurements in the Kondo regime, we uncover directly the charge dynamics of this peculiar mechanism of electron transfer. Strikingly, the Kondo resonance, visible in transport measurements, is 'transparent' to microwave photons trapped in the high finesse cavity. This reveals that, in such a many body resonance, finite conduction is achieved from a charge frozen by Coulomb interaction. This previously elusive freezing of charge dynamics is in stark contrast with the physics of a free electron gas. Our setup highlights the power of circuit quantum electrodynamics architectures to study condensed matter problems. The tools of cavity quantum electrodynamics could be used in other types of mesoscopic circuits with many-body correlations and bring a promising platform to perform quantum simulation of fermion-boson problems.

In a free electron gas, electrical conduction is carried by mobile charges. Its compressibility $\chi = \frac{\partial N}{\partial \mu}$ with N the number of electrons and μ the chemical potential is simply

the density of states at the Fermi energy. It is therefore directly linked to the finite conductivity of the system. This explains for example why both the compressibility and the conductivity provide essentially the same piece of information for alkali metals. But what happens in the case of a strongly correlated electronic gas? A paroxysmal situation is that of an electron localized on a single site with strong Coulomb repulsion, coupled to a continuum of electronic states [3, 5, 96–98]. Through its link to the Kondo problem, such a configuration, besides its apparent simplicity, is relevant for understanding different types of strongly correlated gases, ranging from heavy fermions to high Tc superconductors [99]. A single localized level is expected to have a much smaller electronic compressibility than a piece of metal, since its density of states at the Fermi energy is dramatically reduced. How one could measure the tiny compressibility of a single localized state? Such a measurement requires first to isolate in a controlled manner a single electron, which can be conveniently done using a quantum dot (QD) circuit, but also to measure its tiny effective capacitance, which is equivalent to the compressibility of an electron gas. Although this can be done using low frequency as well as microwave techniques [70, 78, 100, 101], it has been shown recently that this could be achieved alternatively with an unprecedented sensitivity using a circuit Quantum Electrodynamics architecture [74]. The principle of such an architecture is shown in figure 4.1a: the finite compressibility χ shifts the frequency of the microwave resonator (as shown in figure 4.1b), used here as a non-invasive probe. This frequency shift, read-out from the phase of the microwave signal, is only sensitive to variations of the dot charge, in contrast with the conductance for which all degrees of freedom can contribute (charge and spin). The linewidth of the cavity and the electron-photon coupling strength set the limit to the smallest detectable χ

The experimental setup is shown in figure 4.1c. A single quantum dot circuit made out of a single wall carbon nanotube is embedded in a coplanar wave guide cavity [84]. The carbon nanotube is stamped above a bottom gate and contacted with $Pd(4nm)/Al(80nm)$. Gate electrodes are patterned in order to couple capacitively the bottom gate to a DC gate voltage V_g and to the AC potential of the central conductor of the cavity. We measure simultaneously the DC current flowing through the quantum dot and the phase and amplitude of the transmitted microwave signal at the cavity frequency ($f_{cav} = 6.67129GHz$). The base temperature of the experiment is $255mK$. The DC measurements are carried out using standard lock-in detection techniques with a modulation frequency of 77 Hz and an amplitude of $30\mu V$. The quality factor of the microwave cavity is between 10 000 and 20 000 depending on the run of our single shot ^3He cryostat. The average photon number in the cavity is about 30000, yielding a microwave modulation of about $40\mu V$ which ensures that we are in the linear regime. Such a setup

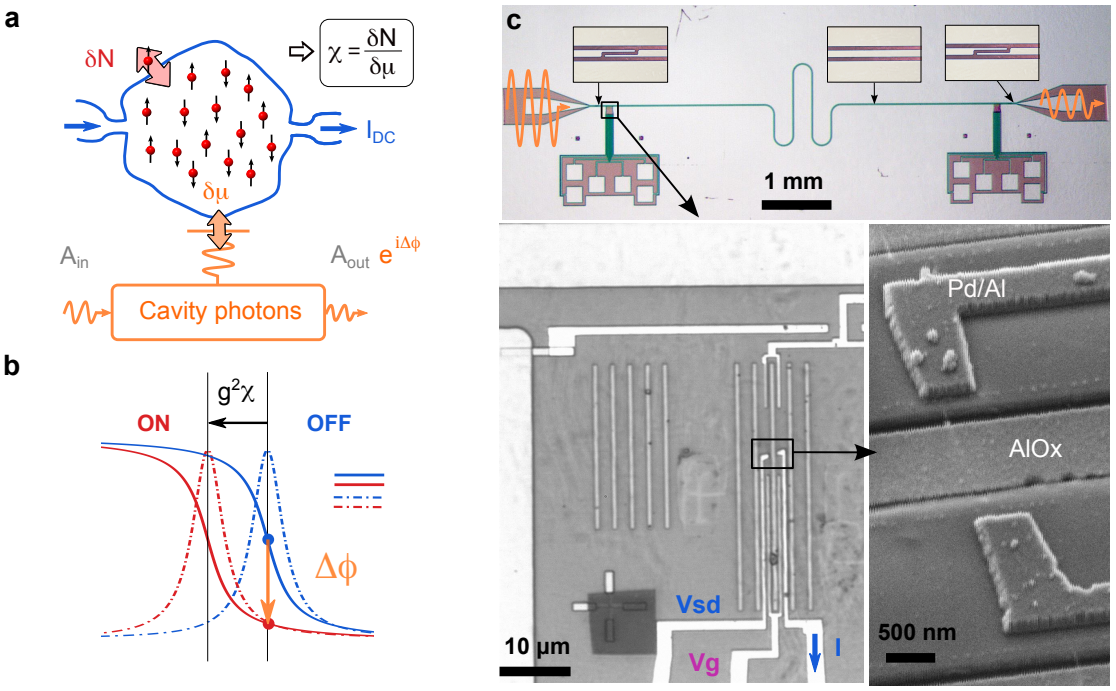

FIGURE 4.1: **Hybrid quantum dot-cavity QED setup. a.** V_s (resp. V_d) The compressibility of an electron gas is associated to the ratio $\frac{\partial N}{\partial \mu}$, with N the number of electrons and μ the chemical potential. **b.** The finite compressibility χ of the electron gas shifts the resonance frequency of a microwave cavity by $g^2\chi$ (ON state) from its bare resonance frequency $f_{cav,\,bare}$ (OFF state). The phase of the transmitted microwave signal at $f_{cav,\,bare}$ is thus shifted by $\Delta\phi$. The constant g is the electron-photon coupling and κ is the cavity linewidth. **c.** A carbon nanotube based quantum dot circuit is capacitively coupled to a coplanar waveguide microwave cavity. The chemical potential of the dot is controlled by the gate voltage V_g. The source-drain bias V_{sd} is applied between the two electrodes (in blue) which delimit the quantum dot.

allows us to characterize accurately the electron-photon interaction- which is essential for performing a compressibility measurement.

Carbon nanotube QDs can be tuned from the deep Coulomb blockade regime to the Kondo regime [30] simply by changing the voltage V_g applied to an electrostatic gate, as the one colored in green in figure 4.1c. For low gate voltages, we observe standard Coulomb diamonds in the $V_g - V_{sd}$ plane, where V_{sd} is the source(S)-drain(D) bias. Figure 4.2a and 4.2b display the characteristic periodic patterns of the conductance and the microwave phase in this regime. The conductance resonances delimiting the Coulomb diamonds appear simultaneously as peaks of about 3 ° in the phase signal. This indicates a finite compressibility of the QD electron gas for these resonances. In contrast, in a Coulomb valley, the charge dynamics in the dot is frozen, which leads to the absence of compressibility as shown in figure 4.2d. The finite compressibility and the peaks in the conductance are perfectly correlated (see figure 4.2c), which is reminiscent of a weakly correlated electron gas although interactions are present manifested by Coulomb blockade.

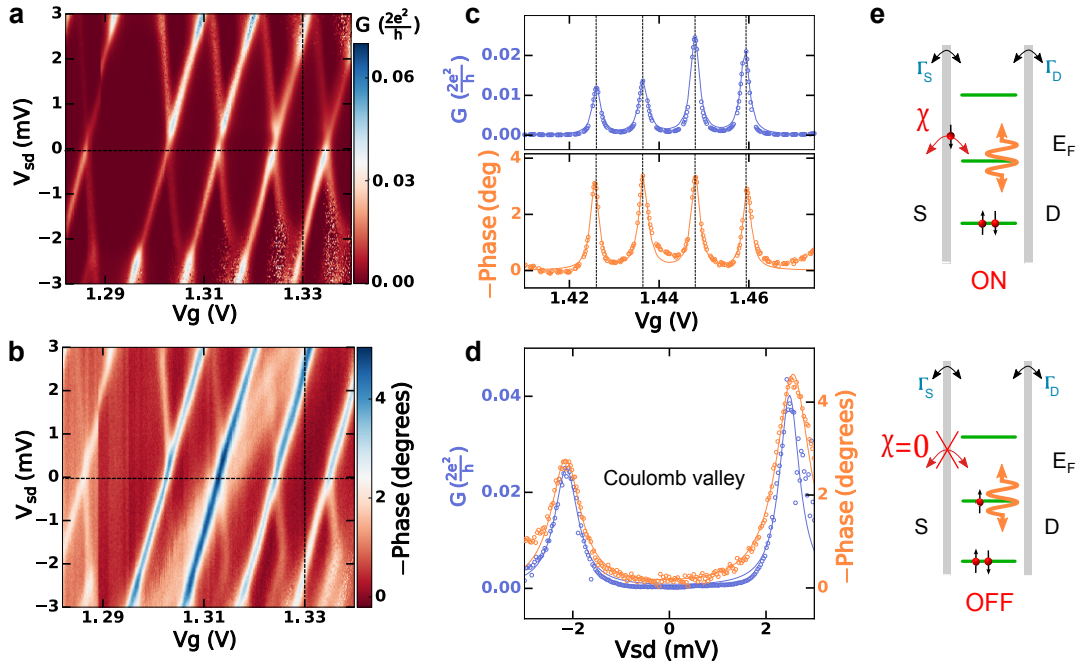

FIGURE 4.2: **Nature of the electron-photon coupling. a.** and **b.** Conductance G and phase maps in the $V_g - V_{sd}$ plane for low gate voltages. The opposite phase is represented in order to map directly the microwave signal onto the compressibility. **c.** Gate sweep for $V_{sd} \sim 0$ for the conductance (top panel) and for the phase (bottom panel). The points are experimental data and the solid lines correspond to lorentzian fits. **d.** Bias sweep at $V_g = 1.33V$. **(E)** Coupling mechanism: the cavity photons modulate adiabatically the chemical potential of the quantum dot. The dot has tunneling rates Γ_S and Γ_D to the source S and the drain D, respectively. A finite dot density of states at the Fermi level E_F turns on electronic transfers between the quantum dot and the leads. This dipole induces a shift in the resonance frequency of the cavity (top panel), which leads to the phase shift seen in B, C and D.

The nature and the strength of the electron-photon coupling in our device is calibrated using a well-known situation, the Coulomb blockade in the linear regime (bias $eV_{sd} < k_BT$, figure 4.2c). In that case, electron transport only occurs when the electron gas in the QD has a finite density of states at the Fermi energy, which also corresponds to a finite compressibility [75, 102, 103]. Because the finite compressibility is linked to back and forth tunneling of electrons between the QD and the leads, it creates a dipole which couples to the cavity (see figure 4.2e, top panel). The compressibility can therefore be read out through a shift of the resonance frequency of the cavity. This yields the corresponding phase shift $\Delta\phi = 2g^2\chi/\kappa$ for the transmitted microwave signal, where κ and g correspond respectively to the linewidth of the cavity and the electron-photon coupling strength. The compressibility of the quantum dot depends on the line width of a Coulomb peak. At low temperatures, in the simplest case, it reads: $\chi = \frac{\partial N}{\partial \epsilon_d} = -\frac{2}{\pi}\frac{\Gamma}{\Gamma^2+4\epsilon_d^2}$, where Γ and ϵ_d are respectively the linewidth of the Coulomb peak and the position of the dot energy level. The parameter $\kappa = 2\pi \times 0.5MHz$, yielding a quality factor $Q = f_{cav}/\kappa = 13000$, can be measured directly from the transmission spectrum of

the cavity (Figure 4.1b). The dot's parameter $\Gamma = \Gamma_S + \Gamma_D$, with $\Gamma_S = 0.7meV$ and $\Gamma_D = 4\mu eV$ can be determined from the conductance measurements (which also allow us to extract the charging energy $E_C = 3.5meV$). As a consequence, the joint conductance / phase measurements presented in figure 4.2c allow us to directly determine the electron-photon coupling constant g on each Coulomb peak. We find for all the Coulomb peaks studied $g \sim 2\pi \times (65MHz \pm 15MHz)$ [13]. This large coupling strength is consistent with our circuit design, shown in figure 4.1c, where a bottom gate (in green) very close to the single wall carbon nanotube combines the AC voltage of the central conductor of the cavity and the DC gate voltage. The negative sign observed for the phase contrast shows directly that the dot reduces the frequency of the resonator. Therefore, the effective admittance of the QD circuit is that of an effective capacitance in parallel with the capacitance of resonator. This stems from the fact that cavity photons are coupled to the gate (and therefore ϵ_d), but not to the source-drain contacts. This feature of our setup is crucial to ensure that we measure only the compressibility of the electron system in the quantum dot, which was not the case in a previous experiment in the Kondo regime [13]. In that case, the compressibility $\frac{\partial N}{\partial \epsilon_d}$ can also be viewed as the zero-frequency charge susceptibility, which stems from the retarded correlator $\chi(t) = -i\theta(t)\langle[\hat{n}(t), \hat{n}(0)]\rangle$, where $\hat{n}(t)$ is the electron number operator of the dot and $\theta(t)$ is a step function. As a conclusion, in the Coulomb blockade regime, both finite conductance and compressibility only arise from the ability of the mobile charges to tunnel in or out of the dot. Importantly, our cQED architecture resolves well a very small compressibility, of the order of $1000(eV)^{-1}$, corresponding to $160aF$, with about $1aF$ resolution. This is about 7 orders of magnitude smaller than the compressibility of a piece of metal of $(1\mu m)^3$. Remarkably, our sensitivity corresponds to a charge of about $2.5 \times 10^{-4}e$, which is about an order of magnitude lower than the charge sensitivity of an RF-SET setup [81] and 3 orders of magnitude lower than low frequency techniques [78, 100].

The physics becomes strikingly different in the Kondo regime. For that purpose, we tune the gate of the device to $V_g \sim 2.5V$, where $\Gamma \sim 1meV$, and $E_C \sim 2.25meV$. As shown in figure 4.3a, the conductance colour-scale plot displays softer Coulomb diamonds with horizontal Kondo ridges close to zero bias. The observation of several adjacent Kondo ridges is consistent with previous observations in carbon nanotubes [30]. It arises from the existence of additional degeneracies besides the spin in the spectrum of the nanotube. From the width of the zero bias peaks, we can estimate a Kondo temperature of about $5K$. The main result of this paper is presented in figure 4.3b. Whereas there is a finite zero bias peak in the conductance (and therefore in the density of states of the dot), the simultaneously measured phase contrast shows that this density of states does not contribute to the compressibility. Importantly, the high energy charge peaks at about

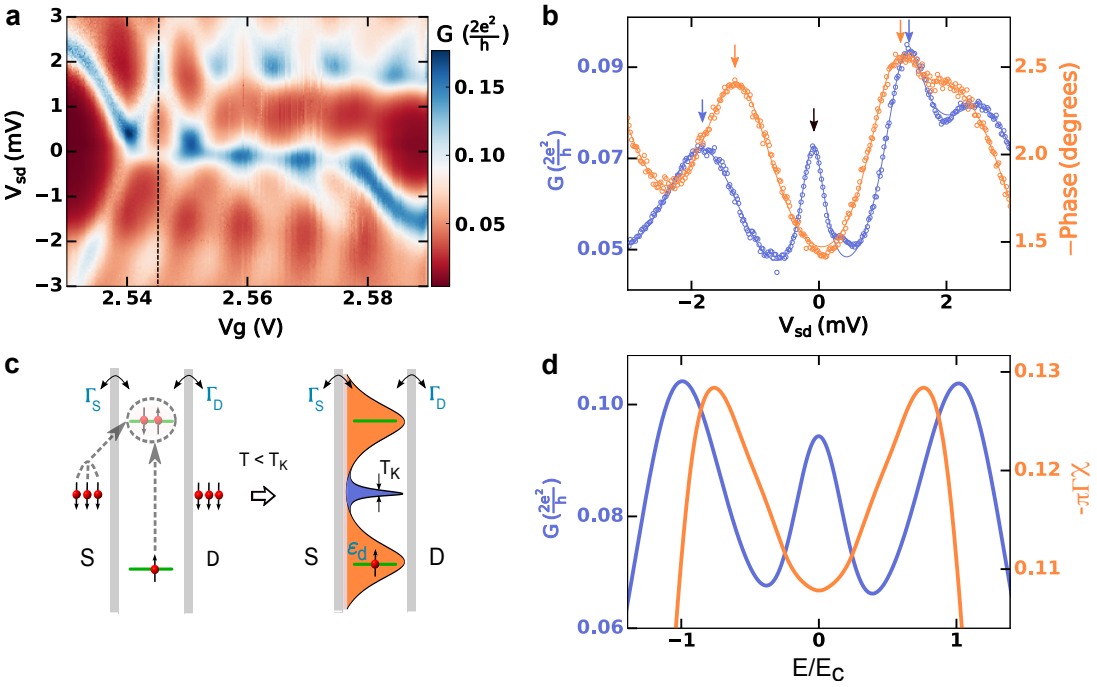

FIGURE 4.3: **Transparent Kondo resonance. a.** Conductance map in the Kondo regime. **b.** Simultaneous bias dependence of the conductance and the phase in the middle of a Kondo ridge along the black dashed line. The blue (orange) arrows mark the charge peaks in the conductance (compressibility). The black arrow marks the Kondo resonance. **c.** A quantum dot level away from the Fermi energy leads to a Kondo resonance through a sum of virtual processes (dashed line). **d.** Numerical renormalization group (NRG) data corresponding to the situation of panel B. The excitation energy E is scaled by the charging energy and the compressibility by $\pi\Gamma$. Both the absence of Kondo peak in the compressibility as well as the shift of the high energy charge peaks between compressibility and conductance are reproduced. The corresponding parameters are $\Gamma = 0.4E_C$ (as extracted from the data) and $T = 10T_K$.

$\pm 2mV$ remain both in the phase and in the conductance, although they do not fully coincide. These experimental result are well reproduced by NRG calculations of the χ and the dot density of states $\nu(E)$. The latter can be directly mapped onto the conductance $G(eV_{sd})$, plotted in figure 4.3d, by making the identification $E = eV_{sd}$, thanks to the small height of the Kondo peak ($\sim 0.12\, 2e^2/h$) which ensures that the dot is much more tunnel coupled to one of the two reservoirs. The low bias data directly show that a finite (DC) current flows through the device, although the charge in the QD is frozen [73, 104]. One can explain this feature within the Kondo model, as illustrated in figure 4.3c. When a QD degenerate level is singly occupied by a frozen charge, an antiferromagnetic coupling appears between the single electron and the conduction electrons at the Fermi energy. The emergent many body state does not contribute to the compressibility, because it arises from virtual tunneling processes. Therefore, our measurements strongly suggest that the Kondo resonance in the conductance, also called Abrikosov-Suhl-Nagaoka resonance, is associated to the fluctuations of the spin degree of freedom whereas the charge fluctuations in the dot are frozen. Interestingly, the NRG

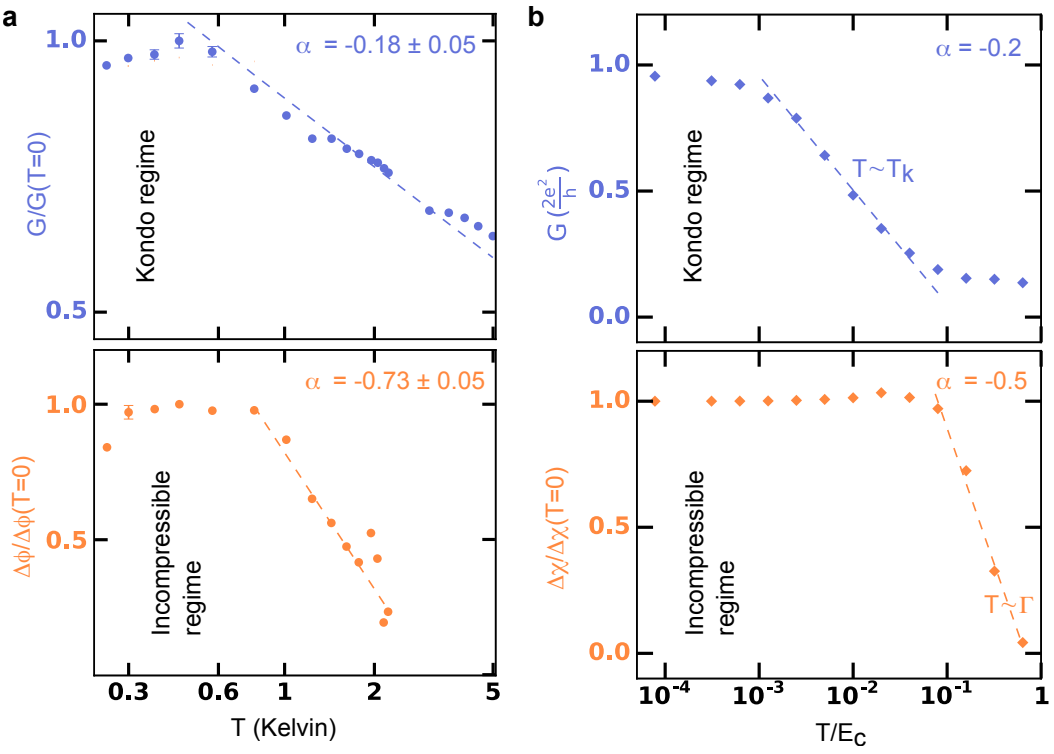

FIGURE 4.4: **Temperature dependence of conductance and compressibility. a.** Temperature dependence of the conductance and the phase on the Kondo ridge at ($V_g \sim 2.567V$,$V_{sd} \sim -0.15mV$). In order to compensate thermal drifts, the phase shift signal ΔPhase on the Kondo ridge is measured with respect to the right adjacent Coulomb peak at a given temperature. The error bars are about the size of these experimental points. The dashed lines show linear fit in log scale that corresponds to a logarithmic law $-\alpha \log(T)$. **b.** NRG data as a function of temperature, for $\Gamma = 0.4E_C$ (as extracted from the data).

data is also able to reproduce the shift between the conductance and compressibility charge peaks around $\pm 2mV$. We speculate that this might be a correlation effect related to an interaction-driven renormalization of the system parameters.

The temperature dependence of the cavity and transport signals further confirms that the conductance and the compressibility obey different physical principles governed by different energy scales. When the temperature increases, the many-body Kondo resonance decreases logarithmically on a temperature scale set by T_K, as shown in figure 4.4a. The residual compressibility χ_v in the valley evolves on a different temperature scale than the many-body Kondo resonance, as it is simply due to single electron tunneling and set by Γ ($\chi_v \sim -0.13/(\pi\Gamma)$ at $T = 0$ from the NRG data). A linear fit to the data plot in log-linear scale in the high temperature range gives a logarithmic law of about $-0.18 \log(T/T_K)$ for the conductance and of about $-0.73 \log(T/\Gamma)$ for the compressibility. In figure 4.4b, we show the corresponding plots obtained by NRG. We find that they are in good agreement with the experimental data. In particular, the NRG data in figure 4.4b indicate that the temperature dependence for the conductance

is governed by T_K whereas for the compressibility it is governed by Γ. Remarkably, the slopes of the logarithmic regime are -0.2 for the conductance and -0.5 for the compressibility, in rather good agreement with our experimental findings. It is important to note however that extracting accurately the value of Γ from our experimental data is not straightforward here because the apparent spectral (dI/dV) width of the charge resonance has been observed to depend on interaction [105]. This is also seen in the NRG data in figure 4.3d. This can explain why the temperature scale for the down-turns for the conductance and the compressibility are less separated in our experimental data than in the NRG data. Nevertheless, both the distinct slopes and the separate down-turns show that the conductance and the compressibility are affected by temperature with different mechanisms. This directly stems from the decoupling of the charge and spin degrees of freedom in a Kondo cloud.

In conclusion, we have directly observed the freezing of charge dynamics which is a crucial feature of a Kondo resonance. Our dual conductance/compressibility measurements illustrate the fundamental difference between a Kondo resonance and a simple resonant level where many body effects are absent.

Our setup can be generalized to many types of mesoscopic circuits [69, 106**?**] and could be transposed in the optical domain to probe the compressibility of other types of conductors. It could be used to study in a controlled manner some important fermion-boson problems. Electron-phonon interactions in solids could be simulated by using the analogy between phonons and the photons in our cavity. Furthermore, the cavity photons are slow here with respect to the electrons of the dot ($hf_{cav} \ll E_C, \Gamma, T_K$), a situation that has allowed us to probe non-invasively the low frequency charge dynamics of the QD, relevant to understand the DC properties of our system. We expect to access dynamical aspects of tunneling [14, 74] and Kondo physics if one of these inequalities is not fulfilled. Among the perspectives offered by our findings, one could also imagine to inject suddenly a coherent field in the cavity to perform a quantum quench of the system which could give interesting insights into the dynamics of the Kondo cloud.

4.2 Further discussion on the experimental results

This section starts with the presentation in section 4.2.1 of additional data from the same sample, that support the observations presented above. We then discuss in section 4.2.2 the coherence of the data with a coupling of the cavity field to the dot chemical potential, using the formalism presented in chapter 2. The section 4.2.3 shows the complete gate and bias voltage scans corresponding to the temperature dependence data, which was

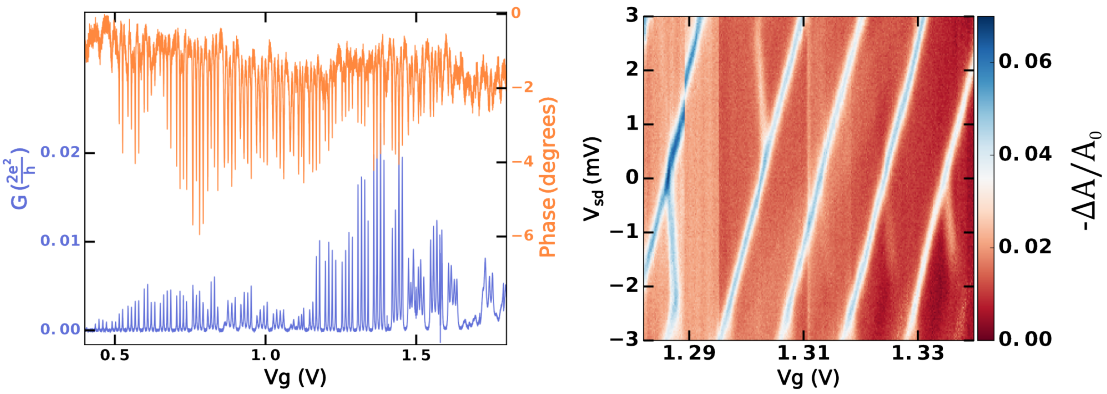

FIGURE 4.5: **Coulomb blockade regime.** Left panel : Phase and conductance on wide scale in Coulomb blockade regime. The observation of groups of four peaks both in the conductance and in the phase contrast arises from the spin/valley degeneracy of the nanotube spectrum. Right panel : Relative amplitude shifts for the Coulomb diamonds presented in figure 4.2 of the section 4.1.

summarized in figure 4.4. The last section describes the model used for the numerical calculation of the conductance and compressibility in the Kondo regime.

4.2.1 Conductance, phase and amplitude

4.2.1.1 Coulomb blockade regime

We show in figure 4.5 the phase contrast and the conductance as a function of the gate voltage at zero bias in the Coulomb blockade regime on a wide gate voltage range. The conductance (in blue lines) displays regularly spaced Coulomb peaks with the expected fourfold periodic shell filling of weakly disordered single wall carbon nanotubes. The corresponding phase of the transmitted microwave signal exhibits a pattern which is very well correlated to the conductance. The phase contrast ranges from 1° to 5° probably due to modifications of the dot electronic wavefunctions due to weak disorder. Nevertheless, the extracted value for the coupling strength remains of about $2\pi \times 50 - 100MHz$.

The relative amplitude shift corresponding to the phase shift and the conductance of figure 4.1 is displayed on the right panel of figure 4.5. The color plot V_g-V_{sd} map has the same resonances as the phase map. The amplitude is nevertheless less sensitive to smooth background variations observed in the phase (see for example around the second Coulomb peak in figure 4.1). This is because the resonance frequency corresponds to a minimum for the amplitude so the amplitude is only sensitive to the second order of the frequency shifts, while the phase is sensitive to the first order.

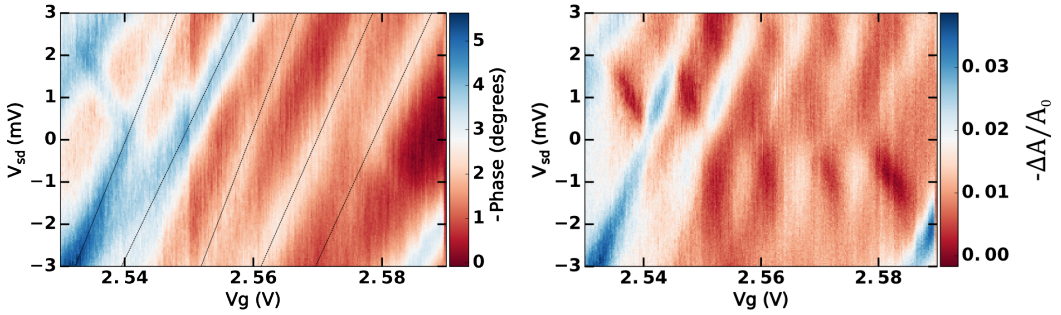

FIGURE 4.6: **Phase and amplitude in the Kondo regime.** Left panel : Colorscale plot of phase in the Kondo regime corresponding to figure 4.3a. We observe tilted lines arising from single charge peaks but no Kondo ridge. The dashed lines are guide for the eyes. A spurious titled red line is also observed. It likely arises from an impurity level coupled to the cavity field. Dotted lines are guide for the eyes. Right panel : Colorscale plot of the relative amplitude corresponding to the phase shift in the left panel. The conductance ridges of figure 4.3a are not visible in the microwave amplitude signal.

4.2.1.2 Colorscale plot in the Kondo regime

We show in the left panel of figure 4.6 the phase colorscale plot measured simultaneously with the conductance colorscale plot shown in figure 4.3a of section 4.1. Similarly to the Coulomb blockade regime (figure 4.2b), the phase contrast is bigger for the left tilted edges of the Coulomb diamonds. The latter are blurred as expected since the Kondo regime corresponds to a gate region with larger $\Gamma's$. There are some phase resonances which are not correlated to the Coulomb diamond edges like in the area around ($V_{sd} = -2mV$, $V_g = 2.54V$). We attribute this effect to spurious impurity levels which are coupled to the cavity. Importantly, the Kondo ridges which are clearly visible in the colormap of the conductance are completely absent from the phase map. The ridges are also absent from the amplitude shifts, shown in the right panel of figure 4.6.

A conductance and the compressibility of a second Kondo resonance corresponding to the third ridge of figure 4.3 is shown with respect to the bias voltage, in figure 4.11. The same features as in figure 4.3 are observed. While a peak is visible in the conductance, signaling the Kondo resonance, it is absent from the compressibility. The charge peaks are still visible in both measurements, around $\pm 2mV$. As for the example shown in section 4.1, they are not fully correlated. Figure 4.11 illustrates the robustness of our findings for another Kondo ridge.

In figure 4.7, we show the conductance and phase V_g-V_{sd} map for a larger scan in the Kondo regime. There is a periodic appearance and disappearance of the Kondo ridges, although the periodicity evolves from five to four ridges when increasing the gate voltage. The fourfold degeneracy of the quantum dot level observed in the Coulomb blockade

regime should lead to either a two-fold (SU(2) Kondo effect) or a four-fold periodicity (SU(4) Kondo effect). As the charging energy is the same, the extra ridge comes from the same dot. The interplay of another sub-band could for example add an orbital in the dot as well as in the electrode, in order to get another degenerate channel for the Kondo effect.

On a large scale, we can see that all the Kondo ridges are tilted. In figure 4.3, the slope of the tilt, $\Delta V_{sd} = -\beta \Delta V_g$, is $\beta \sim 1/20$. This asymmetry is already present within a four-fold set of Coulomb blockade peaks. In figure 4.1, and figure 1.6 of the first chapter which corresponds to a lower gate voltage region, one can see that the conductance is slightly enhanced above zero bias for the two left-most peaks and below zero bias for the right-most peaks.

The phase measured for this large scan shown in figure 4.7 displays the tilted lines corresponding to the left edges of Coulomb diamonds. The absence of Kondo resonances in the phase is confirmed for several Kondo ridges.

4.2.2 On the cavity-quantum dot coupling

4.2.2.1 Coupling to the dot chemical potential

The response of the quantum dot to the cavity photons is adiabatic, as $\Gamma \sim 40 \times h f_{cav}$. In that case, the linear response of the quantum dot to the cavity has been derived in chapter 2 considering the most general situation with both couplings to the dot and to the electrodes. The cavity frequency and bandwidth shifts are :

$$\begin{aligned}\Delta f_{cav} - i\Delta\kappa/2 = \sum_{i,j=qd,-} g_i g_j \chi_{i,j}(\omega_d) =& g_{qd}^2 \hbar \frac{\partial \langle \hat{n}_{qd} \rangle}{\partial \epsilon_d} + g_{qd} g_- \hbar \frac{\partial \langle \hat{n}_{qd} \rangle}{\partial \epsilon_a} \\ & - i \left(g_-^2 \frac{4\hbar}{e^2 \omega_d} \frac{\partial I}{\partial V_{ac}} + g_- g_{qd} \frac{2\hbar}{e\omega_d} \frac{\partial I}{\partial \epsilon_d} \right)\end{aligned} \tag{4.1}$$

The coupling constant g_{qd} corresponds to a modulation of the dot chemical potential and g_- to an anti-symmetric modulation of the source and the drain chemical potential. The transmitted phase is proportional to the real part of equation (4.1), while the relative amplitude is proportional to its imaginary part (see equation (2.44) in chapter 2). At zero bias, the last term $\frac{\partial I}{\partial \epsilon_d}$ is always zero, whichever the quantum dot behavior is, so the transmitted amplitude is proportional to $\frac{\partial I}{\partial V_{ac}} \sim G$, where G is the DC conductance. The Kondo peak is absent from the amplitude data to the experimental uncertainty of 0.001: this implies that $g_- < 2\pi \times 5.0 MHz$ for example for the peak shown in figure 4.11. This is more than an order of magnitude smaller than the coupling constant g deduced from the phase shift in the Coulomb blockade using $g^2 = \pi/4\Delta\phi \times \Gamma \times \kappa$. In

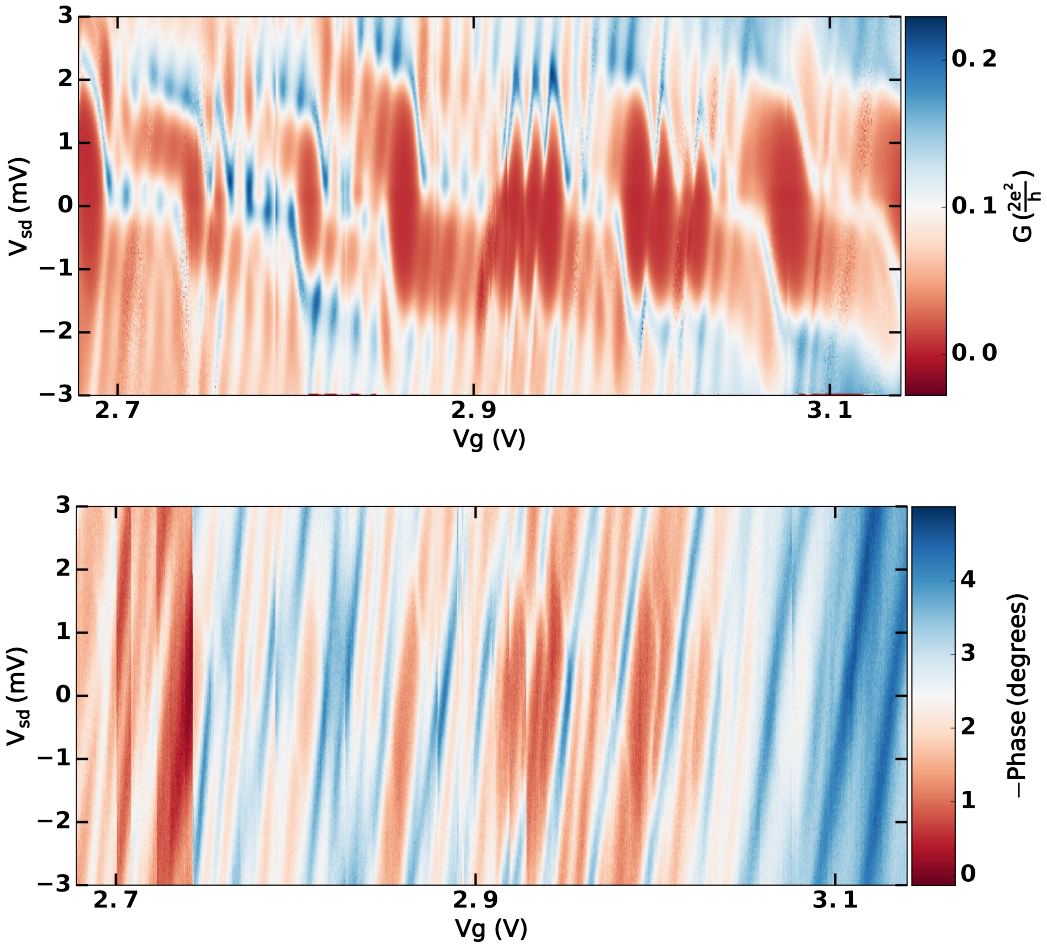

FIGURE 4.7: **Kondo regime on wide scale.** Conductance and phase as a function of source-drain bias and gate voltage on a wide scale in the Kondo regime. The gate voltages have shifted by $+0.15V$ with respect to those in figure **??**. The Kondo ridges shown in section 4.1 would correspond to the first ones seen in the upper panel.

chapter 2 (equation (2.42)), we have established[1] that at zero bias, and for $\Gamma_D \ll \Gamma_S$, $g^2 = g_{qd}\,(g_{qd} - g_-)$. The inequality $g_- \ll g$ implies $g_- \ll g_{qd}$ and therefore one can states that the electron-photon coupling corresponds to a modulation of the dot chemical potential.

As explain in chapter 2, the capacitive coupling constant is proportional to the lever arm α : $g = e\alpha V_{rms} (e > 0)$, where α is the ratio of the dot chemical potential oscillations over the potential oscillations of the central conductor. V_{rms} is the root mean square voltage associated to a single photon. In our experiment, the nanotube is very close to the bottom gate, which is capacitively coupled to the AC central conductor and the DC gate. From the conductance map, we can infer the DC lever arm to about 0.3. From our gate layout (see figure 4.1c), we can estimate that the AC capacitance

[1]The derivation assumes that there are no interactions in the dot. Nevertheless, we consider here that in Coulomb blockade interactions only lead to a renormalization of the coupling constants.

is about 3 times smaller than the DC capacitance. This leads to $\alpha \sim 0.1$, so that $g \sim 2\pi \times 50MHz$, using $V_{rms} \sim 2\mu V$. This order of magnitude is in good agreement with our experimentally determined coupling strength of about $2\pi \times 50 - 100MHz$. This indicates that the microwave couples directly to the bottom gate and therefore to the dot chemical potential.

In the Coulomb blockade $V_g - V_{sd}$ map, there are two slopes corresponding to the onset of the electrons exchange either between the source and the dot or between the drain and the dot (see the explanatory figure 1.5 in chapter 1). In the phase response map (see 4.2b), the lines corresponding to the drain and the dot being at the same chemical potential is $5-10$ times smaller than the ones corresponding to a source-dot alignement. Because $g_- \ll g_{qd}$, this cannot come from a difference in the coupling mechanism. This is in fact related to the asymmetry $\Gamma_D \ll \Gamma_S$, observed in the conductance. From the conductance measurement, we can infer that $\Gamma_D \sim 4hf_{cav}$. For a single contact, when Γ approaches hf_{cav}, the real part of the susceptibility tends to zero because the tunnel barrier goes from a capacitive behavior $\Gamma \gg hf_{cav}$ to an inductive one $\Gamma \ll hf_{cav}$ [46].

4.2.2.2 Photon number dependence of the differential conductance in the Coulomb blockade regime

In this section, we show that one can estimate the electron-photon coupling strength with a complementary method than that used in section 4.1, from the microwave power dependence of the conductance. For a coupling to the gate, and in the adiabatic case $f_{cav} \ll \Gamma$, the conductance is modulated by the cavity photons as :

$$G(t) = G\left(\epsilon_d + 2g\sqrt{\bar{n}}\cos\left(2\pi f_{cav}t\right)\right) \tag{4.2}$$

The conductance is a lorentzian with a width Γ , hence, at $\epsilon_d = 0$, a DC measurement gives

$$G = \int_0^{2\pi} \frac{\mathrm{d}\theta}{2\pi} G\left(2g\sqrt{\bar{n}}\cos\left(\theta\right)\right) = \frac{1}{\sqrt{1+16\bar{n}(g/\Gamma)^2}} \tag{4.3}$$

As explained in chapter 2, the mean number of photons depends on the cavity input power and its transmission :

$$\bar{n} = \frac{10^{\frac{P_{IF}+S_{att}}{10}+\frac{S_{cav}}{20}-3}}{\pi h f_{cav}\kappa} \tag{4.4}$$

The power P_{IF} is in dBm corresponding to the root mean square amplitude V_{IF} of the low-frequency microwave modulation. S_{att} is the attenuation of RF lines to the

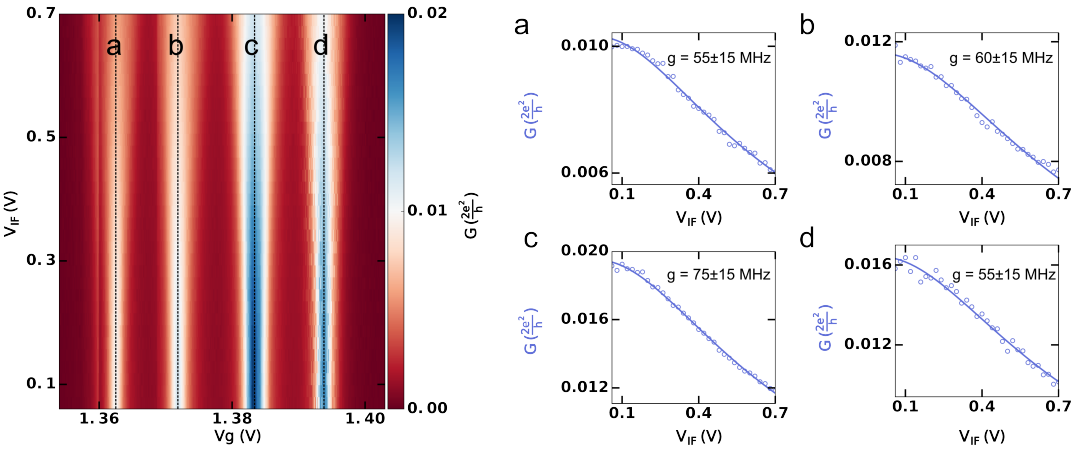

FIGURE 4.8: **Control experiment for calibration of electron-photon coupling.** Power dependence of Coulomb peaks for 4 different peaks (A,B,C and D). Each peak height is plotted on the right panels versus the microwave modulation amplitude which controls the number of photons inside the cavity. The open dots are data and the solid lines are fits using formula (4.3).

cavity, calibrated to $-82 \pm 1dB$ (see section 3.2.3.3 in the third chapter). Here, the transmission of the cavity S_{cav} is $-16dB$. This allows to calibrate the coupling constant $g \sim 2\pi \times 60MHz$, as shown in the right panels of figure 4.8. This is in good agreement with the one deduced from the height of the Coulomb peaks using the formula :

$$g^2 = \frac{\pi}{4}\Delta\phi\Gamma\kappa \tag{4.5}$$

In this estimate of g, we use for the compressibility a simple non-interacting model with no degeneracy ($S = 1$) :

$$\frac{\partial N}{\partial \epsilon_d} = -\frac{2S}{\pi}\frac{\Gamma}{\Gamma^2 + 4\epsilon_d^2} \tag{4.6}$$

The use of $S = 1$ is yet questionable as we observe in the Coulomb blockade a clear four-fold degeneracy. We use here a simple non-interacting model where interactions only lift the dot degeneracy [74]. Nevertheless an accurate quantitative analysis of the compressibility is beyond the scope of our experimental results, as interactions renormalize both the compressibility and the coupling constant g. The determination of g from the power dependence shown in this section relies furthermore on the calibration of the RF lines attenuation, which only gives an accuracy of the number of photons within a factor 2.

4.2.2.3 Figure of merit of our compressibility measurements

We describe in greater details than in the section 4.1 the figure of merit of our compressibility measurement setup. Two main features are important for defining the figure of merit: first, the effective capacitance resolution δC which can be achieved and second, the maximum excitation voltage which is used for that measurement δV. The latter is crucial for keeping the linearity of our detection scheme. These two parameters enter into the charge resolution of the setup: $\delta N = \delta C \times \delta V/e$. In our case, since we estimate $\delta C \sim 1aF$ from our phase noise of about 0.01 degree and we estimate $\delta V \sim 40\mu V$ from the average number of photons in our cavity, this leads to $\delta N \sim 2.5 \times 10^{-4}e$. As a comparison, the minimum δC in ref [100] is $1aF$ but with a δV of about 20 mV.

4.2.2.4 Alternative scenario for the Kondo ridge

In the Kondo regime, we have seen that the conductance peak at zero bias is absent from the cavity signal. Could this conductance peak be attributed to another level, pinned at zero bias, with a chemical potential ϵ'_d which is not coupled to the cavity ?

From the bias dependence, this level would have a width $\Gamma' = T_k$. Its conductance appears and disappears at some gate voltage V_g. The conductance is a quantity that depends only on the chemical potential and Γ. As we look at the scenario where the chemical potential ϵ'_d is not coupled to the cavity, the gate should have also no influence on it, so $\frac{\partial \epsilon'_d}{\partial V_g} \simeq 0$. Therefore, this level should have at least one of its Γ', for example Γ'_d, that depends on the gate : $\frac{\partial \Gamma'_d}{\partial V_g} \neq 0$.

The conductance is a lorentzian with respect to the bias voltage eV_{sd}, so the charge number N' for this level is :

$$N' = \frac{1}{2} - \frac{1}{\pi} \arctan\left(\frac{2eV_{sd}}{\Gamma'_s + \Gamma'_d}\right) \tag{4.7}$$

Its derivative with respect to the gate is then :

$$\frac{\partial N'}{\partial V_g} = \frac{1}{\pi} \frac{\Gamma'}{\Gamma'^2 + 4(eV_{sd})^2} \frac{2eV_{sd}}{\Gamma} \frac{\partial \Gamma'_d}{\partial V_g} \tag{4.8}$$

In the case of a coupling to the dot chemical potential, $\frac{\partial N}{\partial V_g} = \frac{\partial \epsilon_d}{\partial V_g} \frac{\partial N}{\partial \epsilon_d} = \alpha\chi$, where χ is the compressibility and α the lever arm. By analogy[2], $\frac{\partial \Gamma'_d}{\partial V_g}$ corresponds here to a lever

[2] A more formal derivation of the frequency shift induced by the modulation of Γ'_d should be done in the framework presented in chapter 2. The coupling constant would then correspond to γ introduced in section 2.2.1, which is the coupling term corresponding to a modulation of the tunnel coupling t'_d between the dot and the drain. One should then look for the linear response of $\hat{c}'_{dot}$ and not $N' = \hat{c}'^{\dagger}_{dot}\hat{c}'_{dot}$.

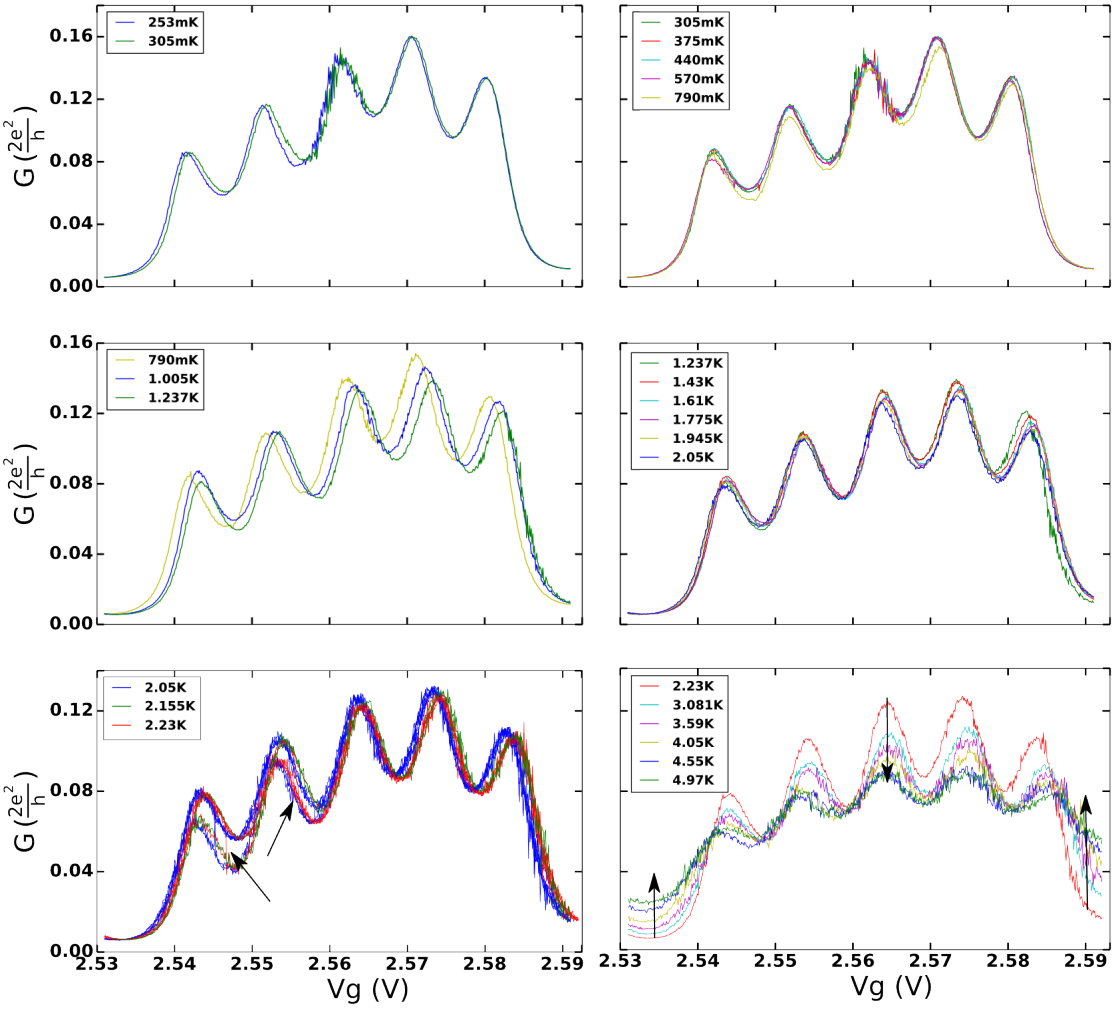

FIGURE 4.9: **Conductance at zero bias with increasing temperature.** For each temperature the data shown is an average of ten consecutive gate sweeps. For $T = 2.05K$ and $T = 2.155K$ (bottom-left panel), the conductance fluctuates between two curves and therefore the average has been done only between similar data. Black arrows show the fluctuations. On the middle-left panel, the conductance shifts between $T = 790mK$ and $T = 1.237K$, which may result from gate jumps. On the bottom-right panel, the increase of the temperature after $T = 2.23K$ reduces significantly the contrast of the conductance, as highlighted by black arrows.

arm α' that enters in the coupling parameter g', describing the response of the level to a modulation of Γ'_d. From the conductance data (see for example 4.9), one can estimate that this lever arm is 0.75 smaller than the lever arm α of the level that give the Coulomb peaks in the Coulomb blockade regime. Therefore the phase should be shifted at the end of each Kondo ridge by the same amount as for the Coulomb peaks. Our setup can therefore exclude such a situation without the need for extra knowledge on the system.

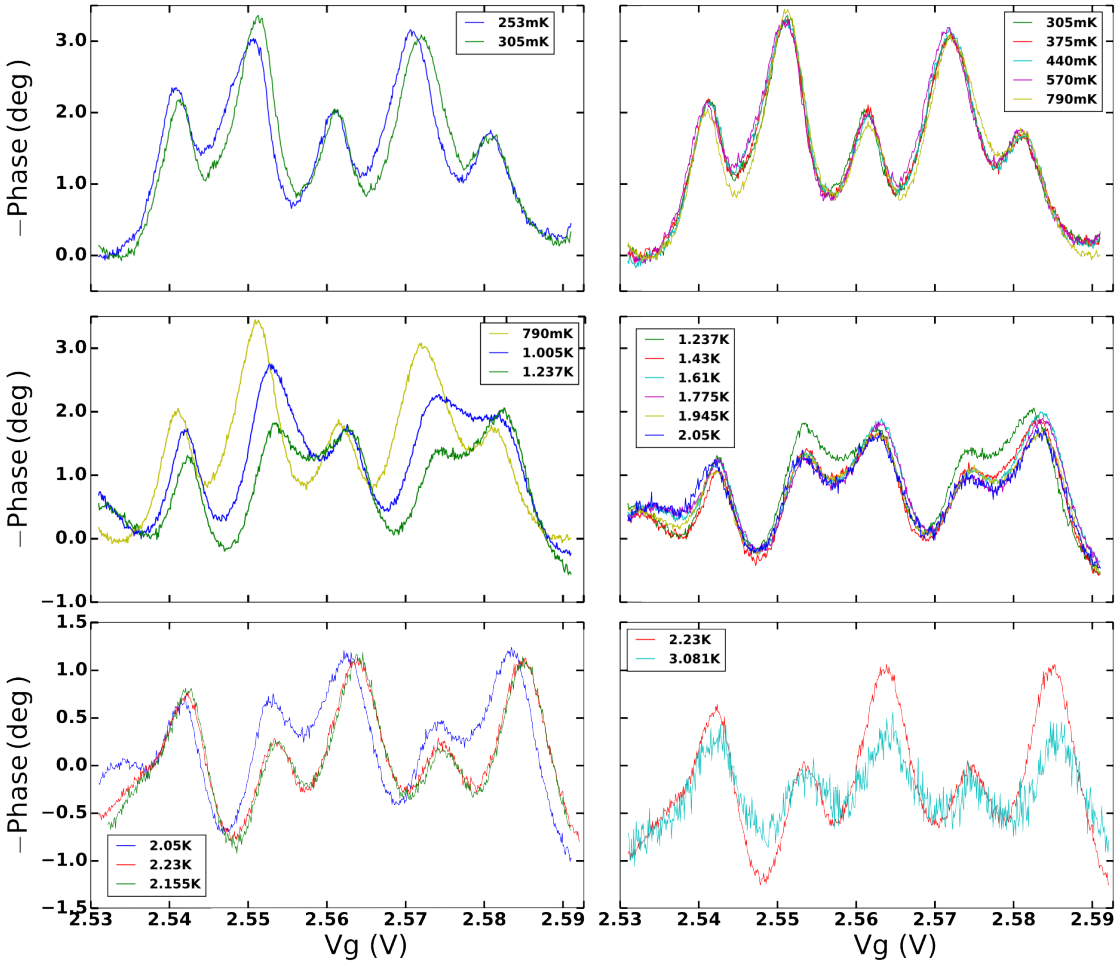

FIGURE 4.10: **Phase at zero bias with increasing temperature.** For each temperature the data shown is an average of ten consecutive gate sweeps. The data have been rescaled to take into account the decrease of the quality factor with the temperature. For each temperature the curve is offset. As there is no clear reference, the choice of the offset for each temperature is arbitrary and has been done to get the smoothest variations. The offset does not correspond to an unique gate voltage reference.

4.2.3 Temperature dependence

The temperature dependence of the conductance and the phase in the Kondo regime are shown in figures 4.9 and 4.10. The resonance frequency and the quality factor change with the temperature, therefore there is a random phase shift between to successive temperatures and one cannot compare directly the phase measured at two different temperatures. In figure 4.9, the phase is offset, and this offset has been chosen to minimize at each temperature step the phase drift. Nevertheless this choice suffers from arbitrariness. To avoid the problem of choosing a reference point, we study the evolution of the phase difference between a Kondo ridge and an adjacent Coulomb peak. In order to compare the evolution of phase variations with respect to the base temperature

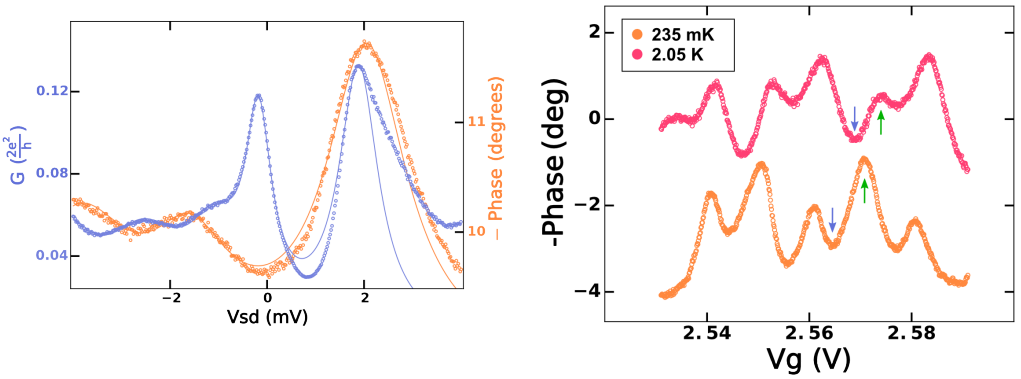

FIGURE 4.11: **Kondo peak for temperature dependence.** Left panel: Bias dependence of conductance and phase for the Kondo ridge used to determine the temperature dependence of figure 4.4a. Right panel: Corresponding gate dependence at base temperature ($235mK$) and at high temperature ($2.05K$). The phase has drifted between the two temperature from approximately two degrees. To get rid of thermal drifts, we compute the difference of the phase between a Coulomb peak (green arrow) and a Coulomb valley (blue arrow), where the Kondo ridge is. The phase at $2.05K$ has been rescaled to take into account the decrease of the quality factor with the temperature ($22000 \rightarrow 18000$).

$T = 253mK$, the phase has been rescaled by the quality factor of the cavity measured at each temperature.

The Kondo resonance shown in figure 4.3b of section 4.1 corresponds to the first ridge. Nevertheless this ridge shows fluctuations in the conductance at higher temperature. This is why we use the third ridge, of which the dual conductance/compressibility measurement of the Kondo resonance is shown in figure 4.11.

Figure 4.12 shows the evolution with the temperature of the conductance of this Kondo resonance. These scans with respect to the bias voltage were not taken at a fixed gate voltage because we have tried to compensate gate jumps observed in figure 4.9.

For this reason, we rather chose the gate scans at $V_{sd} = 0mV$ of figure 4.9 and 4.10 to compute the temperature dependence shown in figure 4.4a. The conductance of the Kondo ridge is taken at the local conductance minimum between the third and the fourth Coulomb peaks. This evolution is compared with the evolution of the relative phase between the Kondo ridge (local minimum of the opposite phase) and the right adjacent Coulomb peak (local maximum), as shown in figure 4.11 right panel.

4.2.4 Numerical Renormalization Group (NRG) calculations

As briefly mentioned in the section 1.2.3, the Kondo resonance should be calculated by summing all the terms of the Taylor expansion of the transmission T-matrix. Wilson

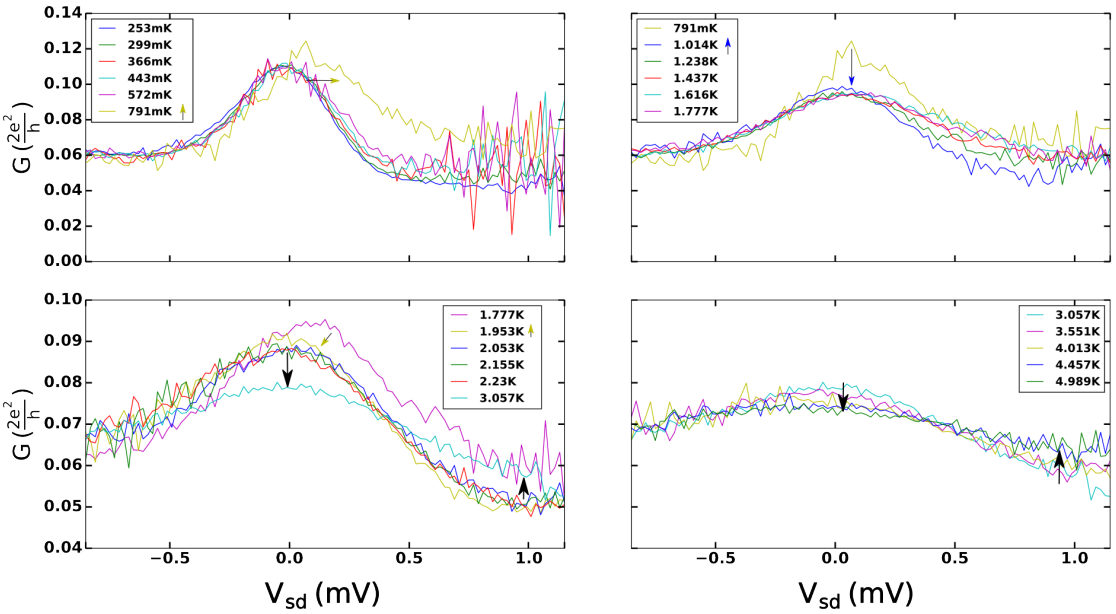

FIGURE 4.12: **Conductance with respect to the bias voltage with increasing temperature.** This set of data corresponds to the third ridge in figure 4.3, for which a cut at constant gate voltage is shown in figure 4.11. Small colored arrows point out shifts that could be due to gate jumps seen in the gate dependence data in figure 4.9. Big black arrows are guide for the eyes showing the overall decrease of the conductance.

simplified the problem by introducing a logarithmic discretization of the energy, with increasing number of slots towards the Fermi energy. The effective Hamiltonian obtained from this discretization can then be diagonalized with Numerical Renormalization Group (NRG) method [42, 107, 108]. Minchul Lee from Kyung Hee University and Mahn-Soo Choi from Korea University used this method to calculate the conductance and the compressibility in the Kondo regime. They adopt the Anderson impurity model:

$$H = \sum_{\sigma} \epsilon_d d_\sigma^\dagger d_\sigma + U n_\downarrow n_\uparrow + \sum_{k\sigma} t_k c_{k\sigma}^\dagger d_\sigma + \sum_{k\sigma} \epsilon_k c_{k\sigma}^\dagger c_{k\sigma} + h.c. \tag{4.9}$$

where $c_{k\sigma}^\dagger$ and $c_{k\sigma}$ are the annihilation and creation operators, respectively, of the conduction electrons with momentum k and spin σ, whose energy is ϵ_k, and $d_\sigma^\dagger$ and d_σ are the same operators for the electrons on the quantum dot, whose energy is ϵ_d. U describes the Coulomb interaction on the dot and $n_\sigma = d_\sigma^\dagger d_\sigma$. Note that in the orthodox charging model $U \sim 2E_C$ ($E_C = e^2/2C$ with C being the capacitance of the dot). In experiments, the tunneling amplitude t_k is assessed through the level hybridization (or tunneling-rate) parameter: $\Gamma(E) = \pi \sum_k |t_k|^2 \delta(E - \epsilon_k)$. Assuming sufficiently wide conduction band, the energy-dependence in $\Gamma(E)$ is ignored.

As the NRG method works only at equilibrium, we adopt the approximation

$$\chi(f \sim 0, V = V_{sd}) \sim \chi_{NRG}(E = eV_{sd}/\hbar, V = 0) \tag{4.10}$$

which is reasonably good in the linear-response regime and static limit $f_{cav} \ll T_K$. Direct application of the dynamical NRG method [42, 107] gives the imaginary part, $Im(\chi)$ of the zero-bias compressibility $\chi(E) \equiv \chi(E, V = 0)$, and the Kramers-Kronig relation yields the real part :

$$Re\left[\chi(E)\right] = -\frac{1}{\pi} Pr \int_{-\infty}^{\infty} \mathrm{dE}' \frac{Im\left[\chi(E')\right]}{E - E'} \tag{4.11}$$

where Pr denotes the Cauchy principal value. The NRG method divides the entire energy range into discrete sectors of the logarithmic scale, and integrates the high-energy sectors iteratively until the required low-energy sector is reached. In this iterative procedure, it is important to keep the same level of accuracy for the higher-energy sectors (earlier stage of the iteration) because we are interested in the high- energy regime ($E \sim \epsilon_d, U$) as well as the low-energy range ($|E| < T_K$). To achieve this goal, we adopt the density-matrix NRG method [109, 110], where the dynamical excitation spectral density is obtained from the reduced density matrix of each energy sector. In order to enhance the speed and efficiency in the sampling of the spectral peaks in the logarithmic energy scale, they have also used the so-called z-trick [111]. Typically they take the z-average over 32 different z values. In this NRG study, we have found two interesting high-energy properties that have been largely overlooked in previous studies (which mostly have focused on low-energy properties): (i) The charging peak at $E \sim \epsilon_d$ of the compressibility is shifted from that of the conductance by an amount comparable to Γ. This shift is clearly observable in the experimental result. (ii) The width of the charging peak (at $E \sim \epsilon_d$) of the conductance for $U \gg \Gamma$ is almost twice wider than that ($\sim \Gamma$) for the non-interacting case ($U = 0$) [105]. This is also consistent with the value of Γ when estimated from the experimentally measured dI/dV data.

Chapter 5

Towards detection with a cQED architecture of Majorana bound states in carbon nanotubes

Majorana fermions are by definition particles that are their own anti-particles. Their detection is challenging since they have no charge and no spin. As presented in the first chapter, they can be engineered as quasi-particles in condensed matter systems. Their emergence has been envisioned by inducing superconducting pairing in semi-conductors with strong spin-orbit coupling and submitted to a magnetic field [21, 22]. A key ingredient in the emergence of Majorana bound states is to have two helical states, which are non-degenerate states with opposite momentum states and opposite spin. Carbon nanotubes are promising candidates as host material, because of their genuine one-dimensional behaviors at low energy. Carbon nanotubes suffer yet from a small g-factor, a weak spin-orbit coupling. A strategy to circumvent this difficulty is to place the nanotube close to a ferromagnetic gate, which has a periodic rotating magnetic field.

This last chapter presents the observation of Andreev bound states in a carbon nanotube above a Ni ferromagnetic gate. We start with a brief review of signatures of Majorana bound states that have been achieved so far, and then focus on their detection with a microwave cavity. After having addressed the specificity of Majorana bound states in carbon nanotube, we show promising preliminary results.

5.1 Detection of Majorana bound states

The first experiments aiming at engineering a Kitaev chain were done using III/V semi-conducting nanowires, like InAs or InSb, which have a strong g-factor and a strong spin orbit coupling [23, 112]. These first experiments have shown the emergence of a conductance peak at zero bias, when applying a magnetic field parallel to wire.

Majorana bound states are not the only explanations for a zero bias peak (ZPB) in a proximitized semi-conductor. Three alternative scenarii are here briefly addressed. As mentioned in the first chapter, the Kondo effect competes with superconductivity. A zero bias Kondo peak can appear above a critical magnetic field, as superconductivity is weakened [113]. Another alternative scenario would come from a doublet of Andreev bound states (ABS) that is split into four states with the magnetic field. When increasing the magnetic field, the lowest ABS with a spin anti-aligned with the magnetic field and the excited ABS with aligned spin see their energy converging towards zero. If the superconducting gap is suppressed at the same time the ABS cross, they stay close to zero bias, like Majoranas would [114]. A ZPB could also appear because of a weak antilocalization effect induced by disorder in the nanowire [115]. These first experiments principally suffer from the fact that the gap induced by the superconducting proximity effect in the nanowire was smooth, mainly because of disorder at the interface between the nanowire and the superconductor.

To rule out these alternative scenarii, efforts were made to improve the transparency of the contact between the superconducting electrode and the semi-conducting nanowire. A high transmission and ballistic transport were recently reported by Zhang et al [24]. In this paper, the subgap density of states is strongly reduced at zero magnetic field and a ZBP emerges above a critical field, which then survives on a long range of magnetic field. This range corresponds to an energy thirty times bigger than the width of the ZBP. Such observations would not be compatible with Kondo effect which disappears for magnetic field bigger than the Kondo temperature. The ballistic properties of the wire rule also out disorder effects such as weak antilocalization.

In the device of Zhang et.al., the proximity effect stems from a planar superconducting electrode placed below the semiconducting nanowire. Another strategy is to wrap the nanowire in a thin superconducting layer. If this layer is deposited in situ after the nanowire growth, one obtains an epitaxial interface between the superconductor and the nanowire [116]. The Al-expitaxed nanowire is then contacted with two normal electrodes to probe the charge occupancy of the proximitized nanowire [25]. The spacing of the Coulomb peak gives information on the spectrum of the Andreev bound states in the nanowire. At zero magnetic field, the periodicity of the charge occupancy is $2e$. As the magnetic field increases, the Coulomb peaks split and move away from another, finally reaching a $1e$ periodicity. This indicates that Andreev bound states at zero energy are present in the nanowire. Furthermore the position of the 1e-periodic Coulomb peaks oscillates with the magnetic field, similar to the oscillations of split Majoranas. The amplitude of the splitting decreases exponentially with the length of the wire, as the splitting of two Majoranas.

Another possible realization of a Kitaev chain is to place a chain of ferromagnetic atoms on a s-wave superconductor. RKKY interactions induce a rotating magnetization along the wire forming a ferromagnetic chain. This system was first realized with iron atoms (Fe) on superconducting lead (Pd) [117]. A normal or superconducting STM tip [118] measures density of states peaks at zero energy at both extremities of the ferromagnetic chain. This suggests the formation of Majorana bound states.

Another signature of Majorana bound states is the 4π periodicity of the current-phase relation of Josephson Junctions (JJ) made with two topological superconductors. The presence of the Majorana bound states in the JJ, instead of Andreev bound states, doubles the periodicity of the Josephson relation. It stems from the fact that the two states of split Majorana doublet do not have the same parity. Therefore at $\phi = \pi$ the lowest and the upper energy branches of the Majorana corresponding to two different parity cross without avoided crossings. Unlike ABS where there is an avoided crossing, the two branches with different parity explore both negative and positive energies, yielding

a periodic condition on the phase twice bigger than for ABS's. Nevertheless, at $\phi = \pi$, when the two parity branches cross, the ground state becomes an excited state. Any switching of the parity by a quasi-particle poisoning would make the system relax in the lowest energy Majorana state and the JJ would therefore recover a 2π-periodicity

To observe the 4π-periodicity of the Josephon relation, it is therefore necessary to sweep the phase faster than the quasi-particle poisoning rate. Radio-frequency measurements were done on a Josephon Junction, where helical edge states of a 3D topological insulator, HgTe, were connected to superconducting electrodes [26, 119]. When shining microwaves on the JJ, Shapiro steps were missing in the $I(V)$ curve for bias voltage V being an odd multiple of the RF frequency. A second experiment also measured an emission of photon at half the Josephon frequency [120]. Both experimental results are evidence of a 4π periodicity current-phase relation.

The most striking signature of Majorana quasi-particles would be the experimental realization of non abelian braiding operations. Several proposals have been made for braiding protocols. They are based on a T-junction, with Majorana bound states at its three edges. The braiding could be realized either by moving them with a keyboard of gates [121], or by sequencially turning on and off the tunnel coupling between the different Majorana bound states. The coupling/decoupling sequence could be realized with electrostatic gates [122]. It could also be done by connecting the T-junction to three superconducting electrodes that define two JJ and tuning independently the ratios E_j/E_c of each JJ [123]. The last proposal also includes a way to initialize and read out the parity with the help of a qubit and a microwave resonator. The braiding of Majorana fermions could also be achieved by a sequence of projectives measurements, which could be done in an electron interferometer setup [124].

The major challenge of the braiding realization is that on one hand it should be done adiabatically in order to avoid contamination from the continuum. On the other hand, it should be done faster than the quasi-particle poisoning time that could switch the total parity. Hence, the presence of a subgap density of states would be strongly detrimental in the braiding realization.

5.2 Probing Majorana bound states with microwave cavities

Transport spectroscopy gave first signatures of zero-energy states, followed by the observation of an anomalous 4π Josephson relation, suggesting that there is no transition

inside the two split Majorana doublet. We now turn on to investigate the possibility to detect additional signatures of Majorana bound states with a microwave cavity.

Majoranas bound states (MBS) have the striking property that an electric field cannot induce any transitions between the two split Majoranas states, since they do not have the same parity. As presented in the following, a pair of MBS have a 'longitudinal coupling' Hamiltonian to the electromagnetic field because of their particle/antiparticle duality.

The low energy Hamiltonian in the Majorana subspace introduced in the first chapter (section 1.4) is :

$$H_{wire} = i\,\epsilon\frac{1}{2}\gamma_1\gamma_2 \tag{5.1}$$

where ϵ is the splitting energy.

The general form for the coupling Hamiltonian of a MBS pair to photons is necessarily :

$$H_{coupling} = i\,g\gamma_1\gamma_2\left(\hat{a}+\hat{a}^\dagger\right) \tag{5.2}$$

since it is the only possible combination between the operator $\gamma_{1,2}^\dagger = \gamma_{1,2}$, as $\gamma_{1,2}^\dagger\gamma_{1,2} = 1/2$ [29][1]. The coupling Hamiltonian (5.2) commutes with the Hamiltonian (5.1) of the wire, so that there is no transverse coupling between the MBS and the cavity. If we represent the two MBS on a Bloch sphere (the south and north pole being the parity), the coupling corresponds to a field in the z-direction. If we consider a coupling of the field to the chemical potential of the wire, the electric field shakes the chemical potential of the wire but cannot induce any transitions inside the MBS pair (see figure 5.1).

In order to get a cavity signal, one must consider transitions outwards the Majorana doublet. One possibility is to use four MBS instead of two. With two pairs of Majorana, the even parity subspace has two states $|00\rangle$ and $|11\rangle$, and the odd parity subspace has two states $|01\rangle$ and $|10\rangle$, $|n_1n_2\rangle$ being the number of electrons associated to a left, right Majoranas. For the even parity subspace, a transverse coupling can appear[2] [29]. Considering a coupling to chemical potential of the nanowire, the coupling constant g is proportional to the exponentially suppressed spatial overlap of the MBS wavefunctions, so the signal in the cavity decreases rapidly when entering the topological phase (see figure 5.1). The smallness of the cavity signal could be nevertheless compensated by increasing the number of photons. In the dispersive regime, there is an additional non linear[3] term $K(\hat{a}^\dagger)^2(\hat{a})^2$ in the coupling Hamiltonian, similar to the Kerr term widely

[1] Note that the coupling Hamiltonian is then proportional to $\imath\gamma_1\gamma_2 = 2c^\dagger c - 1$, the fermionic degree of freedom.

[2] If we consider a symmetric coupling between the two pairs of Majorana (same oscillating chemical potential), there is no transition inside the odd subspace.

[3] The cavity field couples here to the chemical potential of the nanowire. The non-linear coupling stems from the exponential decrease of the spatial overlap between MBS with the chemical potential of the nanowire.

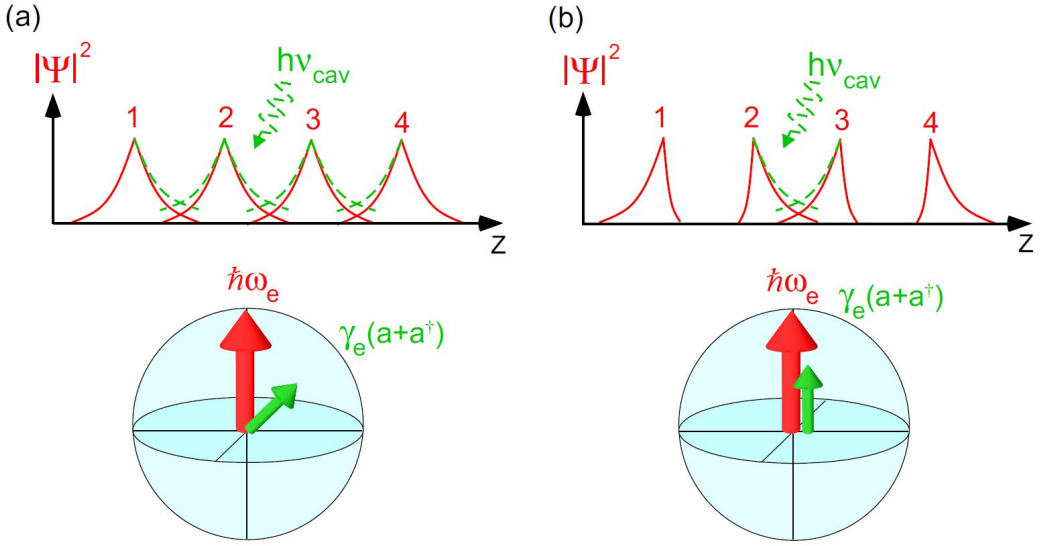

FIGURE 5.1: **Schematic representation of the coupling mechanism between MBS and cavity photons.** (a) The region between 1 and 2 and the one between 3 and 4 is a topological region. The Majorana 2 and 3 are tunnel-coupled to a non-topological central region. If there is a finite spatial overlap of the wavefunctions between four MBS there is a transverse coupling γ_e which on depends on these overlaps. (b) If there is only two Majorana that are hybridized, there is only a longitudinal coupling that do not affect the cavity. Figure taken from [29].

used in non-linear optics. This term could lead to a hysterical transmission of the cavity when sweeping the drive frequency around the cavity resonance frequency, or to a squeezing of the electromagnetic field quadratures [29].

The device mentioned above would be made from a single nanowire with two topological regions separated by a non-topological region, hosting thus four MBSs (see figure 5.1). Such a device coupled to the cavity could also be used to perform operations on the Majorana qubit in the even subspace [125]. If the gap of the topological region is much bigger than the one in the non topological region, the coupling constant to the microwave g is controlled by the strength of the tunnel-coupling ϵ between the two adjacent MBSs that are separated by the non-topological region. When the frequency of the cavity is close to the energy gap of the non-topological region, photo-assisted tunneling towards the continuum increases the tunnel-coupling ϵ and therefore increases the coupling to the cavity. If the coupling is strong enough, photons induce Rabi oscillations in the Majorana qubit on a timescale shorter than the decoherence rate, which therefore could be used to do arbitrary single qubit rotations[4].

[4] As briefly sketched in the first chapter, some braiding operations between four MBSs can perform some rotations of the Majorana qubit, but braiding if not sufficient to achieve universal quantum computing [126].

Another possibility to get a cavity signal is to consider transitions towards the trivial ABS locatted in the nanowire at higher energy[5] or even to the continuum of states above the gap. Close to the topological transition, transitions to the continuum are resonant and induce a phase and amplitude shifts that decay exponentially away from the transition [128].

The transitions between MBS and ABS probed by a microwave cavity could also reveal the singular 4π Josephson relation of the MBS. The transition energy should show a kink around the bias phase $\phi = \pi$, since in this region, the MBS energies vary linearly with the phase, whereas the ABS enery dispersion is flat because of the avoided crossing [129].

An other type of transition that could be probed are transitions to a normal electrode or a superconducting electrode with a residual quasi-particle density inside the gap[6] [130]. In that case, there can be photo-assisted tunneling from the states at Fermi energy of the electrode and the Majorana doublet. This correspond to a change in the parity of the Majorana doublet that costs an energy $\pm\epsilon/2$. Contrarily to trivial ABS, there is a cavity signal at the frequency $\omega_c = \epsilon/2$, while energy difference between the two MBS measured by transport spectroscopy is ϵ [130]. The absence of cavity signal at $\omega_c = \epsilon$ would be a strong signature of the particle/anti-particle duality.

It is therefore appealing to embed a device, where Majorana's could appear, in a microwave cavity and to realize a crossed measurement of the conductance and the cavity signal.

5.3 Majorana bound states in carbon nanotube

Carbon-based materials are much lighter than other semi-conductors in which the first signatures of Majorana fermions were measured (InAs, InSb, HgTe, etc.). Consequently the atomic spin-orbit is much weaker especially in planes of graphene by symmetry reasons.

The nanotube curvature breaks the planar symmetry and the p_x and p_y orbitals are hybridized. The hybridization allows the atomic spin-orbit coupling to mix the spins of these two orbitals. Hence the spin of the electron rotates when the electron moves along the circumference of nanotube, which induces an effective spin orbit coupling.

[5] To have higher ABS, the length of the nanowire should be bigger than the superconducting length ξ. As tackled in the first chapter, higher energy ABS could also appear because of disorder [127], since the disorder increases the length of the electrons trajectories.

[6] As the topological phase requires a magnetic field, it is not unrealistic to state that it induces some depairing of the Cooper pairs.

Benefiting from the high Fermi velocity and small nanotube radius R, this spin-orbit energy splitting $\sim \hbar v_f/R$ is much bigger than the atomic one [131].

The splitting energy of this spin orbit is not linear in momentum as for Rashba and Dresselhaus spin-orbit couplings. Could be it used to engineer Majorana bounds states ? Sau and Tewari found that it requires in addition to the usual magnetic field the breaking of the chiral symmetry [132]. This means that a term $\Delta_{K-K'}$ is needed to hybridize states between both valleys. Such $\Delta_{K-K'}$ term could be induced by the superconducting proximity effect itself, which would mix electrons from different valleys.

Nevertheless, the strength of this spin-orbit coupling happens to vary between different experiments, depending on parameters that may for example be the chirality of the tube or the number of electrons [30]. In addition, the microscopic origin of the $\Delta_{K-K'}$ term is often unclear, and if it comes from disorder that might be then unfavorable for the curvature-induced spin orbit coupling. For both reasons, the use of the curvature-induced spin orbit coupling may not be the best strategy to implement Majorana bound states in carbon nanotubes.

As described in the first chapter (section 1.4.2), another strategy is to create an artificial spin-orbit coupling with a rotating magnetic field [27, 28]. The energy splitting associated to this spin-orbit is $E_{SO} = \frac{hv_f}{2\lambda}$, where λ is the half-period of the rotation and v_f the Fermi velocity of the electrons in the nanotube. The rotating field can be created by a ferromagnetic gate and λ is in that case the size of the a ferromagnetic domain. If a nanotube is lying on a ferromagnetic gate, E_{SO} is the confinement energy times the number of domains seen by the nanotube, and could reach several meV.

In this scenario, we should lift the $K-K'$ degeneracy in order to be in the helical regime, where only one state exists at a given energy. This could come from the superconducting pairing as mentioned previously. The degeneracy could also be lifted by a magnetic field parallel to the nanotube, the rotating K and counter-rotating K' states having an opposite Ahranov-Bohm effect. This could be achieved for example if the oscillating magnetic field has a component along the nanotube axis.

The carbon nanotubes have a g-factor equal close to 2, which is much smaller than the one of other nanowires such as InAs ($g \sim 10$) or InSb ($g \sim 50$). Hence strong fields (of the order of $0.5 - 1T$) may be required for entering the topological regime. In the perspective of coupling Majorana bound states to a microwave cavity, the use of a ferromagnetic gate allows us to have a strong field in the vicinity of the nanotube that decay rapidly away, thus preserving the superconducting cavity from the depairing effect of the magnetic field.

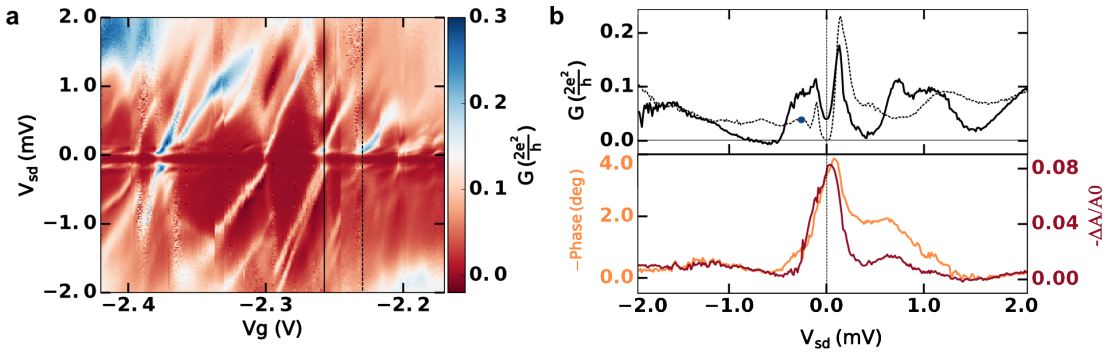

FIGURE 5.2: **A carbon nanotube with two superconducting electrodes and coupled to the cavity. a.** Differential conductance showing a superconducting gap $2\Delta \sim 0.25meV$ on a large gate range. **b.** Top panel : two cuts of a. at constant gate. The dotted curve (corresponding to the dotted line in a.) shows a gap with a BCS-like density of states at zero bias. The conductance in the gap is 5% of the conductance marked by a blue dot. The solid curve (corresponding to the solid line in a.) shows a non-closing gap and negative differential conductance around $V_{sd} \sim -0.5meV$. Low panel : phase and amplitude signal corresponding to the solid line in a.

5.4 Observation of Andreev resonances in a Majorana oriented device

5.4.1 Conductance and phase signals

The experimental results below were obtained in a device that was realized with the aim of engineering and detecting Majorana bounds states in a carbon nanotube. A carbon nanotube lies above a ferromagnetic bottom gate and is connected by two superconducting electrodes $Pd(4nm)/Al(80nm)$. The bottom gate is a $600nm$-wide and $100nm$-thick Ni electrode, which has a magnetic texture. As presented in chapter 3, this texture is an alternation of domains with a mean pitch of $250nm$. The Ni electrode was covered by $3nm$ of aluminium oxide. The sample was measured in a dilution fridge at $30mK$.

Contrarily to the device presented in the chapter 4, the coupling of the nanotube to the cavity was realized by placing, between the bottom gate and one electrode, a top gate which is connected to the central conductor of the microwave cavity. Top gates are generally used to couple quantum dots to microwave cavities, and this strategy has already shown strong coupling constant [14, 46, 69, 106]. We were therefore interested to compare it with the scheme proposed in the former chapter[7].

The presented device shows a well defined superconducting gap, within which the residual conductance is only 5% of the conductance measured at higher bias voltages (see

[7]In this device, the chemical potential is tuned by varying the dc potential of the central conductor of the microwave cavity via a dc gate that was at the other extremities of the cavity, because the dc gate patterned near the measured nanotube was not working.

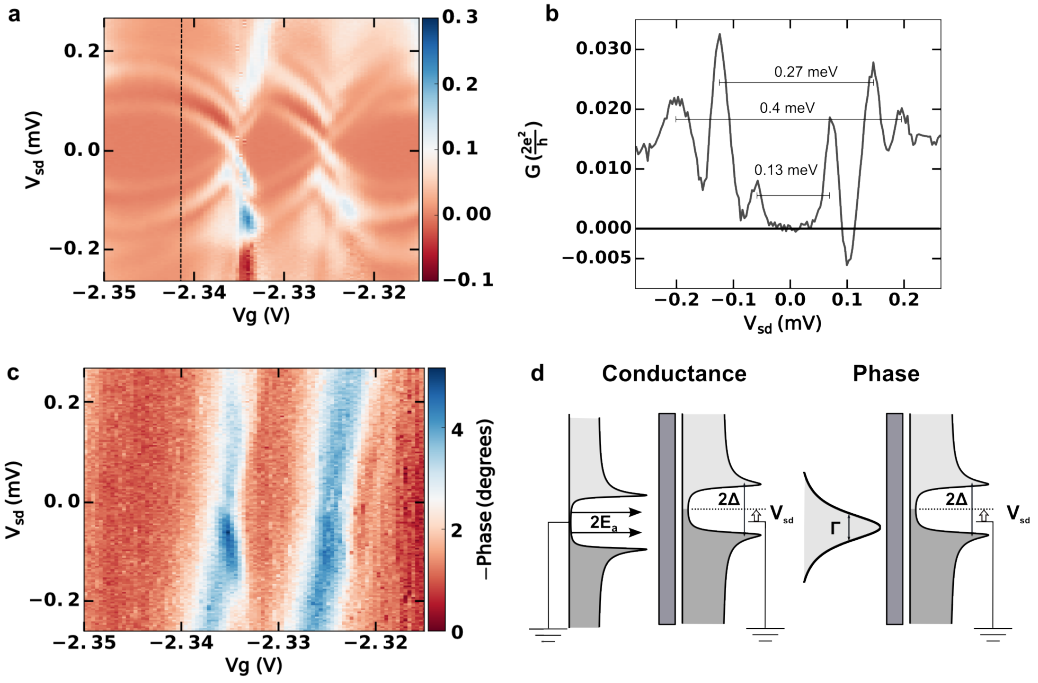

FIGURE 5.3: **Conductance and phase signal. a.** The differential conductance shows discrete resonances that merge towards zero at gate voltage corresponding to a Coulomb peak. **b.** Cut in a. showing these resonances. The one at lowest energy is associated to an Andreev resonance with energy $2E_a = 130\mu eV$. The next resonances correspond to BCS peaks with a superconducting gap $2\Delta = 270\mu eV$. The outermost peaks correspond to replica of the ABS at $\pm(E_a + \Delta)$, coming from the BCS-like density of states of the bias probe. **c.** The phase signal shows only the Coulomb peaks resonances with a width around $200\mu eV$. **d.** The probe with bias potential V_{sd} (on the right) is a superconducting electrode with a finite subgap density of states. Therefore its probes the Andreev spectrum formed by the dot and the drain superconducting electrode like a normal electrode would do it. There is yet at higher energy replica of the Andreev resonances because of the BCS peaks of the probe electrode. The cavity is only sensitive to single electron tunneling between the dot and the probe with its residual density at zero bias. Therefore the phase signal c. exhibits the same resonances as for a dot coupled to a normal electrode.

figure 5.2). Figure 5.2b displays the phase and amplitude signal that vary according to the bias voltage, showing that the carbon nanotube is coupled to the cavity. From the phase contrast of 4° and a width of the phase peak $\Gamma \sim 200\mu eV$, we can deduce a coupling constant $g \sim 40Mhz$, which is quite similar to the one found for the previous device.

Figure 5.3 shows the conductance and the microwave transmitted phase for two adjacent Coulomb peaks[8]. The conductance exhibits resonances, that converge towards zero bias for each Coulomb peaks. We can also see negative differential conductance that is

[8]The electronic circuit parameters, like the gate voltage values, the superconducting gap, ect, change between each figure because the sample had to be warmed up to $50K$, because of problems in the dilution lines.

specific to quantum dots connected to superconducting electrodes. This can happen for instance when a BCS peak crosses a sharp density of states [74, 133]. Here one electrode, called the probe, is biased with respect to the second electrode, the drain, which is kept grounded. The current is proportional to integral of the density of states in the probe $N_{probe}(E)$ times the density of states of a system $N_{syst}(E)$ formed by the drain and the dot :

$$I(E = eV_{sd}) \propto \int \mathrm{dE} N_{probe}(E + eV_{sd}) N_{syst}(E) \left(f_{probe}(E + eV_{sd}) - f_{syst}(E)\right) \tag{5.3}$$

with f the Fermi occupation function.

If both the probe, and the drains have a BCS density of states with gaps Δ_{probe} and Δ_{drain}, we should observe in the conductance measurement a gap $\Delta_{probe}+\Delta_{drain}$. Within this gap, the first Andreev resonance with energy E^A should appear in the conductance at $\pm(E^A + \Delta_{probe})$.

Here we can see that there are resonances at low bias, $eV_{sd} < \Delta_{probe}$. The probe has therefore a significant density of states at zero bias. As for a normal probe an Andreev resonance appears in the conductance spectrum at $\pm E^A$. The density of states of the probe has two BCS peaks at $\pm\Delta_{probe}$. For positive bias, we see therefore four resonances at E_A, Δ_{drain}, $(E^A + \Delta_{probe})$ and $(\Delta_{drain} + \Delta_{probe})$.

The transmitted phase signal of the microwave cavity shows furthermore no dip at low bias, contrary to the conductance that shows a dip due to induced superconductivity. Thus the cavity signal is given by electronic transitions between the dot and a continuum of states at zero bias, which supports the fact that the probe electrode has a significant density of states at zero energy. This difference between both electrodes can be explained by the fact that the probe electrode is closer than the drain electrode to the ferromagnetic bottom gate, because of the insertion of the top gate between the drain and the bottom gate[9]. The superconductivity of the probe electrode is probably weakened by the stray fields of the ferromagnetic gate [10].

Figure 5.3b displays a cut at constant voltage where there are six symmetric resonances. We interpret this as being for the lowest resonance an Andreev resonance at E_A, for the

[9]The probe is $285nm$ away from the bottom gate, while the drain is $520nm$ away.

[10]From the value of the conductance above the superconducting gap $G(eV_{sd} \gg \Delta) = 0.1\frac{2e^2}{h}$, one can deduce that the contact are very asymetric. One of the contact has therefore $\Gamma \sim 200\mu eV$ and the other contact $\Gamma \sim 0.05 * 200\mu eV \sim 10\mu eV$. The electronic transition with the small $\Gamma \sim 10\mu eV \sim 3Ghz$ should not be visible in the cavity. As in the device presented in chapter 4, this explained why only one range of parallel edges of the Coulomb diamonds are visible in the microwave phase signal in the figure 5.3. As this phase signal depends on the bias, one can state that the largest Γ is associated to source-nanotube transition. This is therefore not fully appropriate to call the source electrode the probe, and it is not directly a spectroscopy of Andreev bound states as in ref [134]. We prefer here to use the term of Andreev resonance.

second one the BCS density peaks of the drain electrode Δ and for the one at higher voltage the replica of the Andreev resonance at $E_A + \Delta$. The energies of the Andreev resonances depend on the gate voltage and converge to zero for each Coulomb peak, which may be due to the change of the charge parity in the quantum dot as seen in [134] and explained in chapter 1. We also note that in the Coulomb valley the Andreev resonances do not converge towards the superconducting gap as seen in [134].

The conductance and the phase signal do not bring the same information on the system. The conductance probes only mechanism of electrons transfer that allow the electrons to be transmitted from the probe to the superconducting drain, which are Andreev resonances. The phase signal is only sensitive to transitions between the dot and the probe electrode, and displays Coulomb peaks, as for a dot coupled to a normal electrode.

Surprisingly, we observe that at zero bias, the resonance in the phase at a Coulomb peak is twice wider than the width of the conductance peak (not shown). We also observe that at zero bias, the gate voltage corresponding to the maxima of the conductance and the phase are slightly misaligned (not shown), with a shift around $40\mu eV$ for the phase resonances shown in figure 5.3.

5.4.2 Andreev resonances

Figure 5.4 shows the dispersion of the Andreev resonances with the magnetic field. Figure 5.4a-d correspond to different gate voltages. The gate voltage of a. is in a Coulomb valley, similarly to the cut shown in figure 5.3b. The Andreev resonances disappear at $60mT$, when the superconducting gap closes. Figures 5.4b and 5.4d correspond to gate voltages near a Coulomb peaks where the Andreev resonances have small energies. Both show the presence of two Andreev resonances, with energy $E_1^A \sim 30\mu eV$ and $E_2^A \sim 90\mu eV$. As explained in chapter 1.3.2, there can be several Andreev resonances if the distance between the two superconducting electrodes is longer than the superconducting coherent length ξ defined in equation (1.46). Nevertheless in that case, their energy would be of the same order as the confinement energy hv_f/L, which is a high energy in quantum dots. In our case, the doubling of Andreev resonances could rather come from the two K-K' orbitals, which do not have the same tunnel-coupling with the superconducting electrodes [135]. We exclude that the lowest energy resonances come from a multiple Andreev reflection (MAR) which has been explained in chapter 1.3.2, because we do not see a series of resonances following the MAR distribution $eV = \frac{2\Delta}{n}$ with $n \in N$. This is expected as the bias probe has a finite density of states at zero bias.

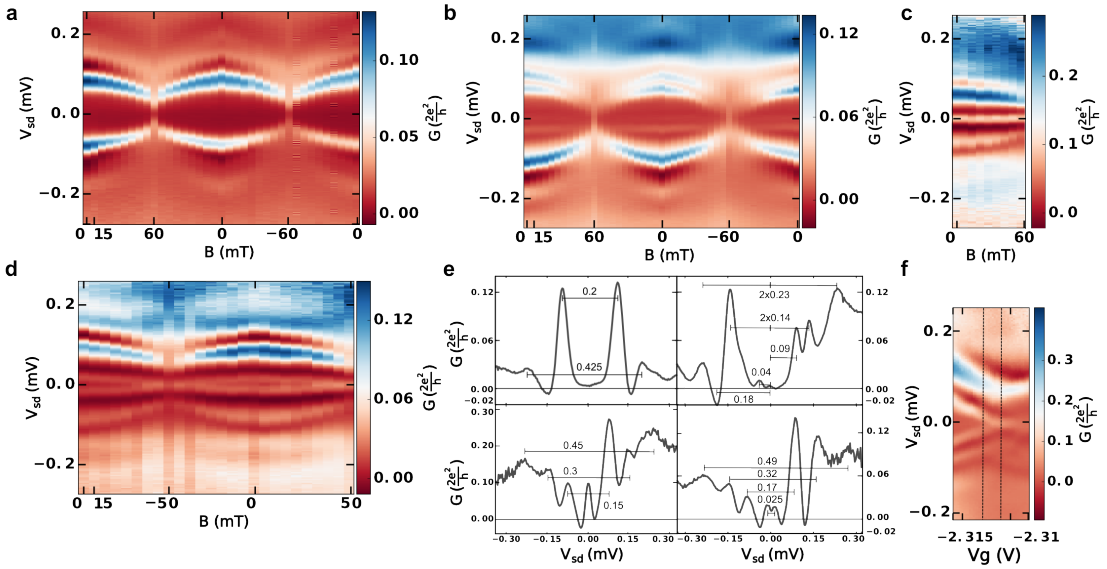

FIGURE 5.4: **Dispersion of the conductance resonances with the magnetic field. a., b., c. and d.** An in-plane magnetic field is swept upwards to $60mT$ ($50mT$ for c. and d.), then downwards to $-60mT$ ($-50mT$ for c.) and finally upwards to zero. The resonances follow the closing of the superconducting gap at 60 mT and no hysteresis is seen between upward and downward sweeps. **e.** : Cuts at zero magnetic field for a.,b.,c. and d. Top-left panel corresponds to a., top-right to b., bottom-left to c. and bottom-right to d. d. shows two Andreev resonances $2E_1^A = 25\mu eV$ and $2E_2^A = 170\mu eV$. Only the replica of the second one is visible at $2E_2^A + 2\Delta = 170 + 320\mu eV = 490\mu eV$. b. exhibits an asymmetry in the electron/hole excitation. A positive energy an ABS is visible at $E_A = 90\mu eV$ as well as its replica at $140 + 90 = 230\mu eV$. For negative energies, an Andreev resonance is visible at $E_A = -40\mu eV$, whereas is replica is not visible, maybe because of the presence of negative differential conductance. At $-230\mu eV$ there is the replica of the Andreev resonance seen at positive energy. c. corresponds to a Coulomb peak gate voltage. **f.** displays a V_g-V_{sd} conductance colorplot for the gate region of c. and d.

Figure 5.4c shows an Andreev resonance at zero energy, which corresponds to a gate voltage of a Coulomb peak, as shown in the V_g-V_{sd} conductance map in figure 5.4f. For this Coulomb peak, the phase and the conductance maxima are also misaligned, with a shift around $80\mu eV$ (not shown).

Note that the lowest resonances shown in 5.4c and 5.4d are followed by a negative differential conductance even if they do not appear as sharp resonances in the conductance.

In figure 5.4, we have measured upward and downward scans with respect to the magnetic field, to detect possible hysterical behavior due to the magnetic texture of the bottom gate. Each upward, resp. downward, scan was brought up to $100mT$, resp $-100mT$, in order to saturate the magnetization of the Ni bottom gate. Nevertheless nothing in the data could let us envision an effect coming from the ferromagnetic bottom gate.

The Andreev resonances at small energies are close to the frequency of the cavity $\hbar\omega_{res} = 30\mu eV$. With a coupling constant $g \sim 40MHz$ and a quality factor $Q \sim 3000$, we

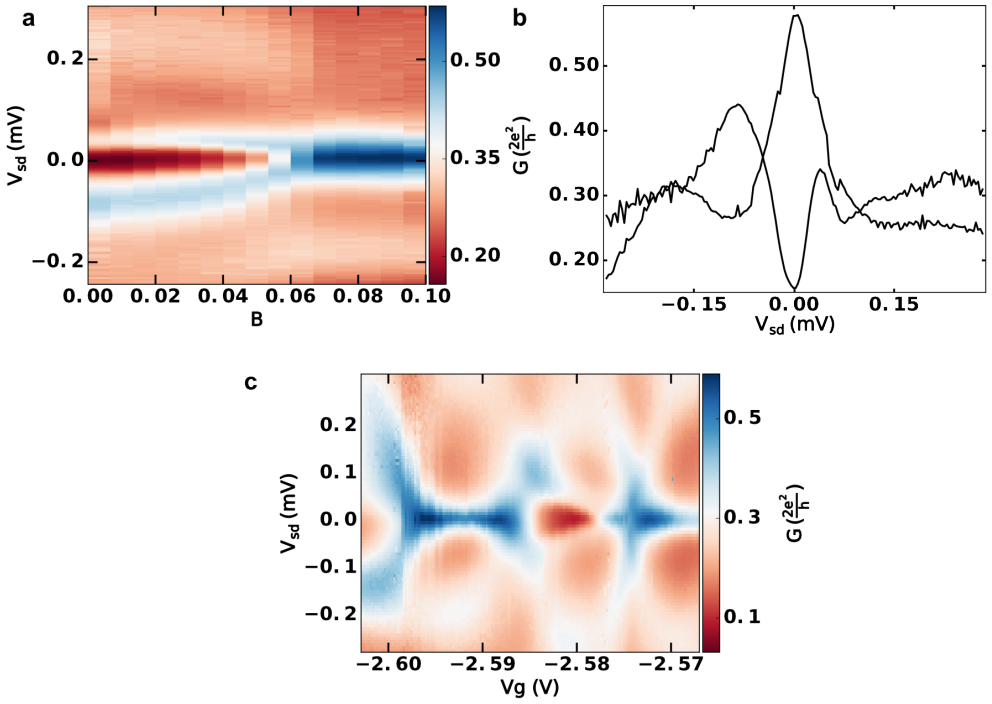

FIGURE 5.5: **Transition between the superconducting state and a Kondo state. a.** A dip in the conductance at zero bias evolves towards a Kondo peak while increasing the magnetic field. **b.** Cut in a. at zero magnetic field showing a gap $2\Delta = 123\mu eV$ filled by a residual density of states, and at $100mT$ showing a Kondo peak with $T_k = 110\mu eV$. **c.** $V_g - V_{sd}$ differential conductance map at $B = 90mT$ showing a Kondo ridge.

should have a phase shift around 10 ° for the Andreev resonances seen in 5.4d, which have $E_A \sim 25\mu eV$ and a width around $20\mu eV$[11]. Nevertheless we do not see a clear signal in the phase or in the amplitude (not shown), that could result from a coupling of Andreev bound states to the photons. This could be explained by the fact that the drain electrode is also coupled to the cavity via the nearby top gate. In that situation, there is only a small AC potential gradient between the dot and the electrode from which the ABSs arise, and thus the coupling constant to the photons is weak.

5.4.3 Competition between the superconducting proximity effect and the Kondo effect

The figure 5.5 reproduces the emergence of a zero bias peak that would mimic Majorana bound states, as already observed in a nanowire-based device [113]. In this measurement,

[11] In the resonant regime, the phase shift is $g^2/(\kappa\Gamma)$, where κ is the width of the cavity, and Γ the one of the ABS.

the probe and the drain electrodes have been swapped[12]. In the gate voltage region considered below, the conductance never drops to zero, but a dip in the conductance is still visible. When the superconductivity in the electrodes is suppressed by the magnetic field around $60mT$, the dip in the conductance is replaced by a Kondo peak. The corresponding ridge is shown in the conductance colormap in figure 5.5c The width of the Kondo ridge is $T_K = 110\mu eV$, of the same order as the superconducting gap in the electrodes, which is around $150\mu eV$, as shown in the figures 5.3 and 5.4. Therefore we are in the situation sketched in the first chapter where the superconducting pairing effect competes with the formation of a Kondo singlet between the dot and the electrodes. We have seen previously that one electrode has a residual density of states even at zero magnetic field. The Kondo effect requires a finite density of states at the Fermi energy, so in that case, the Kondo effect competes even at zero magnetic field with the superconducting pairing, filling the induced superconducting gap. When the magnetic field is switched on, it reduces the effect of superconducting pairing and increases the density of states at zero bias, enhancing the Kondo effect.

5.4.4 Conclusion and perspectives

The observation of Andreev resoances in such a device is a promising first step towards the engineering and detection of Majorana bound states (MBS) in carbon nanotubes. The proximity induced 'hard gap' in the conductance and the splitting of the K-K' degeneracy observed here would be favorable in the emergence of MBS. The presence of negative differential conductance at low bias and the shifts between the conductance and the phase maxima call for a numerical theoretical modeling of the experimental results [44, 74]. This experiment shows also alternative scenarii that would mimic MBS, such as the presence of a zero-bias finite density of state at Coulomb peaks [134] or the competition between the superconductivity and the Kondo effect [113].

The fact that only the closest electrode from the ferromagnetic gate has a residual density of states indicates that the ferromagnetic gate produces finite magnetic stray fields that decrease away from the gate. In multidomain magnetic structures, the typical decay length for the magnetic field is the size of one domain, which is around $210nm$ for the Ni ferromagnetic gate. In our device the probe is $285nm$ away from the bottom gate, while the drain is $520nm$ away. As we still see signatures of BCS peaks in the density of states of the probe, both in the conductance and the phase, we can set that the stray fields seen by the probe are below the critical field which is here around $60mT$. Considering a linear approximation, the field seen by the nanotube on the bottom gate should be at most around $100mT$, which corresponds to an upper bound for the Zeeman

[12] Therefore the cavity signal does not depend on the bias voltage

splitting for an electron in the nanotube of $10\mu eV$. This rough estimate happens to be unfavorable for the emergence of MBS, as the Zeeman splitting should be higher than the superconducting pairing potential .

A solution to increase the magnetic field seen by the nanotube is to use Pt/Co bottom gates (see chapter 3). This multi-layers structure presents up and down domains, and a saturation magnetization that is three times higher than the Ni one. An out-of-plane magnetic field of $500mT$, which is the third of the Co magnetization, would give a Zeeman splitting of $50\mu eV$. The domains length is around $160nm$ as shown in chapter 3, which therefore should increase the spin-orbit coupling energy up to $10meV$[13].

If the magnetic field is of the order of a few hundreds of mT on the nanotube, which is necessary to enter the topological regime, it would induce too much depairing in Al-superconducting electrodes. We should move from Al electrodes to Nb electrodes, which have a much higger critical magnetic field, around $3-4\,T$. Good contacts between a carbon nanotube and Pd/Nb electrodes have already been obtained [50, 135] and these devices have a superconducting gap around $0.5meV$.

A carbon nanotube above a Pt/Co ferromagnetic gates would satisfy all the conditions to enter the topological regime The genuine one-dimensional nature of carbon nanotubes, the large spin-orbit coupling induced by the Pt/Co ferromagnetic domains and the large superconducting gap of the Nb electrodes would furthermore isolate well the Majorana bound states from the quasi-particle poisoning that reduces the topological protection.

[13] We have mentioned in the first chapter that in this case the spin-orbit coupling energy is $E_{SO} = \frac{\hbar v_f}{2\lambda}$

Perspectives

This thesis reports an efficient way to measure with a high sensitivity the compressibility of a carbon nanotube-based quantum dot. This is realized by stamping a nanotube above a bottom gate which is capacitively coupled to a high finesse microwave cavity. The microwave response reveals for example that the electron gas of the dot is incompressible in the Kondo regime. With these measurements, we show that in the Kondo regime there is a finite electrical conductance while the charge in the dot is frozen.

The compressibility is a thermodynamic quantity which corresponds to the low-frequency response of the dot charge susceptibility. Further insights on the Kondo physics could be obtained using this cQED architecture. At frequencies closer to the Kondo temperature T_k, the dynamical response of the quantum dot should be different from the compressibility measurement, as electronic correlations are present at the time scale of order of $\hbar/T_k$. A resonance with Kondo temperature close to $7GHz$ have been recently observed [46].

One could envision to study the dynamical response of such a Kondo resonance to a sudden change of the dot chemical potential. Such a quantum quench would also enable us to probe the dynamics of the formation of the Kondo cloud. One could also study the coupling of a Kondo quantum dot to a superconducting qubit mediated by the cavity. The Kondo quantum dot would modify the electromagnetic bath seen by the qubit and the electronic correlations of the Kondo quantum dot should have an effect on the relaxation processes of the qubit.

Even if the cavity frequency is smaller than the Kondo temperature, the use of a qubit coupled to the cavity could lead to a quantitative study of the dot charge susceptibility. The dispersive read-out of the qubit gives the exact number of photons in the cavity, which combined with the power dependence of the dot conductance, would give with a great accuracy the electron-photon coupling constant g. One could for example compare quantitatively the compressibility with the NRG calculation. One could also compare the dot compressibility in Kondo regimes with different symmetries SU(2) or SU(4), which can appear in carbon nanotubes. This could be even interesting in the Coulomb

blockade regime to determine the renormalization factor of the quantum capacitance with respect to the tunneling rates Γ and the charging energy E_c. The experimental results presented here and the perspectives they open illustrate that quantum dot circuits embedded in a cQED architecture are a powerful probe for condensed matter problems.

The measurement of the frozen charge fluctuations calls for a direct measurement of the spin fluctuations of a Kondo dot. A RF-squid like architecture that measures tiny magnetic fields could be adapted to the microwave cavity scheme, and measure the spin fluctuations that should be also be on the time scale of $\hbar/T_k$.

Frequency shifts of the mechanical motion of a carbon nanotube quantum dot have also been observed [136, 137]. Similarly to the coupling to photons, these frequency shifts were induced by the finite charge susceptibility at the Coulomb peaks. The Kondo regime was not reached, maybe because of disorder induced by the fabrication process. With cleaner nanotubes, similar effects as the one presented in this thesis could be observed.

In the last chapter, we report an observation of Andreev bound states in a carbon nanotube embedded in a microwave cavity. The Andreev bound states were nevertheless not coupled to the cavity. The observation of internal transitions could give more insights in the proximity effect in quantum dots, where interactions dominate. A microwave measurement probes transitions within the same parity subspace whereas electronic transport probes transitions between the even and odd parities. Therefore a dual measurement of the conductance and the cavity transmission may bring additional knowledge in the understanding of the proximity effect.

The opportunity of engineering Majorana bound states has initiated an intense activity in the condensed matter community. Carbon nanotubes present the main advantage to be a genuine one-dimensional material with well separated subbands, contrarily to other materials where first signatures of Majorana fermions were observed. The nanofabrication of carbon-based circuits could become very efficient with the perspective of pristine nanotubes stamping techniques. Besides these long-term perspectives, the preliminary results presented in the last chapter of this thesis let us to believe that carbon nanotubes are good candidates for hosting Majorana bound states.

Observing Majorana bound states in carbon nanotubes above a ferromagnetic gate would also prove that the ferromagnetic gate is an efficient way to induce helical states. Such ferromagnetic textures could even be used with materials that have already a strong spin-orbit coupling. It is in fact interesting to have a localized magnetic field when making for example a T junction, with several nanowires that are not in the same direction, or when scaling up Majorana-based circuits.

The signature of Majorana bound states with a dual measurement of the conductance and the cavity signal would be a strong signature of their particle/antiparticle duality, that has not been shown yet. The integration of such quantum electronic circuit in a cQED architecture would open many opportunities to study the coupling of light to these peculiar electronic excitations and place the topologically protected Majorana qubit at the heart of quantum information technology.

Bibliography

[1] J. Kondo. Resistance Minimum in Dilute Magnetic Alloys. *Prog. Theor. Phys.*, 32:37, 1964. URL https://doi.org/10.1143/PTP.32.37.

[2] W.J. de Haas, J. de Boer and G.J. van den Berg. The electrical resistance of gold, copper and lead at low temperatures. *Physica*, 1:1115, 1934. doi: 10.1126/science.281.5376.540. URL http://dx.doi.org/10.1016/S0031-8914(34)80310-2.

[3] D. Goldhaber-Gordon, H. Shtrikman, D. Mahalu, David Abusch-magder, and M. A. Kastner. Kondo effect in a single-electron transistor. *Nature*, 391(January): 1996–1999, 1998. URL http://dx.doi.org/10.1038/34373.

[4] S.M. Cronenwett, T.H Oosterkamp, and L. P. Kouwenhoven. A tunable Kondo effect in quantum dots. *Science*, 281:540, 1998. URL http://dx.doi.org/10.1038/34373M3.

[5] J. Nygård, D.H. Cobden, and P.E. Lindelof. Kondo physics in carbon nanotubes. *Nature*, 408(November):1–5, 2000. URL http://dx.doi.org/10.1038/35042545.

[6] K v. Klitzing, G Dorda, and M Pepper. New Method for High-Accuracy Determination of the Fine-Structure Constant Based on Quantized Hall Resistance. *Phys. Rev. Lett.*, 45(6):494–497, 1980. doi: 10.1103/PhysRevLett.45.494. URL http://link.aps.org/doi/10.1103/PhysRevLett.45.494.

[7] B J Van Wees, H Van Houten, C W J Beenakker, J Gr Williamson, L P Kouwenhoven, D der Marel, and C T Foxon. Quantized conductance of point contacts in a two-dimensional electron gas. *Physical Review Letters*, 60(9):848, 1988. URL https://doi.org/10.1103/PhysRevLett.60.848.

[8] D C Tsui, H L Stormer, and A C Gossard. Two-Dimensional Magnetotransport in the Extreme Quantum Limit. *Phys. Rev. Lett.*, 48(22):1559–1562, 1982. URL http://link.aps.org/doi/10.1103/PhysRevLett.48.1559.

[9] A K Geim and K S Novoselov. The rise of graphene. *Nat Mater*, 6(3):183–191, mar 2007. ISSN 1476-1122. URL http://dx.doi.org/10.1038/nmat1849.

[10] Y V Nazarov and Y M Blanter. *Quantum Transport: Introduction to Nanoscience*. Cambridge University Press, 2009. ISBN 9781139478175.

[11] R Bacon. Growth, Structure, and Properties of Graphite Whiskers, 1960. URL http://dx.doi.org/10.1063/1.1735559.

[12] Sumio Iijima. Helical microtubules of graphitic carbon. *Nature*, 354(6348):56–58, nov 1991. URL http://dx.doi.org/10.1038/354056a0.

[13] M .R. Delbecq, V. Schmitt, F. D. Parmentier, N. Roch, J. J. Viennot, G. Fève, B. Huard, C. Mora, A. Cottet, and T. Kontos. Coupling a quantum dot, fermionic leads and a microwave cavity on-chip. *Phys. Rev. Lett.*, 107:256804, 2011. URL http://dx.doi.org/10.1103/PhysRevLett.107.256804.

[14] T. Frey, P. J. Leek, M. Beck, J. Faist, A. Wallraff, K. Ensslin, and T. Ihn. Quantum dot admittance probed at microwave frequencies with an on-chip resonator. *Phys. Rev. B*, 86:115303, 2012. URL http://dx.doi.org/10.1103/PhysRevB.86.115303.

[15] Michel Devoret and Ananda Roy. Introduction to Quantum-limited Parametric Amplification of Quantum Signals with Josephson Circuits. *Comptes Rendus Physique*, 17(7):740–755, 2016. URL http://dx.doi.org/10.1016/j.crhy.2016.07.012.

[16] Al. Blais, R. Huang, A. Wallraff, S .M. Girvin, and R. J. Schoelkopf. Cavity quantum electrodynamics for superconducting electrical circuits: An architecture for quantum computation. *Physical Review A*, 64:062320, 2004. URL http://dx.doi.org/10.1103/PhysRevA.69.062320.

[17] A. Wallraff, D. Schuster, A. Blais, L. Frunzio, J. Majer, S. Kumar, S. M. Girvin, and R .J. Schoelkopf. Strong coupling of a single photon to a superconducting qubit using circuit quantum electrodynamics. *Nature*, 431:162–167, 2004. URL http://dx.doi.org/10.1038/nature02851.

[18] S M Girvin, M H Devoret, and R J Schoelkopf. Circuit QED and engineering charge-based superconducting qubits. *Physica Scripta*, 2009(T137):14012, 2009. URL http://stacks.iop.org/1402-4896/2009/i=T137/a=014012.

[19] M A Nielsen and I L Chuang. *Quantum Computation and Quantum Information*. Cambridge Series on Information and the Natural Sciences. Cambridge University Press, 2000. ISBN 9780521635035.

[20] Kitaev A Yu. Unpaired Majorana fermions in quantum wires. *Physics- Uspekhi*, 44(10S):131, 2001. URL http://stacks.iop.org/1063-7869/44/i=10S/a=S29.

[21] Yuval Oreg, Gil Refael, and Felix von Oppen. Helical Liquids and Majorana Bound States in Quantum Wires. *Physical Review Letters*, 105(17):177002, oct 2010. ISSN 0031-9007. doi: 10.1103/PhysRevLett.105.177002. URL http://link.aps.org/doi/10.1103/PhysRevLett.105.177002.

[22] Roman M Lutchyn, Jay D Sau, and S Das Sarma. Majorana Fermions and a Topological Phase Transition in Semiconductor-Superconductor Heterostructures. *Physical Review Letters*, 105(August):077001, 2010. URL http://dx.doi.org/10.1103/PhysRevLett.105.077001.

[23] V. Mourik, K. Zuo, S. M. Frolov, S. R. Plissard, E. P. a M. Bakkers, and L. P. Kouwenhoven. Signatures of Majorana fermions in hybrid superconductor-semiconductor nanowire devices. *Science*, 336(6084):1003–7, may 2012. URL http://dx.doi.org/10.1126/science.1222360.

[24] H. Zhang, Ö. Gül, S. Cones-Boj, K. Zuo, V. Mourik, F.K. de Vries, J. V. Veen, D.J. Woerkom, M. P. Nowak, M. Wimmer, D. Car, E.P.A.M Bakkers, M. Quintero-p, S. Goswami, K. Watanabe, T. Taniguchi, and Leo P. Kouwenhoven. Ballistic Majorana nanowire devices. *(unpublished)*. URL https://arxiv.org/abs/1603.04069.

[25] S M Albrecht, A P Higginbotham, M Madsen, F Kuemmeth, T S Jespersen, J Nygård, P Krogstrup, and C M Marcus. Exponential protection of zero modes in Majorana islands. *Nature*, 531(7593):206–209, 2016. ISSN 0028-0836. doi: 10.1038/nature17162. URL http://dx.doi.org/10.1038/nature17162.

[26] E. Bocquillon, R.S. Deacon, J. Wiedenmann, P. Leubner, T.M. Klapwijk, C. Brüne, K. Ishibashi, H. Buhmann, and L.W. Molenkamp. Gapless Andreev bound states in the quantum spin Hall insulator HgTe. *Nature Nanotechnology*, 12:137–143, 2017. URL http://dx.doi.org/10.1038/nnano.2016.159L3.

[27] Reinhold Egger and Karsten Flensberg. Emerging Dirac and Majorana fermions for carbon nanotubes with proximity-induced pairing and spiral magnetic field. *Phys. Rev. B*, 85:235462, 2012. URL https://doi.org/10.1103/PhysRevB.85.235462.

[28] Morten Kjaergaard, W Konrad, and Karsten Flensberg. Majorana fermions in superconducting nanowires without spin-orbit coupling. *Phys. Rev. B*, 85:020503(R), 2012. URL https://doi.org/10.1103/PhysRevB.85.020503.

[29] Audrey Cottet and Takis Kontos. Squeezing light with Majorana fermions. *Phys. Rev. B*, 88:195415, 2013. URL https://doi.org/10.1103/PhysRevB.88.195415.

[30] Edward A Laird, Ferdinand Kuemmeth, Gary Steele, Kasper Grove-rasmussen, Jesper Nygård, and Leo P Kouwenhoven. Quantum transport in carbon nanotubes.

Rev. Mod. Phys., 87:703, 2015. URL https://doi.org/10.1103/RevModPhys.87.703.

[31] S Sapmaz, J Kong, C Dekker, L P Kouwenhoven, and H S J Van Der Zant. Electronic excitation spectrum of metallic carbon nanotubes. *Phys. Rev. B*, 71 (December 2004):153402, 2005. URL http://dx.doi.org/10.1103/PhysRevB.71.153402.

[32] Simon E. Nigg, Rosa Lopez, and Markus Buttiker. Mesoscopic Charge Relaxation. *Phys. Rev. Lett.*, 97:206804, jun 2006. URL http://dx.doi.org/10.1103/PhysRevLett.97.206804.

[33] A C Hewson. *The Kondo Problem to Heavy Fermions*. Cambridge Studies in Magnetism. Cambridge University Press, 1997. ISBN 9780521599474.

[34] Michael Pustilnik and Leonid Glazman. Kondo effect in quantum dots. *Journal of Physics: Condensed Matter*, 16:R513, 2004. URL http://stacks.iop.org/0953-8984/16/i=16/a=R01.

[35] M. Pustilnik. Kondo effect in nanostructures. *Physica status solidi (a)*, 203(6): 1137–1147, dec 2006. URL https://doi.org/10.1002/pssa.200566191.

[36] Leo Kouwenhoven and Leonid Glazman. Revival of the Kondo effect. *Physics World*, 14(1):33–38, 2001. URL http://stacks.iop.org/2058-7058/14/i=1/a=28.

[37] Abrikosov A.A. Magnetic impurities in nonmagnetic metals. *Usp. Phys. Nauk 97*, 168:403–427, 1969. URL https://doi.org/10.1070/PU1969v012n02ABEH003930.

[38] P. Nozieres. A "fermi-liquid" description of the Kondo problem at low temperatures. *J Low Temp Phys (1974)*, 17(1):31–42, 1974. URL http://dx.doi.org/10.1007/BF00654541.

[39] S. Takada, C. Bäuerle, M. Yamamoto, K. Watanabe, S. Hermelin, T. Meunier, A. Alex, A. Weichselbaum, J .Von Delft, A. Ludwig, A. D. Wieck, and S. Tarucha. Transmission phase in the Kondo regime revealed in a two-path interferometer. *Physical Review Letters*, 113(September):126601, 2014. doi: 10.1103/PhysRevLett.113.126601. URL http://dx.doi.org/10.1103/PhysRevLett.113.126601.

[40] T. Delattre, C. Feuillet-Palma, L. G. Herrmann, P. Morfin, J. M. Berroir, G. Fève, B. Plaçais, D. C. Glattli, M. S. Choi, C. Mora, and T. Kontos. Noisy Kondo

impurities. *Nature Physics*, 5(2):1–5, 2010. URL http://dx.doi.org/10.1038/nphys1186.

[41] J. Basset, A. Yu. Kasumov, C.P. Moca, G. Zarand, P. Simon, H. Bouchiat, and R Deblock. Measurement of quantum noise in a carbon nanotube quantum dot in the Kondo regime. *Physical Review Letters*, 108(January):046802, 2012. URL http://dx.doi.org/10.1103/PhysRevLett.108.046802.

[42] Kenneth G Wilson. The renormalization group : Critical phenomena and the Kondo problem. *Rev. Mod. Phys.*, 47:773, 1975. URL https://doi.org/10.1103/RevModPhys.47.773.

[43] M Tinkham. *Introduction to Superconductivity: Second Edition*. Dover Books on Physics. Dover Publications, 2004. ISBN 9780486435039.

[44] Jean-Damien Pillet. *Tunneling spectroscopy of the Andreev Bound States in a Carbon Nanotube*. PhD thesis, 2011.

[45] Landry Bretheau. *Localized Excitations in Superconducting Atomic Contacts : Probing the Andreev Doublet*. PhD thesis, 2013.

[46] Laure Bruhat. *Microwaves as a probe of quantum dot circuits : from Kondo dynamics to mesoscopic quantum electrodynamics*. PhD thesis, 2016.

[47] Eduardo J H Lee, Xiaocheng Jiang, Manuel Houzet, Charles M Lieber, and Silvano De Franceschi. Spin-resolved Andreev levels and parity crossings in hybrid superconductor-semiconductor nanostructures. *Nature Nanotechnology*, 9:79–84, 2014. URL http://dx.doi.org/doi:10.1038/nnano.2013.267.

[48] J Cleuziou, W Wernsdorfer, V Bouchiat, and T Ondarcuhu. Carbon nanotube superconducting quantum interference device. *Nature Nanotechnology*, 1:53–59, 2006. doi: 10.1038/nnano.2006.54.

[49] Silvano De Franceschi, Leo Kouwenhoven, Christian Schönenberger, and Wolfgang Wernsdorfer. Hybrid superconductor-quantum dot devices. *Nature Nanotechnology*, 5(10):703–711, 2010. ISSN 1748-3387. doi: 10.1038/nnano.2010.173. URL http://dx.doi.org/10.1038/nnano.2010.173.

[50] R. Delagrange, R. Weil, A. Kasumov, M. Ferrier, H. Bouchiat, and R. Deblock. 0-π quantum transition in a carbon nanotube Josephson junction: universal phase dependence and orbital degeneracy. *Phys. Rev. B*, 93:195437, 2016. URL https://doi.org/10.1103/PhysRevB.93.195437.

[51] Vincent Mourik and Kun Zuo. *Signatures of Majorana Fermions in Hybrid Superconductor-Semiconductor Nanowire Devices*. PhD thesis, 2016.

[52] Bernd Braunecker, Pascal Simon, and Daniel Loss. Nuclear Magnetism and Electronic Order in 13 C Nanotubes. *Phys. Rev. Lett.*, 116403(March):6–9, 2009. URL http://dx.doi.org/10.1103/PhysRevLett.102.116403.

[53] Chen-Hsuan Hsu, Peter Stano, Jelena Klinovaja, and Daniel Loss. Antiferromagnetic nuclear spin helix and topological superconductivity in 13C nanotubes. *Phys. Rev. B*, 92:235435, 2015. URL https://doi.org/10.1103/PhysRevB.92.235435.

[54] Serge Haroche and Jean Michel Raimond. *Exploring the Quantum: Atoms, Cavities, and Photons*. Oxford Univ. Press, Oxford, 2006.

[55] Alain Aspect, Claude Fabre, and Grynberg Gilbert. *Optique quantique*. Ecole poly edition, 2006.

[56] M Brune, A Maali, J Dreyer, E Hagley, J M Raimond, and S Haroche. Quantum Rabi Oscillation : A Direct Test of Field Quantization in a Cavity. *Phys. Rev. Lett.*, 76:1800, 1996. URL https://doi.org/10.1103/PhysRevLett.76.1800.

[57] Sebastien Gleyzes, Stefan Kuhr, Christine Guerlin, Julien Bernu, Samuel Deleglise, Ulrich Busk Hoff, Michel Brune, Jean-Michel Raimond, and Serge Haroche. Quantum jumps of light recording the birth and death of a photon in a cavity. *Nature*, 446(7133):297–300, mar 2007. ISSN 0028-0836. URL http://dx.doi.org/10.1038/nature05589.

[58] C. Sayrin, I. Dotsenko, X. Zhou, B. Peaudecerf, P. Rouchon, M. Mirrahimi, H. Amini, M. Brune, J-M. Raimond, and S. Haroche. Real-time quantum feedback prepares and stabilizes photon number states. *Nature*, 477:73–77, 2011. URL http://dx.doi.org/10.1038/nature10376.

[59] A. Facon, E-K. Dietsche, D. Grosso, S. Haroche, J-M. Raimond, M. Brune, and S. Gleyzes. A sensitive electrometer based on a Rydberg atom in a Schrödinger-cat state. *Nature*, 535(7611):262–265, 2016. URL http://dx.doi.org/10.1038/nature18327.

[60] Y Nakamura, Yu A Pashkin, and J S Tsai. Coherent control of macroscopic quantum states in a single-Cooper-pair box. *Nature*, 398(April):786, 1999. URL http://dx.doi.org/10.1038/19718.

[61] D Vion, A Aassime, A Cottet, P Joyez, and H Pothier. Manipulating the Quantum State of an Electrical Circuit. *Science*, 296(May):886–889, 2002. URL http://dx.doi.org/10.1126/science.1069372.

[62] J Q You, Xuedong Hu, S Ashhab, and Franco Nori. Low-decoherence flux qubit. *Phys. Rev. B*, 75:140515(R), 2007. URL http://dx.doi.org/10.1103/PhysRevB.75.140515.

[63] Steven M Girvin. *Superconducting Qubits and Circuits : Artificial Atoms Coupled to Microwave Photons*. Number Lecture Notes of the Les Houches Summer School. 2011.

[64] Steven M Girvin. Circuit QED : Superconducting Qubits Coupled to Microwave Photons. In *Lecture Notes of the Les Houches Summer School: Volume 96*, page 114. Oxford University Press, 2011.

[65] J A Schreier, A A Houck, Jens Koch, D I Schuster, B R Johnson, J M Chow, J M Gambetta, J Majer, L Frunzio, M H Devoret, S M Girvin, and R J Schoelkopf. Suppressing charge noise decoherence in superconducting charge qubits. *Phys. Rev. B*, 77:180502(R), 2008. URL http://dx.doi.org/10.1103/PhysRevB.77.180502.

[66] Max Hofheinz, H Wang, M Ansmann, Radoslaw C Bialczak, Erik Lucero, M Neeley, A D O Connell, D Sank, J Wenner, John M Martinis, and A N Cleland. Synthesizing arbitrary quantum states in a superconducting resonator. *Nature*, 459(7246):546–549, 2009. URL http://dx.doi.org/10.1038/nature08005.

[67] Z Leghtas, S Touzard, I M Pop, A Kou, B Vlastakis, A Petrenko, K M Sliwa, A Narla, S Shankar, M J Hatridge, M Reagor, L Frunzio, R J Schoelkopf, M Mirrahimi, and M H Devoret. Confining the state of light to a quantum manifold by engineered two-photon loss. *Science*, 347(6224):853–857, 2015. URL http://dx.doi.org/10.1126/science.aaa2085.

[68] Y.-Y. Liu, J Stehlik, C Eichler, M J Gullans, J M Taylor, and J R Petta. Semiconductor double quantum dot micromaser. *Science*, 5415:864–866, 2014. URL http://dx.doi.org/10.1126/science.aaa2501.

[69] J J Viennot, M C Dartiailh, A Cottet, and T Kontos. Coherent coupling of a single spin to microwave cavity photons. *Science*, 349(6246):408–411, 2016. URL http://dx.doi.org/10.1126/science.aaa3786.

[70] J Gabelli, G Feve, B Placais, J.-M. Berroir, A Cavanna, B Etienne, Y Jin, and D C Glattli. Violation of KirchhoffâĂŹs Laws for a Coherent RC Circuit. *Science*, 313:499, 2006. URL http://dx.doi.org/10.1126/science.1126940.

[71] Matthieu Delbecq. *Coupling quantum dot circuits to microwave cavities*. PhD thesis, 2013.

[72] Christophe Mora and Karyn Le Hur. Universal Resistances of the Quantum RC circuit. *Nature Physics*, 6:697–701, 2009.

[73] Minchul Lee, Rosa Lopez, Mahn-Soo Choi, Thibaut Jonckheere, and Thierry Martin. Many-body correlation effect on mesoscopic charge relaxation. *Phys. Rev. B*, 83:201304(R), 2011. URL http://dx.doi.org/10.1103/PhysRevB.83.201304.

[74] L E Bruhat, J J Viennot, M C Dartiailh, M M Desjardins, T Kontos, and A Cottet. Cavity photons as a probe for charge relaxation resistance and photon emission in a quantum dot coupled to normal and superconducting continua. 021014:1–16, 2016. URL http://dx.doi.org/10.1103/PhysRevX.6.021014.

[75] A Cottet, T Kontos, and B Douçot. On the electron-photon coupling in Mesoscopic Quantum Electrodynamics. *Physical Review B*, 91:205417, 2014. URL https://doi.org/10.1103/PhysRevB.91.205417.

[76] A A Clerk, M H Devoret, S M Girvin, Florian Marquardt, and R J Schoelkopf. Introduction to Quantum Noise, Measurement and Amplification. *Rev. Mod. Phys.*, 82:1155, 2008. URL https://doi.org/10.1103/RevModPhys.82.1155.

[77] J. P. Eisenstein, L. N. Pfeiffer, and K. W. West. Compressibility of the two-dimensional electron gas: Measurements of the zero-field exchange energy and fractional quantum Hall gap. *Phys. Rev. B*, 50(3):1760–1779, 1994. URL https://doi.org/10.1103/PhysRevB.50.1760.

[78] R C Ashoori, H L Stormer, J S Weiner, L N Pfeiffer, S J Pearton, K W Baldwin, and K W West. Single-electron capacitance spectroscopy of discrete quantum levels. *Physical Review Letters*, 68(20):3088–3091, 1992. URL https://doi.org/10.1103/PhysRevLett.68.3088.

[79] D Berman, N B Zhitenev, and R C Ashoori. Observation of quantum fluctuations of charge on a quantum dot. *Phys. Rev. Lett.*, 82,:161–164, 1999. URL https://doi.org/10.1103/PhysRevLett.82.161.

[80] J. Martin, N. Akerman, G. Ulbricht, T. Lohmann, J.H. Smet, K. von Klitzing, and A. Yacoby. Observation of electron-hole puddles in graphene using a scanning single electron transitor. *Nature Physics*, 4:144 – 148, 2008. URL http://dx.doi.org/10.1038/nphys781.

[81] K W Lehnert, B A Turek, K Bladh, L F Spietz, D Gunnarsson, P Delsing, and R J Schoelkopf. Quantum charge fluctuations and the polarizability of the single-electron box. *Phys. Rev. Lett.*, 91:106801, 2003. URL https://doi.org/10.1103/PhysRevLett.91.106801.

[82] R J Schoelkopf, P Wahlgren, and A A Kozhevnikov. The radio-frequency single-electron transistor (RF-SET): a fast and ultrasensitive electrometer. *Science*, 280 (5367):1238–1242, 1998. URL http://dx.doi.org/10.1126/science.280.5367.1238.

[83] M Göppl, A Fragner, M Baur, R Bianchetti, S Filipp, J M Fink, P J Leek, G Puebla, L Steffen, and A Wallraff. Coplanar waveguide resonators for circuit quantum electrodynamics. *Journal of Applied Physics*, 104:113901, 2008. URL http://dx.doi.org/10.1063/1.3010859.

[84] J. J. Viennot, J. Palomo, and T. Kontos. Stamping single wall nanotubes for circuit quantum electrodynamics. *Applied Physics Letters*, 104(11):113108, 2014. URL http://dx.doi.org/10.1063/1.4868868.

[85] Jeremie Viennot. *Charge and spin dynamics in a hybrid circuit quantum electrodynamics architecture*. PhD thesis, 2014.

[86] Ji. Ali Javey, Q. Wang, M. Lundstrom, and H. Dai. Ballistic carbon nanotube field-effect transistors. *Nature*, 424(August):654, 2003. URL http://dx.doi.org/10.1038/nature01797.

[87] S H Lee, F Q Zhu, C L Chien, and N Markovic. Effect of geometry on magnetic domain structure in Ni wires with perpendicular anisotropy: A magnetic force microscopy study. *Phys. Rev. B*, 77(13):132408, 2008. URL http://dx.doi.org/10.1103/PhysRevB.77.132408.

[88] M. Labrune and J. Miltat. Numerical simulation of weak stripe domains. *Journal of Magnetism and Magnetic Materials*, 104-107:241–242, 1992. URL http://dx.doi.org/10.1016/0304-8853(92)90781-I.

[89] C. A. Neugebauer. Saturation magnetization of nickel films of thickness less than 100 A. *Physical Review*, 116(6):1441–1446, 1959. URL http://dx.doi.org/10.1103/PhysRev.116.1441.

[90] Joseph E. Davies, Olav Hellwig, Eric E. Fullerton, Greg Denbeaux, J. B. Kortright, and Kai Liu. Magnetization reversal of Co/Pt multilayers: Microscopic origin of high-field magnetic irreversibility. *Physical Review B - Condensed Matter and Materials Physics*, 70(22):1–8, 2004. ISSN 10980121. doi: 10.1103/PhysRevB.70.224434. URL http://dx.doi.org/10.1103/PhysRevB.70.224434.

[91] R. Sbiaa, Z. Bilin, M. Ranjbar, H. K. Tan, S. J. Wong, S. N. Piramanayagam, and T. C. Chong. Effect of magnetostatic energy on domain structure and magnetization reversal in (Co/Pd) multilayers. *Journal of Applied Physics*, 107(10):16–21, 2010. ISSN 00218979. doi: 10.1063/1.3427560.

[92] O. Donzelli, D. Palmeri, L. Musa, F. Casoli, F. Albertini, L. Pareti, and G. Turilli. Perpendicular magnetic anisotropy and stripe domains in ultrathin Co/Au sputtered multilayers. *Journal of Applied Physics*, 93(12):9908–9912, 2003. URL http://dx.doi.org/10.1063/1.1577394.

[93] G. N. Phillips, K. O'Grady, Q. Meng, and J.C. Lodder. Domain structure and magnetisation processes in magneto-optic co/pt thin films. *IEEE Transactions on Magnetics*, 32(5):4070–4072, 1996. URL http://dx.doi.org/10.1109/20.539266.

[94] T. Hingant, L. J. Martinez, S. Rohart, A. Thiaville, L H. Herrera Diez, K. Garcia, G. Gaudin, L. Vila, B. Ocker, D. Ravelosona, and V. Jacques. The nature of domain walls in ultrathin ferromagnets revealed by scanning nanomagnetometry. *Nature Communications*, 6:6733, 2014. URL http://dx.doi.org/10.1038/ncomms7733.

[95] Fei Pei, E. A. Laird, G. A. Steele, and L. P. Kouwenhoven. Valley-spin blockade and spin resonance in carbon nanotubes. *Nature Nanotechnology*, 7(10):630–634, 2012. URL http://dx.doi.org/10.1038/nnano.2012.160.

[96] Nicolas Roch, Serge Florens, Vincent Bouchiat, Wolfgang Wernsdorfer, and Franck Balestro. Quantum phase transition in a single-molecule quantum dot. *Nature*, 453(7195):633–637, may 2008. ISSN 0028-0836. URL http://dx.doi.org/10.1038/nature06930.

[97] Z Iftikhar, S Jezouin, A Anthore, U Gennser, F D Parmentier, A Cavanna, and F Pierre. Two-channel Kondo effect and renormalization flow with macroscopic quantum charge states. *Nature*, 526(7572):233–236, oct 2015. ISSN 0028-0836. URL http://dx.doi.org/10.1038/nature15384.

[98] A J Keller, L Peeters, C P Moca, I Weymann, D Mahalu, V Umansky, G Zarand, and D Goldhaber-Gordon. Universal Fermi liquid crossover and quantum criticality in a mesoscopic system. *Nature*, 526(7572):237–240, oct 2015. ISSN 0028-0836. URL http://dx.doi.org/10.1038/nature15261.

[99] Antoine Georges, Gabriel Kotliar, Werner Krauth, and Marcelo J Rozenberg. Dynamical mean-field theory of strongly correlated fermion systems and the limit of infinite dimensions. *Reviews of Modern Physics*, 68(1):13–125, jan 1996. URL http://link.aps.org/doi/10.1103/RevModPhys.68.13.

[100] S. Ilani, L. A. K. Donev, M. Kindermann, and P. L. McEuen. Measurement of the quantum capacitance of interacting electrons in carbon nanotubes. *Nature*

Physics, 2(10):687–691, oct 2006. ISSN 1745-2473. URL http://dx.doi.org/10.1038/nphys412.

[101] Bertrand Reulet, Michel Ramin, Hélène Bouchiat, and Dominique Mailly. Dynamic Response of Isolated Aharonov-Bohm Rings Coupled to an Electromagnetic Resonator. *Physical Review Letters*, 75(1):124–127, jul 1995. URL http://link.aps.org/doi/10.1103/PhysRevLett.75.124.

[102] M Büttiker, A Prêtre, and H Thomas. Dynamic conductance and the scattering matrix of small conductors. *Physical Review Letters*, 70(26):4114–4117, jun 1993. URL http://link.aps.org/doi/10.1103/PhysRevLett.70.4114.

[103] A Prêtre, H Thomas, and M Büttiker. Dynamic admittance of mesoscopic conductors: Discrete-potential model. *Physical Review B*, 54(11):8130–8143, sep 1996. URL http://link.aps.org/doi/10.1103/PhysRevB.54.8130.

[104] M. Filippone, K. Le Hur, and C. Mora. Admittance of the SU(2) and SU(4) Anderson quantum RC circuits. *Phys. Rev. B*, 88:045302, 2011. URL https://doi.org/10.1103/PhysRevB.88.045302.

[105] Rok Žitko and Thomas Pruschke. Energy resolution and discretization artifacts in the numerical renormalization group. *Physical Review B*, 79(8):85106, feb 2009. URL http://link.aps.org/doi/10.1103/PhysRevB.79.085106.

[106] T Frey, P J Leek, M Beck, A Blais, T Ihn, K Ensslin, and A Wallraff. Dipole coupling of a double quantum dot to a microwave resonator. *Phys. Rev. Lett.*, 108(4):46807, jan 2012. URL http://dx.doi.org/10.1103/PhysRevLett.108.046807.

[107] T. A. Costi and A. C. Hewson. Transport coefficients of the Anderson model. *Journal of Physics: Condensed Matter*, 5(30):L361, 1993. ISSN 0953-8984. URL http://stacks.iop.org/0953-8984/5/i=30/a=001.

[108] T .A Costi, A. C. Hewson, and V. Zlatic. Transport coefficients of the Anderson model via the numerical renormalization group. *Journal of Physics: Condensed Matter*, 6(13):2519, 1994. URL http://stacks.iop.org/0953-8984/6/i=13/a=013.

[109] Walter Hofstetter. Generalized numerical renormalization group for dynamical quantities. *Physical Review Letters*, 85(7):1508–1511, aug 2000. URL https://doi.org/10.1103/PhysRevLett.85.1508.

[110] Andreas Weichselbaum and Jan von Delft. Sum-Rule Conserving Spectral Functions from the Numerical Renormalization Group. *Physical Review Letters*, 99(7):

76402, aug 2007. URL http://link.aps.org/doi/10.1103/PhysRevLett.99.076402.

[111] M Yoshida, M A Whitaker, and L N Oliveira. Renormalization-group calculation of excitation properties for impurity models. *Physical Review B*, 41(13):9403–9414, may 1990. URL http://link.aps.org/doi/10.1103/PhysRevB.41.9403.

[112] Anindya Das, Yuval Ronen, Yonatan Most, Yuval Oreg, and Moty Heiblum. Zero-bias peaks and splitting in an AlâĂŞInAs nanowire topological superconductor as a signature of Majorana fermions. *Nature Physics*, 8:887–895, 2012. URL http://dx.doi.org/10.1038/nphys2479.

[113] Eduardo J H Lee, Georgios Katsaros, Xiaocheng Jiang, Charles M Lieber, and Silvano De Franceschi. Zero-Bias Anomaly in a Nanowire Quantum Dot Coupled to Superconductors. *Phys. Rev. Lett.*, 109:186802, 2012. URL http://dx.doi.org/10.1103/PhysRevLett.109.186802.

[114] Diego Rainis, Luka Trifunovic, Jelena Klinovaja, and Daniel Loss. Towards a realistic transport modeling in a superconducting nanowire with Majorana fermions. *Phys. Rev. B*, 87:024515, 2013. URL http://dx.doi.org/10.1103/PhysRevB.87.024515.

[115] D.I Pikulin, J.P. Dahlhaus, M. Wimmer, and H. Schomerus. A zero-voltage conductance peak from weak antilocalization in a Majorana nanowire. *New J. Phys.*, 14:125011, 2012. URL http://dx.doi.org/10.1088/1367-2630/14/12/125011.

[116] P Krogstrup, N L B Ziino, W Chang, S M Albrecht, M H Madsen, E Johnson, J Nygård, C M Marcus, and T S Jespersen. Epitaxy of Semiconductor-Superconductor nanowires. *Nature Materials*, 14:400–406, 2015. URL http://dx.doi.org/10.1038/nmat4176.

[117] Stevan Nadj-perge, Ilya K Drozdov, Jian Li, Hua Chen, Sangjun Jeon, J Seo, MacDonald A.H., B.A. Bernevig, and A. Yazdani. Observation of Majorana fermions in ferromagnetic atomic chains on a superconductor. *Science*, 346(6209):602–607, 2014. URL http://dx.doi.org/10.1126/science.1259327.

[118] Michael Ruby, Falko Pientka, Yang Peng, Felix Von Oppen, Benjamin W Heinrich, and Katharina J Franke. End states and subgap structure in proximity-coupled chains of magnetic adatoms. *Phys. Rev. Lett.*, 115:197204, 2014. URL https://doi.org/10.1103/PhysRevLett.115.197204.

[119] J Wiedenmann, E Bocquillon, R S Deacon, S Hartinger, O Herrmann, T M Klapwijk, L Maier, C Ames, C Gould, A Oiwa, K Ishibashi, S Tarucha, H Buhmann, and L W Molenkamp. 4π-periodic Josephson supercurrent in HgTe-based

topological Josephson junctions. *Nature Communications*, 7:10303, 2016. URL http://dx.doi.org/10.1038/ncomms10303.

[120] R S Deacon, J Wiedenmann, E Bocquillon, T M Klapwijk, P Leubner, and C Br. Josephson radiation from gapless Andreev bound states in HgTe-based topological junctions. 2016.

[121] Jason Alicea, Yuval Oreg, Gil Refael, Felix Von Oppen, and Matthew P A Fisher. Non-Abelian statistics and topological quantum computation in 1D wire networks. *Nature Physics*, 7:412–417, 2011. URL http://dx.doi.org/10.1038/nphys1915.

[122] M Burrello, B Van Heck, and A R Akhmerov. Braiding of non-Abelian anyons using pairwise interactions. *Phys. Rev. A*, 87:022343, 2013. URL http://dx.doi.org/10.1103/PhysRevA.87.022343.

[123] T. Hyart, B. Van Heck, I. C. Fulga, M. Burrello, A. R. Akhmerov, and C. W J Beenakker. Flux-controlled quantum computation with Majorana fermions. *Physical Review B - Condensed Matter and Materials Physics*, 88(3):1–17, 2013. URL http://dx.doi.org/10.1103/PhysRevB.88.035121.

[124] Sagar Vijay and Liang Fu. Teleportation-based quantum information processing with Majorana zero modes. *Phys. Rev. B*, 94:235446, 2016. URL https://doi.org/10.1103/PhysRevB.94.235446.

[125] Thomas L Schmidt, Andreas Nunnenkamp, and Christoph Bruder. Majorana qubit rotations in microwave cavities. *Phys. Rev. Lett.*, 110:107006, 2013. URL https://doi.org/10.1103/PhysRevLett.110.107006.

[126] Chetan Nayak, Steven H Simon, Ady Stern, and Michael Freedman. Non-Abelian anyons and topological quantum computation. *Reviews of Modern Physics*, 80 (September):1083, 2008. URL https://doi.org/10.1103/RevModPhys.80.1083.

[127] Jie Liu, Andrew C Potter, K T Law, and Patrick A Lee. Zero-bias peaks in the tunneling conductance of spin-orbit-coupled superconducting wires with and without Majorana end-states. *Phys. Rev. Lett.*, 267002(December):1–5, 2012. URL https://doi.org/10.1103/PhysRevLett.109.267002.

[128] Olesia Dmytruk, Mircea Trif, and Pascal Simon. Cavity quantum electrodynamics with mesoscopic topological superconductors. *Phys. Rev. B*, 92:245432, 2015.

[129] Jukka I. Väyrynen, Gianluca Rastelli, Wolfgang Belzig, and Leonid I. Glazman. Microwave signatures of Majorana states in a topological Josephson junction. *Phys. Rev. B*, 92:134508, 2015.

[130] Matthieu Dartiailh, Takis Kontos, Benoit Doucot, and Audrey Cottet. Direct cavity detection of Majorana pairs. *unpublished*, 2016.

[131] F Kuemmeth, S Ilani, D C Ralph, and P L McEuen. Coupling of spin and orbital motion of electrons in carbon nanotubes. *Nature*, 452:448–52, 2008. URL http://dx.doi.org/10.1038/nature06822.

[132] Jay D Sau and Sumanta Tewari. Topological superconducting state and Majorana fermions in carbon nanotubes. *Phys. Rev. B*, 88:054503, 2013. URL https://doi.org/10.1103/PhysRevB.88.054503.

[133] D. C. Ralph, C. T. Black, and M. Tinkham. Spectroscopic Measurements of Discrete Electronic States in Single Metal Particles. *Phys. Rev. Lett.*, 74(16): 3241–3244, 1995. URL https://doi.org/10.1103/PhysRevLett.74.3241.

[134] J.-D. Pillet, P Joyez, Rok Zitko, and M F Goffman. Tunneling spectroscopy of a single quantum dot coupled to a superconductor : From Kondo ridge to Andreev bound states. *Phys. Rev. B*, 88:045101, 2013. URL https://doi.org/10.1103/PhysRevB.88.045101.

[135] A Kumar, M Gaim, D Steininger, A Levy Yeyati, A Martin-Rodero, A. K. Hüttel, and C. Strunk. Temperature dependence of Andreev spectra in a superconducting carbon nanotube quantum dot. *Phys. Rev. B*, 075428:1–6, 2014. URL https://doi.org/10.1103/PhysRevB.89.075428.

[136] G. A. Steele, A. K. Hüttel, B. Witkamp, M. Poot, H. B. Meerwaldt, L. P. Kouwenhoven, and H. S. J. van der Zant. Strong coupling between single-electron tunneling and nanomechanical motion. *Science*, 325(5944):1103–1108, 2009. URL http://dx.doi.org/10.1126/science.1176076.

[137] Benjamin Lassagne, Yury Tarakanov, Jari Kinaret, David Garcia-Sanchez, and Adrian Bachtold. Coupling mechanics to charge transport in carbon nanotube mechanical resonators. *Science*, 325(5944):1107–1110, 2009. URL http://dx.doi.org/10.1126/science.1174290.